THÈSE POUR OBTENIR LE GRADE DE DOCTEUR
DE L'UNIVERSITÉ DE MONTPELLIER

En Mécanique et Génie Civil ED I2S

École doctorale : Information, Structures, Systèmes

Unité de recherche Laboratoire de Mécanique et Génie Civil (LMGC)

Modélisation du calandrage des électrodes Li-ion en tant que matériau granulaire cohésif : des propriétés des grains aux performances de l'électrode

---

Simulation of the calendering process of Li-ion electrodes as cohesive granular material : from grain properties to electrode performances

Présentée par

Max SONZOGNI

Soutenue le 24 Novembre 2023

Devant le jury composé de

Jean-Noël ROUX, Chercheur IFSTTAR, Laboratoire Navier, U. Gustave Eiffel	Rapporteur
Vanessa MAGNANIMO, Professeure, University of Twente (NL)	Rapporteur
Olivier MILLET, Professeur, Université de La Rochelle	Examinateur
Yvan REYNIER, Ingénieur chercheur CEA, LITEN, CEA-Grenoble	Examinateur
Sébastien MARTINET, Ingénieur chercheur CEA, LITEN, CEA-Grenoble	Examinateur
Farhang RADJAI, Directeur de recherche, CNRS-LMGC	Directeur de thèse
Katerina IOANNIDOU, Chargée de recherche, CNRS -LMGC	Co-encadrant
Jean-Mathieu VANSON, Ingénieur chercheur CEA, IRESNE, CEA-Cadarache	Co-encadrant

UNIVERSITÉ DE MONTPELLIER

THÈSE POUR OBTENIR LE GRADE DE DOCTEUR
DE L'UNIVERSITÉ DE MONTPELLIER

En Mécanique et Génie Civil ED I2S

École doctorale : Information, Structures, Systèmes

Unité de recherche Laboratoire de Mécanique et Génie Civil (LMGC)

Modélisation du calandrage des électrodes Li-ion en tant que matériau granulaire cohésif : des propriétés des grains aux performances de l'électrode

---

Simulation of the calendering process of Li-ion electrodes as cohesive granular material : from grain properties to electrode performances

Présentée par

Max SONZOGNI

Soutenue le 24 Novembre 2023

Devant le jury composé de

Jean-Noël ROUX, Chercheur IFSTTAR, Laboratoire Navier, U. Gustave Eiffel	Rapporteur
Vanessa MAGNANIMO, Professeure, University of Twente (NL)	Rapporteur
Olivier MILLET, Professeur, Université de La Rochelle	Examinateur
Yvan REYNIER, Ingénieur chercheur CEA, LITEN, CEA-Grenoble	Examinateur
Sébastien MARTINET, Ingénieur chercheur CEA, LITEN, CEA-Grenoble	Examinateur
Farhang RADJAI, Directeur de recherche, CNRS-LMGC	Directeur de thèse
Katerina IOANNIDOU, Chargée de recherche, CNRS -LMGC	Co-encadrant
Jean-Mathieu VANSON, Ingénieur chercheur CEA, IRESNE, CEA-Cadarache	Co-encadrant

UNIVERSITÉ DE MONTPELLIER

To my one and only
Without whom I would not have made it
Who supported me through these hard times
And helped me become a better self

نموت عليك وردتي

Aknowledgments

During all these years working on this thesis, I had the chance to meet interesting and helpful people, in terms of work but also in themselves. I would like to acknowledge the financial support from the FOCUS program of the CEA to this thesis that allowed me to complete my professional formation, first in Cadarache and then in Montpellier.

I first would like to thank the reviewers, Jean-Noël Roux and Vanessa Magnanimo, that have accepted to be part of this thesis jury. Thanks also to the president Olivier Millet and examiners of this jury for taking the time to read my manuscript, for all their commentaries and attention to this work.

My sincere thanks go to my supervisors whose help was precious to me. I would like to express my deepest gratitude to my thesis director Farhang Radjai, a never-ending source of knowledge on granular materials and life in general. Your ideas and views on mechanics opened my mind to new subjects, and they will follow me through my entire life.
I am deeply grateful to my CEA supervisor Jean-Mathieu Vanson, whose contribution on this thesis is invaluable. Your presence during the first years of this thesis in Cadarache and your support throughout the entire journey kept me going and never surrender to defaitism and hopelessness.
I am also grateful to Katerina Ioannidou, whose help on understanding cohesive materials was really appreciated during this thesis.
Special thanks to Yvan Reynier and Sébastien Martinet at CEA Liten, our discussions gave me a better overview on the capabilities of electrical batteries and helped me understand them better.

I want to give a special attention to the people at the LMGC, part of whom I knew beforehand and none of whom will be forgotten. To the PMMD team members, Yohann, Duy, Chung, Lama, Anthony, Mohammad and Saeid, your support was priceless and the fruitful discussions we had often got me the spark to reignite my mind.
To my fellow PhD students, Thomas, Lea, Agathe B., Agathe S., Sam, Chenghe, Theo, Sneha, Nathan, Emilie, William, I really enjoyed the moments we spent together, laughing at our own despair, knowing what lies ahead of us but determined to face it. I hope for all of you to succeed in your career and I wish you all the best for the future.

Special thanks to the people I met in Cadarache, Simon, Louis B., Marius, Alexandre, Leo, Mohamed, Guilherme, Louis M., Josiane, Bruno and everyone else. Your support during the first years of this thesis helped me push through the beginning of this tough journey.

Finally, thanks to my parents and my brothers, who have been very supportive and proud of all my accomplishments. And of course, many thanks to my love Kamilia, the one who stood by my side and helped me face the many difficulties and harsh times. Your presence and help were what kept me going during these 3 years, I hope to keep you by my side forever.

Contents

Introduction **i**

List of Symbols **v**

1 Lithium-ion batteries: context and materials **1**
1.1 Lithium-ion batteries . . . 3
1.1.1 History of Lithium-ion batteries . . . 3
1.1.2 Working principle of Lithium-ion batteries . . . 5
1.1.3 Composition of a Lithium-ion battery . . . 6
1.1.4 Manufacturing process . . . 10
1.1.5 Experimental characterization . . . 14
1.2 Numerical simulations applied to the manufacturing process of Lithium-ion batteries . . . 17
1.2.1 Discrete Element Method . . . 18
1.2.2 Simulation of the calendering process of Lithium-ion battery electrodes using DEM . . . 24
1.2.3 Numerical characterization . . . 32
1.3 Conclusion . . . 36

2 Dynamic compaction of cohesive granular materials **39**
2.1 Introduction . . . 41
2.2 Methodology . . . 44
2.2.1 Force laws . . . 44
2.2.2 Sample preparation and system parameters . . . 47
2.3 Scaling of porosity . . . 50
2.3.1 Parametric study . . . 50
2.3.2 Modified cohesion number . . . 54
2.3.3 Fitting forms . . . 56
2.3.4 Effect of damping parameter . . . 58
2.4 Bonding structure . . . 60
2.4.1 Force networks . . . 60
2.4.2 Coordination numbers . . . 62
2.4.3 Force distributions . . . 64

2.5 Conclusion . . . 67

3 Triaxial compression of cohesive granular materials 71
3.1 Methodology . . . 73
3.2 Evolution of state variables . . . 74
3.2.1 Void ratio . . . 74
3.2.2 Stresses . . . 76
3.2.3 Cohesive strength . . . 77
3.2.4 Coordination number . . . 78
3.2.5 Anisotropies . . . 79
3.3 Relationships between state variables . . . 82
3.3.1 Void ratio and stresses . . . 82
3.3.2 Anisotropy and coordination . . . 82
3.4 Conclusion . . . 83

4 DEM simulation of the calendering process 87
4.1 Materials and methods . . . 91
4.1.1 Contact force laws . . . 91
4.1.2 Simulation of calendering . . . 93
4.1.3 Calculation of ionic and electric conductivities . . . 95
4.2 Results and discussion . . . 97
4.2.1 Calendering steps . . . 97
4.2.2 Thickness, porosity, and elongation . . . 98
4.2.3 Evolution of microstructure . . . 103
4.2.4 Electronic properties . . . 107
4.3 Conclusion . . . 110

General conclusions 115

Extended summary in french 119

Bibliography 124

Introduction

The usage of electronical devices developed tremendously in the last years and the demand is exponentially increasing on the market. For electric vehicles and portable devices such as smartphones and laptops, the demand is mainly focused on energy storage. Electrical energy storage is performed using electrical batteries, which can store and deliver electrical energy through chemical reactions. Today's 3rd generation batteries are based on electrodes exchanging Li^+ ions, hence the name Lithium-ion batteries. To achieve higher-performance batteries, two ways of improvement may be investigated: either using new materials, which means developing new battery materials, or improving the already existing manufacturing processes. The second option appears to be more suited to the reduction of production costs and optimization of the current models.

The manufacturing process of Li-ion batteries consists of five main steps: mixing, coating, calendering, assembly and filling (see Figure 1). Calendering involves passing the coated electrodes between two rotating cylinders to reduce their thickness (see Figure 2). It increases their volumetric density, and consequently their energy density, enabling to produce smaller batteries with the same storage capacity. However, it has been shown that when electrodes are over-calendered, i.e. when their thickness is highly reduced, the batteries that are produced struggle to deliver the entirety of the energy they contain when subjected to high charging power.

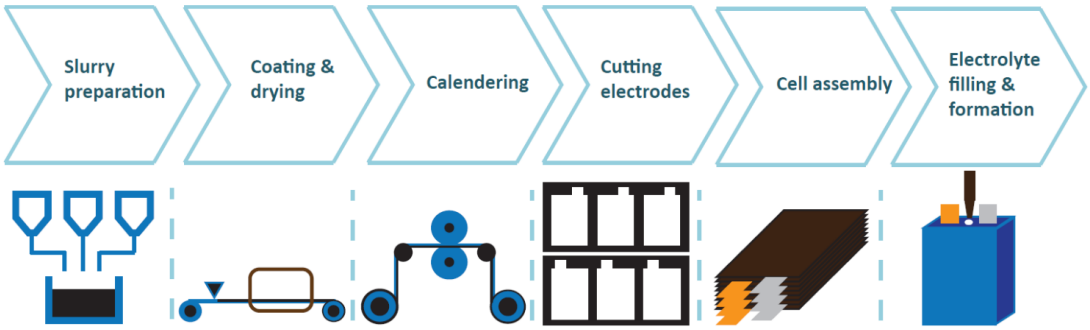

Figure 1: *Steps of the manufacturing process of Li-ion batteries [160].*

Industrials are thus facing a dilemma between energy storage capacity and charging rate. We aim here to study the effects of the calendering process on electrode properties in order to better understand the influence of each manufacturing parameter on the electrode



Figure 2: *Calendering machines used for the manufacturing of Li-ion battery electrodes (CEA LITEN).*

final properties by means of simulations. The usage of simulation tools to study the influence of calendering makes it possible to carry out test campaigns numerically allows to study more parameters at a lower cost. Numerical simulations can reveal physical mechanisms and properties appearing at scales that cannot be easily detected experimentally, enabling us to develop new solutions and improve the manufacturing process. As shown in Figure 3, the electrodes can be modeled as cemented granular materials composed of nearly spherical active material particles and a binding matrix of polymer and conductive additives. For this reason, the numerical approach based on the Discrete Element Method (DEM) provides a natural tool for the simulation of Li-ion electrodes.

The goal of this thesis work is to develop DEM simulations to model the calendering process and understand its effects on the conductivity and energy density of Lithium-ion electrodes, which control the charge/discharge rate and autonomy of Li-ion batteries. The nature of this process raises scientific issues that can be addressed owing to recent advances in the cross-disciplinary field of granular materials:

1. What is the range of porosities that can be be obtained in a granular material and how it depends on the preparation method?

2. How does the volume change behavior of cohesive granular materials depend on their initial porosity?

3. Can the effect of calendering process on the electrode be reduced to that of uniaxial compaction or triaxial compression? Does shear deformation induced by rolling play a role?

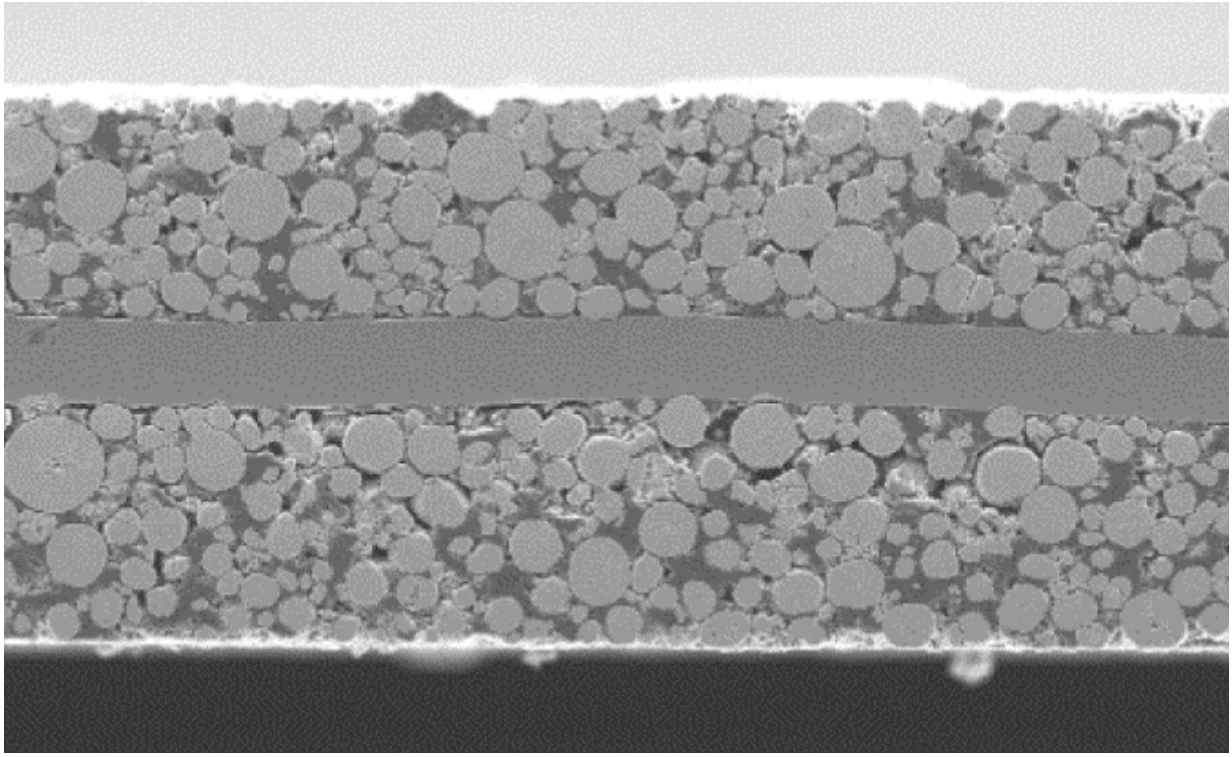

Figure 3: *Cross-section of a Li-ion cathode composed of active material particles and binding matrix (CBD). The central sheet is the electric current collector.*

4. How is the bonding structure of the electrode modified by the level of calendering? Is the mechanical strength of the electrode increased?

To address these issues, we perform DEM simulations of calendering, dynamic isotropic compaction, and triaxial compression. For the simulations of the calendering process we develop a new cohesive elasto-plastic force law to account for the binding material and a realistic model of the calendering setup. Extensive parametric study is carried out to analyze the effects of thickness reduction and calendering speed on electrode porosity and its microstructure (particle connectivity, anisotropy, force transmission). We also calculate the effective electrical and ionic conductivities by means of Fast Fourier Transform (FFT). On the other hand, we characterize the effects of dynamic isotropic compaction on the porosity and microstructure of cohesive granular materials to determine the range of accessible porosities and their scaling with system parameters. We characterize the mechanical strength and volume change behavior of cohesive numerical samples under triaxial boundary conditions to assess the effect of initial porosity.

Thesis outline

The first chapter is a literature review on Li-ion batteries, calendering process, and granular materials. We present the important characteristics of a battery, the different elements forming an electrode and their manufacturing process. We focus on the importance of the calendering process on the battery properties. We present different simulation models developed around the calendering of Li-ion battery electrodes, each one with its advantages and short-comings. We also briefly present general aspects of cohesive granular materials.

The second chapter is devoted to a parametric study of the isotropic compaction of cohesive granular materials. We study how the material parameters and compressive pressure influence the microstructure of the granular medium. The different parameters considered are particle size, elastic stiffness, adhesion force and applied pressure. We analyze in detail the combined effects of these parameters on the porosity, microstructure and force transmission. We introduce a dimensionless scaling parameter and deviations from the proposed scaling due to finite size effects.

The third chapter is devoted to triaxial compression of the configurations obtained in the previous study to assess their mechanical and microstructural properties. In particular, we are interested in the evolution of void ratio and cohesion of these configurations. We study the evolution of stress ratio, void ratio, coordination number and anisotropy for different levels of adhesion. We show that all the parameters are closely linked to one another through the adhesive force and that in cohesive granular materials, triaxial compression does not allow to significantly modify the porosity even in the case of highly porous materials.

In the fourth chapter, we present our numerical calendering simulation model including a cohesive elasto-plastic force law and a rotating cylinder. We consider the evolution of porosity, elongation and microstructure for different levels of thickness reduction and calendering speed. We compute the electrical and ionic conductivities of our numerically calendered electrodes using the FFT method. We show how they are related to the calendering parameters and the different microstructural properties of the granular medium and which ones are the most influent. These simulations, together with the results of triaxial compression prove that the shearing of the material imposed by rolling is the most important source of compaction in the calendering process and lead also a profound modification of the bonding structure.

The last chapter presents the main conclusions of this work and its perspectives. We also include an extended abstract in French.

List of Symbols

Calendering

C_f	Final thickness reduction ratio
C_r	Applied thickness reduction ratio
h_f	Thickness of the mixture deposit after calendering (μm)
h_g	Gap between cylinder and current collector (μm)
h_i	Thickness of the mixture deposit before calendering (μm)
v_{cal}	Calendering speed (m/s)

DEM parameters

α	Damping coefficient
δ_c	Equilbrium overlap for elasto-adhesive particles (μm)
δ_n	Normal overlap between two particles (μm)
δ_n^{max}	Largest overlap reached before unloading (μm)
δ_t	Cumulative tangential displacement between two particles (μm)
ϵ	Restitution coefficient (*Chapters 1,2,4*)
$\vec{f}$	Total contact force vector (N)
$\vec{f_t}$	Tangential force vector (N)
$\vec{n}$	Contact normal
ζ	Hardening exponent
f_a	Pull-off force (N)
f_c	Adhesion force (N)
f_n	Normal force (N)
f_v	Damping force (N)
k_1	Plastic stiffness (N/m)
k_2	Elastic stiffness (N/m)
k_n	Normal stiffness (N/m)
k_p	Reduced binding stiffness (N/m)
k_t	Tangential stiffness (N/m)

Mechanical

$\boldsymbol{a}$	Anisotropy matrix
$\boldsymbol{F'}$	Deviatoric fabric tensor
$\boldsymbol{F}$	Fabric tensor
ϵ	Axial strain (*Chapter 3*)
ϵ_q	Shear strain

η	Cohesion number
η^*	Modified cohesion number
ϕ	Solid fraction
σ	Normal stress (MPa)
σ_c	Cohesive stress (MPa)
σ_e	Elastic stress (MPa)
σ_{max}	Maximal stress measured on the calendering roll (MPa)
τ	Shear stress (MPa) (*Chapter 3*)
τ	Tortuosity (*Chapter 1*)
ε	Porosity
a	Contact radius (μm)
c	Cohesive strength (MPa)
e	Void ratio
e_r	Relative void ratio
e_{max}	Maximal void ratio
I	Inertial number
M	Critical shear stress ratio
N_0	Total number of floating particles
N_c	Total number of contacts
N_p	Total number of particles
p	Pressure or mean stress (MPa)
p_h	Pressure applied on lateral walls (MPa)
p_{crit}	Critical pressure (MPa)
q	Deviatoric stress (MPa)
v_{crit}	Critical velocity (m/s)
Z	Total coordination number
Z^+	Compressive coordination number
Z^-	Tensile coordination number

Material

δ_e	Yield strain of the active material (μm)
γ	Surface energy (J/m^2)
λ_{el}	Electric conductivity (mS/cm)
λ_{ion}	Ionic conductivity (mS/cm)
μ	Friction coefficient
ν	Poisson ratio
ρ	Density (g/cm^3)
σ_a	Yield strength of the binder (MPa)
d_{50}	Mean size of AM particles (μm)
E	Young modulus (MPa)
G	Shear modulus (MPa)
m	Mass of a particle (g)
R	Radius of a particle (μm)
R_p	Coating layer thickness (μm)

Chapter 1

Lithium-ion batteries: context and materials

Lithium-ion batteries finds their application in a wide range of industrial and customer products. Their performances, such as charging rate and energy storage capacity, are highly influenced by the microstructure of the electrodes, and thus the manufacturing process. For modern batteries, it involves a compaction step called calendering where the thickness of the electrode is reduced between two cylinders in order to increase its density. However, this compaction step increases also the tortuosity of the electrode, which decreases the final charging rate of the battery ; thus, a compromise is necessary between energy storage and charging rate.

The first part of this chapter focuses on Li-ion batteries in general : their development history, how they work, the various components composing them, the current manufacturing process, and the tools and methods used to characterize them experimentally. In the second part we present numerical methods used to study the calendering of Li-ion battery electrodes. Focus is made on the Discrete Element Method as it is the one used in this thesis. Various models from the literature are explained, how they simulate the calendering process, the representation of the different components of the electrode and how they interact. Some numerical properties characterized with these methods are shown and how they are obtained.

Introduction

In the last decades, the usage of electronic devices has greatly increased and recent studies show an ever-growing demand [156, 37]. In the case of electric vehicles and portable devices such as telephones and laptops, demand is mainly focused on energy storage. This relies on electrical batteries, which store and deliver electrical energy through chemical reactions. Current battery models, known as batteries of 3rd generation, are based on electrodes exchanging Li^+ ions. To improve the performances of the batteries, two ways may be explored : either using new materials, which means developing new battery designs in terms of both architecture and usage, or improving the already existing manufacturing processes; this second alternative is better suited to reduce the production costs and optimize current designs [193, 81].

Currently, the manufacturing process of Li-ion batteries follows 5 steps : mixing, coating, calendering, assembly and filling. Calendering involves passing the coated electrodes between two rotating cylinders to reduce their thickness. This increases their volumetric density, and consequently their energy density, enabling to produce smaller batteries with the same storage capacity. However with over-calendered electrodes, *i.e.* when their thickness is greatly reduced, the batteries that are then produced have difficulty delivering the entierety of the energy they contain when submitted to high charging power [64, 86] ; they struggle to deliver all the energy they contain quickly.

Manufacturers are thus facing a compromise between energy storage capacity and charging rate. It would therefore be interesting to look at the effects of calendering process on the electrode properties in order to better understand the influence of each parameterand the interplay between these parameters, energy storage capacity and charging rate. The goal of this thesis work is to study the effects of the calendering process on the electrode in order to better understand the influence of the manufacturing parameters on the electrode final properties.

1.1 Lithium-ion batteries

1.1.1 History of Lithium-ion batteries

A battery contains two electrodes, an anode and a cathode, separated by a chemical compound called electrolyte, which exchange ions in order to create a chemical potential difference, generating thus an electrical current. The voltage of this current and the amount of energy that can be delivered depend on the battery's composition and microstructure. Batteries can be distinguished into 2 categories : primary and secondary, also known respectively as cells and accumulators. Primary batteries are designed to have only one cycle of use, *i.e.* unlike secondary batteries they are not designed to be recharged. Therefore, once completely "drained" of their electrical energy, they can no longer be used. Hereafter, the word *battery* will be used to designate accumulators (*i.e.* rechargeable batteries).

Over the years, several different types of rechargeable battery have emerged [6]. Starting

with the first lead-acid batteries developed in the 1850s, the Nickel-Cadmium (Ni-Cd or NiCad) models of the late 19th century were replaced by the more efficient Nickel-Metal Hydride (Ni-MH) models of the 1960s. The arrival and development of Li-ion batteries since the 1970s has enabled us to achieve better performance in terms of power and energy as shown in Figure 1.1.

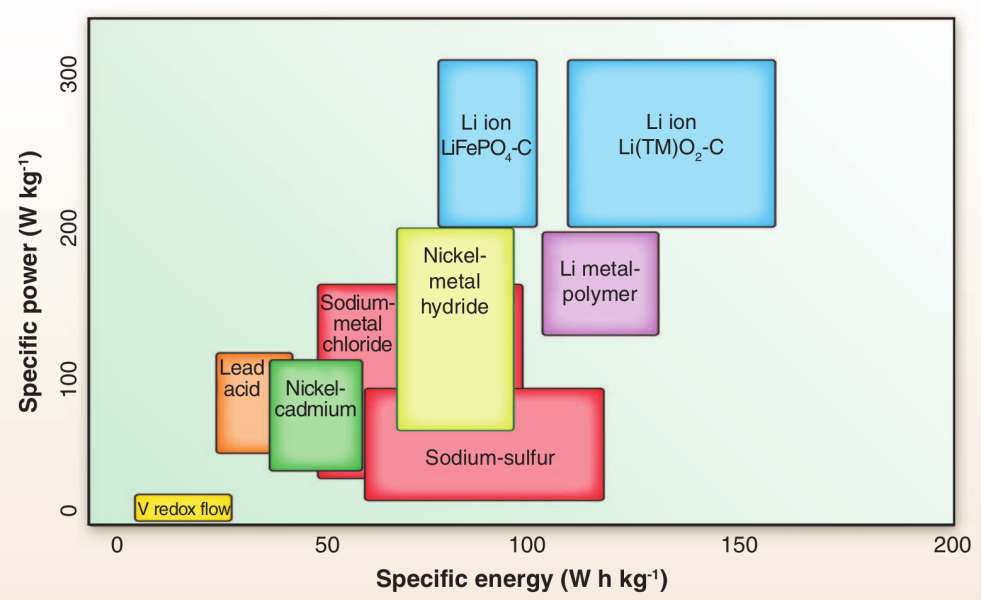

Figure 1.1: *Specific power and energy for different types of rechargeable batteries [37]*

The first lithium battery model, developed by Whittingham [190], goes back to the 1970s. This version used $LiTiS_2$ as cathode and pure lithium and anode, making it impossible for the battery to be recharged and resulting in high manufacturing costs. By replacing the cathode material with cobalt oxide ($LiCoO_2$), Goodenough succeeded in producing rechargeable lithium batteries, which were later produced by Sony in the 1990s. The use of carbon black as an anode material, proposed in 1985 by Yoshino [202], resulted in more stable and less expensive lithium batteries. These three men will be awarded the Nobel Prize of Chemistry in 2019 for their work on the development of lithium-ion batteries.

There exists different types of rechargeable Lithium-ion batteries, divided into "generations" according to the type of material composing them [166]. Table 1.1 lists these different generations ; currently, industrially produced batteries are based on 1st and 2nd generation materials, although 3rd generation batteries are starting to emerge [96]. A 2017 European Commission report predicts their full deployment by 2025, while the switch to all-solid (generation 4) or Lithium-air (generation 5) batteries is not yet considered [166].

The transition to 4th generation all-solid batteries will involve replacing the liquid electrolyte with a solid compound, but also using pure lithium anodes as well as so-called conversion cathode materials which are expected to be more efficient than the current ones

Cell generation	Cell chemistry
Generation 5	• Li/O_2 (lithium-air)
Generation 4	• All-solid-state with lithium anode • Conversion materials (primarily lithium-sulphur)
Generation 3b	• Cathode: HE-NMC, HVS (high-voltage spinel) • Anode: silicon/carbon
Generation 3a	• Cathode: NMC622 to NMC811 • Anode: carbon (graphite) + silicon component (5-10%)
Generation 2b	• Cathode: NMC523 to NMC622 • Anode: carbon
Generation 2a	• Cathode: NMC111 • Anode: 100% carbon
Generation 1	• Cathode: LFP, NCA • Anode: 100% carbon

Table 1.1: *Classification of the different generations of Lithium-ion batteries [166]*

[119, 203]. These models are still under development or at the experimental stage, which would still require a phase of adaptation to industrial manufacturing processes before seeing this new type of battery go live on the market [28].

The goal of this section is to investigate the current manufacturing process of Li-ion batteries. Given that 3rd generations batteries and below are currently industrially produced at a large scale, the study will focus on these models.

1.1.2 Working principle of Lithium-ion batteries

An electrical battery works by creating a difference in electrical and chemical potential between 2 poles. Figure 1.2 shows the composition and working principle of a conventional Lithium-ion battery. There are 3 main components in a Li-ion battery : the negative and positive electrodes (respectively called anode and cathode) and a separative phase made up of an electrolyte and possibly a separator. The main component of the electrodes is the active material, such as graphite for the anode and $LiCoO_2$ (LCO) for the cathode. The electrolyte consists of a liquid phase in which lithium-based salt compounds are dissolved to enable and improve the flow of ions from one electrode to the other.

During the first run of the battery, the cathode contains most of the Li^+ ions. During the charging phase, the electrons contained in the cathode will flow through an external circuit to the anode. In order to balance the ionic charges inside the battery, the Li^+ ions present in the cathode will flow through the electrolyte to reach the anode, which was negatively charged due to the external supply of electrons. Inversely, when the battery is discharged, a negative charge is applied to the cathode, causing the Li^+ ions contained in the anode to come back to the cathode. The battery's state of charge can then be checked by comparing the quantity of ions present in each electrode : the battery will be considered

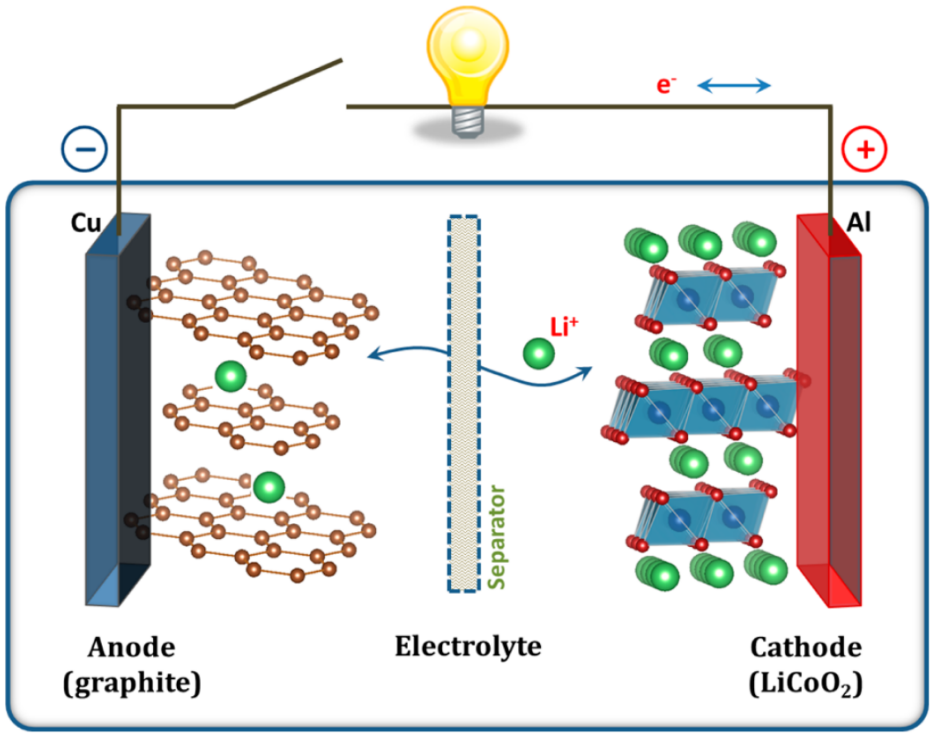

Figure 1.2: *Working principle of a Li-ion battery [53]*

charged when the majority of the ions are present in the anode, and discharged when they are in the cathode.

1.1.3 Composition of a Lithium-ion battery

A current-generation Lithium-ion battery consists of an assembly of anodes and cathodes, between which a liquid electrolyte has been poured. Each type of electrode contains a specific active material which characterize it, as well as a binder to maintain its integrity, and a current collector in order to transport the electrical current between the battery's poles. Electronic additives can also be added to the cathode in order to improve its electrical conductivity. As far as cathode and anode materials are concerned, we will be focusing on the materials of 3rd generation batteries (see Table 1.1).

Cathode active materials

Among cathode materials, the first one to be used in commercial batteries was the $LiCoO_2$ (LCO). Introduced in the 1980s [104], it is still widely used in commercial battery production due to its high storage capacity and relatively simple manufacturing process. The relatively high cost of cobalt has led to the emergence of new designs that reduce the proportion of cobalt in the active material. The $LiNi_{0.8}Co_{0.15}Al_{0.05}O_2$ (NCA) largely replaces

cobalt with nickel and aluminum. Its usage has grown exponentially in recent years due to its use in Tesla's first electric vehicle models [114]. The main feature of NCA-based batteries is their high theoretical storage capacity, making them ideal for electric vehicles. Another widely used material in industrial batteries is the $LiNi_xCo_yMn_zO_2$ (NCM or NMC), not only for its high theoretical storage capacity, but also for its reduced cobalt proportion compared to LCO [198, 157]. An interesting aspect of this compound is that the proportion of each of the elements can be varied to get different performances depending on the desired use, the best known of which being the $LiNi_{0.33}Co_{0.33}Mn_{0.33}O_2$ (NMC-333) [199, 27]. Previous active materials used elements from the transition metal category but there is another category of intercalation materials which use polyanions. These can be easily recognized through their chemical name which contains a compound $(XO_4)^{3-}$ (where X = S, P, Si...,) giving them a higher reduction potential [115]. The emblematic material in this category is $LiFePO_4$ (LFP), which is known to give cathodes with good thermal stability [35].

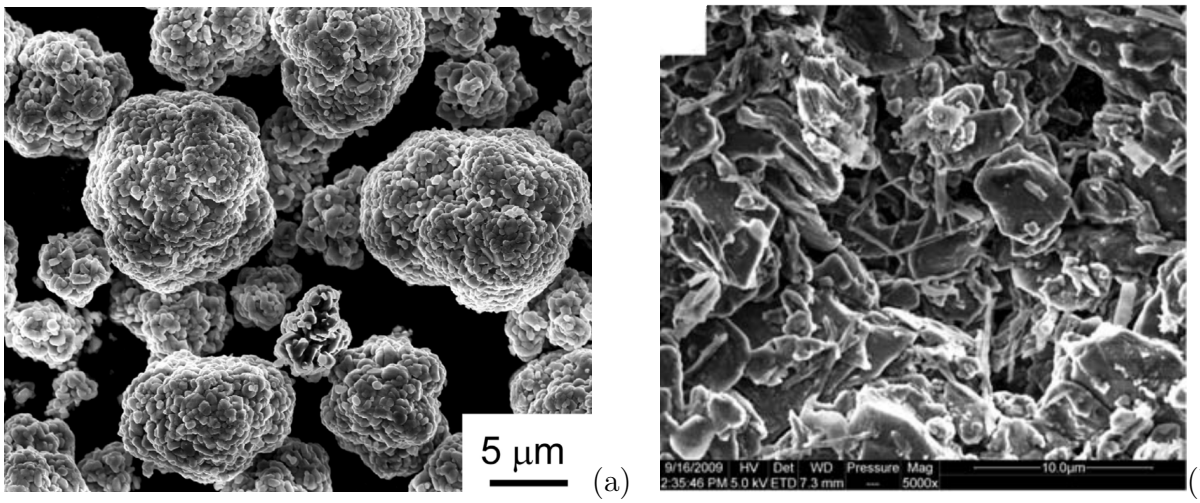

(a) (b)

Figure 1.3: *Active material particles observed through SEM (a) NMC-333 grains [27] (b) Graphite particles [85]*

Anode active materials

Regarding anodes of Li-ion batteries, few different materials are currently used. Historically, carbon-based compounds were used, with the first graphitic electrode designs developed in the late 1970s [7]. Because carbon is abundant and therefore relatively inexpensive, it quickly became the material of choice for anodes in commercial batteries. Graphite is the one with the best properties as an intercalation material [85, 65]. Anodes based on new carbon structures, such as carbon nanotubes or nanosheets, started to emerge in the last years [146]. An alternative to graphitic intercalation models is titanium oxides, the most widely used being $Li_4Ti_5O_{12}$ (LTO) [209]. Their distinctive features are that their rigid crystalline structure meaning that they undergo very little volume change during the

operational phase [29]. The presence of titanium, however, implies a higher manufacturing cost, an important parameter in the choice of materials for a battery intended for commercial use. Another material studied in the last years is silicon (Si). This element has theoretically the highest massic and volumetric electrical storage capacity [212]; its use as an active material in lithium battery anodes has therefore been envisaged since the end of the previous century [197]. The main drawback to its use is the significant volume variation that occurs during (de)lithiation phases, with up to 400% increase in volume [113].

Binder and conductive additives

To be mechanically stable the electrode needs, in addition to active material, to contain a binding polymeric compound. It plays an important role in the life and safety of the battery, as it will modify the overall mechanical stability of the electrodes [207]. During the first step of the battery manufacturing, the mixing phase, the binder initially solid is dissolved into a liquid solvent to disperses evenly. It will then mix with the active material particles, and infiltrate them if they are porous (see Figure 1.4a). After being coated onto the current collector, the solvent evaporates from the mixture during the drying step and the binder solidifies, creating solid bonds (Figure 1.4b) and/or cohesive surfacic forces (Figure 1.4c) [208]. Therefore, depending on the type of binder and the proportions of each components inside the electrode, the binder will produce different phases (see Figure 1.4d) which will influence the final properties of the battery [187, 73].

Among the binders used in the manufacturing of Lithium-ion batteries, polyvinylidene fluoride (PVDF) is by far the most popular [206]. Used since the 1970s, it is suitable for both anodes and cathodes, thanks to its high chemical resistance but also because it is chemically inert. As a result, it can only be dissolved in organic solvents such as N-methyl-2-pyrrolidone (NMP). NMP is known to be a flammable pollutant compound, and has been identified as toxic on chronic exposure, as well as having adverse effects on embryonic growth. [100] However there exist alternatives to NMP, with water-soluble binders such as polyacrylic acid (PAA) or carboxymethylcellulose (CMC) [91, 206]. The environmental impact of battery production and recycling is greatly reduced, as are manufacturing costs. On the industrial side, anode manufacturing has successfully moved towards the use of these solvents, but PVDF still remains the standard for cathode manufacturing.

These binders have a major inconvenient: as they bind around the active material particles (Figure 1.4d), they reduce not only the contact surface between the active material and the electrolyte, but also the contact surface between the particles of active material themselves. As they are not good electrical conductors, they create electrically insulating areas which have a major impact on the battery's charge-discharge rate [80]. To overcome this problem, another type of component is added during the mixing phase : conductive additives. These are carbon powder compounds like carbon black or acetylene black, carbon nanotubes or even sheets like graphene [205, 164]. Since the additives tend to mix with the binder due to their nanometric size during the drying phase, they form a phase known as *Carbon-Binder Domain* (CBD). The geometric structure of the additives has a strong influence on the final performance of the battery. Its proportion plays an important role in

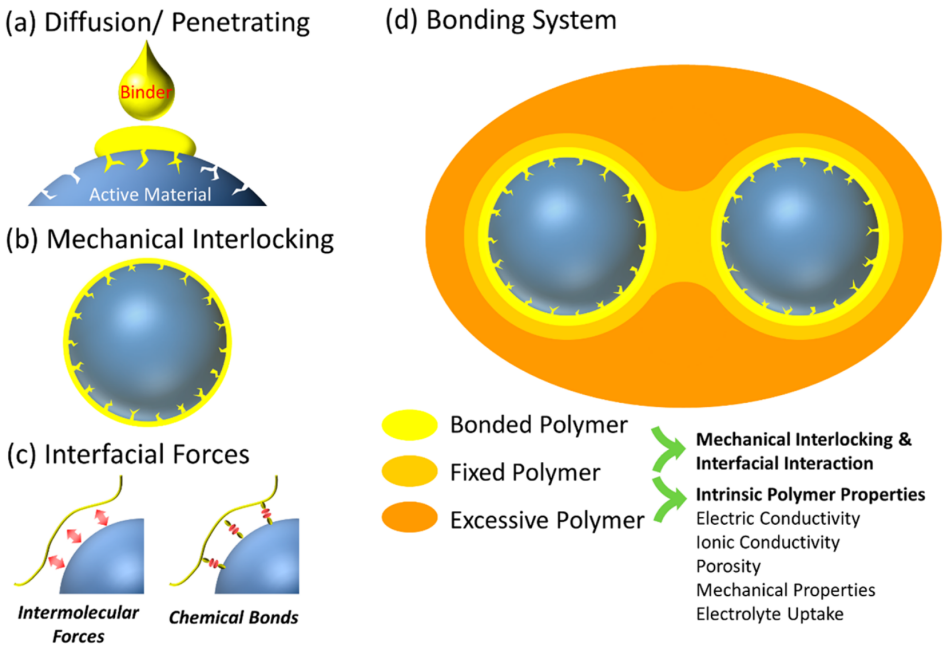

Figure 1.4: *Schematic illustration of the binding mechanism : (a) diffusion/penetrating process during electrode preparation (b) formation of mechanical interlocking during the drying process (c) interfacial bonding forces (d) polymer states in a bonding system [25]*

the final microstructure [79, 73]. The main issue with the use of electronic additives is that CBD has a low electrical storage capacity, which results in reduced battery storage density. In addition, the conductive additive particles tend to agglomerate together, increasing the tortuosity and hence the internal resistance [72].

Electrolyte

In a battery, the two electrodes can not be directly in contact : it would create an internal short circuit which would instantly drain it from its energy, which can lead to swelling followed by combustion [191]. To prevent any contact between the two electrodes, a separator is placed between them. It is a thin layer of porous polymer that allows ionic flow between the electrodes. However, to ensure that ion transportation is possible, a conductive compound called electrolyte is added after the electrodes have been assembled with the separator (see Section 1.1.4). It allows the lithium ions to flow between the electrodes during charge-discharge phases, thus closing the electrical circuit when the battery is in use. There are 2 categories of electrolyte : liquid and solid. A liquid electrolyte infiltrates the pores of the electrodes to maximize the diffusive surface area, while a solid electrolyte is inserted directly between the electrodes. In today's industrial Li-ion batteries, liquid electrolytes are used.

Liquid electrolytes are formed from lithium salts dissolved in polar solvents. Most of these salts, such as lithium perchlorate ($LiClO_4$) or lithium hexafluorophosphate ($LiPF_6$), have long been known and used in other fields, but new salts have been developed specifically for lithium batteries, such as lithium bis(oxalato)borate (LiBOB) or lithium bis(trifluoromethane-sulfonyl)imide (LiTFSI) [95]. Among the solvents used in industrial batteries, the first one to be employed was propylene carbonate (PC). Its good ionic conductivity and its hability to easily dissolve salts made it an ideal solvent for battery manufacturing. However, PC tends to facilitate the disaggregation of the carbon in the interface during the first use cycles, which can lead to internal battery failure. It was then replaced by ethylene carbonate (EC) which, although not as good as all the other solvents in terms of conductivity and solvency, creates more electrochemically stable interfaces [170]. The fact that EC is solid at room temperature can be counterbalanced by mixing it with another solvent, dimethyl carbonate (DMC). Unfortunately, this mixture is constrained by DMC's low ignition temperature (18°C vs. 160°C for EC, 55°C for the mixtures), thus limiting the battery's maximum operating temperature [196]. However, it is this blend that is used in the majority of commercial Li-ion batteries today, as it remains the best compromise between performance and safety [95].

Current collector

The current collector is the element onto which the other electrode components are coated. It is a metallic plate, made of copper for the anodes and aluminum for the cathodes, a few micrometers thick. During the operation phase, it allows for the electrons to flow from the active material particles to the poles of the battery.

1.1.4 Manufacturing process

The manufacturing process of industrial Li-ion batteries is divided in different steps illustrated in Figure 1.

Battery manufacturing begins with the mixture preparation of each electrode. First, the different solid components (active material and binder + conductive additives) are ground together in a mixer. The resulting powder is then poured into a liquid solvent and mixed to make the solution homogeneous.

The mixture obtained is then coated onto the current collector, and the thickness of the electrode is controlled using a blade. The composition of the mixture and the imposed thickness are used to define the mass loading (in g/m^2) of the electrode. The electrodes are then dried in an oven, if necessary under vacuum, to eliminate the solvent which is then no longer required. It is not uncommon for drying to be carried out in several stages and at different temperatures to ensure that all the solvent is evaporated [56].

Next comes the calendering step, in which the electrodes are compacted between two rotating cylinders to reduce their thickness and increase their energy density. Figure 1.5(b) shows a cross-section of an electrode after calendering, where the grains of active material, the binder+additive matrix and the current collector are clearly visible.

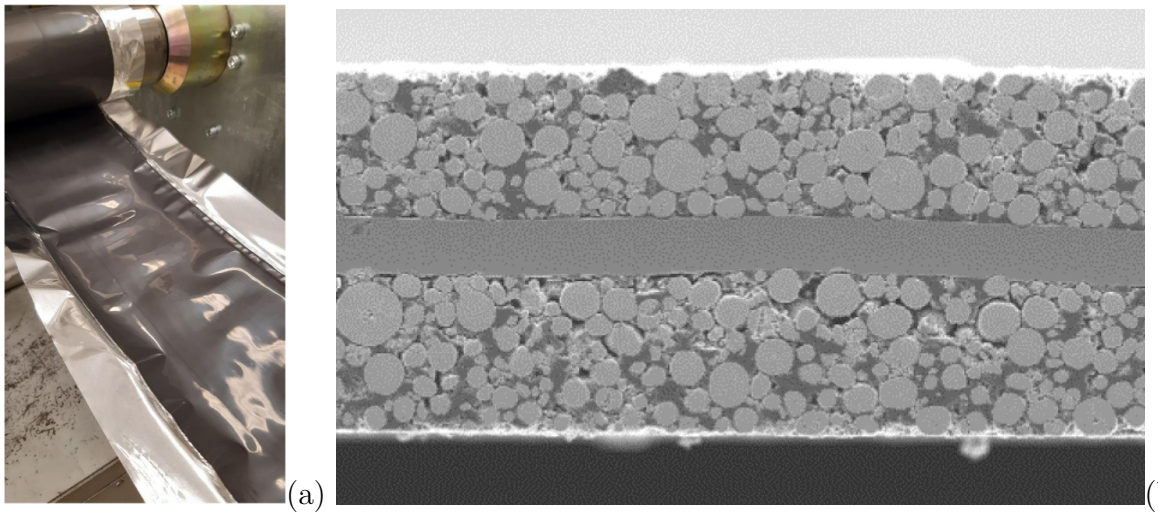

Figure 1.5: *Cathode after calendering (CEA Liten, 2018) (a) Electrode strip (b) Cross-section observed through SEM*

Once calendered, the electrodes form long strips like in Figure 1.5(a), which are then shaped and assembled according to the type of battery to be manufactured. Although a "functional" battery requires only a cathode and an anode, it is preferable to make multi-layer assemblies, where each electrode is physically isolated from the others by a separator, in order to increase the energy storage capacity. To obtain cylindrical batteries (Figure 1.6a), a positive and a negative strip are assembled with a separator, then folded to obtain the cylindrical shape. This results in batteries with a higher volumetric energy density. For batteries with a parallelepipedic geometry, called prismatic (Figure 1.6b), the strips are also rolled together, but this time by confining them in a box. With this form, the batteries can fit more easily to their final usage. For a third type of battery called a "pouch" (Figure 1.6c), electrodes are cut from strips, then stacked alternating between positive and negative elements. These batteries are simpler to produce on a large scale but also in a laboratory, which is why this form is often used in experimental studies [56, 77].

The next step consists in filling the previous assembly with liquid electrolyte to fill the remaining pores between and in the electrodes and separator. It is important that the electrolyte fills as many pores as possible to get the highest possible conductivity. Once filled, the battery is hermetically sealed to prevent any contact between the electrolyte and the air as some electrolyte components react easily with oxygen and water, leading to irreversible damage or even destruction of the battery [191].

Why study the calendering process

The calendering stage is one of the most important steps in the manufacturing process regarding the performance of the final battery : by reducing the thickness of the electrodes, their volumetric density will increase, and consequently their energy density and storage capacity. However, this compression brings the particles closer together, closing

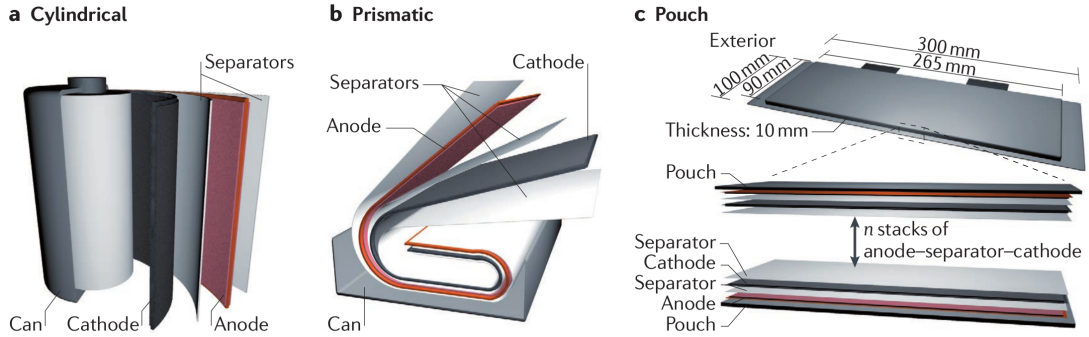

Figure 1.6: *Types of Lithium-ion cells : (a) Cylindrical (b) Prismatic (c) "Pouch" [28]*

the electrode's internal pores. With fewer open pores the contact surface between the electrolyte and the active material particles is reduced, and at the same time the battery's ionic conductivity (see Figure 1.7) [207, 75].

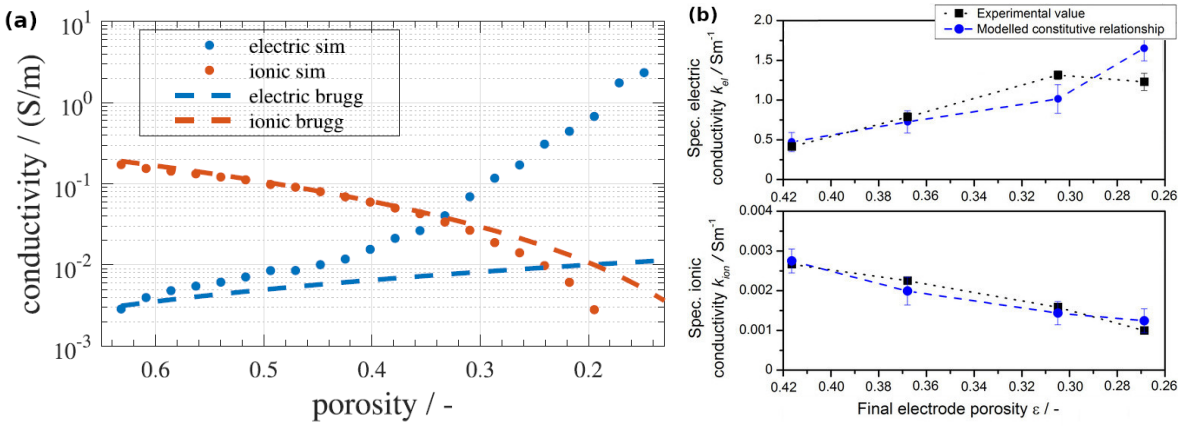

Figure 1.7: *Evolution of electrical and ionic conductivities of cathodes depending on their porosity [75, 151]*

It is therefore necessary to understand the influence of the numerous calendering parameters in order to obtain batteries with optimum properties [155]. The electrode composition will obviously have a major influence, particularly in terms of electronical but also mechanical properties [64, 86, 101]. Indeed, an electrode with a high proportion of binder will offer better adhesion of the active material particles onto the collector, thus avoiding its delamination during the calendering step. The electrode's initial porosity will influence its resistance to this compression; at equivalent stress, an initially more porous electrode will emerge from calendering with a higher porosity [151].

Regarding the calendering machines, influential parameters will depend on the machine's complexity. On the simplest ones, only the pressure applied by the cylinders

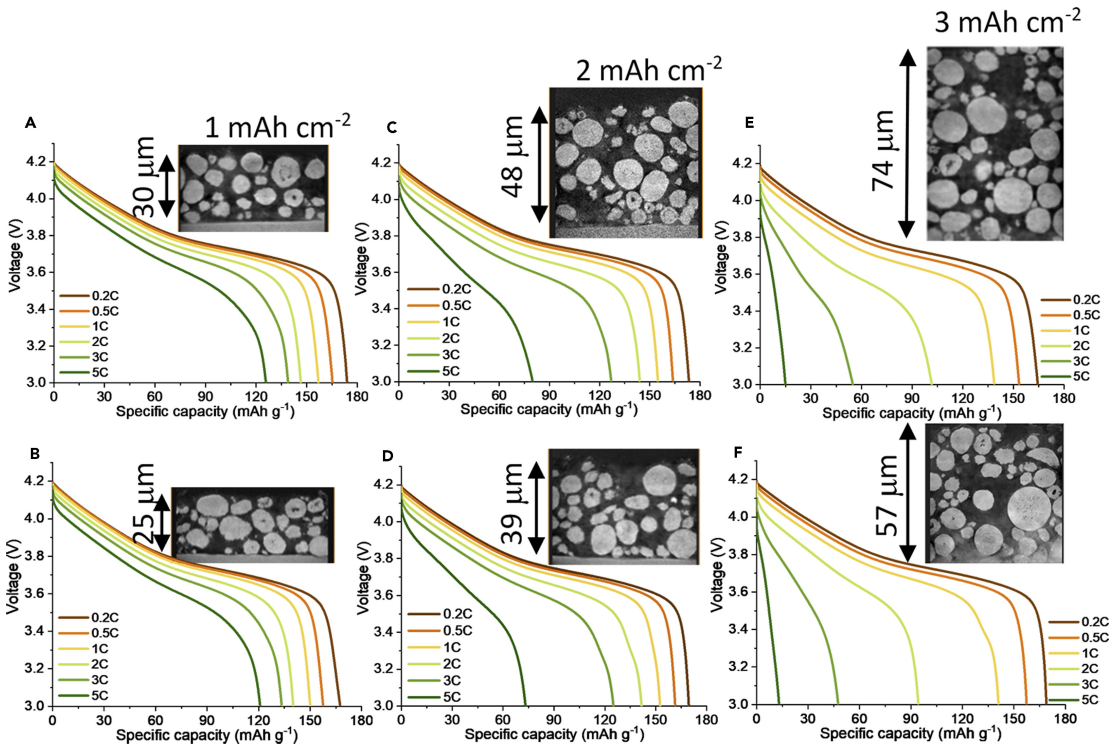

Figure 1.8: *Comparison of the discharge performance between electrodes of different mass loadings before and after calendering [86]*

and/or the opening gap between the cylinders can be controlled (even though the two are linked). However these parameters are the most influential on the final battery performances machinewise [155, 52, 117, 127]. Higher pressures lead to lower porosities, but can also induce fragmentation of the active material particles ; electrodes will be more compact, but their specific capacity will be highly reduced for high discharge electrical currents [128] (Figure 1.8). The higher the initial density of the electrodes, the greater their specific capacitance at high discharge levels is affected by the thickness reduction.

The travelling speed of the electrode between the rollers is controlled, but this does not appear to have a significant effect on the final properties if this speed is sufficiently low (of the order of 1 m/min) [155] ; however, most industrial production lines use calendering speeds between 30 and 100 m/min [81]. Calendering speed plays an important role in the battery manufacturing rate as it maximizes the production cadency. In addition, the size of the rolls will differ between a "laboratory" calendering machine and an industrial one : where the former use cylinders around 20cm in diameter, the latter can go up to 1m in diameter [71]. This size will have an important effect on the compressive part of calendering, as larger cylinders will allow pressure to be applied more gradually, favoring the vertical normal force over the horizontal tangential force, thus reducing the chances of the microstructure to break apart. Thus, some problems associated to calendering can only

be studied via industrial machines. There is hence a whole range of calendering parameters, both at machine and electrode level, which influence the final properties of the battery. It would therefore be interesting to study in detail the influence of each of these parameters during the calendering step.

1.1.5 Experimental characterization

Electrical characterization

Electrical batteries are identified by their energy capacity and electrical capacity. The electrical capacity, noted Q and measured in Ah or mAh, gives an indication of the total electrical charge that can be delivered by the battery. This value is obtained by using the battery at constant electrical current I and measuring the time required to discharge it completely ; the capacity is then given by the product of the electrical current and the time spent ($Q = I \times t$). Theoretical electrical capacity is given for 20h cycles. Energy capacity, measured in Wh, provides information on the amount of energy stored in the battery. It depends on the electrical capacity, and is calculated by multiplying the electrical capacity by the nominal battery voltage ($E = Q \times U$). This voltage corresponds to the potential difference between the battery's two poles, and represents therefore its state of charge : the lower the voltage, the more discharged the battery. For current Li-ion batteries, the voltage can vary between 3 and 5V depending on the active materials used [119].

However, depending on how the battery will be used, the electrical currents to which it might undergo will vary in intensity ; it has been shown that batteries do not react in the same way depending on the electrical currents to which they are subjected [86]. Under high currents, they are unable to deliver the full electrical charge they contain, resulting in lower electrical capacity values. The "different" electrical capacities of the battery are recorded during cycling tests with varying electrical currents ; this type of test is called *C-rate cycling* [57].

To get a more precise idea of battery performance, particularly at high frequencies, there exists a characterization method called Electrochemical Impedance Spectroscopy (EIS). By stimulating the sample with an alternating current of equation $E(t,\omega) = E_0 sin\,(\omega t)$, it will give a response similar to the solicitation but slightly offset, noted $I(t,\omega) = I_0 sin\,(\omega t + \phi)$. By comparing the solicitation and the response, the impedance $Z = \frac{E}{I}$ of the sample can be computed, which can be rewritten in complex form $Z\,(\omega) = \frac{E_0}{I_0} exp(j\phi) = Z_0\,(cos\,(\phi) + j sin\,(\phi))$, giving an intensity Z_0 and a phase shift ϕ. By repeating the process with different frequencies, it is possible to plot Bode diagrams for Z_0 and ϕ, which combined give a Nyquist diagram (Figure 1.9(a)). This diagram allows to approximate the behavior of the sample with an equivalent electrical circuit [10, 189], giving then a simplification of the battery's operating diagram (Figure 1.9(b)).

Knowing the diffusivity properties of the electrolyte and the geometry of the electrode, the effective ionic conductivity of the electrode can be computed. By comparing with the ionic properties of the electrolyte, this gives an estimation of the distance the lithium ions will have to travel to pass through the electrode; the ratio between this distance and the

thickness of the electrode is more commonly known as tortuosity, noted τ. Thus, a battery with a high equivalent resistance will generally have fairly tortuous electrodes along with a lower charge-discharge speed [55].

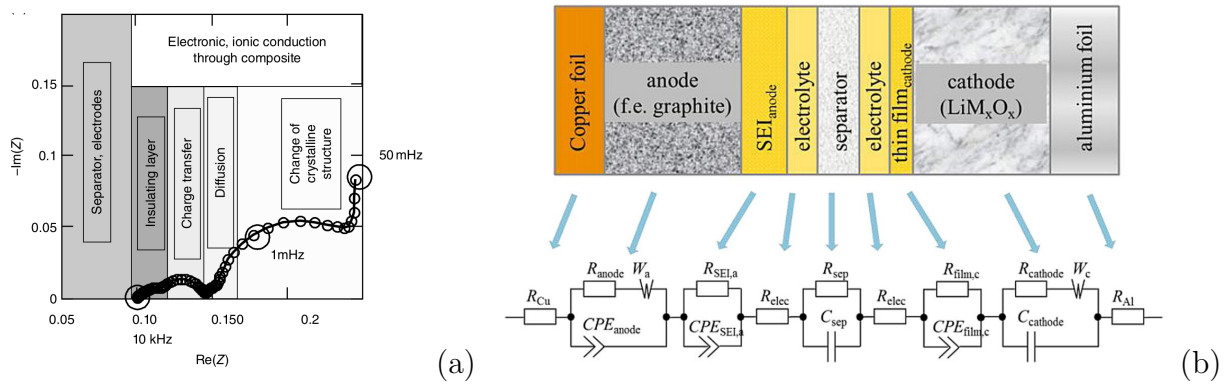

Figure 1.9: *EIS analysis of Li-ion batteries (a) Nyquist diagram of a cathode [10] (b) Equivalent electrical circuit of an entire Li-ion battery [189]*

Geometrical characterization

Tortuosity is dependent on the applied calendering but also on electrode composition. Indeed, depending on the type of active material used and the proportion of each component, electrode microstructure will differ [73]. The size and distribution of the pores is an important factor, as it defines the porosity of the electrode and the path taken by the ions when the battery is used. Some approaches exist to geometrically estimate the porosity of an electrode [14]. The simplest and most obvious one is to weigh the electrode and then, knowing its dimensions and the proportion of each of its components, determine the difference in volume with a "full" electrode ; this difference corresponds to the volume of internal pores [97]. However, this method is highly sensitive to precision errors, particularly when measuring electrode thickness. Alternatively, mercury porosimetry may be used. However this method, known as intrusion porosimetry, can only identify the volume of open pores, *i.e.* those accessible from the outside, and those large enough to allow the fluid to pass through. Closed or undersized pores cannot be identified, which can lead to significant errors in the porosity measurement depending on the microstructure [45].

These measurement techniques can not indicate whether or not there are local variations in the microstructure [14]. It is nevertheless possible to use imaging tools to directly observe the morphology of the sample, and thus its local microstructure. The Scanning Electron Microscopy (SEM) provides detailed images of the sample surface. A beam of electrons is projected onto a point on the surface of the sample, from which other electrons of lower energy but dependent on the material and its morphology are "stripped off". By scanning its entire surface, it is possible to analyze the sample in its entirety ; where an optical microscope can only achieve resolution down to the micrometer, SEM allows to get images

with nanometric precision. Figure 1.10a gives a clear view of each NMC grain and the surrounding binder matrix. For Li-ion electrodes, SEM is particularly useful for observing the state of the active material grains, especially their deformation and fragmentation due to calendering [207, 56]. X-ray computed microtomography (XCT) can be used to produce a 3D map of a sample without damaging it. It produces a series of cross-sectional views of the sample which, once digitally assembled, are used to recreate a 3D model of the sample. This provides a representation of the overall microstructure with an accuracy up to 50 nm (depending on the device and the material); it is thus possible to visualize the internal pores of the electrode and estimate its tortuosity and ionic conductivity [108]. However, only the microstructure of the active material particles can be obtained by XCT, as the absorption range of the CBD is too small to be able to differentiate it from the pores [211]. Figure 1.10b shows a 3D reconstruction of a cathode microstructure obtained by combining XCT images and phase contrast microscopy, where LCO grains are identified in black and additive particles in red.

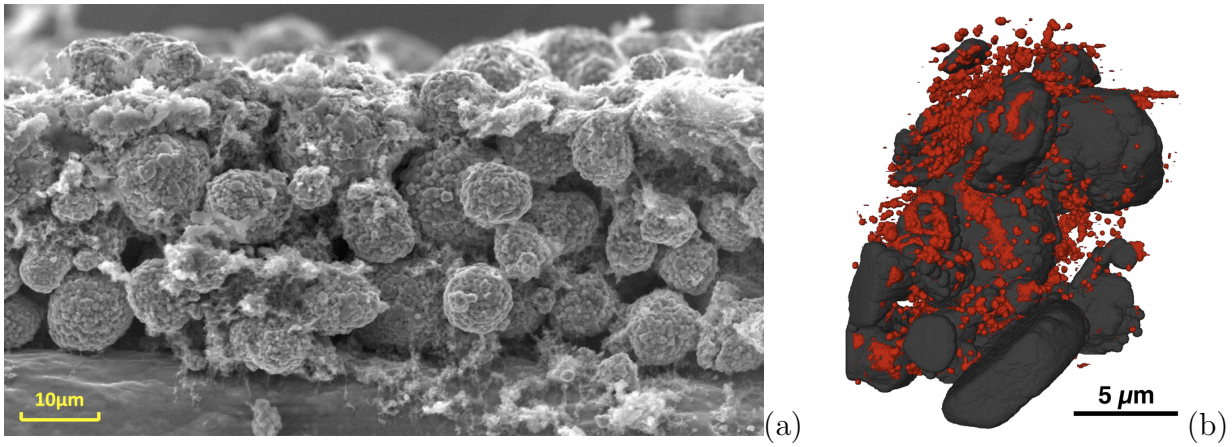

(a) (b)

Figure 1.10: *Cathode visualizations (a) SEM cross-section [32] (b) 3D reconstruction from XCT images [9]*

Mechanical characterization

From the microstructure, it is then possible to obtain information on the mechanical properties of the electrode, regarding both its components and the electrode as a whole. The most commonly used method to determine the behavior of micrometric grains is nanoindentation. Depending on the force and displacement measured and the punch used, it is possible to determine several characteristics of the studied material, the most common one being the hardness H and the elastic modulus E [121]. Applied to cathodes, nanoindentation showed that the values of H and E were much higher for NMC grains than for the CBD matrix [32, 210] and that the plastic deformation of the active material grains was dependent on their size [151].

Mechanical characterization of the entire battery can also be carried out using more traditional methods, such as tensile/compressive or shearing tests. With tensile/compressive studies, it is fairly straightforward to estimate the elastic modulus of the overall electrode, and if they are pushed to failure, plasticity and/or fracture criteria [210].

Peel tests are often used to check if the components of the electrode are firmly attached to each other and onto the collector. The electrode is held stationary by gluing either its collector or one of its faces, depending on whether the current collector has one or both of its faces coated, then the AM–CBD mixture is "peeled off" at a given angle, usually 90° or 180° [90]. This type of study measures the adhesion between the current collector and the mixture ; usually it is the adhesion of the binder to the collector that is studied due to the non-existent adhesion of grains of active material alone [186].

1.2 Numerical simulations applied to the manufacturing process of Lithium-ion batteries

In order to reduce the production and development costs of Lithium-ion batteries, one investigation solution is to employ numerical simulation methods. These tools can represent all or part of a real system in order to study its characteristics while reducing the number of experimental tests required to characterize it correctly. Furthermore they provide access to physical properties that are difficult, if not impossible, to measure experimentally. This not only reduces production costs, but also enables more extensive numerical test campaigns to be carried out once the model has been calibrated.

There are various numerical simulation methods applicable to battery simulation. Depending on the studied system, some methods will be more appropriate : while studying Li-ion battery electrodes, the Finite Element Method and the Discrete Element Method are mainly used, as they can represent the structural changes that electrodes undergo during the manufacturing process. It should be noted however that other methods have also been used to simulate the electrodes, such as the one developed by Lenze et al. [77] which relies on a purely mathematical model to estimate the electrical characteristics of the final battery. The model of Duquesnoy et al. [40] used a database of experimental results to build an artificial intelligence able to determine the characteristics of the final electrode given certain input data.

The Finite Element Method (FEM) is based on a continuous representation of the system. It employs deformable geometric elements, which are linked together by their vertices, called nodes. The computation of the elements deformation and the displacement speed of the nodes is carried out by doing matrix computations, in which the interactions between the elements are defined in a stiffness matrix. This method is specially useful to represent material deformations or fluctuations that may occur between elements [179, 178, 99].

The Discrete Element Method (DEM) represents matter as a divided medium, with each element considered as an isolated body. Each element is then defined with a specific

position, velocity, shape and material. The movement of the elements is determined by the equations of dynamics into which the forces resulting from the interactions between the elements are computed. This numerical simulation method is commonly used to study the mechanics of rocks and soils [61], but also other industrial fields dealing with granular media, such as the production of pharmaceutical tablets [99], the grinding of grains in a rotating drum [122], or, in the case of this study the manufacturing process of electrical batteries [52, 149, 153]. Indeed, given the granular composition of the electrodes, it is appropriate to use the Discrete Element Method to represent the calendering of Li-ion electrodes.

1.2.1 Discrete Element Method

The Discrete Element Method was first introduced in 1979 by Cundall, initially as the Distinctive Element Method, to study assemblies of disks and spheres [30]. Since that, variants of DEM have been developed depending on the numerical method employed to compute the contact force between elements [133] ; the most common are Contact Dynamics (CD) and Molecular Dynamics (MD).

Contact Dynamics, introduced in the 1980s-90s by Moreau [60, 106, 107], is based on the fact that elements are rigid and cannot overlap (principle of unilaterality). This translates into the inequation $\delta \geq 0$, where δ represents the distance between two elements. When two elements are in contact ($\delta = 0$), it results in a contact force $f \geq 0$. Inversely, when the elements are no longer in contact ($\delta > 0$), then the contact force f is zero. The unilateral contact law (or Signorini criterium) results from this observation and, as shown in Figure 1.11a, stipulates that :

$$f \geq 0, \quad \delta \geq 0, \quad f.\delta = 0 \tag{1.1}$$

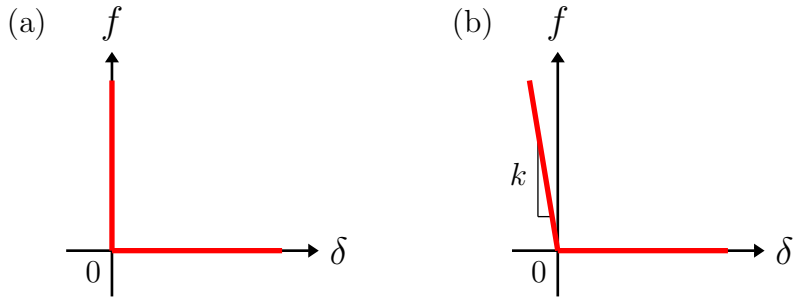

Figure 1.11: *Contact law graph (a) unilateral (CD) (b) allowing overlap (MD)*

On a contact, the resulting force can be defined as a vector $\vec{f}$ and decomposed into 2 parts, normal and tangential, in the form $\vec{f} = f_n\vec{n} + f_t\vec{t}$. The vector $\vec{n}$ gives the contact direction, while the vector $\vec{t}$ corresponds to the tangential direction of the contact and is

defined according to the relative velocity of the elements in contact : $\vec{t} = \vec{v}_t/||\vec{v}_t|$, where $\vec{v}_t = \vec{v} - (\vec{v}.\vec{n})\,\vec{n}$. Note that the tangential force $f_t\vec{t}$ (also denoted $\vec{f_t}$). Depending on the intensity difference between the normal and the tangential forces, Coulomb's criterion $f_t \leq \mu f_n$, with μ the friction coefficient, links the relative velocity of the elements to these forces. Indeed, if the tangential force is not big enough to overcome the resulting frictional force of the contact ($f_t < \mu f_n$), then the contact will be described as frictional and the sliding velocity between the elements v_t will be zero. Inversely, if the tangential force is able to compensate for the friction force ($f_t = \mu f_n$), then the contact will be described as sliding and any additional energy "added" to the tangential force will be transferred to the sliding velocity ($v_t \geq 0$). Therefore, similarly as for Signorini criterium, Coulomb's friction law can be defined with 2 inequations and one equation :

$$\mu f_n - f_t \geq 0, \quad v_t \geq 0, \quad (\mu f_n - f_t)\,.v_t = 0 \tag{1.2}$$

These two laws of solid mechanics are necessary to describe the behavior of two elements in contact, but they are not sufficient in themselves as they do not allow us to compute force and velocity values directly. It is then necessary to use appropriate resolution methods, such as the non-linear Gauss-Seidel algorithm (NLGS), which will iterate over all the contacts with provisional values until a convergence criterion is reached [36].

Molecular Dynamics on the other hand is based on other ways of managing contacts. Unlike Contact Dynamics, the molecular approach considers that on a very small scale the surface of the materials is covered with asperities that deform elastically upon contact. The impenetrability and Coulomb friction laws are approximated with high rate linear functions (see Figure 1.11b). Therefore, when two elements come into contact, δ the distance between them becomes negative and the elements can overlap. The unilateral contact law defining the system is no longer valid, and the relationship between distance and contact force is given by :

$$\delta > 0 \rightarrow f = 0, \quad \delta \leq 0 \rightarrow f = -k\delta \tag{1.3}$$

with k a rigidity stiffness coefficient. Hence the resulting contact force will depend on the overlap between the elements, and its value can be determined directly from the contact. Thus, the computation of contact forces is simpler, more flexible and more straighforward.

The Discrete Element Method algorithm is divided into 3 main steps as illustrated in Figure 1.12. First, starting from a given configuration, the couples of elements in contact are identified and a list of interactions is established. Based on the pairs of elements in contact, the resulting forces and moments are computed through contact laws. These forces and moments are then integrated into the equations of motion to obtain the position and velocity of the elements at the next time step, creating a new configuration.

Contact detection

To avoid testing whether each pair of elements is in contact for a given configuration (N×(N-1) possible pairs) and thus reduce the overall computational cost, the contact detection phase is broken down into 3 steps [133]. First, a proximity search phase will create

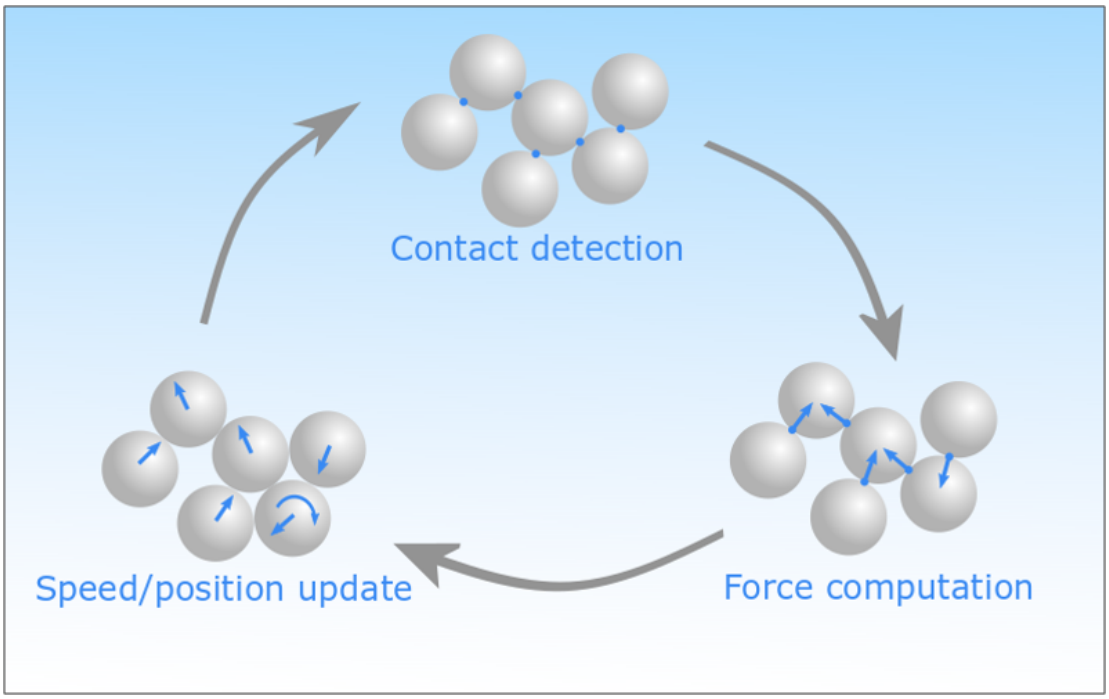

Figure 1.12: *Working principle of the Discrete Element Method algorithm*

a list of neighboring elements likely to come into contact. There are various methods for searching for an element's neighbors. The simplest one is to divide the space into uniform cubic elements and then, for each element, list those located in neighboring cubes, as illustrated in Figure 1.13a. This method is suitable for compact configurations where the elements do not move a lot, but reaches its limits when polydispersity is important and when there is a big difference in size between the smallest and largest elements. Another method involves enclosing each element in an equivalent volume (whose shape can be variable), and then projecting this volume onto the axes to define a list of intervals ; when two elements have all their intervals matching, they are then considered neighbors. Figure 1.13b illustrates this method. This second technique is more accurate in detecting neighbors, but can lose precision when the dimensions of the system differ by orders of magnitude.

The neighbors list is often refined before moving on to the next step. For simple elements such as spheres, it is common to reuse the same technique as in the previous step, with increased precision in order to reduce uncertainty about the contact point. For more complex elements (concave and/or multi-faceted), the refinement is carried out around each element's structure. Here each of the element's vertices, edges and faces will be endowed with an equivalent volume, specifying then which of these are most likely to be in contact with the partner element [183]. Finally, the contact points between each element is determined from this refined list. There are plenty of contact types, illustrated in Figure 1.14, which can be either point, line or planar, depending on the geometric

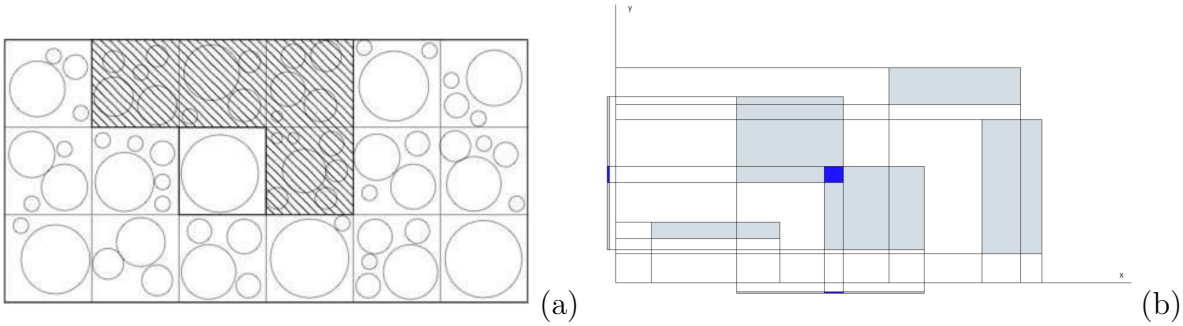

Figure 1.13: *Scheme for contact detection algorithms [133] (a) Neighboring cubes (b) Intervals*

entities in contact. However, it is possible to consider that all contacts can be defined as a combination of simple contacts, i.e. vertex-summit, vertex-edge, vertex-face and edge-edge; this way it is possible to redefine complex contacts as a set of contact points.

Although precise contact detection must be performed at every time step, less precise steps can be postponed in order to further reduce the computational cost. For example, for configurations where the relative speed between elements is low, it is possible to postpone the neighbor detection step. One of these methods is called the Verlet list, which will update the list of neighbors according to a time step linked to the overall movement of the configuration [184].

Force computation

Once the contacts have been identified, the resulting forces are computed for each one of them. Here we will focus on how to compute these values using the Molecular Dynamics method. A contact law is established to compute the normal and tangential components of the resulting force, defined as a function of the overlap between the elements and whose parameters are linked to the materials. The simplest contact law is Coulomb's linear elastic law with friction, illustrated in Figure 1.15.

Here, as defined in Equation 1.3, f_n the normal force is given by :

$$f_n = -k_n \delta_n \tag{1.4}$$

where k_n is the normal stiffness of the contact and δ_n the distance between the elements. The tangential force component is computed similarly as the normal force with :

$$\Delta \vec{f_t} = -k_t \Delta \vec{\delta_t} \tag{1.5}$$

where k_t is the tangential stiffness of the contact. Here an increment of force is computed as the tangential force depends on the relative velocity between the elements, with $\Delta \vec{\delta_t} = \vec{v_t} \Delta t$; if this velocity is null in the tangential direction($\vec{v_t} = \vec{0}$), the tangential force will not be changed. For frictional contacts, Coulomb criterium must be respected, as illustrated in Figure 1.15c, where :

$$||\vec{f_t}|| \leq \mu f_n \tag{1.6}$$

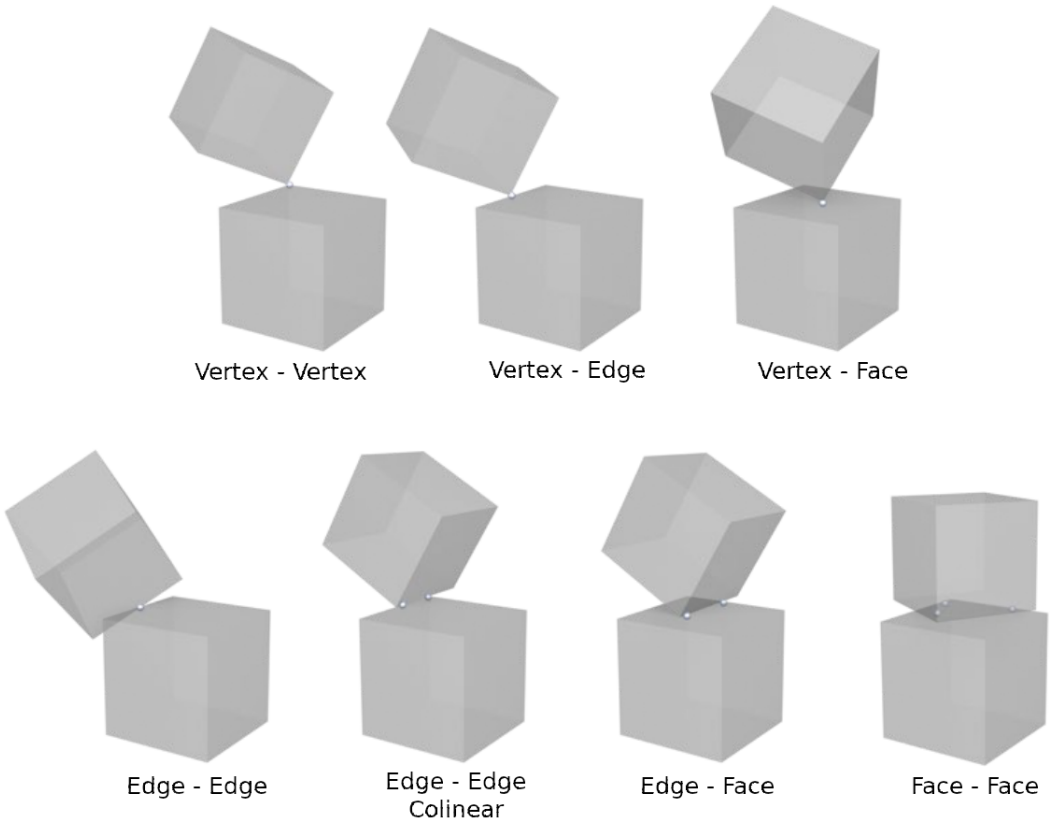

Figure 1.14: *List of possible contact types between polyhedra [23]*

with μ a friction coefficient. Hence, if the contact force reaches $||\vec{f_t}|| > \mu f_n$, the tangential force will be set to $\vec{f_t} = \mu f_n . \vec{f_t}/||\vec{f_t}||$ in order to stay satisfy the Coulomb criterium.

Since this contact law is purely repulsive, it may lead to unstable simulations if the time step is too large. A normal damping force $f_v = -\alpha_n (\vec{v} \cdot \vec{n})$ dependent on the relative velocity $\vec{v}$ is introduced, with α_n a normal damping coefficient ; the total force resulting from the contact is then $\vec{f} = (f_n + f_v)\,\vec{n} + \vec{f_t}$ with only normal damping, although it can be applied to the tangential component. For non-viscous damping cases, the normal damping coefficient α_n is usually given by :

$$\alpha_n = -\frac{2\ln(\epsilon_n)}{\sqrt{\ln^2(\epsilon_n) + \pi^2}} \tag{1.7}$$

with $\epsilon_n \in]0;1]$ a user-defined coefficient of restitution.

Position and velocity update

Once the resulting forces and moments are computed for each contact, the position and velocity of each element are updated. To do this, DEM relies on Newton's laws of motion

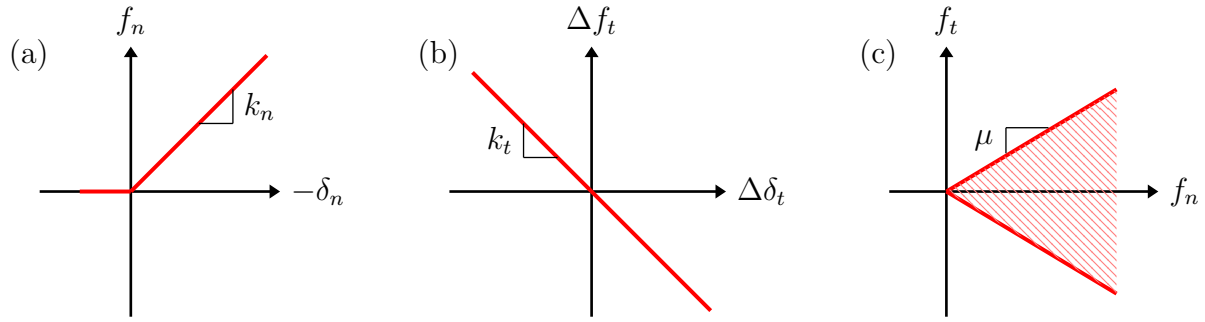

Figure 1.15: *Linear elastic contact law (a) Normal force (b) Tangential force (c) Coulomb criterium*

which give the following equations for the element i :

$$m_i \ddot{\vec{x}}_i = m_i \vec{g} + \sum_{j \neq i} \vec{f}_{ij} \tag{1.8}$$

$$[I_{i,O_i}] \dot{\vec{\Omega}}_i = \sum_{j \neq i} \vec{M}_{O_i} \left(\vec{f}_{ij} \right) \tag{1.9}$$

with $\vec{x}_i$ the position of element i, $\vec{\Omega}_i$ its angular velocity, $[I_{i,O_i}]$ its inertia matrix at point O_i (corresponding to its center of mass), and $\vec{M}_{O_i}(\vec{f}_{ij})$ the angular momentum induced by the force $\vec{f}_{ij}$ on point O_i.

By integrating these equations, it is then possible to determine the position, velocity, orientation and angular velocity of the elements. However, continuous temporal integration is not always possible, particularly as the rupture of some contacts can lead to discontinuities in the forces computation. It is therefore necessary to discretize the integration of these differential equations with suited algorithms. Verlet's integration algorithm is often used in Molecular Dynamics, as it is more stable than the classical Euler method [184]. However, with this algorithm, position and velocity are not computed at the same instant, but shifted by half a time step. This offset is necessary, especially for kinetic energy calculations. An alternative consists in modifying this algorithm to "synchronize" the computation instants; for example, the Velocity Verlet algorithm allows to compute the position and velocity of elements at the same instant [168].

With the positions, angles and velocities known at time t, Eq. 1.8 and 1.9 allow to compute the values of $\ddot{\vec{x}}_i$ and $\dot{\vec{\Omega}}_i$ at time $t + \Delta t$. It is then possible to compute the position, velocity, orientation and rotation speed values of the elements at the next time. A new configuration of elements is then obtained, and can be reintroduced into the algorithm to continue the simulation.

1.2.2 Simulation of the calendering process of Lithium-ion battery electrodes using DEM

Modeling of the components

In order to obtain a representative numerical electrode, it is necessary to correctly model its main component : the active material. For cathodes, they are lithium-based grains (LCO, NMC, LFP...), and graphite for anodes (see Section 1.1.3). The shape of the elements will play an important role : the properties of the electrode, both mechanically and electronically, will not be the same depending on which grains are used. It is possible to recover the "real" shape of the electrode particles using XCT measurements, and thus obtain more representative particles. Usually each grain has its own shape, which is an inconvenient in DEM : indeed, complex particle shapes increase the computational cost of the contact detection phase [167]. It is better to use shapes that are as simple as possible. The simplest form to represent an element is the sphere ; this shape may be suitable for some types of active material grains such as NMC, but not for graphite, which usually has a flatter shape as shown in Figure 1.3. In most numerical cathode models, active material particles are represented with spheres [52, 117, 153, 188]. Some models even represent particles of active material as assemblies of spheres, in order to obtain more complex shapes while keeping computational costs reasonable [118]. Regarding the particle size, for models not built from tomographic results, this size is either the same for all grains (monodisperse) or the sizes are variable and their volumetric proportions are chosen to respect an experimental distribution [117, 51].

In models designed to take into account the influence of the binder and conductive additives, these components are represented through one common type of element, the Carbon Binder Domain, due to their small size relative to the active material particles and their tendency to merge after the mixing phase. In order for the model to be representative of real electrodes, the mass proportions between each component must be respected. It varies around 90-95% for the active material, 2.5-5% for the binder and 2.5-5% for the conductive additives, *i.e.* the mass ratio between active material and CBD that can vary from 90-10% to 95-5%. However, since the CBD has a lower bulk density than the active material, and the grains are usually of nanometric size, the volumic distribution will be different, with CBD representing between 12 and 25% of the total volume. Thus, by respecting actual particle densities and sizes, the number of CBD particles will vary between 500 and 1000 for each particle of active material introduced in the simulation [165]. It can therefore become costly in terms of time and resources to carry out simulations explicitly taking into account all electrode components. This is why it is common to find models that do not explicitly take into account the presence of these components [167, 188, 51], but which nevertheless include CBD-related parameters in their simulations.

The current collector is easier to model : as it is a smooth metal sheet, made of aluminum for the cathodes and copper for the anodes, it will be represented using a plane or a rigid block [118, 51], or can even be completely absent if the study focuses on grains alone [167, 40]. The fact that it is non-deformable is inherent to the models developed

to date, assuming that the collector will retain its shape throughout battery manufacture. This assumption is, however, rather unrepresentative of reality, as it has been observed that particles of active material can deform the current collector during extensive calendering, resulting in electrodes with high densities [155].

Once the solid elements have been defined, the question of the electrolyte remains. Ideally, the electrolyte is only present in the electrode from the filling stage onwards ; it is therefore not necessary to take it into account during the calendering stage. The presence of the electrolyte will only be useful for ionic conductivity measurements. Thus, DEM calendering models do not have to worry about it, as the electrolyte is not needed ; moreover, for conductivity measurements, DEM is not useful, as the particles are then considered fixed, and so only the electrode microstructure is needed [151, 159].

Interactions between the elements

Once the components have been modeled separately, then establishing the interactions between each of them is needed. As explained in Section 1.2.1, these relationships are defined by contact laws, which allow to determine the resulting forces and moments from the contacts. The contact laws presented here are those employed in DEM simulations applied to Li-ion electrodes, but they represent only a fraction of the existing laws, which can be used to represent more or less complex mechanical behaviors. For a more exhaustive list, see [133, 176, 171].

Elasticity In the simplest simulations, *i.e.* those only taking into account the presence and influence of active material particles, the contact law is just elastic. Since the contact is between metallic materials (like the one presented in Section 1.2.1). The Hertz-Mindlin law is frequently an alternative [102]. Both are expressed as :

$$f_n\Big(\delta_n\Big) = -k_n\delta_n \quad ; \quad \Delta\vec{f_t}\Big(\Delta\vec{\delta_t}\Big) = -k_t\Delta\vec{\delta_t} \tag{1.10}$$

The normal and tangential stiffnesses k_n and k_t are related to the elastic properties of the elements in contact. For spherical elements they are given, within the framework of Hertz theory, by :

$$k_n = \frac{4}{3}E^*\sqrt{-R^*\delta_n} \quad ; \quad k_t = 8G^*\sqrt{-R^*\delta_n} \tag{1.11}$$

with R^* the effective radius, E^* the effective elastic modulus and G^* the effective shear modulus. For two different materials, denoted i and j, these equivalent parameters are defined by :

$$R^* = \frac{2R_iR_j}{R_i+R_j} \quad ; \quad \frac{1}{E^*} = \frac{1-\nu_i^2}{E_i} + \frac{1-\nu_j^2}{E_j} \quad ; \quad \frac{1}{G^*} = \frac{2(2-\nu_i)(1+\nu_i)}{G_i} + \frac{2(2-\nu_j)(1+\nu_j)}{G_j} \tag{1.12}$$

The values of k_n and k_t as defined in Eq. 1.11 are here dependent on δ_n, which makes the force evolution non-linear (the corresponding f_n evolution graph is given in Figure 1.16a).

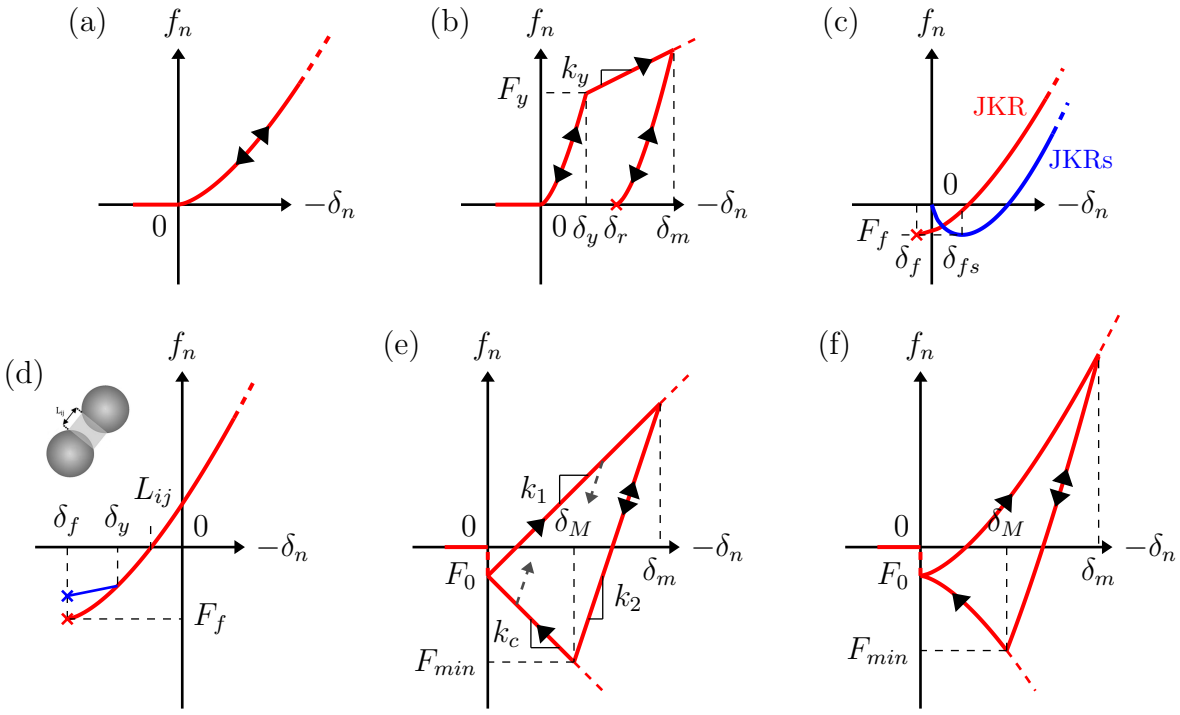

Figure 1.16: *Graphs of normal force for various contact laws (a) Hertz (b) Rigid plastic (c) JKR(s) (d) Hertzian-bond (e) Luding (f) EEPA*

However, it is possible to use constant values for these rigidities that are independent of δ_n and still respect the order of magnitude of the elastic deformations of the contacts, thus dealing with a linear evolution of the contact force [133]. Choosing between a linear elastic contact law and a Hertz model will depend on the purpose of the study. Here, the contact forces are proportional to the pressure applied by the cylinder and to the particle size. The difference between these two laws lies in the value of the normal interpenetration δ_n, which is low and has little influence on overall deformation. In the following, the elastic component of the contacts will be described using the Hertz-Mindlin law, *i.e.* with a non-linear evolution.

The contact between the active material particles and the current collector is usually defined through an elastic contact since they are both composed of a metallic material ; their contact being strongly rigid, it is thus similar to an elastic behavior [52].

Plasticity A large number of numerical models seek to represent, or at least take into account, the damaging of active material particles. Indeed, grains of active material only behave elastically for small deformations, up to 5% of their size ; beyond the deformations they undergo will be irreversible, consequently changing their behavior [32]. Numerically, this change is represented by a change in the contact law : the initially elastic behavior will switch into another evolution phase once the plasticity threshold is reached. The most

commonly used law to represent the plastic damage of active material particles is the rigid plastic law [177, 52, 54]; the corresponding normal force graph is shown in Figure 1.16b. This law stipulates that beyond a critical force F_y, reached in δ_y and which can be linked to the elastic limit of the material, the normal compressive force is defined by :

$$f_n\Big(\delta_n\Big) = F_y - k_y(\delta_n - \delta_y) \tag{1.13}$$

with k_y a constant stiffness independent on δ_n. Beyond the plasticity threshold, the force will evolve linearly with the overlap, whereas it previously evolved in ${\delta_n}^{\frac{3}{2}}$ with Hertz's law. Once the plasticity criterion is reached, the maximum overlap reached $\delta_m \leq \delta_y$ is stored. Thereafter, when the elements separate, the normal force will revert to an elastic evolution $f_n^{Hertz}\Big(\delta_n - \delta_r\Big)$ with f_n^{Hertz} the function defined in Eq. 1.10 giving the normal elastic force, and δ_r the residual plastic strain such that $f_n^{Hertz}\Big(\delta_m - \delta_r\Big) = F_y + k_y\left(\delta_m - \delta_y\right)$; the contact is broken when the force is zero at $\delta_n = \delta_r$. If the elements move closer together before the contact breaks, the force will still follow this elastic evolution, until their interpenetration reaches δ_m, where it will follow back the evolution from Equation 1.13.

The value of k_y can be defined according to the actual behavior of the materials in contact : indeed, during a nanoindentation test, the force-displacement curves obtained will not have the same evolution under loading and unloading once the material has reached its plastic domain. The slope of the curve at the beginning of the discharging phase is characteristic of the elastic modulus, while the slope at the end of the loading step can be assimilated to the plastic evolution. Thus, the ratio between these two experimental slopes can be used to define a relationship between the numerical stiffnesses k_n and k_y [172].

Since the current collector is made of aluminum or copper and due to its planar geometry, it tends to deform quite easily during the calendering process, due to the stamping of active material particles ; thus, it would be sensible to also assign it a contact law including plasticity. However, literature models including the current collector consider it as a rigid undeformable element, capable only of an elastic response as its deformation is not the central subject of the study [52, 118]. So far, to our knowledge, there is no DEM model that takes into account the plastic deformation of the current collector.

Adhesion The adhesive component of the electrodes mechanical behavior is mainly due to the presence of the binder. In the previous section, two types of numerical model were presented that include the binder (or CBD) : those that represent it explicitly in particle form, and those that take it into account only implicitly.

The first ones consider two new types of contacts : one for the contact between the active material particles and those of CBD, and another one for the CBD particles between themselves. To describe the behavior of CBD particles when they come into contact, new contact laws need to be introduced. Although criteria exist for choosing the most suitable law based on the elastic and adhesive properties of the elements in contact, the most commonly used laws are those of Lennard-Jones [43] and Johnson-Kendall-Roberts (JKR)

[117, 165]. The Lennard-Jones potential [76] describes the attractive Van der Walls distant forces between two particles as :

$$f_n\Big(\delta_n\Big) = \frac{8\pi\gamma R^*}{3}\left(\frac{1}{4}\left(\frac{\delta_n}{\delta_0}\right)^{-8} - \left(\frac{\delta_n}{\delta_0}\right)^{-2}\right) \tag{1.14}$$

where γ represents the adhesive surface energy (in J.m^{-2}) and $\delta_0 > 0$ the equilibrium overlap. The adhesive surface energy between two materials is deduced from their surface energies using formula :

$$\gamma_{ij} = 2\sqrt{\gamma_i^d\gamma_j^d} + 2\sqrt{\gamma_i^p\gamma_j^p} \tag{1.15}$$

with γ^d and γ^p the dispersive and polar surface energies respectively. Although applicable in DEM, the Lennard-Jones contact law shows an infinite force upon contact between the elements ($\delta_n = \delta_0$), making it more suitable for CD than MD. The JKR model is adapted from Hertz's theory for the contact of large, flexible spheres [62]. The contact forces are computed by :

$$f_n\Big(\delta_n\Big) = \frac{4E^*a^3}{3R^*} - \sqrt{8\pi E^*\gamma a^3} \tag{1.16}$$

with a the contact radius between the particles, which can be related to the displacement by $|\delta_n| = \frac{a^2}{R^*} - 2\sqrt{\frac{\pi\gamma a}{E^*}}$. Numerical implementation of Equation 1.16 is difficult in DEM, as here the relationship between a and δ_n is not linear. Thus, a second version of this contact law has been developed, entitled JKRs (for JKR simplified), which assumes that for small deformations $a^2 \simeq -R^*\delta_n$. This then gives :

$$f_n\Big(\delta_n\Big) = -\frac{4}{3}E^*\sqrt{-R^*\delta_n}\delta_n - \sqrt{6\pi\gamma E^*}\left(-R^*\delta_n\right)^{\frac{3}{4}} \tag{1.17}$$

The two corresponding graphs are plotted in Figure 1.16c, with Eq. 1.16 in red and Eq. 1.17 in blue. It can thus be observed in Eq. 1.17 that when $\gamma = 0$, *i.e.* when the attraction between the particles is zero, the evolution of the contact force is then identical to Hertz's law from Eq. 1.11. Moreover, in both cases, the maximum attractive force is $F_f = -\frac{3}{2}\pi\gamma R^*$, and is obtained at $\delta_f = \frac{3}{4}\left(\frac{\pi^2\gamma^2R^*}{E^{*2}}\right)^{\frac{1}{3}}$ for JKR [177] and $\delta_{fs} = -\left(\frac{9\pi^2\gamma^2R^*}{E^{*2}}\right)^{\frac{1}{3}}$ for JKRs [133]; this value corresponds to the force required to separate the particles.

In the second types of models - those who do not include the binder particles - only the cohesive component of the binder is modeled, by modifying the contact law between the particles of active material to be adhesive. These models often use an Hertzian law with breakable bonds [98, 188, 51], which is based on the *Bonded Particle Method* [126], whose force graph is illustrated in Figure 1.16d. Once the active material particles are introduced in the simulation, the initial distance $L_{ij} = ||\vec{x_i} - \vec{x_j}|| - R_i - R_j$ between each pair (i,j) of particles is measured, and a link will be formed between them if this distance complies with the equation :

$$L_{ij} < (R_i + R_j)f_b \tag{1.18}$$

with f_b a coefficient controlling bond formation. This coefficient is directly linked to the proportion of binder in the electrode : knowing that the volume of a cylindrical bond is $\pi r^{*2} L_{ij}$ with $r^* = 0.5R^*$, it is then possible to compute the volume of all created bonds, considered then as the total volume of binder [51]; this coefficient thus controls the distribution of active material and binder in the sample. The breaking distance δ_f is given by $f_n^{Hertz}\Big(\delta_f - L_{ij}\Big) = -F_f \geq 0$. Thus, the normal contact force computation can be reduced to a form similar to Hertz's law :

$$f_n^{Bond}\Big(\delta_n\Big) = f_n^{Hertz}\Big(\delta_n - \delta_f\Big) + F_f \tag{1.19}$$

When using adhesive contact laws, which allow the normal force to reach negative values, it is possible to have configurations where Coulomb's criterion as defined in Eq. 1.2 is no longer valid. To overcome this problem, the normal component of the criterion needs to be "brought back" to non-negative intervals. This way the Coulomb criterion is redefined as follows :

$$\mu\left(f_n - F_f\right) - f_t \geq 0 \;\Leftrightarrow\; f_t \leq \mu\left(f_n - F_f\right) \tag{1.20}$$

Adhesion and plasticity The most comprehensive models used to represent electrodes mechanical behavior are those with both adhesive and plastic components [154, 153, 188]. As it is often impractical to define several contact laws and use them together when computing the contact force, there are laws that allow both aspects to be considered together [176].

The simplest models just combine existing laws. For example, to represent the embrittlement of bonds formed by the binder between active material particles [188], it is possible to add a tensile plasticity criterion to the previously defined adhesive law with breakable bonds (*Hertzian-bond*). Thus, when the separation between particles reaches δ_y, such that $L_{ij} < \delta_y < \delta_f$ and $f_n^{Bond}(\delta_y) > F_f$, the normal force will evolve similarly to Equation 1.13 :

$$f_n\Big(\delta_n\Big) = f_n^{Bond}\Big(\delta_y\Big) - k_y\left(\delta_n - \delta_y\right) \tag{1.21}$$

This evolution is shown in blue on Figure 1.16d ; the contact is considered as broken either when the distance between the particles exceeds δ_f or when the normal force reaches F_f.

Considering contact laws including adhesive and plastic behaviors which do not combine simpler laws, the only one that is used for calendering simulations is the linear elasto-plastic law with adhesion [153], also known as Luding's law [87, 88], illustrated in Figure 1.16e. The normal force is given by :

$$f_n\Big(\delta_n\Big) = F_0 + \begin{cases} -k_1\delta_n & \text{si } \delta_n \leq \delta_m \\ -k_2\left(\delta_n - \delta_m\right) - k_1\delta_m & \text{si } \delta_m < \delta_n \leq \delta_M \\ k_c\delta_n & \text{si } \delta_M < \delta_n \end{cases} \tag{1.22}$$

where $F_0 \leq 0$ corresponds to the initial attractive force, defined according either to the JKR or DMT models depending on the "deformability" of the elements [169].

This law is divided in 3 phases : first, at contact initiation, the force will evolve linearly along a slope k_1 ; this first phase corresponds to plastic behavior, as the force can only follow this evolution when the contact has exceeded the maximum interpenetration δ_m (initially zero), which implies plastic deformation of the material. When the elements separate after the compression, the force will evolve following another stiffness, of value k_2, which here corresponds to the elastic behavior. If the elements continue to separate, once the overlap reaches $\delta_M = \delta_m \frac{k_2 - k_1}{k_2 + k_c}$, the contact area between the elements will be assumed to be a maximum, and the attractive contact force will have reached its extremal value $F_{min} = F_0 + k_c \delta_M$. Thus, any configuration of the elements that increases their separation will result in a weaker adhesion force, and this force will then evolve according to an "adhesive" stiffness k_c until complete separation. One of the main drawbacks of this model is that, similarly to the plastic evolution during compression, force evolution following the k_c slope is only possible during decompression; thus, if the elements have to move closer together, the contact would behave elastically, and the force would then follow the k_2 slope, but this time up to the maximal overlap $\delta_m{}'$ which will have been defined according to the last decompression configuration in $\delta_M{}'$. This phenomenon reflects a reversibility of plasticity, which is not physically realistic. Other contact laws correct this physical error [124], but their validation is still too weak to be applied to real models.

Another inconvenient of this model is that it is based on a linear force–overlap relationship, which is not valid following Hertz's theory [17]. Thus there is another version of this law which has been put into the form of a power law, called the *Edinburgh Elasto-Plastic Adhesive* (EEPA) contact law [111, 154] :

$$f_n\Big(\delta_n\Big) = F_0 + \begin{cases} -k_1 \delta_n^P & \text{si } \delta_n \leq \delta_m \\ -k_2 \left(\delta_n^P - \delta_m^P\right) - k_1 \delta_m^P & \text{si } \delta_m < \delta_n \leq \delta_M \quad (EEPA) \\ k_c \delta_n^P & \text{si } \delta_M < \delta_n \end{cases} \tag{1.23}$$

with the exponent $P \geq 1$ and $\delta_M^P = \delta_m^P \frac{k_2 - k_1}{k_2 + k_c}$; the corresponding normal force graph is shown in Figure 1.16f. Note that if $P = 1$ the law reverts to the initial Luding law defined in Eq. 1.22, and that with $P = 1.5$ the evolution of the force will be typical of an Hertzian behavior.

Modeling of the calendering process

In the numerical models representing DEM electrodes, only a handful explicitly study the calendering process [151, 52, 117, 165, 154, 153]; some of these are shown in Figure 1.17. Numerical representation of the calendering process is often based on simplification. Indeed, since the size of the calendering roll is much greater than the thickness of the electrode (several dozens of centimetres versus hundred of micrometers), and its rotational speed sufficiently low, the calendering process is represented as uniaxial compaction [52, 117, 165]. This model represents well the compressive effect of the calendering to reduce the electrode thickness and increase its bulk density, but it neglects the tangential shearing aspect due to the rotation of the cylinder and the translation of the electrode [52]. At industrial scale the high calendering speeds induce shearing forces that can not be neglected.

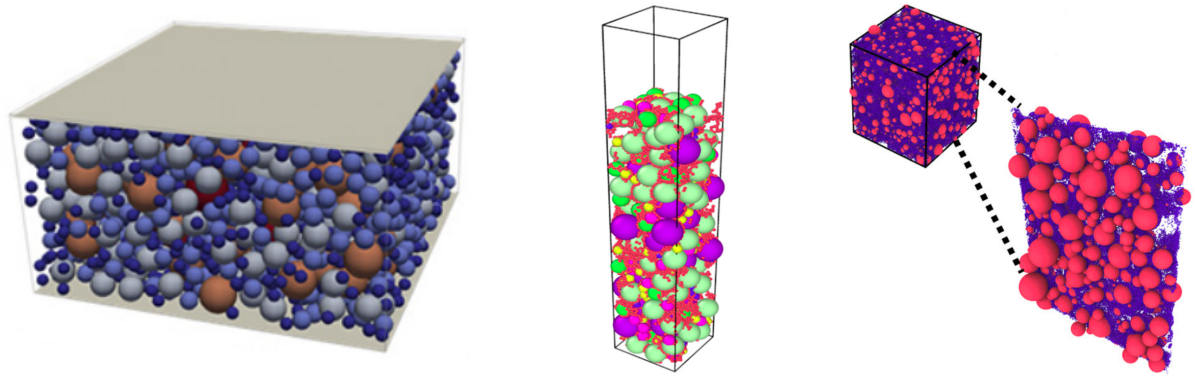

Figure 1.17: *Numerical models used to simulate the calendering process of Li-ion battery electrodes using DEM [52, 117, 165]*

In these simulations, the driving calendering parameters are the compression rate and/or the pressure applied vertically. Because the sides of the sample are periodic, the thickness of the sample determines its volume, and consequently its porosity. In order to reach a desired electrode porosity, the vertical compression speed is controlled and kept constant until the corresponding thickness is reached [117, 165]. Similarly, by controlling the vertical pressure, the applied force is kept constant [52].

In order to have a simulation with reasonable boundary effects, the sample dimensions must be at least 20 elements wide. The sample size will mainly be driven by the active material particles. Thus, the lateral dimensions of the samples are similar in all models, with a length around 200 µm. This size is also small enough to consider that the contact between the cylinder and the electrode is flat throughout the sample, due to the large size differences between the two, thus validating this simplified representation of calendering. However, the thickness of the sample may vary depending on the simulations. For models that explicitly take the binder into account, the drying stage is also simulated prior to calendering : the simulation starts with a sample at a very low volume fraction – of the order of 10% – which is then compressed vertically to represent solvent evaporation ; the elements will then move closer together until the desired porosity is reached. Thus, to achieve realistic electrode characteristics after drying (volume fraction $\simeq 50\%$ and thickness of 100 µm), the initial thickness of these samples must be 5 times greater than that of simulations implicitly including the binder ; moreover, these simulations require a greater number of elements to respect the proportions of the components (up to 1000 times more [165]) : the computational cost of these simulations will therefore be much higher than without CBD particles.

1.2.3 Numerical characterization

Mechanical characterization

Simulations of electrode compaction allow to study virtually the characteristics of the samples. Among these, the models that rerieve their initial microstructure from XCT analyses enable more accurate estimations of the active material particles shape [167]. These models also make it possible to study grain contacts before and after calendering, by comparing experimental data on grain orientation and contacts with numerical results obtained after compressing the microstructure created by the XCT images. It was demonstrated that, for NMC-based cathodes, modeling the active material grains as spheres and assuming a purely elastic behavior is only representative at low compressions, as the grains deform when the calendering pressure is too high ; their behavior is therefore no longer purely elastic but includes plastic and damaging components. This plastic evolution is due to two phenomena : for low compressions, the grains will rearrange in the sample to create a more energetically stable microstructure, thus inducing macroscopic deformation ; but once the rearrangement reaches its limit, the grains themselves start to deform and plasticize, inducing then microscopic deformation. In addition, modeling the active material grains as spheres, compared with an ellipsoidal representation, facilitates microstructure compaction and reduces the internal electrode tortuosity, but nevertheless reduces the electrical conductivity [11]. However for monodisperse spherical models the lowest porosity can be determined based on the coefficient of friction μ and the coordination number Z, *i.e.* the number of contacts per element [161].

The most commonly used model to simulate calendering is based on a uniaxial compression representation [151, 52] ; some of the samples used to carry out these studies are illustrated in Figure 1.17. This model represents the active material particles in different sizes (between 5 and 18 µm), and the presence of CBD is included in an Hertzian-bond contact law. The behavior of the sample was compared with the use of a purely elastic contact law, and it was observed that the values of internal porosities and pressures recorded at the compression plane are closer to the experimental results using a plastic contact law. The study of contact orientation using the fabric tensor highlighted the rearrangement of the particles, with the majority of contacts initially vertical, becoming horizontal as compression increased. Similarly, the internal stresses measured on the grains increased with the compression. This model also showed that an initially more porous electrode will allow greater rearrangement of the grains, and thus achieve lower final porosities.

An online simulation tool called the *ARTISTIC Online Calculator* [83] provides mixing, drying and calendering simulation results based on a set of existing models [128, 117, 127, 40, 84, 38]. By specifying the initial volume fraction and the massic ratio between the active material and the CBD, the tool will first generate a microstructure representing the state of the mixture as it is deposited on the current collector (Figure 1.18). The red grains, representing the CBD mixed with the solvent, are then reduced in size to simulate the drying step. The rate of shrinkage can depend on the vertical position of the particle to be even more representative, as the solvent evaporates faster if it is closer to the electrode

surface [117]. Once these particles have reached their final size, calendering is represented by an uniaxial compaction [128, 127]. The final result can then be analyzed in terms of porosity or bulk density, and the microstructure can be recovered by the user at a later stage.

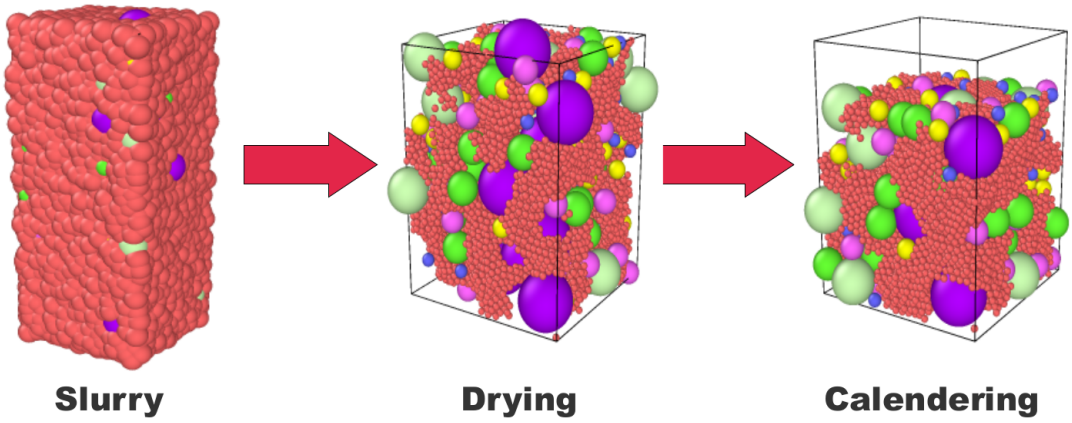

Figure 1.18: *Successive simulation steps of the numerical tool developed in [83]*

Very few calendering parameters are taken into account here. Indeed, by representing calendering as an uniaxial compaction, it is not possible to properly study all the parameters involved in the real calendering process. The calendering speed for example, can not be studied effectively, as it can only be modeled here by a variation in compression rate. This representation is only valid for low calendering speeds ($<$ 1 m/min), which is not realistic for industrial production lines, where calendering speeds are of the order of 30-100 m/min [71, 81].

Regarding larger scale simulations, studies on adhesion have focused on the tensile/ compressive response. By considering only the presence of active material grains and using Hertz's contact law with breakable bonds (*Hertzian-bond*), bond failure is strongly dependent on the amount of binder and on the particle size, whereas a quasi-uniform size distribution allows higher strains to be reached before breaking [188]. By explicitly adding CBD grains, simulations have shown that k_n and k_t the normal and tangential stiffnesses influence the most the microstructure in loading/unloading test [153]. The same study showed that for a Luding-type contact law, the different coefficients of friction μ, adhesive surface energies γ and ratios between plastic and elastic stiffnesses are the most influential parameters [154].

Electronical characterization

As shown in Section 1.1.5, conductivity measurements are carried out when the battery is in use, i.e. when the electrical current is flowing through the electrodes ; since this flow is not related to mechanical movement, it can not be represented using the Discrete Element

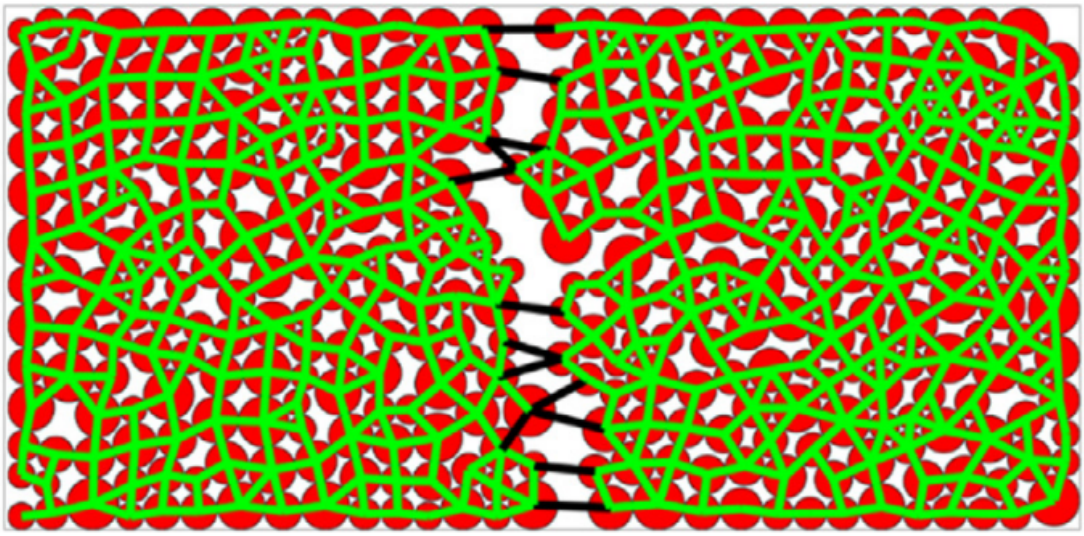

Figure 1.19: *DEM simulation of an uniaxial tensile failure test between NMC particles [188]*

Method alone and therefore require other computation methods. DEM simulations can be coupled with these other methods, which will take the microstructures obtained in DEM as reference configurations [178, 159, 67].

However some studies have developed models and formulations that can estimate the relative electrical and ionic conductivities of microstructures obtained via DEM simulations [151]. The electric current flows through the electrodes thanks to the contact between the grains of active material. Its operation can thus be linked to heat transfer within a granular medium. A first preliminary study focused on heat exchange within an anode, heat being considered as propagated via conduction, and therefore by contacts between particles [149]. This study showed that thermal conductivity decreases when the internal porosity increases or when the grain size is reduced, due to the reduction in the overall contact area between grains. Thus a formula estimating the electrical conductivity k_{el} of an electrode was proposed, deriving from those used to determine the thermal conductivity of a granular assembly [151]. Based solely on geometric properties related to the granular microstructure, this formulation gives :

$$\lambda_{el} = C_{el}\,(1-\varepsilon)\,Z\mathbf{F}_{zz}\frac{a}{R^*}\lambda_p \tag{1.24}$$

This formulation implies that a decrease in porosity ε leads to an increase in electrical conductivity. Similarly, an increase in the number of contacts between grains, represented by the coordination number Z, together with a higher contact area a/R^*, will result in a better flow of the electrical current. The parameter $\mathbf{F}_{zz}$, which represents the diagonal component of the fabric tensor in the vertical direction, accounts for the directionality of the contacts between the grains ; thus, the more vertically oriented the contacts, the higher this value will be, and consequently the better the electrical conductivity in this direction.

However, these microstructural parameters alone can only give a relative estimate of the electrical conductivity of the microstructure. It is therefore needed to include λ_p the specific conductivity of the material, as well as a correction coefficient C_{el} in order to match numerical values with experimental measurements.

As mentioned in Section 1.1.5, characterizing the ionic conductivity mainly involves measuring the electrode tortuosity. The formula usually employed to numerically determine the tortuosity is based on Bruggeman's relationship, which suggests that for battery electrodes, tortuosity τ and porosity ε are linked via the formula $\tau = \varepsilon^{-0.5}$ [45]. However, it has been observed that this relationship is not always correct, and is only valid in the case where the electrode is composed of monodisperse spherical particles [185].

Thus, new formulations were developed, based solely on microstructural properties of the microstructure [151] :

$$\lambda_{ion} = C_{ion}\varepsilon FSA\frac{\mathbf{F}_{zz}}{0.5\left(\mathbf{F}_{xx}+\mathbf{F}_{yy}\right)}\lambda_{ion}^{bulk} \tag{1.25}$$

The ionic diffusion is proportional to the porosity ε and free surface *FSA* of the grains. The directionality of contacts affects the internal diffusivity, as contacts in directions parallel to the current collector $\mathbf{F}_{xx}$ and $\mathbf{F}_{yy}$ increase electrode tortuosity, unlike contacts $\mathbf{F}_{zz}$ perpendicular to the plane ; thus the ratio between the components of the fabric tensor in these two directions is useful to estimate the tortuosity of an electrode. As for the electrical conductivity, this formulation is related to the properties of the actual material, represented here by λ_{ion}^{bulk} the ionic conductivity of the electrolyte in the pores of the electrode. The addition of the corrective coefficient C_{ion} allows numerical values to be fitted with experimental data. However, these formulas give a global estimation over the whole sample, and are therefore not suitable for representing local variations in conductivities that might appear within the electrode.

Fast Fourier Transform

In order to account for the real microstructure of the electrodes in the conductivities computation, one alternative is to use the Fast Fourier Transform [112]. It is an homogeneization technique which aims to compute the effective or equivalent property of a multi-phased medium, and is employed in several domains like mechanic, thermal transfer or diffusion [22]. The multi-phase geometry of the sample is described explicitely on a cartesian meshing grid. Each voxel of the grid has a value corresponding to its local property. The diffusion gradient is considered as homogeneous inside the volume. The method assumes periodic boundary conditions and the effective properties of the matrix (mesh) is computed considering a steady state regime. Compared with finite-element method the FFT is able to handle more degrees of freedom and may be accelerated thanks to parallelization technique (openMP was employed in this thesis work). Moreover the cartesian mesh allows a very simple definition and easy to process geometry.

Voxelisation To compute the effective conductivities of the DEM samples using the FFT method, the samples must first be discretized [22]. Usually a regular cartesian 3D grid is used where each subvolume, called a voxel, is defined with a side length dl. Depending on the type of element inside each voxel, a different phase is attributed to this voxel. Each phase corresponds to a material, with its own conductive properties. For voxels entirely inside or outside an element, this attribution is easy, however the phase of the voxels at the interface between two elements or on the edge of an element is more complicated to choose. Usually the phase is chosen depending on the element at the center of the voxel.

Computation of effective conductivity In the steady-state regime, the flux (denoted by $\mathbf{j}$) is solution of ($\mathbf{x} \in \mathbf{V}$):

$$\nabla \,.\, \mathbf{j}\,(\mathbf{x}) = \mathbf{0} \;\text{ with }\; \mathbf{j}\,(\mathbf{x}) = \lambda\,(\mathbf{x})\,\mathbf{e}\,(T\,(\mathbf{x})) \tag{1.26}$$

where $\lambda\,(\mathbf{x})$ is the conductivity and $\mathbf{e}\,(T\,(\mathbf{x})) = -\nabla.T\,(\mathbf{x})$ is the intensity field. To solve the boundary value problem of Equation 1.26, we consider periodic boundary conditions [112]. The unknown intensity field is set constant for each voxel, allowing to simplify the computation. By alternating the resolution between real and Fourier space, the flux $\mathbf{j}$ can be determined.

The effective conductivity λ^e in a given direction is computed by looking at the intensity in this direction, for example here in the $\mathbf{z}$ direction:

$$\mathbf{e} = e_0\mathbf{z} \Rightarrow \lambda^e_{\mathbf{z}} = \frac{\langle \mathbf{j}.\mathbf{z} \rangle}{e_0} \tag{1.27}$$

with $\langle . \rangle$ the volume average on the RVE.

1.3 Conclusion

In this chapter we reviewed the existing literature on the calendering of Li-ion battery electrodes. The first part described the history of electrical batteries and the current technology of Lithium-ion batteries. The working principle of this type of batteries was presented, as well as different versions of Li-ion batteries and their internal components: active materials, binders or electrolytes. The manufacturing process of these batteries is composed of different steps, one of them being calendering. The importance of the calendering step on the performances of the batteries was explained. We presented methods to characterize experimentally the electrodes and different measurable parameters. The second part of this review chapter was focused on the simulations used to numerically study the calendering of Li-ion battery electrodes. Since the electrodes are a granular medium, we focused our work on the DEM and used it for our simulations. Each step of the algorithm, respectively contact detection, force computation and position updating, was thoroughly described. To represent the Li-ion battery electrodes, various simulation models are used, each one accounting for the components of the electrodes in a different

way. While representing explicitly all the particles composing the electrode requires high computational costs, most of the simulation models represent only the active material grains and account for the binder implicitly by considering a cohesive elasto-plastic contact law. In most past numerical work, the calendering is represented as an unaxial compaction, considering that the calendering speed is relatively low ($\simeq$ 1m/min) and the roll much larger than the electrode.

Chapter 2

Dynamic compaction of cohesive granular materials

The compaction of cohesive granular materials is a common operation in powder-based manufacture of many products. However, the influence of particle-scale parameters such as bond strength on the packing structure and the general scaling of the compaction process are still poorly understood. We use particle dynamics simulations to analyze jammed configurations obtained by dynamic compaction of sticky particles under a fixed compressive pressure for a broad range of the system parameter values. We identify an asymmetric sigmoidal scaling of porosity with a modified cohesion number that combines adhesion force, confining pressure, and particle size, as well as contact stiffness, which is often assumed to be ineffective but is shown here to play an essential role for compaction. A functional form based on two power laws provides a physically plausible fit to the data. The statistical properties of the bond network reveal self-balanced force structures and exponential fall-off of the number of both tensile and compressive forces. Remarkably, the properties of the bond network depend on the cohesion number rather than the modified cohesion number, suggesting that similar bond network characteristics are compatible with a broad range of porosities mainly due to the effect of contact stiffness. We also discuss the origins of data points escaping the general scaling of porosity and show that they reflect effects related to either finite system size or rigid confining walls.

Contents

1.1 Lithium-ion batteries 3

1.1.1 History of Lithium-ion batteries 3

1.1.2 Working principle of Lithium-ion batteries 5

1.1.3 Composition of a Lithium-ion battery 6

1.1.4 Manufacturing process 10

1.1.5 Experimental characterization 14

1.2 Numerical simulations applied to the manufacturing process of Lithium-ion batteries 17

1.2.1 Discrete Element Method 18
1.2.2 Simulation of the calendering process of Lithium-ion battery electrodes using DEM 24
1.2.3 Numerical characterization 32
1.3 Conclusion 36

2.1 Introduction

Granular materials represent a ubiquitous form of solid matter in nature and a major component of manufacturing process in several industries. The mobility of grains and their versatile interactions underlie the ability of granular materials to undergo diverse mechanical and chemo-physical transformations in response to external forcing and environmental changes. These transformations are strongly coupled with change of porosity or volume, which for this reason plays a key role in all granular processes [5, 103]. For example, the compaction and gradual consolidation of sediments deposited in lakes and oceans are at the origin of sedimentary rocks such as sandstone, limestone, and shale [59]. The compaction of fine cohesive particles in response to mechanical stress or vibrations is also one of the most common operations in powder metallurgy, ceramic industry, and pharmaceutical industry for the production of stable agglomerates of desired composition, shape, strength, and porosity. Some examples are pharmaceutical pills [1, 63, 195, 99, 44], nuclear fuel pellets [147, 148], detergent tablets [31, 66], titanium compact tools [120, 158, 136], and Li-ion battery electrodes [119, 64, 82, 81, 128].

The physics of volume change in granular materials is complex due to the interplay of the concurrent effects of mutual particle exclusions, collisional energy dissipation, friction, bond forces, and collective dynamics involving arching and force correlations [58, 143]. The Reynolds dilatancy (volume change by shear), sensitive dependence of packing fraction on the confinement strategy, and highly inhomogeneous distribution of local porosities as a result of shear-banding and wall boundary conditions are among well-known features that heavily bear on the practical handling of granular materials and raise fundamental issues about the microstructural origins and controllability of volume change [49, 192, 20, 34, 4, 130, 145]. Although experimental methods are often designed to meet the specific challenges and types of materials of interest in each field, such common features prompt also the basic question of whether a universal or inherent volume-change behavior can be extracted.

This question has been so far mostly addressed in the case of cohesionless granular materials in soil mechanics[152, 103]. A nearly logarithmic dependence of porosity on confining pressure or on the number of vibration cycles has been evidenced [68, 103, 18, 34]. This scaling holds within two limits of porosity corresponding to the lowest and highest porosities that can be reached by applying an assembling procedure to a granular material. The lowest porosity represents the densest random packing state that is compatible with steric exclusions whereas the highest porosity is a property of the loosest state that is compatible with static equilibrium and stability of the packing. Most work on cohesive granular materials concerns compaction by ballistic aggregation or under the action of a compressive pressure [49, 181, 182]. A remarkable effect of adhesion between particles is to increase the range of accessible porosities as compared to cohesionless materials [180, 21]. Indeed, much higher porosities can be reached due to the stabilizing effect of tensile forces on the particles. However, in most experiments reported on powder compaction only a limited range of porosities is considered, the main concern often being the mechanical

strength induced by compaction together with specific target functionalities such as specific surface or permeability rather than porosity alone [141, 131, 42, 46].

Several different compaction laws have been proposed in the case of cohesive powders including logarithmic dependence of the porosity on the applied pressure for quasi-static compaction and power-law dependence on the cohesion number for dynamic compaction [63, 128, 192]. However, the particle-scale physical mechanisms deriving the compaction process are not the same in all processes. At low compressive stresses, the compaction is mainly due to diffusive-like motions, aggregation, and rearrangements of the particles whereas at high compressive stress the porosity increases also as a result of plastic particle shape change and breakage. Very low levels of porosity can be reached in the latter case [105, 70, 116, 82]. It is also important to distinguish the *primary compaction* of a granular material as a consequence of the preparation method, such as filling a die, from the *secondary compaction*, which is applied with the intension of reducing porosity or enhancing the tensile strength of the compact.

Beyond many insights provided by compaction experiments, a systematic understanding of the microstructural mechanisms that underlie the compaction behavior of cohesive granular materials may be achieved by means of particle dynamics simulations based on the Discrete Element Method (DEM) [30, 125, 175, 142, 134]. In this method, the classical equations of motion of rigid particles are incrementally integrated by accounting for the interactions between particles. For example, 2D simulations of the compaction of sticky particles with and without rolling resistance were carried out to analyze the influence of the assembling protocol on the resulting microstructures [49, 50]. In these simulations, a primary process of ballistic aggregation was first applied to obtain a stable packing of high porosity. Then, the packing was compressed by quasistatic stepwise increase of isotropic pressure under periodic boundary conditions. The simulations reveal the fractal structure of the packing below a correlation length of the order of a few diameters (fractal blobs). During compaction, loose structures collapse as the tensile strength of contacts is overcome by the externally imposed forces. It is found that the consolidation process is governed by the reduced pressure p^* defined as a the ratio of applied pressure to the internal cohesive stress. A nearly logarithmic dependence of porosity on reduced pressure is observed as in experiments, followed by a power-law fall-off down to the porosity of a cohesionless material. A similar compaction process was simulated in 3D and similar results were obtained [174, 173]. There are few simulations accounting for particle shape change. A new algorithm coupling Material Point Method (MPM) for the simulation of particle deformation with DEM for frictional contact interactions in 2D was able to simulate the compaction of a collection of soft disks down to a porosity close to zero [116]. Interestingly, the logarithmic scaling of porosity in these simulations were found to hold when compaction enters a stage of particle deformation without rearrangements. Similar simulations in 3D by coupling DEM with Finite Elements were recently reported [70].

In this chapter, we employ 3D particle dynamics simulations to analyze the compaction of a collection of sticky spheres enclosed inside a box whose walls are subjected to a constant isotropic compressive pressure. The particles are assumed to be rigid and unbreakable so that the compaction is merely due to particle aggregation and rearrangements. In contrast

to quasi-static simulations, where the pressure is increased in a step-wise manner after an initial aggregation process, the compaction process in our simulations is a consequence of the action of the confining pressure without step-wise control and equilibration of the packing. In this sense, our simulations are fully dynamic and represent the natural process of primary compaction under load. We also apply a small kinetic agitation to the particles to randomize the initial particle positions. Hence, the compaction is a consequence of diffusion, ballistic aggregation, and collective rearrangements of the particles.

We are interested in the characteristics of the packing and its internal structure as a function of adhesion force, compressive pressure, particle size, and contact stiffness. Recent simulations of sheared cohesive granular materials evidenced an unexpected influence of contact stiffness on the location of shear bands [93, 94]. Previous simulations of the fluidization of cohesive powders have also revealed a significant influence of contact stiffness on the onset of fluidization, but this effect has never been studied in the compaction process [110, 69]. As we shall see, the combination of contact stiffness with cohesion number, defined as the ratio of adhesive stress to the confining stress and corresponding to the inverse of reduced pressure, leads to a new dimensionless parameter that properly scales the porosity. Nevertheless, as we shall see, the bonding structure is more appropriately scaled by the cohesion number, implying that packings with a wide range of porosities can have similar bond networks.

An important important goal of this work is to clarify the effects of rigid walls, which are essential elements of most applications and are expected to play a major role in cohesive granular materials. For this reason, periodic boundary conditions were avoided. The walls and their motion with a finite mass under the action of the applied pressure lead to strong inhomogeneity of the bonding structure at very low and very high pressures. Such inhomogeneities are often observed in cohesive powders and we will show that they lead to average porosities that escape the proposed scaling [34].

In the following, we first describe the simulation method with focus on the force laws and the characteristics of the simulated system in Section 2.2. In Section 2.3, we present a detailed parametric study of porosity as a function of system parameters. We consider the scaling of the data with a modified cohesion number, the origin of the influence of contact stiffness, the dependence of the highest porosity on system parameters, the effect of damping parameter, and the functional form of the collapsed porosity data on the modified cohesion number. In Section 2.4, we investigate and characterize the bonding structures in terms of connectivity and force transmission, as well as the origins of the data points escaping the general scaling proposed. Finally, in Section 2.5, we conclude with a summary of the main findings of this work and open issues for further investigation.

2.2 Methodology

2.2.1 Force laws

For simulations, we used an in-house code based on DEM (code called Rockable; see Ref. [140]). The classical velocity-Verlet time-stepping scheme of the equations of motion and contact detection procedures are used in this code [2]. The total interaction force $\boldsymbol{f}$ between two particles is the sum of normal and tangential components f_n and $\boldsymbol{f}_t$, respectively:

$$\boldsymbol{f} = f_n \boldsymbol{n} + \boldsymbol{f}_t, \tag{2.1}$$

where $\boldsymbol{n}$ is the contact normal. The directions of $\boldsymbol{n}$ and $\boldsymbol{f}_t$ are generally defined to point from a neighboring particle to the particle considered. The interaction force is a function of the overlap δ_n, assumed to be negative when a contact occurs, and cumulative tangential displacement δ_t.

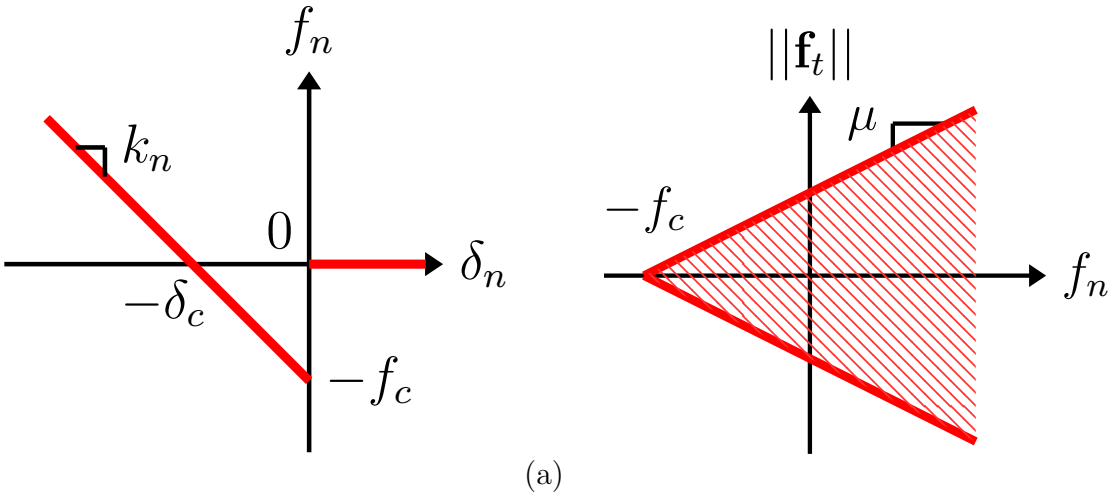

Figure 2.1: *Graphs of normal force law (Eq. (2.2)) and Coulomb criterion (Eq. (2.7)).*

We used an elasto-adhesive contact law, in which the normal force is the sum of a linear elastic repulsion force $f_n^e = -k_n \delta_n$, where k_n is the normal stiffness, and a constant adhesion force $-f_c$:

$$f_n = \begin{cases} f_n^e - f_c = -k_n \delta_n - f_c & \text{for } \delta_n < 0, \\ 0 & \text{for } \delta_n \geq 0, \end{cases} \tag{2.2}$$

The graph of this force law is plotted in Fig. 2.1(a).

The adhesion force f_c is assumed to represent the vdW (van der Waals) force, which is the main source of bonding for fine particles. The vdW force between two particles is given by

$$f_w = \frac{Ad}{24h^2}, \tag{2.3}$$

where A is the Hamaker constant, d is particle radius, and h is the gap distance between the surfaces of the two particles. As the force falls off rapidly with distance, it can be set with a good approximation equal to its value at the minimal distance h_0 allowed by surface roughness:

$$f_c \simeq \frac{Ad}{24h_0^2}. \tag{2.4}$$

Such a constant adhesion force acting only at the contact between two particles may be coined as *simple adhesion* law. Equivalently, we may consider that f_c is the pull-off force required to break the cohesive bond [62]:

$$f_c = \frac{3}{4}\pi\gamma d, \tag{2.5}$$

where $\gamma = A/(18\pi h_0^2)$ is the surface energy.

In the numerical model, we assume that f_c is independent of the overlap between particles. Second-order effects related to the variations of the adhesion force with the overlap or gap [109, 110], can be more suitably evaluated by comparison with simple adhesion law. In the absence of external forces acting on two touching particles, the adhesion force is exactly balanced by the elastic repulsive force so that $f_n = 0$ and the overlap in equilibrium is given by

$$\delta_c = -\frac{f_c}{k_n}. \tag{2.6}$$

When two particles are pulled apart from this equilibrium configuration, a tensile force is mobilized ($f_n < 0$) and increases in absolute value up to $-f_n = f_c$ for $\delta = 0$, where the cohesive bond fails. During compaction only compressive pressure is exerted on the sample but tensile forces develop in the contact network as a consequence of forced collective particle rearrangements.

For the tangential force, we used a linear elastic law together with a Coulomb dry friction criterion:

$$\boldsymbol{f}_t = \begin{cases} -k_t\boldsymbol{\delta}_t & \text{for } ||\boldsymbol{f}_t|| \leq \mu\left(f_n + f_c\right), \\ -\mu\left(f_n + f_c\right)\frac{\dot{\boldsymbol{\delta}}_t}{||\dot{\boldsymbol{\delta}}_t||} & \text{otherwise,} \end{cases} \tag{2.7}$$

where μ is friction coefficient and k_t is tangential stiffness. Throughout this work we set $k_t = 1.5k_n$. We checked that the ratio k_t/k_n has negligibly small influence on the compaction and porosity of bonding structures although its role in shear simulations may be significant. Note also that, as compared to the Coulomb criterion $||\boldsymbol{f}_t|| \leq \mu f_n$ for cohesionless contacts, here the Coulomb cone is shifted to account for the adhesion force added to the normal force, as shown in Fig. 2.1(b) [135, 134]. This means that only the repulsive part $f_n^e = f_n + f_c$ of the normal force comes into play.

For energy dissipation, in addition to frictional sliding and bond breaking as two natural mechanisms of dissipation, we assume inelastic collisions with a restitution coefficient $\epsilon_n <$

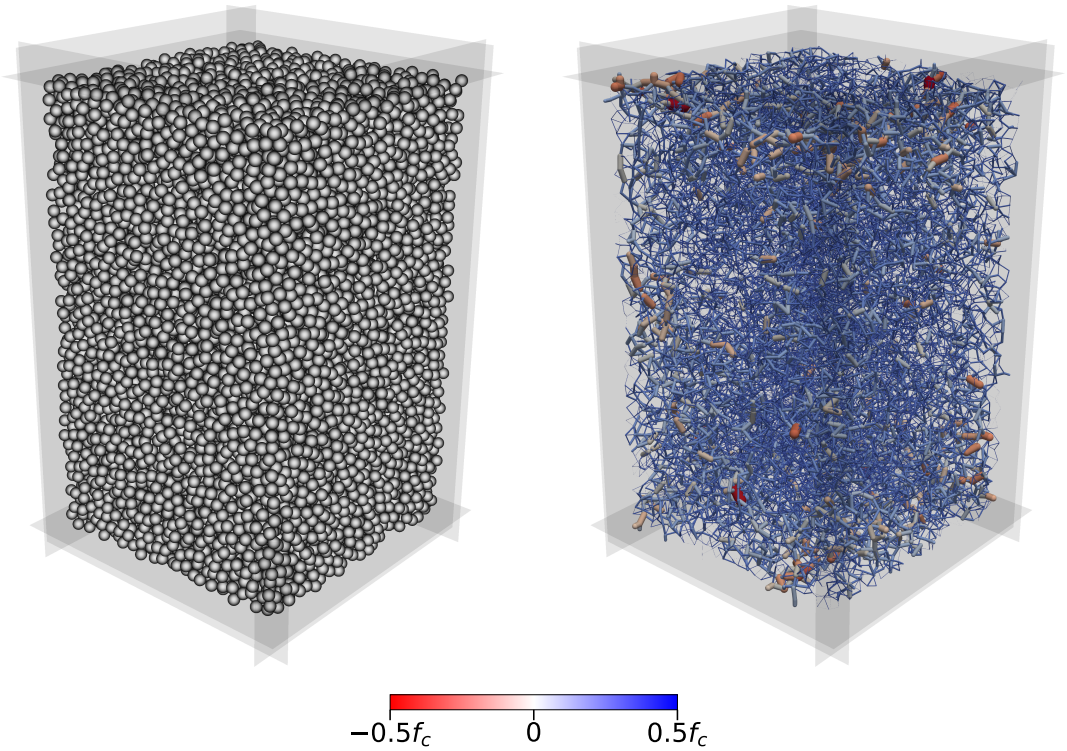

Figure 2.2: *3D representation of a jammed configuration and its bonding structure. Line thickness and color level are proportional to normal force with compressive (positive) forces in blue and tensile (negative) forces in red.*

1. In cohesionless contacts, the value of ϵ_n is controlled by adding a viscous normal force f_n^v to the elastic and adhesion forces:

$$f_n^v = -2\alpha_n \sqrt{k_n m}\ \dot{\delta}_n, \tag{2.8}$$

where m is particle mass. With this parametrization of the damping force, α_n is simply given by

$$\alpha_n = -\frac{\ln(\epsilon_n)}{\sqrt{\ln^2(\epsilon_n) + \pi^2}}. \tag{2.9}$$

The value of ϵ_n represents inelasticity of the contact independently of adhesion. As we shall see in Section 2.3.2, the effective restitution coefficient for cohesive contacts is lower and can be calculated as a function of both α_n and f_c. In particular, for a range of impact velocities below a critical velocity depending on f_c the effective restitution coefficient vanishes and colliding particles aggregate [16]. In nearly all simulations, we set $\epsilon_n = \sqrt{0.2}$, corresponding to $\alpha_n \simeq 0.25$. In Section 2.3.4, we will discuss the effect of ϵ_n on the scaling of porosity. Finally, we set the cohesionless tangential damping to zero. This implies that the aggregation of colliding particles is controlled only by normal damping.

2.2.2 Sample preparation and system parameters

The initial granular sample is created by randomly placing 17657 monodisperse particles inside a rectangular 3D box without overlap between them. The box size is $25d \times 25d \times 40d$. The compactness of the system can also be measured in terms of packing fraction ϕ, porosity $(1 - \phi)$, and void ratio e. The latter is defined as the ratio of pore volume to particle volume, so that [19]

$$e = \frac{1}{\phi} - 1. \tag{2.10}$$

Void ratio is more commonly used in soil mechanics where the volume of the particles does not change during compaction, providing therefore a reference volume for the void space [152, 103, 194, 24]. With this definition, $e = 1$ corresponds to equal volumes of particles and pores and a solid fraction $\phi = 0.5$. In our compaction simulations the initial void ratio is $e_i = 1/\phi_i - 1 \simeq 1.72$, corresponding to $\phi = \phi_i \simeq 0.37$.

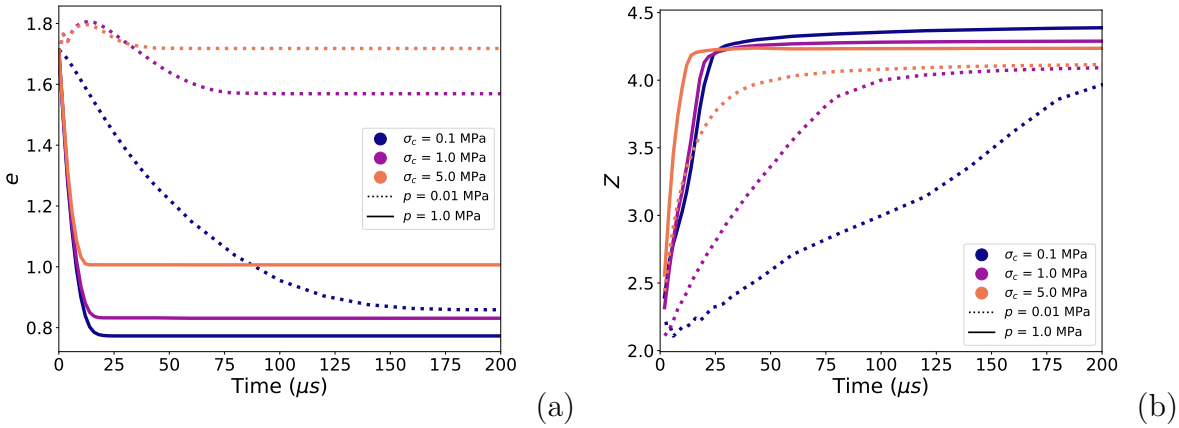

Figure 2.3: *Evolution of the void ratio e and coordination number Z as a function of time for three values of cohesive stress $\sigma_c = f_c/d^2$ and two values of pressure p.*

Isotropic compaction was applied by imposing the same pressure p on all six walls of the box. The gravity is set to zero to keep the sample in an isotropic stress state. Under the action of p, the walls move inward, compressing the particles until a stable mechanical equilibrium is reached. The simulation is stopped when the ratio of kinetic energy to the total elastic energy stored in the contacts is 2×10^{-7}. This process is fully dynamic and depends not only on the initial void ratio e_0 but also on the wall mass m_w. The pressure p being kept constant, the force acting on each wall decreases as pS, where S is the surface area of the wall. The initial dynamics of compaction is governed by the acceleration pS/m_w. In all simulations we kept m_w constant and equal to 96 times the mass m of a single particle.

As the walls move inward, they collide with particles and we may distinguish two limit scenarios depending on the dissipation rate or adhesion force between particles. In one limit, the walls sweep and capture the particles and a densification front propagates from

Parameters	**Values**
Cohesive stress σ_c [MPa]	11 values $\in [2 \times 10^{-3}, 4 \times 10^{2}]$
Pressure p [MPa]	4 values $\in [10^{-2}, 1]$
Elastic stress σ_e [MPa]	5 values $\in [5 \times 10^{2}, 2 \times 10^{5}]$
η	$[2.5 \times 10^{-3}, 4 \times 10^{4}]$
η^*	$[3.5 \times 10^{-5}, 31.6]$

Table 2.1: *Values of system parameters used in this work.*

the walls towards the center of the simulation box. In the other limit, they push the particles away and the induced kinetic agitation leads to bulk aggregation of the particles. In both cases, the initial aggregation stage is followed by particle rearrangements under the action of the compressive pressure. This second stage may fully erase the memory of the initial aggregation stage if the pressure is sufficiently high or the adhesion force is sufficiently small. Then, the initial void ratio e_i will not affect the resulting bonding structure and porosity of the packing. Otherwise, the compressive pressure is not high enough to destroy the bonding structure created by aggregation and the initial void ratio will fully determine the bonding structure. Figure 2.2 displays an example of a jammed configuration and its bonding structure at the end of compaction. The force chains are composed of both compressive and tensile forces.

To enhance the randomness of particle positions, we added a small initial velocity $v_k = 10^{-3}$ m/s of random orientation to all particles. This kinetic energy is rapidly dissipated in the initial stages of compaction. The initial kinetic pressure $p_k = \rho\phi v_k^2$ is 57 times smaller than our lowest pressure $p_0 = 0.01$ MPa. Nevertheless, for this pressure, the walls are initially pushed outward. Hence, the void ratio e increases beyond e_i and the subsequent aggregation under load leads to a slightly higher void ratio $e_0 \simeq 1.76$ ($> e_i = 1.72$) while the pressure is too low to induce further particle rearrangements. In the opposite case of high compressive pressure and low adhesion, we obtain the lowest void ratio e_{min}, which coincides with that of a packing of cohesionless frictional particles. We obtain $e_{min} \simeq 0.76$ ($\phi \simeq 0.57$) in agreement with previous studies [161]. All values of e reached during compaction vary therefore between e_{min} and e_0.

The two limits of compaction and the two stages of evolution of porosity can be clearly distinguished in Fig. 2.3, which displays the evolution of e and coordination number Z with time for several values of the cohesive stress $\sigma_c = f_c/d^2$ and p. At low pressure (dotted lines), e declines with time only at low cohesive stress, otherwise it slightly increases as a result of the expansion of the simulation box before decreasing again to a constant value when all particles aggregate. In this regime, the time needed for aggregation decreases as σ_c is increased. Note that Z continues to increase slowly as a result of rearrangements even when e reaches a nearly constant value. At high pressure (solid lines), the initial aggregation is fast and Z jumps from the very beginning to a finite value. e declines much faster for all values of adhesion force and we observe slow evolution of Z even when e levels off. In all cases, the compaction results from the combined effects of diffusion, aggregation

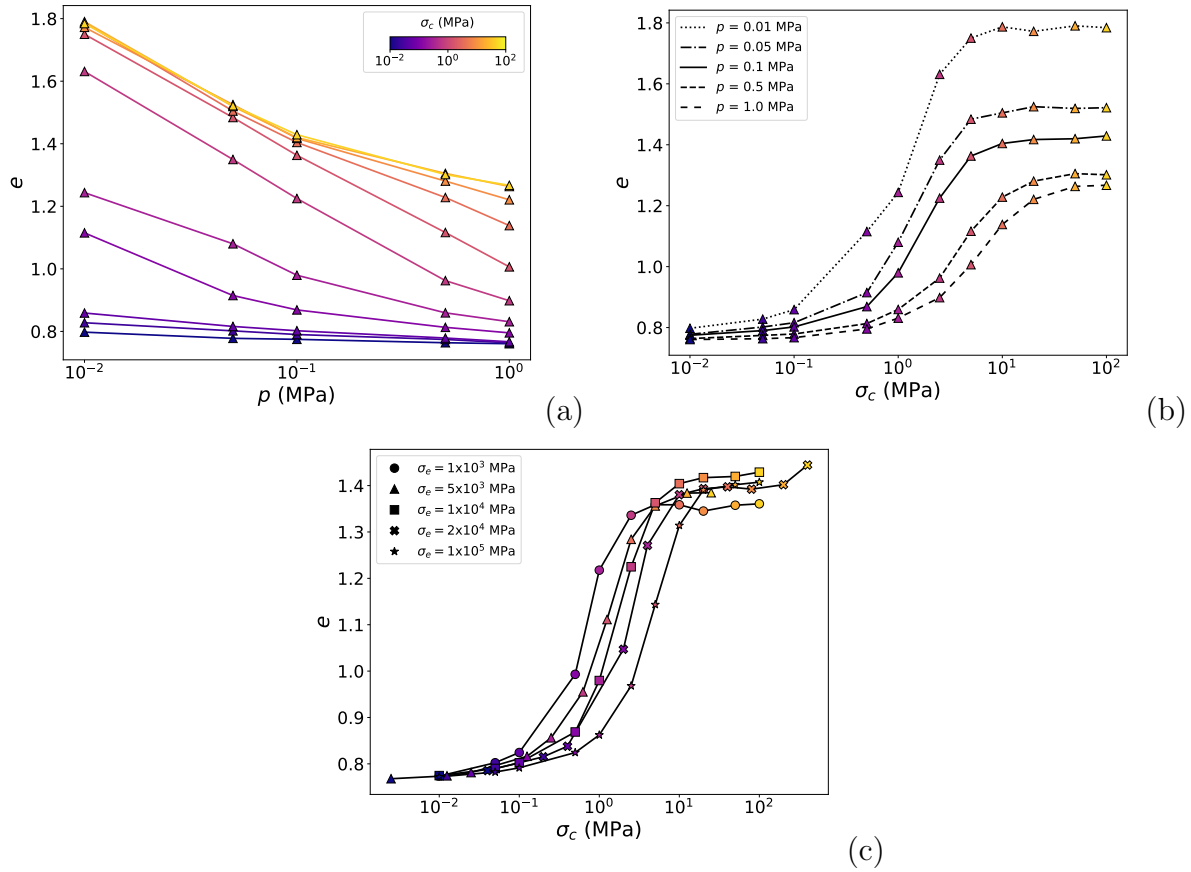

Figure 2.4: *Void ratio e of the stable packing obtained by compaction as a function of (a) applied pressure p for different values of cohesive stress σ_c and fixed values of σ_e; (b) σ_c for different values of the applied pressure p and fixed value of σ_e; (c) σ_c for different values of elastic stress σ_e and fixed value of p. The fixed values of applied pressure and elastic stress are $p = 0.1$ MPa and $\sigma_e = 10^4$ MPa, respectively.*

and compression.

We performed compaction simulations with different values of the cohesive stress $\sigma_c = f_c/d^2$, applied pressure p, and elastic stress $\sigma_e = k_n/d$. The latter represents the order of magnitude of the elastic moduli of jammed configurations. To vary σ_c we varied both the values of f_c and d. For dimensional reasons, particle size is irrelevant and, as we shall see, the void ratio is controlled by only two dimensionless variables that can be defined from the above three parameters. The ranges of values of these parameters are given in Table 2.1. All other parameters are kept constant. In particular, we set $m_w/m = 96$ and $\mu = 0.4$. The initial void ratio is likely to influence the aggregation phase but it was not considered in this work and all simulations of compaction start with the same value e_i of void ratio. We initially performed 220 simulations with all combinations of the parameters mentioned in Table 2.1. This corresponds to the number of data points used for the scaling of void ratio. Further 55 simulations were run to assess the effect of the damping parameter α_n

(see Section 2.3). In the following, e refers only to the void ratio of the stable configuration obtained by isotropic compaction.

2.3 Scaling of porosity

In this section, we are interested in the effect of system parameters on the void ratio e of stable packings obtained by compaction with the goal of identifying dimensionless scaling parameters that control e.

2.3.1 Parametric study

Figure 2.4(a) shows e as a function of pressure p for different values of cohesive stress σ_c and fixed value of σ_e. As expected, void ratio declines with increasing pressure. Furthermore, since adhesion tends to hinder particle rearrangements, higher cohesive stress leads to larger void ratio. Figure 2.4(b) shows e as a function of σ_c for different values of p and fixed value of σ_e. We identify three phases in the evolution of e in agreement with previous studies [50, 173]. At low adhesion, e increases slowly with p from e_{min}. As adhesion further increases, e increases more rapidly at a rate increasing with pressure. Finally, at even higher levels of adhesion, e tends to level off to a plateau value e_{max}. The value of e_{max} declines as the confining pressure increases. As discussed previously, the highest value of e in our simulations is $e_0 = 1.76$, corresponding to the highest adhesion and lowest pressure. The occurrence of a plateau suggests that a minimum value of σ_c is required to freeze the contact network in a configuration that is stable enough to withstand rearrangements under the action of a given value of p. The increase of σ_c beyond this value is ineffective.

Figure 2.4(c) shows e as a function of σ_c for different values of $\sigma_e = k_n/d$ and fixed value of p. We see here a clear dependence of void ratio on contact stiffness. As σ_e increases, the same level of compaction occurs for higher values of σ_c. We also observe that e_{max} depends only slightly on σ_e. These effects of σ_e are not quite intuitive since particle stiffness is generally irrelevant for the rheology of cohesionless granular materials. This point will be discussed in more detail below in connection with the scaling of porosity.

A key question is whether the void ratio can be scaled with dimensionless parameters combining the parameters σ_c, p, and σ_e. Dimensional analysis yields two independent dimensionless parameters, $\sigma_c/p = f_c/pd^2$ and $p/\sigma_e = pd/k_n$. Equivalently, the parameters $\sigma_c/\sigma_e = f_c/k_n d$ and $p/\sigma_e = pd/k_n$ may be considered. Hence, it might be possible to express the void ratio as an additive or multiplicative combination of these two parameters. The product of arbitrary powers of σ_c/p and p/σ_e provides a simple function:

$$s = \left(\frac{\sigma_c}{p}\right)^a \left(\frac{p}{\sigma_e}\right)^b, \tag{2.11}$$

where a and b are two exponents that depend on the local mechanisms governing the compaction process. Only the ratio b/a being physically significant, we set $a = 1$.

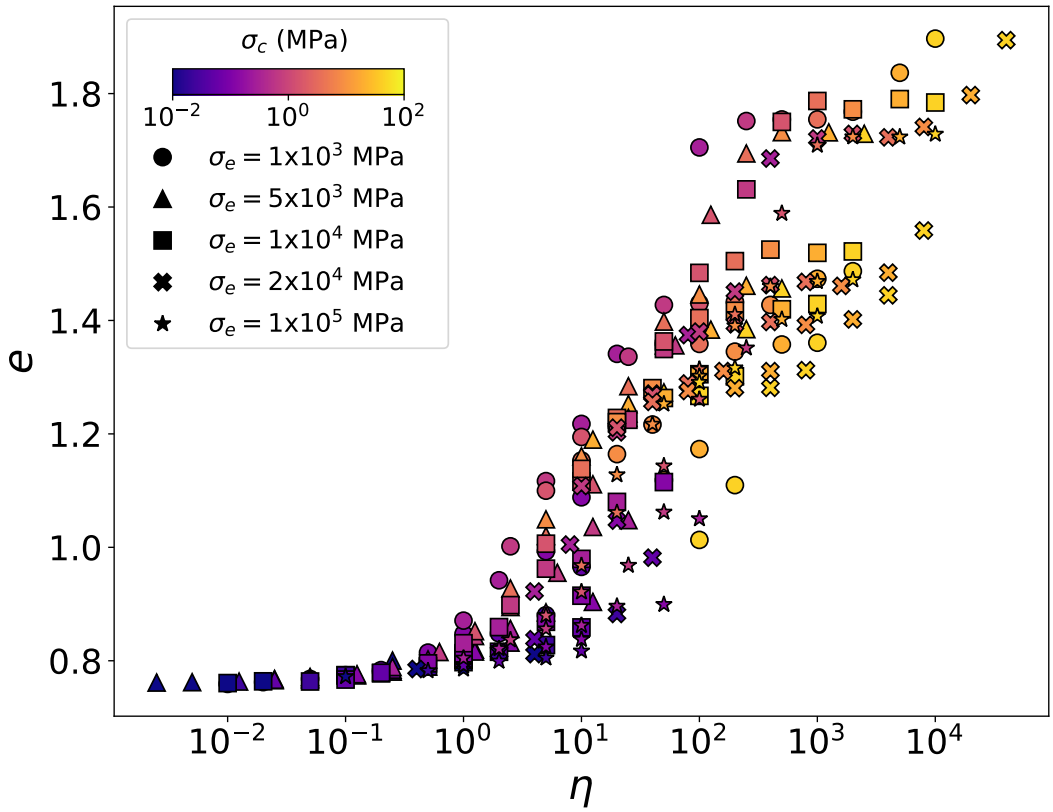

Figure 2.5: *Void ratio e as a function of cohesion number η. Each data point represents an independent compaction with parameter values represented by symbols and colors.*

By setting $b = 0$, we obtain the cohesion number,

$$\eta = \frac{\sigma_c}{p} = \frac{f_c}{pd^2}, \tag{2.12}$$

which is a measure of the relative values of cohesive stress and compressive pressure p induced by confining pressure [24]. Its inverse, called reduced pressure, has been used to scale packing fraction in previous studies in which k_n was set to a constant value [143, 50, 13]. Figure 2.5 shows e as a function of η for all our compaction simulations. We see that in the dense regime below $\eta = 1$, the data points collapse well as a function of η. Above $\eta = 1$, we observe a general trend of e to increase, but the data points are highly dispersed. This shows that e does not reflect only the condition of static equilibrium, which basically involves the balance of pressure-induced force pd^2 with adhesion force f_c, but it depends also on the dynamic process of compaction, which involves k_n in addition to f_c and p.

We find that the data points are much better regrouped together when b is set to a nonzero value. Considering mainly the points in the intermediate range of values of e, the best fit was obtained by setting $b = 1/2$ in Eq. (2.11). The corresponding scaling

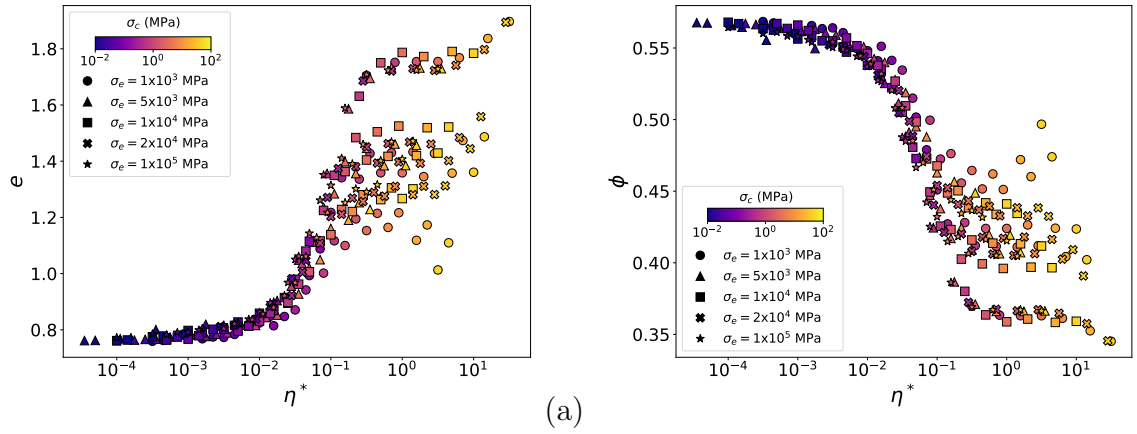

Figure 2.6: *Void ratio e (a) and packing fraction (b) as a function of modified cohesion number η^*. Each data point represents an independent compaction with parameter values represented by symbols and colors.*

parameter is

$$\eta^* = \frac{\sigma_c}{\sqrt{p\sigma_e}} = \frac{f_c}{\sqrt{pk_n d^3}}. \tag{2.13}$$

The void ratio and packing fraction are plotted as a function of this *modified cohesion number* η^* in Fig. 2.6. We see that the data points are now structured in several well-separated curves that differ in their plateau levels corresponding to different values of e_{max} and ϕ_{min}. The plateaus are well defined except for a few datapoints that are either above (resp. below) or below (resp. above) the plateau of e (resp. ϕ) at high values of η^*. These datapoints will be discussed in connection with wall effects. For the definition of the plateau we therefore refer to the value $e = e_{max}$ or $\phi = \phi_{min}$ reached at $\eta^* \simeq 1$.

We also observe that the differences between different datasets in the intermediate range are related to their differences in plateau levels e_{max}. The values of e_{max} for different sets of parameter values can be extracted from the plots of void ratios as a function of p for different values of σ_c and σ_e. The plateau corresponds to the range of pressures $p < p^{crit}$ with

$$p^{crit} = \frac{\sigma_c^2}{\sigma_e}. \tag{2.14}$$

Note that the right-hand quantity is the order of magnitude of the cohesive energy per unit volume stored in the bond network. In other words, the plateau level e_{max} is reached when the applied pressure is not too high to cause plastic rearrangements for given values of σ_c and σ_e.

Figure 2.7(a) displays e_{max} as a function of p^{crit}/p_0. We see that the data are reasonably well collapsed and e_{max} decreases with increasing p^{crit} according to the following function:

$$e_{max} = e_0 - \frac{c\ln(p_{crit}/p_0)}{1 + c\ln(p^{crit}/p_0)}, \tag{2.15}$$

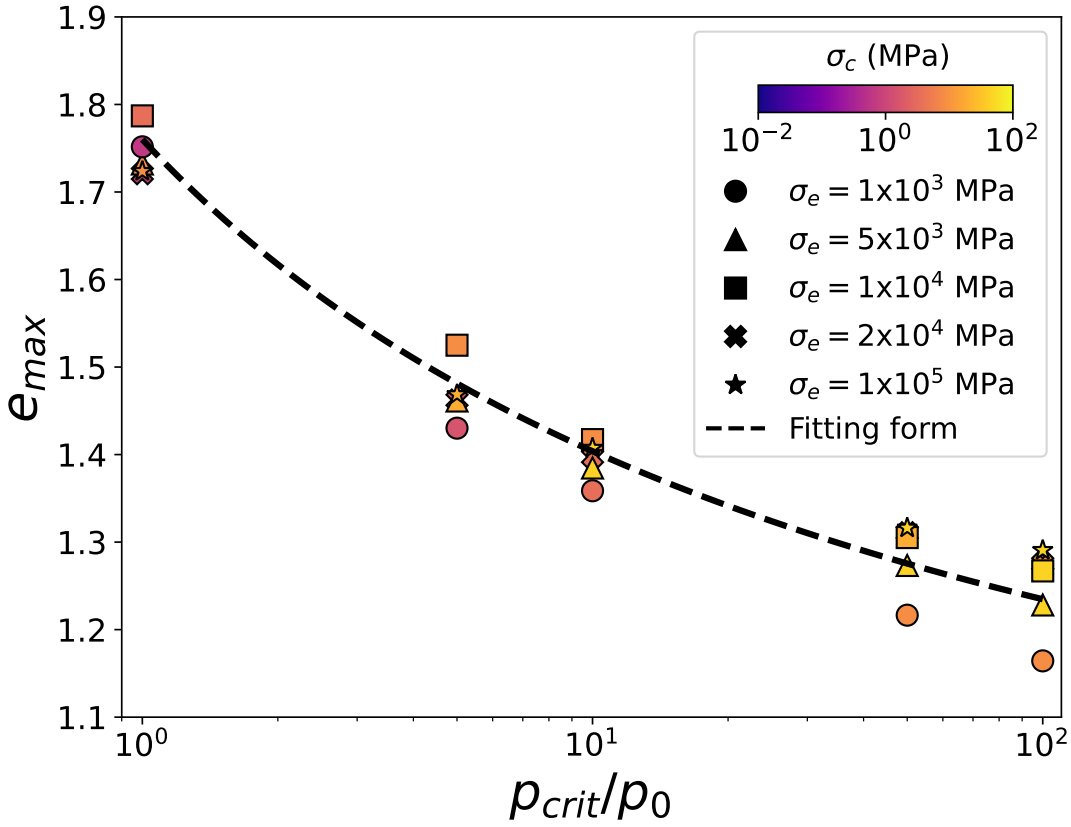

Figure 2.7: *The upper bound values e_{max} of void ratio (plateau levels) as a function of the critical compressive pressure $p^{crit} = \sigma_c^2/\sigma_e$ normalized by the lowest pressure p_0, corresponding to void ratio e_0, for different sets of system parameters. The dashed line is the logarithmic fitting function of Eq. (2.15).*

where $e_0 \simeq 1.76$ is the highest void ratio obtained with the lowest pressure $p_0 = 0.01$ MPa. The data points are fitted by adjusting only the parameter c to 0.24. The low pressure limit corresponds to $p^{crit} = p_0$ for which we have $e_{max} = e_0$. In the high pressure limit, this relation predicts $e_{max} \to e_0 - 1 \simeq 0.76$, which corresponds to the highest packing fraction $\phi = 0.57$. These two limits are independent of the value of c, which controls the curvature of the fitting form on the semi-logarithmic scale.

We now can rescale the data points of Fig. 2.13 by considering the *relative void ratio* e_r defined from e_{min} and e_{max}:

$$e_r = \frac{e - e_{min}}{e_{max} - e_{min}}. \tag{2.16}$$

It varies from 0 for $e = e_{min}$ to 1 for $e = e_{max}$. Fig. 2.8(a) displays e_r as a function of η^*. We observe an excellent collapse of the data on a master curve, implying that e_r is a well-defined function of η^* which combines all our system parameters. A similar collapse naturally occurs for packing fraction, as shown in Fig. 2.8(b), for the relative packing fraction $\phi_r = (\phi - \phi_{min})(\phi_{max} - \phi_{min})$. Interestingly, this scaling makes clearly appear a

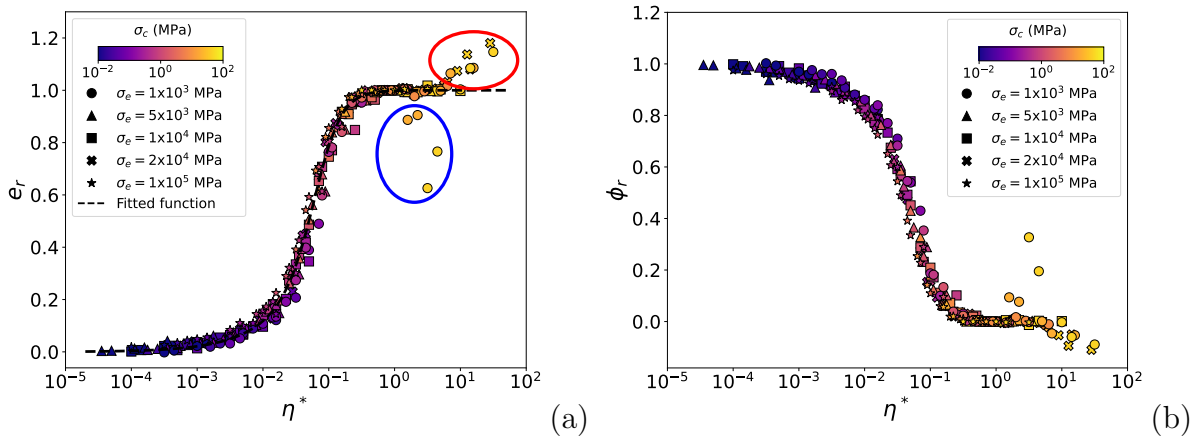

Figure 2.8: *Relative void ratio e_r (a) and relative packing fraction ϕ_r (b) as a function of modified cohesion number η^* for the data obtained from all compaction simulations. The dotted line represents the fitting function given by Eq. (2.30). The encircled symbols are the data points escaping the general scaling.*

few datapoints, marked in Fig. 2.8(a), that lie either slightly above or slightly below the plateau, revealing two limit conditions that will be discussed below.

This collapsed form of the porosity data and the presence of data points escaping the general trend raise several questions that will be further discussed below: 1) How to interpret the expression of the modified cohesion number η^* in Eq. (2.13)? 2) Is the intermediate range of porosities best fit to a logarithmic function as often suggested by compaction experiments and simulations? 3) What is the effect of the damping parameter α_n? 4) What is the origin of deviating data points?

2.3.2 Modified cohesion number

The cohesion number η represents the relative importance of the cohesive stress σ_c acting at all contact points with respect to the pressure p in static equilibrium. However, compaction under load is a dynamic process and the porosities of the jammed configurations arise from the balance of energy rates as in thermodynamic description of the propagation and arrest of cracks in a solid material [74]. We may attribute a surface energy of the order of $G = f_c^2/(k_n d^2)$ to each contact. During compaction, particle rearrangements occur if this energy is overcome by the work $W = pd$ supplied by the action of p per unit surface and over a distance of the order of particle size. Hence, the ratio $G/W = f_c^2/(pk_n d^3) = \sigma_c^2/(p\sigma_e) = (\eta^*)^2$ is expected to control the compaction level, i.e. the void ratio for which the particles get jammed in a stable configuration. The modified cohesion number η^* is the square root of this ratio. Hence, η^* can be considered as a measure of the relative level of inertia during compaction. For this reason, we expect that for low values of η^*, where dynamic effects are less important, the void ratio is also well scaled by η, and this is what we observe in Fig. 2.5.

The effect of the attraction force on the dynamics can be analyzed in a more straightforward way by considering the collision of a particle with a rigid wall [69]. The equation of motion of the particle is given by:

$$m\ddot{\delta}_n = -k_n\delta_n - 2\alpha_n\sqrt{k_n m}\dot{\delta}_n - f_c \tag{2.17}$$

where δ_n is the distance between the wall and the particle. Considering that upon collision at time $t = 0$ we have $(\delta_n(t=0) = 0)$ and the particle has an impact velocity of v_0 $\left(\dot{\delta}_n(t=0) = -v_0\right)$, the solution of Eq. 2.17 is given by:

$$\delta_n(t) = exp^{-t/\tau_2}\left(A\ cos\left(t/\tau_1\right) + B\ sin\left(t/\tau_1\right)\right) - A \tag{2.18}$$

with

$$A = -\delta_c = \frac{f_c}{k_n}, \tag{2.19}$$

$$B = \tau_1\left(\frac{2f_c}{\sqrt{k_n m}}\alpha_n - v_0\right), \tag{2.20}$$

$$\tau_1 = \frac{1}{(1-\alpha_n^2)}\sqrt{\frac{m}{k_n}}, \tag{2.21}$$

$$\tau_2 = \frac{1}{\alpha_n}\sqrt{\frac{m}{k_n}}. \tag{2.22}$$

The evolution of δ_n follows a typical linear-spring-dashpot movement with the equilibrium position $\delta_n = \delta_c$.

Depending on the impact velocity v_0, two different scenarios occur. If v_0 is relatively low, the particle will stick to the wall and δ_n tends to δ_c after a few damped oscillations. Otherwise, the contact will open up and the particle rebounds with a lower velocity. The contact duration τ_c in this case satisfies the condition $\delta_n(\tau_c) = 0$, which can be shown to be equal to the solution of the following implicit equation:

$$e^{-\tau_c/\tau_2}cos\left(\tau_c/\tau_1 - \gamma\right) = cos\left(\gamma\right) \tag{2.23}$$

with

$$\gamma = \arctan\left\{\tau_1\left(2\alpha_n\sqrt{\frac{k_n}{m}} - \frac{k_n v_0}{f_c}\right)\right\} \tag{2.24}$$

Since the breakage of the contact should happen during the first period of the elastic bounceback $(\tau_c/\tau_1 < \gamma)$, Eq. (2.23) implies $\gamma > 0$. This leads to the following criterion for contact opening:

$$v_0 > v_{crit} = 2\alpha_n\frac{f_c}{\sqrt{k_n m}}. \tag{2.25}$$

From the critical velocity v_{crit}, we can define a critical adhesion force in the case of compaction under load p:

$$f_c^{crit} = \frac{\sqrt{k_n m}v_0}{2\alpha_n} = \frac{\sqrt{pk_n d^3}}{2\alpha_n}, \tag{2.26}$$

where we have set $v_0 = \sqrt{pd^3/m}$ as the typical velocity induced by the force pd^2 on particles. The critical adhesion force represents the adhesion force above which the particles stick together and aggregate. Obviously, compaction is not a binary process since the particle velocities are unevenly distributed. However, f_c^{crit} provides a reference adhesion force from which we can define a dimensionless adhesion force,

$$\frac{f_c}{f_c^{crit}} = 2\alpha_n \frac{f_c}{\sqrt{pk_n d^3}} = 2\alpha_n \eta^*, \tag{2.27}$$

which is expected to be a control parameter of the compaction dynamics. Up to the damping coefficient, which is kept constant in our simulations, this ratio is the same as η^*. Its derivation from binary collisions sheds a new light on the role of η^* as a parameter that accounts for the probability of aggregation. In the previous argument based on the ratio of elastic energy release rate and the work of external forcing, the accent was on the likelihood of rearrangements. The aggregation and rearrangements are, however, two facets of the compaction process, which involves both loss and gain of contacts, as well as collective motion and deformation of aggregates. The critical velocity below which the effective restitution coefficient vanishes despite the nonzero value of the nominal restitution coefficient, is an important dynamic effect of adhesion, which explains why the void ratio is not simply scaled by η. Based on this analysis, it can be conjectured that if the compaction is incremental and the particles are allowed to dissipate their energy to reach static equilibrium after each increment of compressive pressure, η will provide an appropriate parameter and the void ratio will not depend on the contact stiffness.

2.3.3 Fitting forms

Let us turn now to the functional form of the collapsed data $e_r(\eta^*)$ in Fig. 2.8. The intermediate range of this plot looks like a logarithmic function. However, as can also be checked in past simulations reported in the literature, this range actually concerns only a small part of the whole range of the values of η^*, which covers at least 5 orders of magnitude. A power law has also been suggested in the dense regime ($e_r < 0.2$) [192, 49]. We found no fits in the literature for the loose regime ($e_r > 0.8$). In 2D simulations of compaction with samples prepared by aggregation, the upper plateau is not reached as an asymptotic state and the crossover between the intermediate and loose regimes is discontinuous since it reflects a transition from stable aggregates to collapsed aggregates. However, previous 3D simulations based on the same preparation process do show a gradual transition to the loose state as in our simulations of Fig. 2.8 [174, 173].

The trend in this intermediate-to-loose crossover observed in Fig. 2.8 is similar to that of dense-to-intermediate crossover, but there is an obvious asymmetry between them. In particular, the evolution of e_r in the dense regime is slow and takes place over several decades whereas in the loose regime it occurs for less than one decade. To make clearly appear this difference, let us consider the ratio

$$s \equiv \frac{1 - e_r}{e_r} = \frac{e_{max} - e}{e - e_{min}}, \tag{2.28}$$

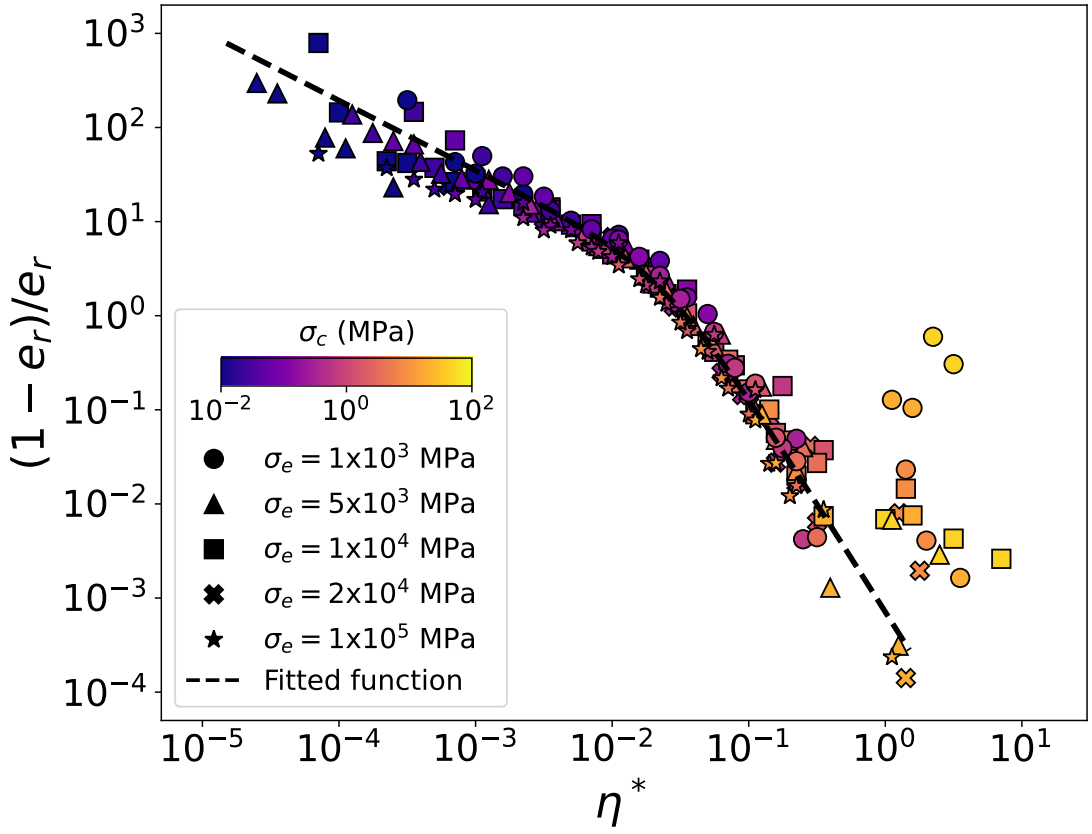

Figure 2.9: *Rescaled data of the relative void ratio e_r as a function of scaling parameter η^*.*

which compares the differences of e from its maximum and minimum values. It is plotted in Fig. 2.9 as a function of η^*. We see that the data are divided into two regimes, each plausibly described by a power law. In fact, a single fitting function excellently describes the whole range of data:

$$s = \frac{1}{A(\eta^*/\eta_m^*)^\alpha + (s_m^{-1} - A)(\eta^*/\eta_m^*)^\beta}, \tag{2.29}$$

with $A \simeq 0.475$, $\alpha \simeq 0.74$, and $\beta \simeq 2.3$. The point with coordinates $\eta^* = \eta_m^* \simeq 0.045$ and $s = s_m \simeq 1.55$ is the crossover point. This representation suggests that the intermediate logarithmic regime is practically absent and simply simply reflects the transition between the two power-law regimes. Interestingly, a similar power-law behavior with $\alpha = 3/4$ for the dense regime was found by contact dynamics simulations of dynamic compaction in 2D [192]. However, the effect of contact stiffness was not included in the scaling proposed and all the data were described as a function of η.

From Eq. (2.29), we get the following fitting form for $e_r(\eta^*)$:

$$e_r = \frac{A(\eta^*/\eta_m^*)^\alpha + (s_m^{-1} - A)(\eta^*/\eta_m^*)^\beta}{1 + A(\eta^*/\eta_m^*)^\alpha + (s_m^{-1} - A)(\eta^*/\eta_m^*)^\beta}. \tag{2.30}$$

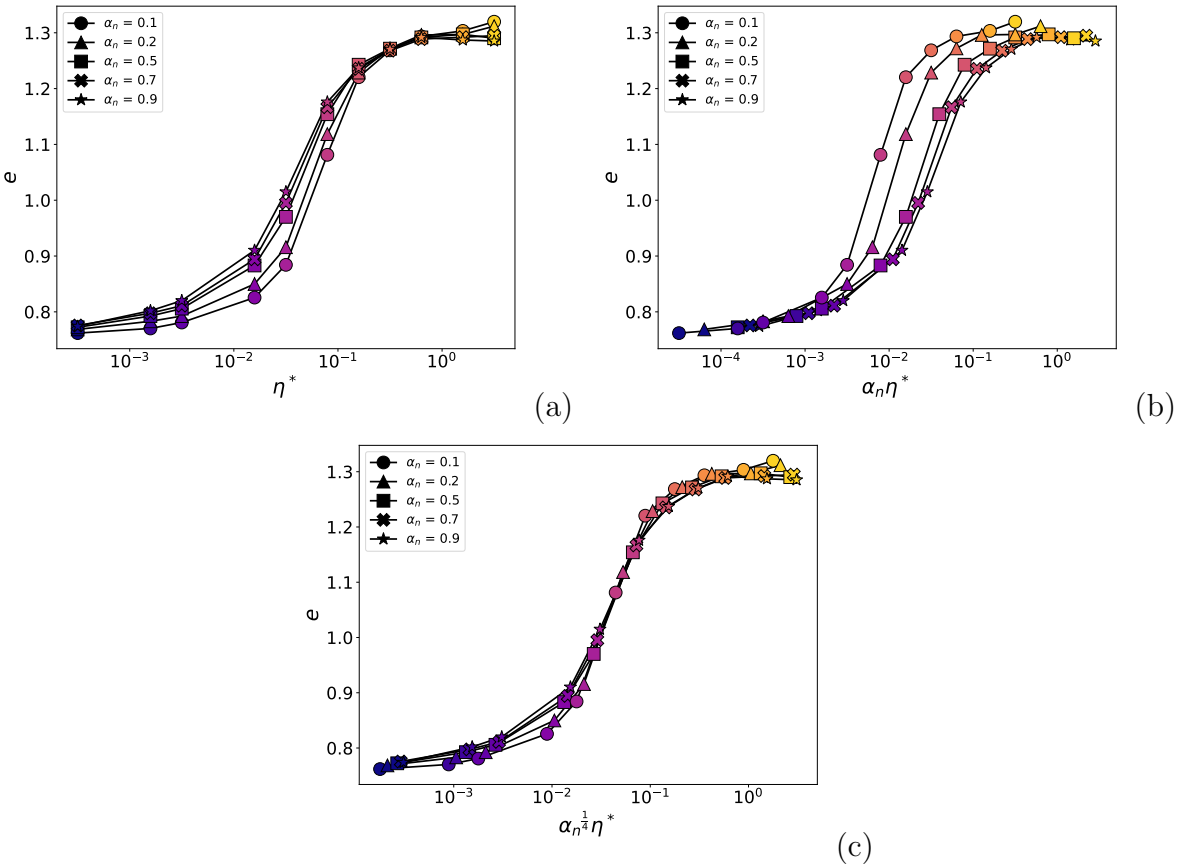

Figure 2.10: *Evolution of void ratio e as a function of η^* (a), $\alpha_n\eta^*$ (b), and $\alpha_n^{1/4}\eta^*$ (c), for different values of damping parameter α_n.*

This functional form is plotted in Fig. 2.8(a) together with the simulation data. We see that it provides an excellent fit for the relative void ratio as a function of the modified cohesion number. In this fit, the ratio β/α captures the asymmetry of the curve. This asymmetry may depend on the initial void ratio e_i, mass ratio m_w/m and whether the compaction pressure is applied incrementally or not.

2.3.4 Effect of damping parameter

All the void ratio data discussed so far were obtained from simulations with a fixed value of dissipation parameter $\alpha_n = 0.25$. However, Eq. (2.27) naturally suggests $\alpha_n\eta^*$ as scaling parameter rather than η^*. The issue is therefore whether α_n can be included in a simple way in the scaling of void ratios. To assess the effect of α_n, we ran a series of simulations with different values of α_n while also varying σ_c for $p = 0.1$ MPa and $\sigma_e = 10^4$ MPa. The results are shown in Fig. 2.10(a). As expected, for each value of η^*, e increases with α_n because of the stabilizing effect of energy dissipation or, equivalently, because of the decrease of the effective restitution coefficient or increase of the critical velocity, as suggested by Eq.

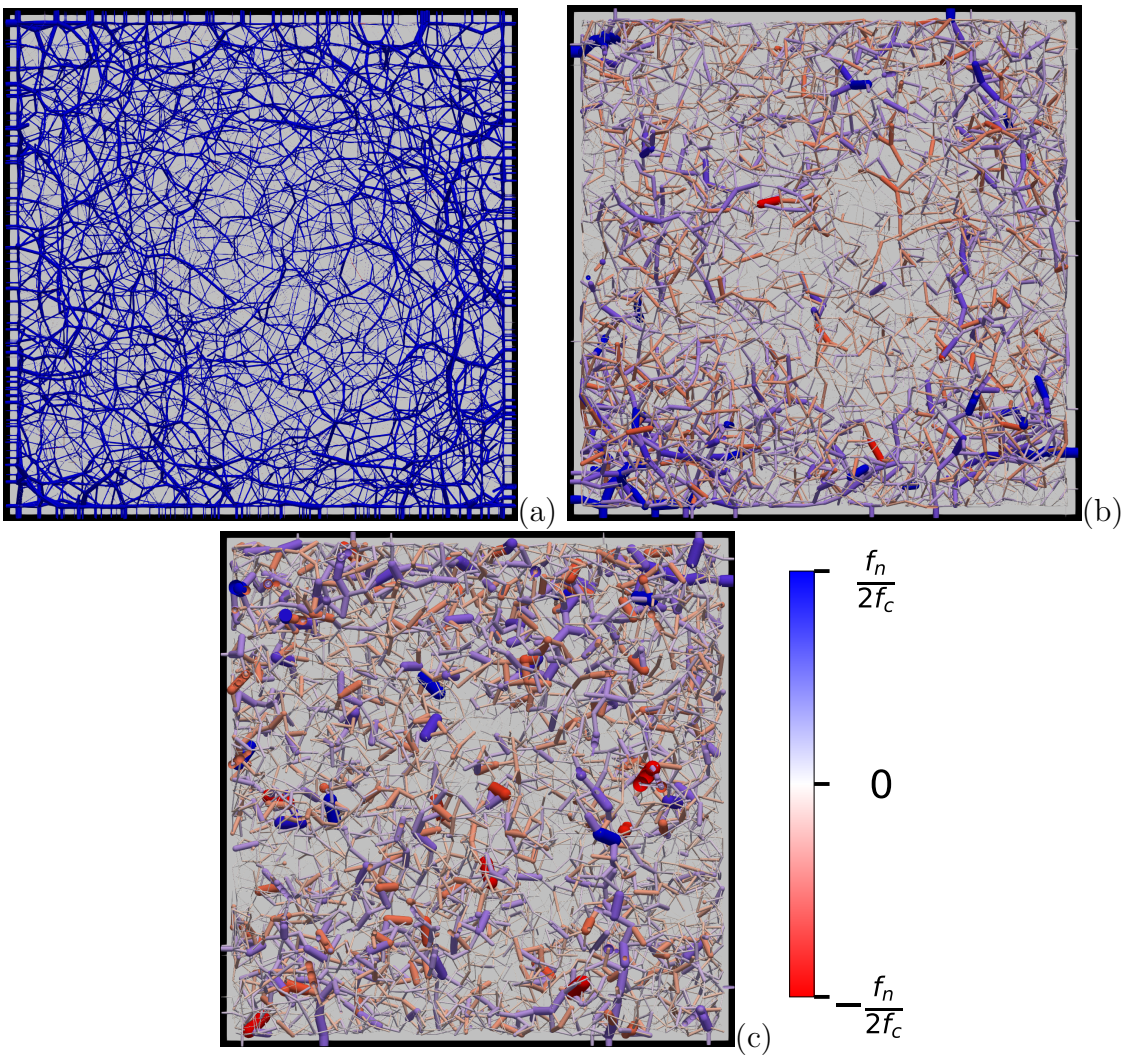

Figure 2.11: *Force network in a thin slice inside the packing for (a)* $\eta^* = 10^{-3}$*, (b)* $\eta^* = 0.05$*, and (c)* $\eta^* = 0.5$*. Line thickness is proportional to force magnitude.*

(2.25). This effect is most pronounced for intermediate values of η^*. In transition to the plateau, the effect of α_n declines since the stabilizing effect of f_c prevails in this regime. For the same reason, e_{max} is independent of α_n.

If, as suggested by Eq. (2.27), we plot the same data as a function of $\alpha_n\eta^*$, we obtain Fig. 2.10(b). We see that the the data collapse indeed in the dense regime, but the discrepancy increases everywhere else. The best collapse is obtained by using the scaling parameter $\alpha_n^{1/4}\eta^*$ as shown in Fig. 2.10(c). Data collapse is nevertheless mediocre in the dense regime. Note that a dependance on $\alpha_n^{1/4}$ was observed in shear localization [93, 94]. The same authors found a scaling of cohesion with $\alpha_n^{0.7}$ in a different problem [94]. It seems therefore that the void ratio depends in a nonlinear and unmonotonic way on the level of adhesion. Further simulations are necessary to arrive at a scaling that includes the

dissipation parameter. This can be done by investigating the influence of α_n on the general shape of $e_r(\eta^*)$, i.e. by quantifying the dependence of the parameters of the functional form of Eq. (2.30) on α_n.

2.4 Bonding structure

Particle configuration, contact network and force transmission are key features that evolve during the compaction process. Besides porosity, these features underlie mechanical properties and functionalities for which compaction is used in industry. For example, while void ratio is essential for transport of a fluid in the pore space, the contact network underlies electronic and heat conductivity across a packing. The pore and solid phases are, however, related together through two constraints: 1) geometrical duality of the particle and pore phases, and 2) force balance at the level of each particle. A fundamental issue is therefore whether void ratio and variables pertaining to the bonding structure are correlated across the parametric space, i.e. in the whole range of values of compressive pressure, contact adhesion, and contact stiffness. Hence, we consider in this section several aspects of the bonding structure and investigate their scaling with system parameters.

2.4.1 Force networks

Figure 2.11 displays three examples of the bond network with increasing value of the modified cohesion number η^*. At low cohesion (Fig. 2.11(a)), nearly all force chains are in the compressive state. Although it is difficult to fully appreciate the force chains in a 3D perspective, the strongest forces are clearly located in the vicinity of the walls, featured by several arches along the walls or spanning the space between adjacent walls in the corners of the box. Such wall effects are common in cohesionless packings and their presence together with a small gradient of forces from the walls towards the center of the box indicate that mesoscopic force inhomogeneities occur in our system on top of the well-known particle scale force inhomogeneity [135, 92, 139, 12, 41]. At higher cohesion (Fig. 2.11(b)), we observe both compressive and tensile force chains. The void ratio is higher but higher density of forces occurs at the corners of the box. We also see that the number of particle-wall contacts is reduced, implying that the transmission of the applied pressure from the walls to the sample is concentrated over a few contacts. At even higher level of cohesion (Fig. 2.11(c)), the network is even looser and the tensile and compressive forces are almost equally present everywhere.

Figure 2.12 displays the bond networks for one data point of each of the two groups of data escaping the general scaling in Fig. 2.8. The first group, encircled in red in Fig. 2.8, occurs at lowest pressures ($p \leq 5.10^{-2}$ MPa) and the data points are above the plateau $e_r = 1$. Fig. 2.12(a) is an example of the corresponding bonding network. As a result of very low pressure and high adhesion, the particles fully aggregate before the wall moves and comes in touch with only a few particles. The higher porosity of these samples is in agreement with 3D quasi-static compaction simulations [173].

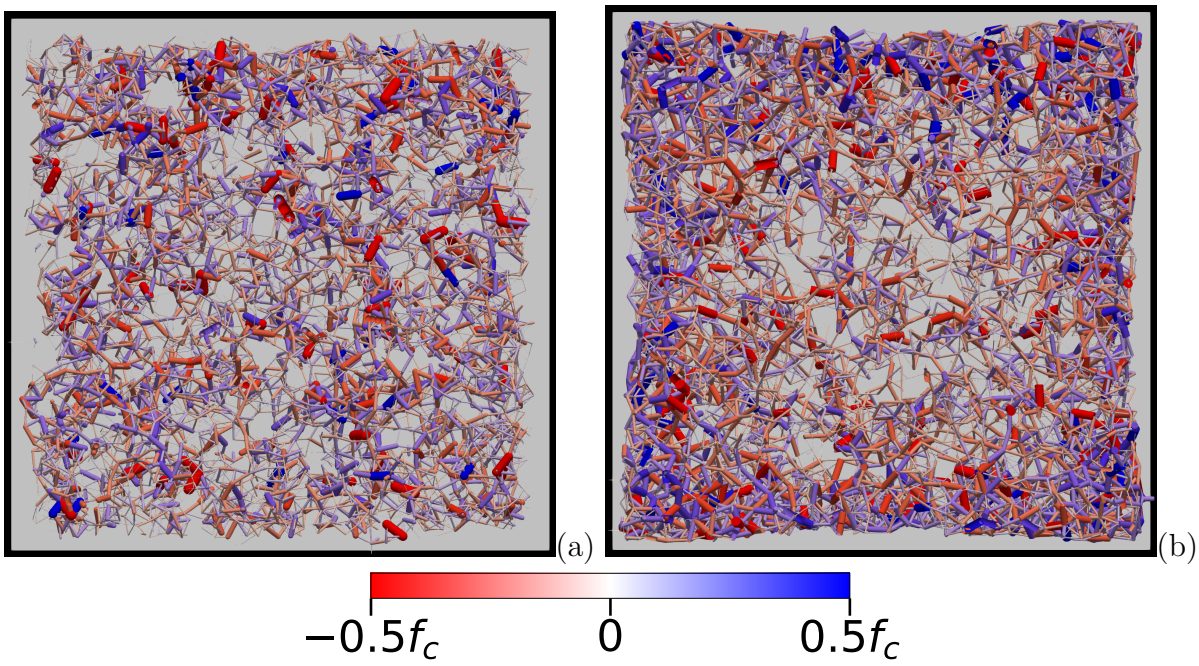

Figure 2.12: *Force network in a thin slice inside the packing for (a)* $\eta^* = 15$, $e_r > 1$ *and (b)* $\eta^* = 3$, $e_r < 1$. *Line thickness is proportional to the force magnitude.*

The second group, encircled in blue in Fig. 2.8, occurs for very high pressures ($p \geq 0.5$ MPa) and high cohesive stress. Fig. 2.12(b) is an example of the corresponding bonding network. High pressure leads to fast creation of stable and strong force chains along the walls followed by their buckling. As a result, most particles in the bulk are screened and receive a small amount of the external pressure. The high density in a thick layer close to the walls leads to lower global void ratio. Such inhomogeneous structures at low and high pressure in highly cohesive granular materials show the effect of both wall dynamics and finite sample size on the compaction process. In particular, high pressures lead to fast motion of the walls and dynamic jamming, tending to enhance force correlations and giving rise to stable arches across the system.

To better characterize the bonding structure for the 'regular' and 'deviating' data points, we calculated the void ratio as a function of distance r from the center of the samples. To do so, we calculated the void ratios inside a cubic probe of side $2r$ and centered on the center of the sample. Figure 2.13 shows e as a function of r/L, where L is the sample size. The five curves correspond to the five bond networks of Figs. 2.11 and 2.12. In all cases, we observe higher void ratio in the center of the sample and in the vicinity of the walls. The observed oscillations in the center reflect local ordering of particles or cohesive aggregates due to steric exclusions. Between these two limits, we observe either a plateau (for $\eta^* = 0.5$) or a small gradient for the regular data points (for $\eta^* = 10^{-3}$ and $\eta^* = 0.05$). For the deviating points, we observe either a strong gradient (case of $\eta^* = 15$ with $e_r > 1$) or a very high void ratio at the wall (case of $\eta^* = 3$ with $e_r < 1$). These

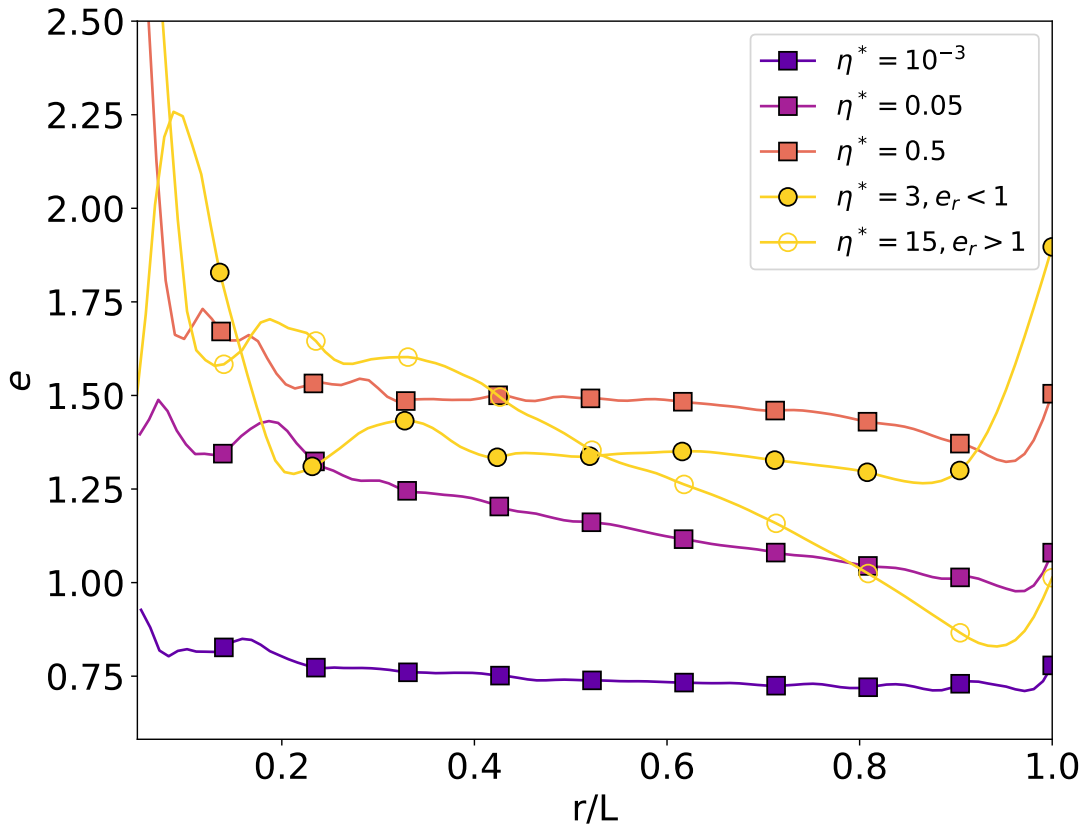

Figure 2.13: *Void ratio e in a cubic probe of side $2r$ and the same center as the sample as a function of r/L, where L is the length of the sample, for $\eta^* = 10^{-3}$ (corresponding to Fig. 2.11(a)), $\eta^* = 0.05$ (corresponding to Fig. 2.11(b)), $\eta^* = 0.5$ (corresponding to Fig. 2.11(c)), $\eta^* = 15$ (corresponding to Fig. 2.12(a)), and $\eta^* = 3$ (corresponding to Fig. 2.12(b)).*

pathologies reflect therefore a strong finite size effect in the former case and a strong wall effect in the latter case. In this latter case, we also see that the oscillations of e extend from the center to mid-distance from the wall, indicating the presence of aggregates, as can also be observed in Fig. 2.12(b). The finite size effects are naturally expected in the case of highly cohesive granular materials due to the clustering of cohesive particles. We find it interesting that the general scaling of e_r with η^* occurs despite such effects and porosity gradients inside the samples.

2.4.2 Coordination numbers

The coordination number Z is the lowest-order scalar variable characterizing the contact network. We find that in all packings and independently of system parameters, Z varies between 4 and 4.2. Since the coordination number of an isostatic frictional packing of spheres is 4, this means that bonding structures are only weakly hyperstatic even in the

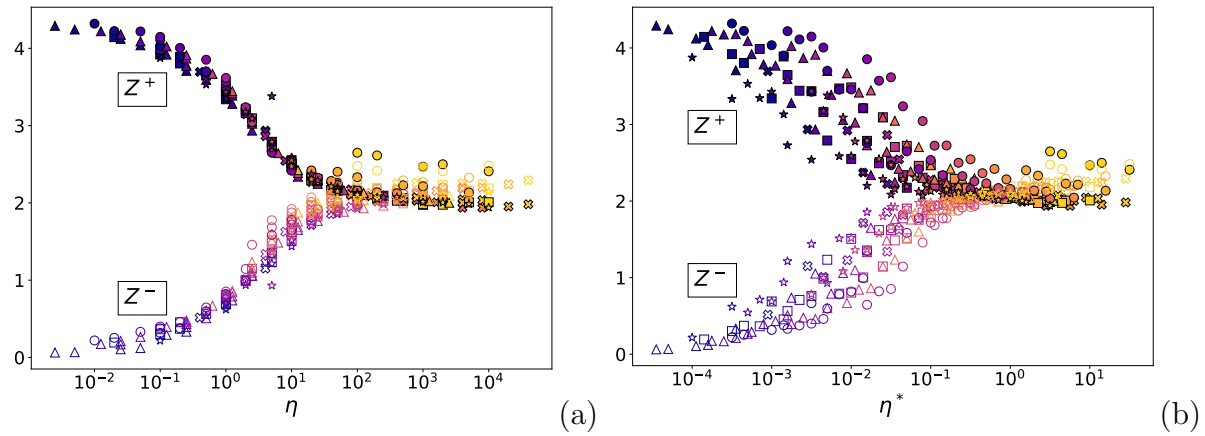

Figure 2.14: *Evolution of the coordination numbers Z^- (empty symbols) and Z^+ (plain symbols) as a function of η and η^*. The symbols and colors are the same as in Fig. 2.8.*

dense regime and the force networks are almost uniquely defined. A similar result was found by compaction simulations with 3D periodic boundary conditions [173]. The contact network is therefore *fragile* in the sense that, although it is globally stable, it can easily break or undergo large deformations under the action of shear stresses. The fact that Z remains low throughout the parametric space indicates that low coordination is a consequence of isotropic compaction, which is common to all our simulations. Higher levels of coordination can be reached by shearing or for soft deformable particles.

Since Z does not discriminate the generated packings, we consider tensile and compressive contacts whose numbers vary with the level of cohesion as observed in Fig. 2.11. Let Z^+ and Z^- be the compressive and tensile coordination numbers, i.e. the average numbers of compressive contacts ($f_n > 0$) and tensile contacts ($f_n < 0$), respectively. We have $Z = Z^+ + Z^-$. Figure 2.14 shows both Z^+ and Z^- as a function of η^* and η with all simulation compaction data points. We see that Z^- increases steadily with η and levels off around 2 at large values of η while at the same time Z^+ declines and tends to the same value of 2. Hence, in the asymptotic state each particle has 2 tensile contacts and 2 compressive contacts on the average. This symmetry between the tensile and compressive networks in the asymptotic state reflects the fact that at large values of η the force network (with its both tensile and compressive contacts) is mainly induced by adhesion forces which are well above the forces induced by the confining pressure [137].

Remarkably, in contrast to void ratio, the coordination number data collapse much better as a function of η rather than η^*! This means that, since $\eta^* = \sqrt{\eta}\sqrt{\sigma_c/\sigma_e}$, the same values of Z^+ and Z^- for a fixed value of η are compatible with a range of values of void ratio obtained by simply changing σ_e. This is quite important for the range of intermediate values of e_r where the latter changes significantly with η^*. Fig. 2.15 shows e_r as a function of the proportion Z^-/Z of tensile contacts. We see that for each value of Z^-/Z (depending on η), e_r varies indeed in a broad range of values with the widest variation occurring just before the plateau. We also see that the largest (resp. lowest) values of e_r correspond

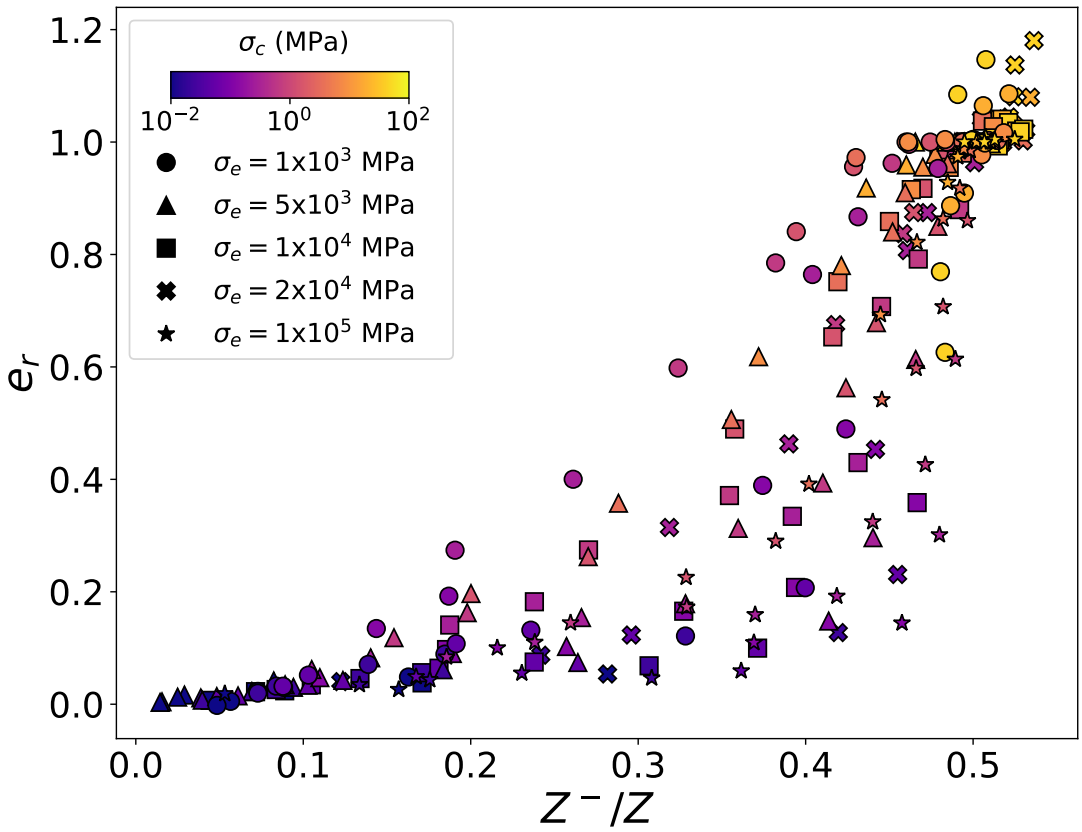

Figure 2.15: *Relative void ratio e_r as a function of the proportion Z^-/Z of tensile contacts for all simulations.*

to the lowest (resp. largest) values of σ_e. Figure 2.16 shows force networks for $\eta = 10$ but with different values of σ_e. We clearly see that force gradient increases from center towards the walls with increasing relative void ratio e_r although the distributions of tensile and compressive contacts are similar in the three networks.

The scaling of compressive and tensile coordination numbers with η rather than η^*, although unexpected, is actually a consequence of static equilibrium. This equilibrium is ensured at the level of each particle by the balance of forces induced by the applied pressure, which is of the order of pd^2, and the adhesion forces f_c acting at all contacts. The connectivity of the contact network characterized by Z being nearly the same for all compacted configurations, it is plausible that the force network characterized by the proportion Z^-/Z of tensile contacts depends on the relative importance of adhesion force and applied pressure via the ratio $\eta = f_c/pd^2$.

2.4.3 Force distributions

The bonding structure can be analyzed in more detail by considering the probability density function (PDF) of normal forces f_n. As f_c is the reference internal force which varies in

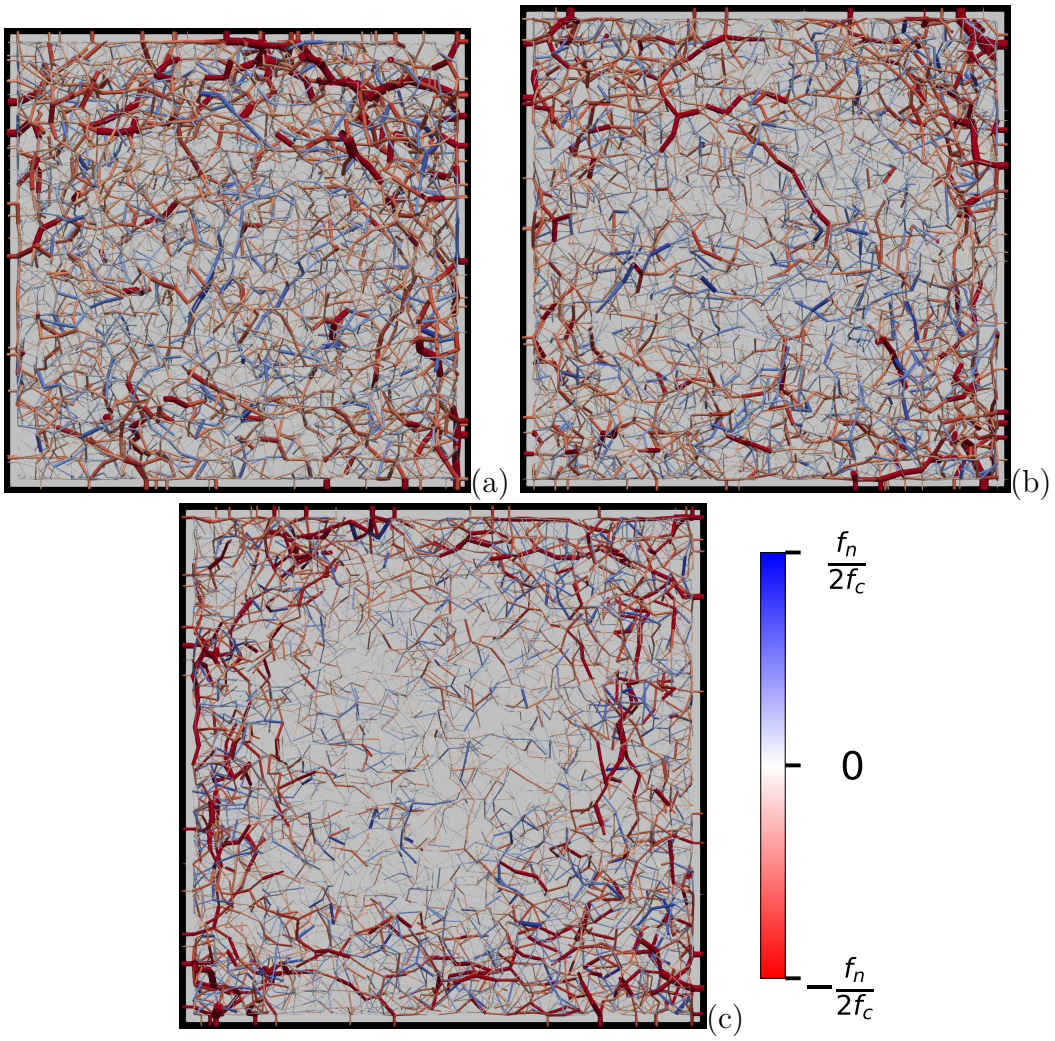

Figure 2.16: *Force networks in a thin slice inside the packing for* $\eta = 10$ *and* $e_r = 0.1$ *(a),* $e_r = 0.5$ *(b), and* $e_r = 0.9$ *(c).*

our parametric study, we focus on the distribution of force ratios f_n/f_c. Since we have $f_n = f_n^e - f_c$ at every contact point, the force ratio is $f_n/f_c = f_n^e/f_c - 1$ so that the PDF of force ratios actually represents the statistics of the mobilization of repulsive forces in the bond network as compared to the adhesion force. Fig. 2.17 shows three examples of the PDFs of normalized forces f_n/f_c. For the three values of η^*, we observe a double-exponential distribution:

$$P(f_n) \propto \begin{cases} e^{\beta^- f_n/f_c} & \text{for } f_n \leq 0, \\ e^{-\beta^+ f_n/f_c} & \text{for } f_n \geq 0, \end{cases} \tag{2.31}$$

characterized by the exponents $\beta^- > 0$ and $\beta^+ > 0$ for the ranges of tensile and compressive forces, respectively. These exponents describe the width of the distribution in the two ranges, which change with η^*. We also observe a Dirac peak at $f_n = 0$ when adhesion

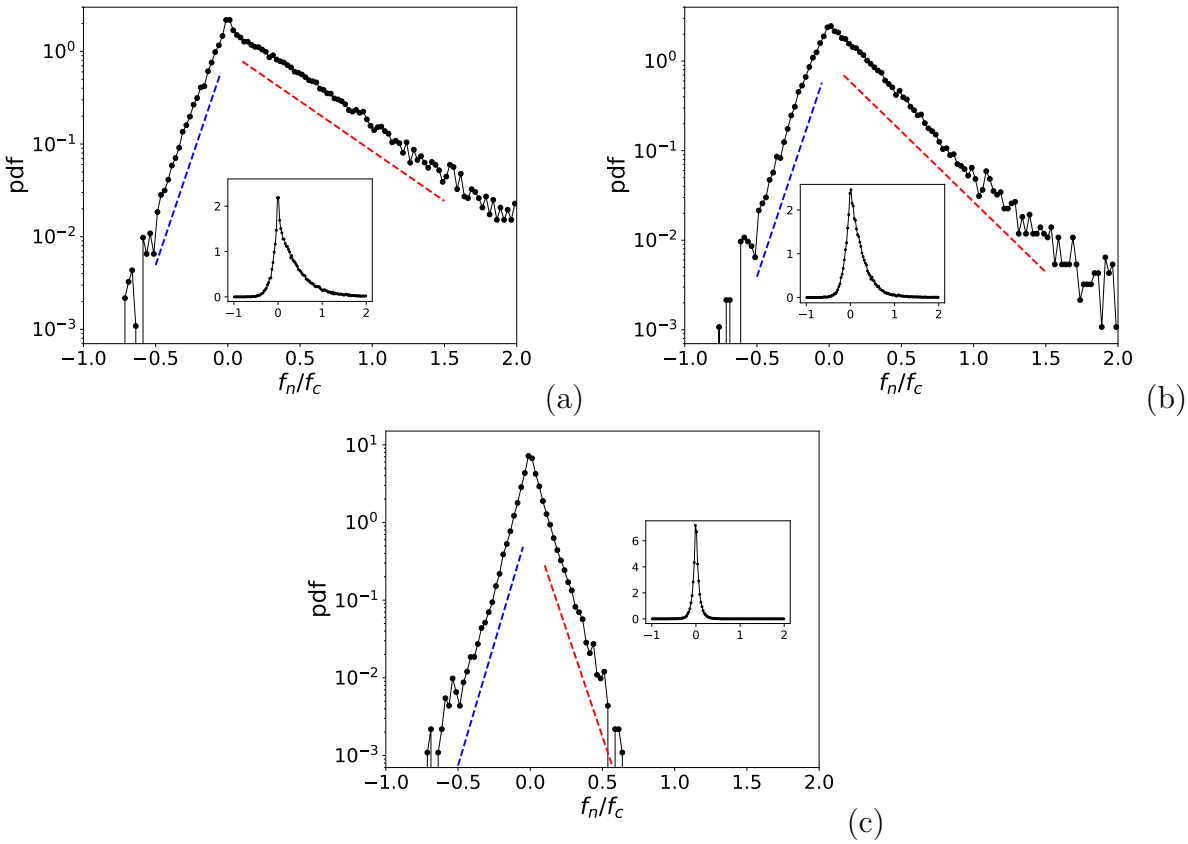

Figure 2.17: *Probability density function of normal force f_n normalized by adhesion force f_c for (a) $\eta^* = 10^{-3}$, (b) $\eta^* = 0.05$, and (c) $\eta^* = 0.5$. The dashed lines are guide to eyes for a purely exponential function.*

is low. Similar distributions have been reported in the past and the Dirac peak was attributed to the interface between particles or regions of mean positive (compressive) and mean negative (tensile) pressures [137].

We computed the values of β^- and β^+ in the ranges $[-0.5f_c, 0]$ and $[0, 1.5f_c]$ for which we generally have sufficient statistics. The precision is low in the range of tensile forces at low values of η due to a much lower number of tensile forces. Fig. 2.18 shows β^- and β^+ as a function of both η and η^*. Consistently with the behavior of Z^- and Z^+ and within our statistical precision, we find that β^- and β^+ are much better scaled by η than η^*. Hence, as in the case of Z^-/Z, the force distributions are increasingly uncoupled from the relative void ratio as η increases. Interestingly, both β^- and β^+ first decrease and then increase again at larger values of η. The initial decrease is more pronounced for β^+. The minimum value occurs at $\eta \simeq 0.2$ ($e \simeq 0.8$) and, according to Fig. 2.6, it corresponds to transition from the dense regime to the intermediate regime. The two exponents tend to the same value at large η.

To understand the unmonotonic evolution of the exponents with η, it must be reminded that the evolution of force PDF reflects the effect of adhesion on the distribution of elastic

forces $f_n^e = -k_n\delta_n$. In the dense regime, the effect of increasing adhesion is to reinforce strong force chains via weak tensile forces that play in this way the same role with respect to the strong force network as the weak compressive forces. As a result, the number of strong compressive forces and the inhomogeneity of the force network increase, the force PDFs become wider, and β^+ declines. Beyond $\eta \simeq 0.2$, the tensile network grows and self-sustained groups of particles mixing compressive and tensile forces appear as observed in Fig. 2.11(b). The amplitude of strong compressive forces is increasingly dictated by the adhesion force rather than external pressure. As a result, the scale of the compressive force is increasingly imposed by σ_c rather than p and the value of β^+ tends to that of β^-. In this sense, the force network becomes more symmetric around $f_n = 0$ with equal numbers of tensile and compressive forces.

The observed behavior of the exponents indicates a fundamental asymmetry between the effects of confining pressure and adhesive forces on the equilibrium of a granular packing. This point is not trivial when a variable such as η is used as control parameter, suggesting that the pressure p and compressive stress σ_c play identical roles with respect to the equilibrium of the force network. In fact, in the limit where the confining pressure p prevails ($\eta \ll 1$), the PDF $P_1(f_n/pd^2) \propto e^{\beta' f_n/pd^2}$ of normalized normal forces is independent of p (i.e. β' does not depend on p). When $\eta \gg 1$ and the effect of adhesion prevails, f_c is the relevant force scale and $P(f_n/f_c)$ is independent of f_c (i.e. β^+ does not depend on f_c). Statistically, the crossover from the regime ruled by p to the regime ruled by f_c occurs when the probabilities for the two alternative normalizations are equal: $P_1(f_n/pd^2)\delta f_n/pd^2 = P(f_n/f_c)\delta f_n/f_c$. Given the exponential form of the PDFs, this condition translates into $\beta^+ f_n/f_c = \beta' f_n/pd^2$, which implies $\beta^+ \simeq \eta\beta'$. The value of β' can be evaluated at $\eta = 1$, where $f_c = pd^2$ and therefore $\beta^+ = \beta'$. Figure 2.18 shows that at this point we have $\beta^+ \simeq 1$, implying $\beta' \simeq 1$. Since β' does not depend much on p in this limit, we may assume that its value remains equal to 1 for lower values of η. Hence, at crossover between the two regimes, we have $\beta^+ = \eta\beta' \simeq \eta$. Fig. 2.18(a) shows that this condition holds with a good approximation at $\beta^+ \simeq 0.2$, which corresponds to the minimum of the curve.

2.5 Conclusion

Particle dynamics simulations were performed to investigate the scaling of porosity and structural characteristics with system parameters in cohesive granular materials assembled under the action of an isotropic compressive pressure. Spherical particles governed by linear elasto-adhesive and frictional interactions were used in the simulations for broad ranges of values of cohesive stress, contact stiffness, compressive pressure, and particle size. In contrast to previously reported simulations, the compaction process in our simulations is fully dynamic due to the action of the applied compressive pressure. Because of the initially non-overlapping configuration of particles, this process involves ballistic aggregation, dynamic jamming, and particle rearrangements before a stable packing in static equilibrium is reached. In this work, the adhesion force was assumed to represent the vdW interactions.

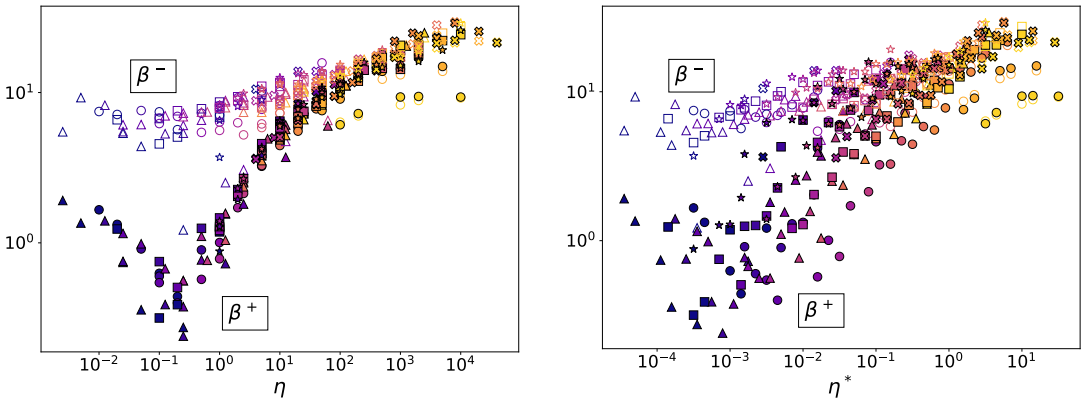

Figure 2.18: *Evolution of the exponents β^- (empty symbols) and β^+ (plain symbols) of the force PDFs for the tensile and compressive force domains. The symbols and colors are the same as in Fig. 2.8.*

However, the results hold also for other types of cohesive materials provided the attraction force is short-ranged and localized at the contact point and the cohesive stress σ_c can be clearly defined from the nature of the interaction. For example, liquid-bonded contacts in the limit of low liquid volume fraction are characterized by a short debonding distance (nearly equal to the cubic root of liquid volume) and a maximum capillary force proportional to the liquid-gas surface energy at the contact point [78, 138]. We also investigated in this work the effect of walls.

A key finding is the scaling of porosity (void ratio) with a new dimensionless parameter η^* which combines pressure p, cohesive stress σ_c, and characteristic elastic stress σ_e. It was argued that this *modified cohesion number* arises naturally by considering that, as in fracture mechanics, particle rearrangements depend on the work supplied by the applied pressure as compared to the elastic energy stored in the contact network. This scaling was also related to the critical velocity of aggregation between colliding adhesive particles. Particle stiffness appears therefore as a control parameter of dynamic compaction as it was previously found for fluidization and shear banding in cohesive granular materials.

We also found that the functional dependence of void ratio on η^* is best fit by a general form involving two power laws for 1) the increase of void ratio from the lowest porosity in the limit ruled by pressure and 2) the asymptotic increase of void ratio towards its highest value in the limit ruled by adhesion forces. Furthermore, the asymptotic void ratio was found to be a function of a critical pressure depending on cohesive stress, and elastic stress. We showed that the effect of damping parameter on porosity depends on the level of adhesion, and can not be included in a simple way in the general scaling proposed. We also discussed the origins of a few data points escaping the proposed scaling and showed that they result either from a slow motion of the walls and full ballistic aggregation of the particles due to very low pressure applied or from a fast inward motion of the walls due to very high pressure applied, causing dynamic jamming and high porosity gradients inside

the packing. In both cases, the presence of the walls and the finite size of the sample as compared with force correlations play a crucial role. An important finding of this work is that, despite such effects, the overall void ratio follows a well-defined scaling with η^* within the limits that were discussed, clarified, and illustrated.

The bonding structure was analyzed in terms of contact network connectivity, tensile/compressive networks, and force PDFs. These features were found to be rather dependent on the cohesion number $\eta = \sigma_c/p$ rather than η^*. This implies the remarkable property that a given force distribution is compatible with a wide range of values of void ratio. This variability reflects the effect of the characteristic elastic stress σ_e on the assembling process and increases with η. For all values of η, the coordination number Z is only slightly above 4, which is the isostatic coordination number for frictional spheres, showing therefore the weak hyperstaticity of the packings generated by isotropic compaction. The PDFs of both tensile and compressive forces are generically exponential with exponents that vary unmonotonically with η, revealing a transition from the dense regime, characterized by the stabilizing effect of adhesion, to the loose regime, mainly controlled by adhesion forces. As η increases, the bond network tends to a symmetric structure with similar PDFs and equal numbers of tensile and compressive forces.

Our results prove that granular materials can be assembled by dynamic compaction in packings of high void ratio with only normal adhesion forces and no need for rolling resistance. Previous simulations have shown that high levels of void ratio can not be reached by quasi-static incremental compression without rolling friction or without allowing the particles to aggregate freely before the application of the compaction pressure [49]. However, in dynamic compaction the influence of the initial void ratio needs to be investigated in order to arrive at a quantitative understanding of the role of the initial aggregation. Furthermore, our simulations may be considered as primary compaction to build a granular sample since the initial state is a granular gas. It will therefore be interesting to perform dynamic compaction simulations starting from a different state (*e.g.* the loosest state of our simulations or a packing obtained by ballistic aggregation) and investigate the relevance of the modified cohesion number for the scaling of porosity.

It is also important to consider the effect of Hertzian contacts for which the characteristic elastic stress explicitly depends on the pressure. It can be conjectured that the scaling proposed in this chapter based on the elastic stress as an independent parameter continues to hold by replacing the elastic stress by bulk modulus, which explicitly depends on the confining pressure in the case of a Hertz contact. This will then modify the expression of η^*. Another significant parameter is the friction coefficient μ between particles. Its value was fixed to 0.4 throughout our parametric investigation. However, the effect of μ on the proposed scaling is nontrivial. In particular, it is interesting to see whether μ controls only the value of e_{max} without modifying the scaling or it has a more extensive influence on the compaction process. The aggregation of particles and force correlations inside the packings and their link with finite size effects and deviating data points were discussed in this chapter, but more simulations are needed with increasing number of particles or simulation cell size to quantify such effects. Finally, we investigated the shear response of the packings obtained in this work with focus on the evolution of void ratio.

Chapter 3

Triaxial compression of cohesive granular materials

Our second study of the behavior of cohesive granular media is based on triaxial compression since this loading is relatively close to the models found in the literature representing calendering. Starting from the configurations obtained in chapter 2, the side walls are subjected to constant pressure while the bottom wall is fixed and the top wall is driven downward at constant speed. Porosity, anisotropy and stresses are measured as compression proceeds. We focus on the influence of adhesion force for fixed values of particle size, contact stiffness and confining pressure. The key issue is how the porosity changes during compression and what is the cohesive strength of the samples. We find that shear stress increases linearly with void ratio in the critical state (state of continuous deformation). The void ratio keeps a value close to its initial value, meaning that the void ratio obtained by dynamic compaction in each sample is close to its critical state void ratio. We show that the cohesive strength is linearly dependant on the adhesion force between the particles. Furthermore, the shear strength and the void ratio are linearly linked in the critical state. We also identify two limit behaviors in the evolution of the microstructure based on the coordination number and the anisotropy of the contact network: (1) increase of coordination number at constant anisotropy (most cohesive cases) (2) increase of anisotropy at constant coordination number (least cohesive cases). We show that these two microstructural parameters linked together in the fabric space as a result of steric exclusions.

Contents

2.1 Introduction 41

2.2 Methodology 44

2.2.1 Force laws 44

2.2.2 Sample preparation and system parameters 47

2.3 Scaling of porosity 50

2.3.1 Parametric study 50

2.3.2 Modified cohesion number 54
2.3.3 Fitting forms 56
2.3.4 Effect of damping parameter 58
2.4 Bonding structure 60
2.4.1 Force networks 60
2.4.2 Coordination numbers 62
2.4.3 Force distributions 64
2.5 Conclusion 67

Introduction

In the previous chapter we studied the behavior of cohesive granular materials under isotropic compaction. We determined a new dimensionless number linking the system parameters to the void ratio of the sample. However this model is not fully representative of the real calendering process. Based on the hypothesis that the calendering roll is much larger than the electrode and that the calendering speed is slow, several models introduced in the literature represent the calendering process as an uniaxial compaction [52, 117, 151, 165]. This loading compacts the electrode sample vertically while its lateral sides are periodic. By fixing the horizontal extension of the electrode this approach does not consider possible elongation of the electrode. In reality, the electrode lengthens in both horizontal directions during the calendering process, and mostly in the transversal direction [97]. It would therefore be more representative of the real process to consider deformation of the sample in all directions. In this chapter, we perform dynamic numerical simulations of the triaxial compression of cohesive granular materials. We use as initial configurations the isotropically compacted samples from the previous chapter. This allows us to start from a well-defined isotropic configuration, as electrodes already have a low porosity before being calendered. A constant pressure is applied to the lateral walls while the upper wall is lowered at a constant rate. We measure the evolution of electrode properties for samples of increasing adhesion.

3.1 Methodology

To perform this study, we use the microstructures obtained at the end of the study of Chapter 2 as initial configurations. One example of initial microstructure is shown in Figure 3.1. However, we consider fixed values of applied pressure, contact stiffness and particle size to focus on the effect of the adhesion force.

Starting from a stable isotropic configuration, the applied pressure p_h is maintained on the 4 lateral walls while the top and bottom walls are fixed. Once a new stable configuration is reached, the upper wall is lowered at constant speed $\dot{\epsilon}$. To reduce dynamic effects, we chose a low value of $\dot{\epsilon}$ to ensure a quasi-static regime. The inertial number I is used to determine whether a system is submitted to dynamic effets [133]. It is given by :

$$I = \frac{\dot{\epsilon} d}{\sqrt{p/\rho}} \tag{3.1}$$

A quasi-static regime corresponds to $I < 10^{-3}$. We therefore chose the value of $\dot{\epsilon}$ such that $I = 10^{-4}$ in the initial state with $p = p_h$. p increases during the compaction, reducing further the value of I.

The samples are compacted up to 40% of axial strain ϵ. Figure 3.2 shows the initial and deformed configurations for different values of cohesive force f_c. As explained in Chapter 2, the isotropic configurations differ with the value of the adhesion force. Higher values of

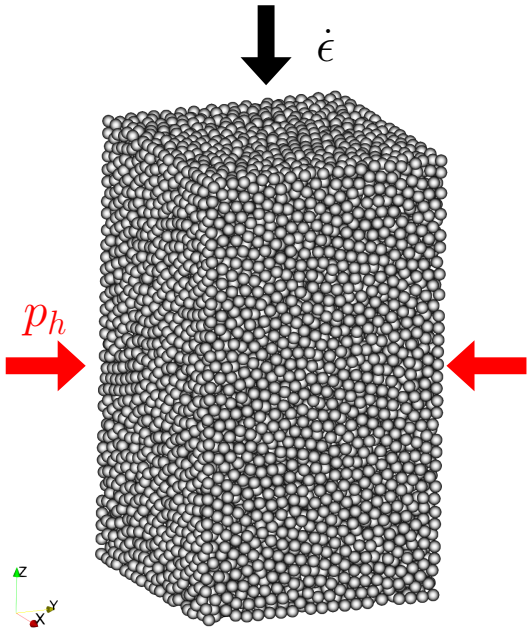

Figure 3.1: *Example of a sample used for triaxial compression.*

f_c yield looser samples with a broader range of forces. Before the top wall starts is set to move, the sample is in an isotropic state with no specific orientations of contacts. During triaxial compression, the microstructure orients itself vertically, with strong resistive force chains pointing in this direction. We observe that the shape of the samples tend to a rounded and isotropic configuration all the more that adhesion is higher. This leads to less contacts with the lateral walls and the whole load is supported by only a few particles.

3.2 Evolution of state variables

3.2.1 Void ratio

We are more specifically interested in the evolution of void ratio e for different levels of adhesion and initial porosity. Intuitively, one expects that for all samples which have a high initial porosity e_0, e will decrease during triaxial compression. However, the high values of e_0 are due to adhesion and it may well happen that shearing of the sample by triaxial compression will simply deform the sample without significant volume change. The motions of the walls allow us to compute the deformations of the initial box in the three principal directions (which are here equivalent to the 3 cartesian directions). The shear strain ϵ_q is given by:

$$\epsilon_q = \epsilon_1 - \epsilon_3, \tag{3.2}$$

where ϵ_1 is the strain along the vertical axis and ϵ_3 along the horizontal axis. Since the loading is equal in both horizontal directions, we have $\epsilon_2 \simeq \epsilon_3$.

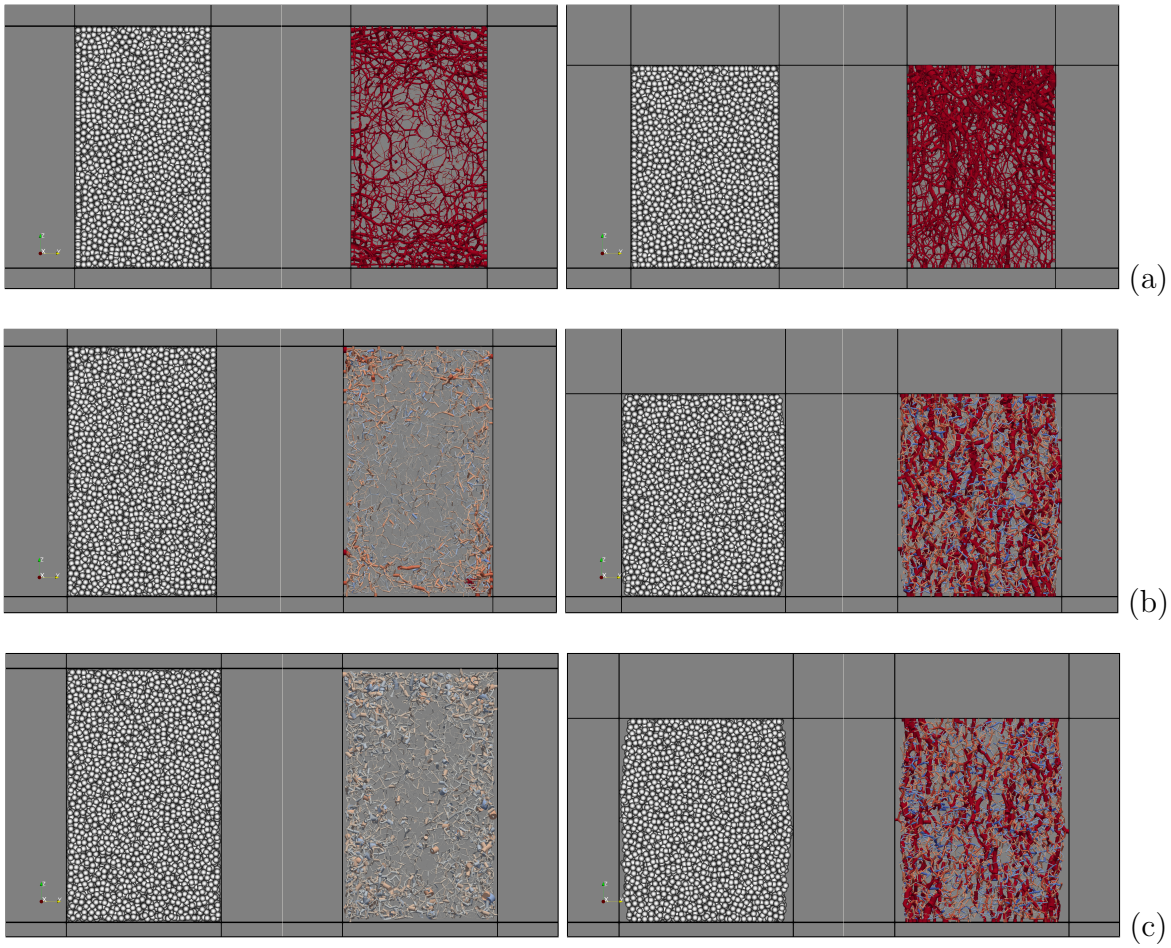

Figure 3.2: *Microstructures and force networks of samples at* $\epsilon = 0\%$ *and* $\epsilon = 20\%$ *for different values of the adhesion force (a)* $f_c = 5$ *µN (b)* $f_c = 250$ *µN (c)* $f_c = 5000$ *µN*

Figure 3.3(a) shows the evolution of e as a function of ϵ_q for different values of f_c. For low values of f_c, *i.e.* for initially denser configurations, the system starts from an already compact configuration, and the value of e can not naturally decrease much. However, we see that even configurations of high values of f_c – and therefore initially loose microstructures – first undergo a small compaction phase but then the porosity increases again! All configurations reach a plateau value of e after almost 50% of deformation. This latter behavior is typical of rather dense granular materials, where the material dilates after an initial compaction. Since the dilation is very small in all cases, we may state that all samples are close to their critical-state void ratios. The plateau values of e are plotted in Figure 3.3(b) as a function of f_c. The evolution follows an asymmetric sigmoid curve similar to the one in Figure 2.4(a). The data points are close to their initial values of the isotropic state. This shows that the porosity obtained by isotropic compaction is the same as the critical porosity reached by triaxial compaction.

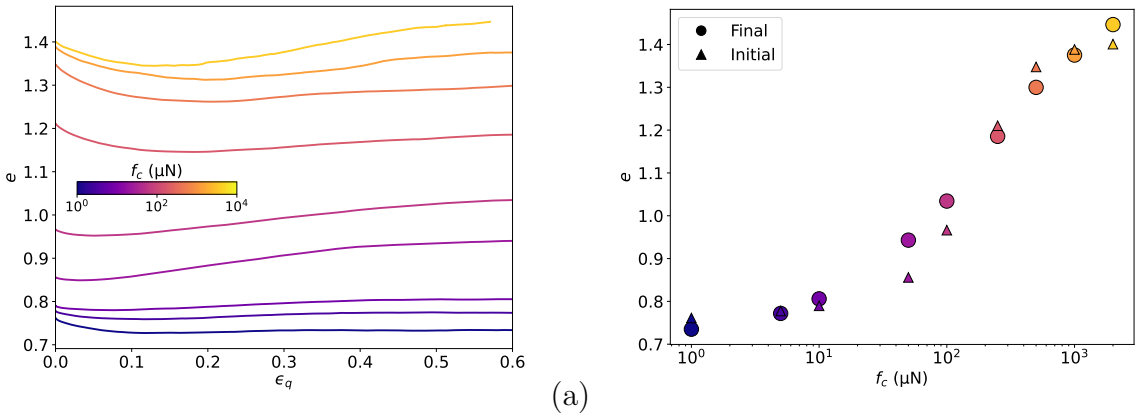

(a) (b)

Figure 3.3: *(a) Evolution of void ratio e as a function of ϵ_q (b) Initial and final values of e as a function of f_c.*

3.2.2 Stresses

The major principal stress σ_1 is directed along the compression axis while the two others σ_2 and σ_3 are directed along the extension axes. The mean stress p – not to confuse with p_h the confining stress applied on the lateral walls – and the deviatoric stress q are defined in 3D by

$$p = \frac{1}{3}\left(\sigma_1 + \sigma_2 + \sigma_3\right) \ , \ q = \sigma_1 - \sigma_3, \tag{3.3}$$

under axisymmetric conditions [132]. Figure 3.4(a) displays the shear stress q/p as a function of ϵ_q for different values of adhesion force. In the beginning, q/p is close to 0 due to isotropic initial state. Once compression begins, the shear stress ratio increases at a rate depending on f_c; the higher the adhesion force, the faster the increase rate. This means that more porous samples show a more stiff behavior A peak stress value is reached followed by a slight softening until a plateau is reached. The absence of a pronounced peak is consistent with small dilatancy of the samples observed in Fig. 3.3. The evolution is globally consistent with an initial critical void ratio.

The values of q/p in the critical state are denoted by M. They are plotted in Figure 3.4(b) as a function of f_c. We observe that the relationship between M and f_c seems to follow a sigmoidal evolution, similar to that of void ratio e. This confirms that, despite lower packing fractions, higher adhesion forces lead to higher shear strength. The minimal value of M is 0.7 for $f_c \to 0$, which corresponds to the shear strength of a cohesionless material [147]. The maximum value of M seems to tend to 3 as a logarithmic function of f_c.

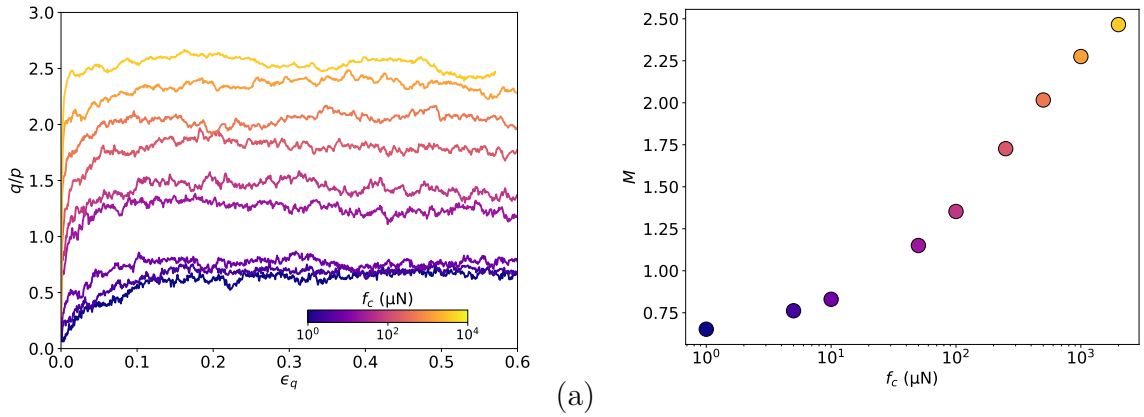

Figure 3.4: *(a) Evolution of shear stress ratio q/p as a function of shear strain, and (b) Critical values of $q/p = M$ as a function of f_c.*

3.2.3 Cohesive strength

The cohesive strength can be determined from the Mohr-Coulomb failure criterion, which for the normal stress σ and shear stress τ on the failure surface implies

$$\tau = \sigma \tan\phi + c, \tag{3.4}$$

where c is the cohesive strength and ϕ is the internal angle of friction. Mohr circles are plotted in Fig. 3.5 for the principal stresses σ_1 and $\sigma_2 = \sigma_3$ in the critical state. Since $\sigma_2 = \sigma_3$, two circles coincide, with radius $(\sigma_1 - \sigma_3)/2$ and center located at $((\sigma_1 + \sigma_3)/2, 0)$. From this figure and Equation (3.4), we have:

$$\frac{\sigma_1 - \sigma_3}{2} = \frac{\sigma_1 + \sigma_3}{2} \sin\phi + c\cos\phi \tag{3.5}$$

The value of c is therefore given by

$$c = \frac{\sigma_1 - \sigma_3}{2\cos\phi} - \frac{\sigma_1 + \sigma_3}{2} \tan\phi \tag{3.6}$$

The value of c depends on ϕ, which can be determined from a cohesionless configuration in which the cohesive strength c is nil so that $\tan\phi = \tau/\sigma = \mu_c$. Given the definition of p and q in Eq. (3.3), the angle of friction ϕ is given in 3D by:

$$\sin\phi = \frac{3q}{2p+q} = \frac{3M}{2+M}. \tag{3.7}$$

The lowest cohesive configuration at $f_c = 1$ μN is very close to a cohesionless system. We used the corresponding data to compute the value of ϕ. We get $\phi \simeq 0.298\ rad = 17.07°$.

The values of c obtained from Eq. (3.6) using the estimated value of ϕ are displayed in Fig. 3.6(a). Remarkably, the cohesive strength increases almost linearly with the adhesion

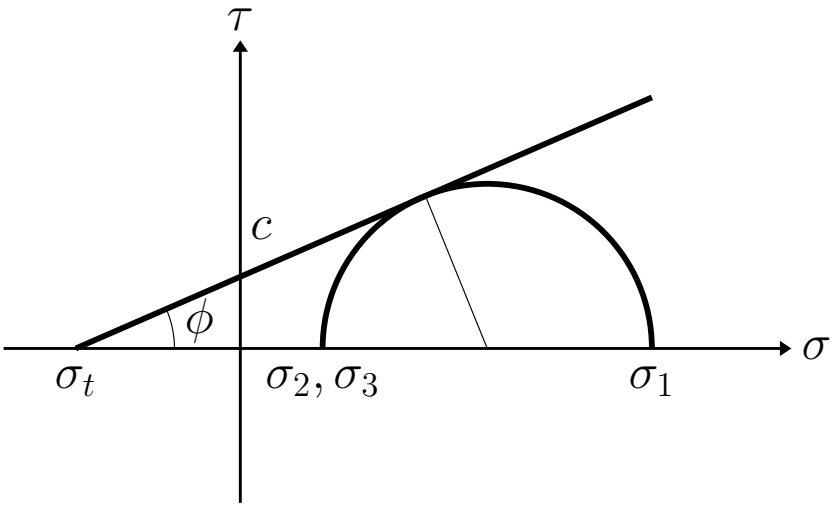

Figure 3.5: *Mohr circle corresponding to the triaxial compression.*

force. Alternatively, Fig. 3.6(b) shows normalized cohesion c/p as a function of cohesion number $\eta = f_c/pd^2$. Note that p is the average pressure and has not the same value in all samples. We see again a nearly linear dependence of c/p on η. The most porous samples are also the most cohesive ones. This cohesion can be attributed to the initial state, i.e. the configurations generated by dynamic compaction. We find it also remarkable that for values of η as large as 10, the ratio c/p is only about 1. This value can be compared to $\mu = \tan\phi \simeq 0.3$, showing that adhesion forces prevails over friction forces.

3.2.4 Coordination number

Figure 3.7(a) shows the evolution of coordination number Z as a function of shear deϵ for different values of f_c. Starting around 4.2 in all cases, Z increases until it reaches a plateau value. The plateau is reached more slowly for highly cohesive systems. Remarkably, the plateau value Z_f is an increasing function of f_c as observed in Fig. 3.7(b). Z_f increases almost exponentially with f_c. This increase of Z_f despite the decrease of packing fraction appears in this way as a mechanism that allows porous configurations to sustain higher shear stress. This observation suggests the following physical picture: As adhesion force increases, the microstructure is is 'coarse-grained' in the sens that individual particles are replaced by dense aggregates, with larger pores between them. This explains the higher porosity of the packing despite higher coordination number.

Figure 3.8(a) shows the evolution of the proportion of tensile contacts Z^-/Z as a function of the shear strain. Independently on the value of adhesion force, the proportion of tensile contacts decreases with the deformation until it reaches a plateau value in the critical state. However, this value is reached at a strain below 5% in all cases, in contrast to the total coordination number Z. During the compaction and before reaching the plateau value of Z, the transition rate for a given contact from tensile to compressive is slower

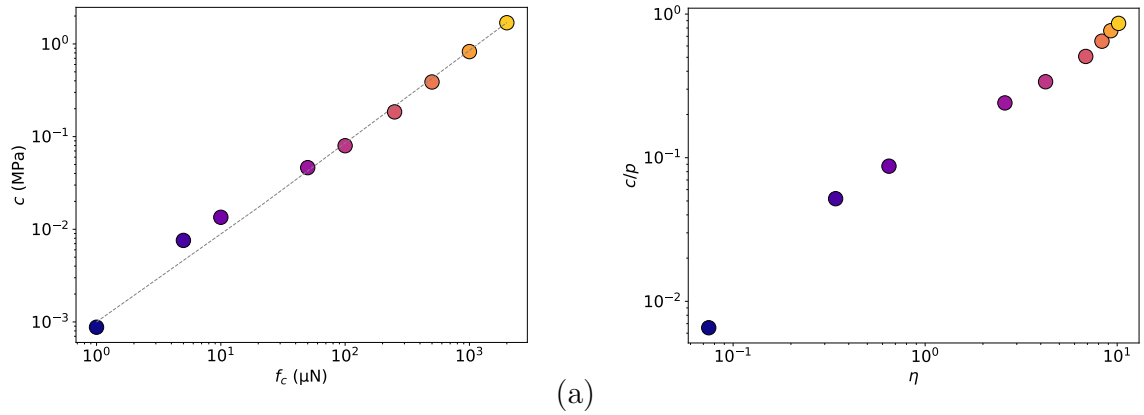

(a) (b)

Figure 3.6: *(a) Cohesive strength c as a function of adhesion force f_c; (b) normalized cohesive strength c/p as a function of cohesion number η.*

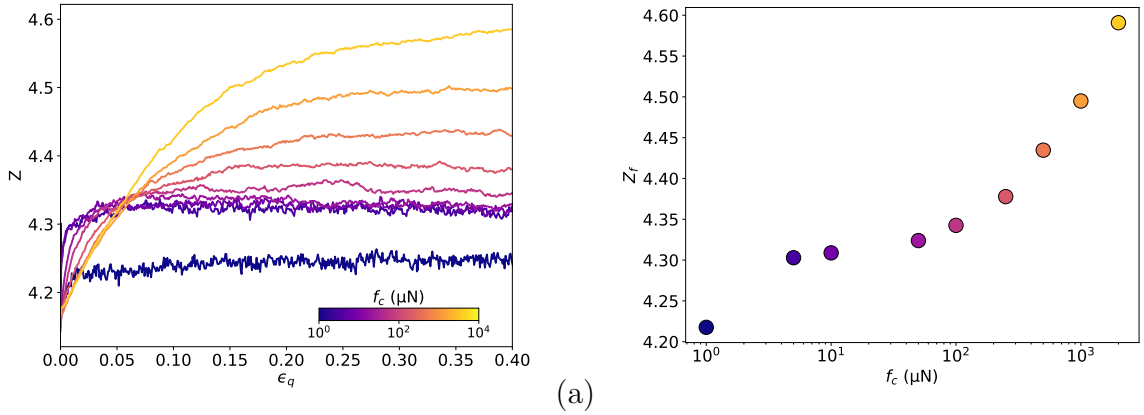

(a) (b)

Figure 3.7: *(a) Evolution of coordination number Z as a function of shear strain; (b) Final values Z_f of coordination number as a function of adhesion force f_c.*

than the creation of new contacts. Similarly to the observations in the isotropic case of Chapter 2, the final value Z_f^-/Z follows a sigmoidal evolution with f_c, as shown in Fig. 3.8(b). This shows that like void ratio, the proportion of tensile contacts in the critical state reflects the material parameters.

3.2.5 Anisotropies

The connectivity of the samples is also characterized by their anisotropy. The mean orientation of contacts inside a granular sample is given by fabric tensor **F**:

$$F_{ij} = \frac{1}{N_c} \sum_{\alpha=1}^{N_c} n_i^\alpha n_j^\alpha \tag{3.8}$$

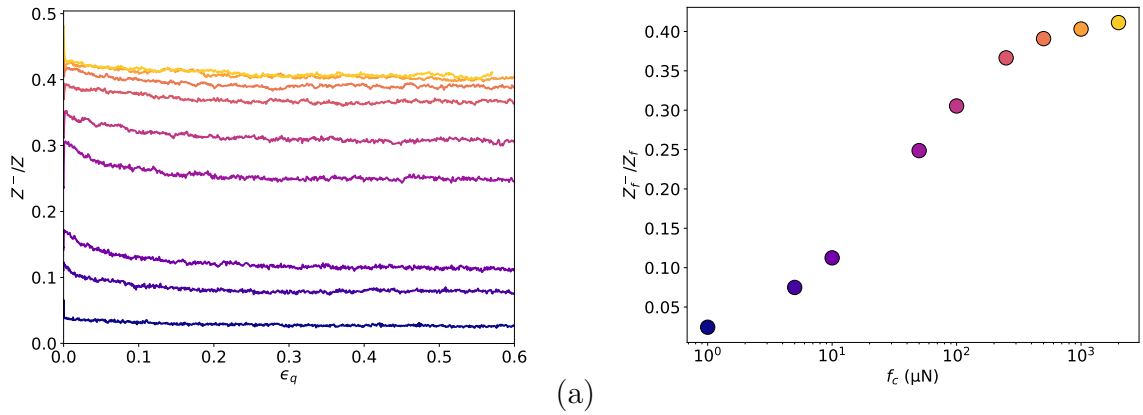

Figure 3.8: *(a) Evolution of Z^-/Z as a function of shear strain; (b) Final values Z_f^-/Z as a function of f_c.*

where N_c is the total number of contacts inside the sample. The contact anisotropy a_c of a granular material is obtained through the deviatoric part of its fabric tensor $\mathbf{F}$ [200]:

$$\mathbf{a_c} = \frac{15}{2}\left(\mathbf{F} - \frac{\mathbf{I}}{3}\right) \tag{3.9}$$

where $\mathbf{I}$ if the identity matrix. The deviatoric invariant of a_c is given by:

$$a_c = \text{sign}\,(S_c)\sqrt{\frac{3}{2}\mathbf{a_c} : \mathbf{a_c}} \tag{3.10}$$

S_c is a normalized first joint invariant between $\mathbf{s} = \boldsymbol{\sigma} - p\mathbf{I}$ and the anisotropy tensor given by:

$$S_c = \frac{\mathbf{a_c} : \mathbf{s}}{\sqrt{\mathbf{a_c} : \mathbf{a_c}}\sqrt{\mathbf{s} : \mathbf{s}}} \tag{3.11}$$

Figure 3.9(a) shows the evolution of a_c of the different samples as a function of shear strain ϵ. Starting from a relatively isotropic configuration, a_c increases with ϵ. We observe that a_c reaches higher values when adhesion force is low. At higher values of f_c, the evolution is much slower. This shows the lower mobility of the particles in the more cohesive samples. As a result of the initial relaxation step before triaxial compression, the anisotropy of the lowest cohesive samples starts at small negative values. The anisotropy tends to a critical state value a_c^f which depends on the adhesion force f_c as displayed in Fig. 3.9(b). Two regimes can be identified in this graph. For relatively low cohesion, the critical-state anisotropy is of the order of 0.1. For $f_c > 10$ μN, the critical-state anisotropy declines with increasing adhesion and tends to a very low value.

The orientational values of mean contact forces can be also obtained from weighed fabric tensors:

$$\chi_{ij}^n = \frac{1}{N_c}\sum_{\alpha=1}^{N_c} f_n^\alpha n_i^\alpha n_j^\alpha \quad , \quad \chi_{ij}^t = \frac{1}{N_c}\sum_{\alpha=1}^{N_c} f_t^\alpha n_i^\alpha n_j^\alpha. \tag{3.12}$$

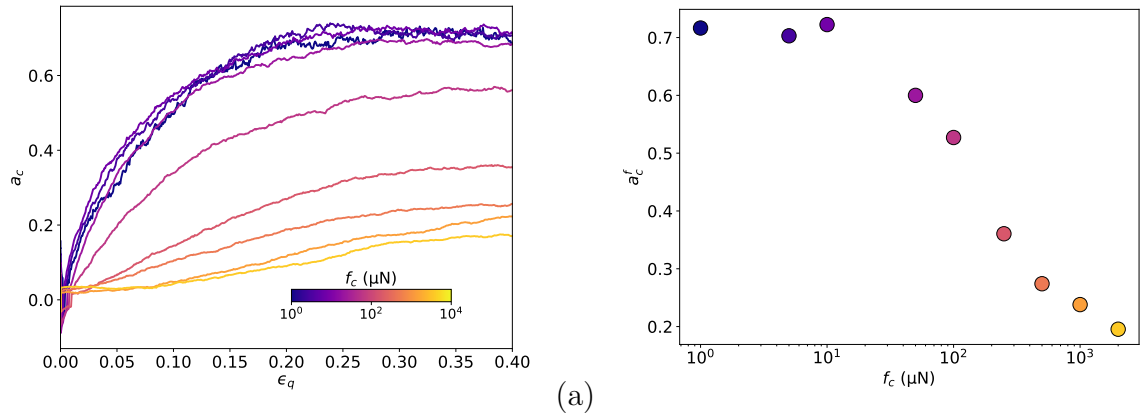

Figure 3.9: *(a) Contact anisotropy a_c as a function of shear strain (b); Final value a_c^f of anisotropy as a function of adhesion force f_c.*

We have $\mathrm{tr}(\boldsymbol{\chi}^n) = \langle f_n \rangle$. In the same way as for the contact anisotropy, the anisotropies of normal and tangential force networks can be also obtained from weighed fabric tensors:

$$\mathbf{a_n} = \frac{15}{2}\left(\frac{\boldsymbol{\chi}^n}{\mathrm{tr}(\boldsymbol{\chi}^n)} - \frac{\mathbf{I}}{3}\right) \tag{3.13}$$

$$\mathbf{a_t} = \frac{15}{3}\frac{\boldsymbol{\chi_t}}{\mathrm{tr}(\boldsymbol{\chi}^n)} \tag{3.14}$$

The deviatoric invariant of $\mathbf{a_n}$ and $\mathbf{a_t}$, noted respectively a_n and a_t, are given in the same way as a_n in Equation 3.10 and 3.11 by replacing the contact with respectively normal and tangenial forces.

The final values of a_n and a_t as a function of adhesion force f_c are shown in Fig. 3.10. In contrast to a_c^f in Figure 3.9(b), both force anisotropies increase with adhesion. They also follow a sigmoidal evolution, just as e and M do. However, their ranges differ considerably, between 0.5 and 4.1 for a_n^f and 0 and 1.05 for a_t^f. The high values of a_n correspond to highly oriented force chains along the vertical and horizontal directions. The tangential force anisotropy a_t corresponds to friction mobilization and its relatively lower value as compared with a_n reflects the reduced role of friction for the equilibrium and stability of the packing in cohesive granular materials.

From the above definitions, it is easy to show that [144, 123, 8]:

$$M \simeq \frac{2}{5}\left(a_c + a_n + \frac{3}{2}a_t\right) \tag{3.15}$$

Figure 3.11 shows both M and $\frac{2}{5}(a_c + a_n + \frac{3}{2}a_t)$ as a function of f_c. We see that, the two curves coincide well. The small difference is mainly due to the approximation that only the first-order anisotropy terms are included in the calculation. This shows that, the decrease of contact anisotropy is largely compensated by the increase of force anisotropies, allowing the shear stress ratio to increase to very high values as a result of force anisotropy and reflecting the structure of the bonding structure.

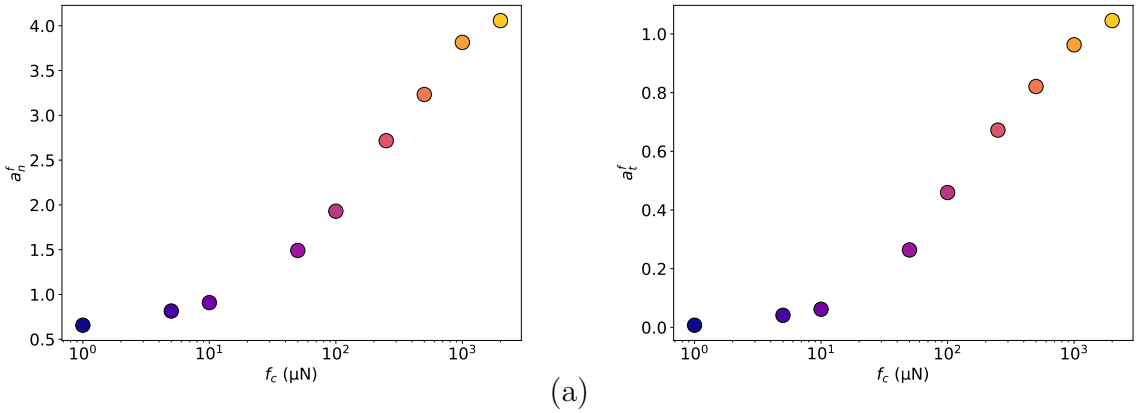

(a) (b)

Figure 3.10: *Final values of normal force anisotropy a_n^f (a) and tangential force anisotropy a_t^f as a function of adhesion force f_c.*

3.3 Relationships between state variables

3.3.1 Void ratio and stresses

It was shown in Section 3.2.3 that the cohesive strength of a granular medium is directly proportional to the adhesion force between the particles. Figures 3.3(b) and 3.4(b) show that both e and q/p follow a sigmoidal evolution as a function of adhesion force f_c in the critical state. Figure 3.12 displays q/p as a function of e for all tests. The peak values of q/p are clearly observed here. The final approach to the critical state point always corresponds to an increase of e and decrease of q/p. Remarkably, in the critical state the shear strength increases linearly with void ratio. The relationship between M and e is well described by

$$M = M_0 + A\,(e - e_0) \tag{3.16}$$

where $M_0 = 0.68$, $e_0 = 0.72$ and $A = 0.878$. As mentioned before for cohesion, this is an unexpected result as it means that looser configurations can withstand higher shear load.

3.3.2 Anisotropy and coordination

The variations of the contact network can be represented in the fabric parametric space (Z, a_c). In cohesionless granular media, it has been shown that as a consequence of steric exclusions between particles, all values of Z and a_c are not accessible, and the limits of the accessible range can be described as a relation between Z and a_c [132]. We show in Fig. 3.13 the relative evolution of the samples in the space (Z,a_c). We see well-defined trajectories between two limit behaviors: In the case of weakly cohesive samples, the coordination number remain constant and anisotropy increases whereas in highly cohesive systems the coordination increases while the anisotropy is nearly constant. The first limit is typical of dense granular materials, where mainly the gain and loss of contacts are orientation

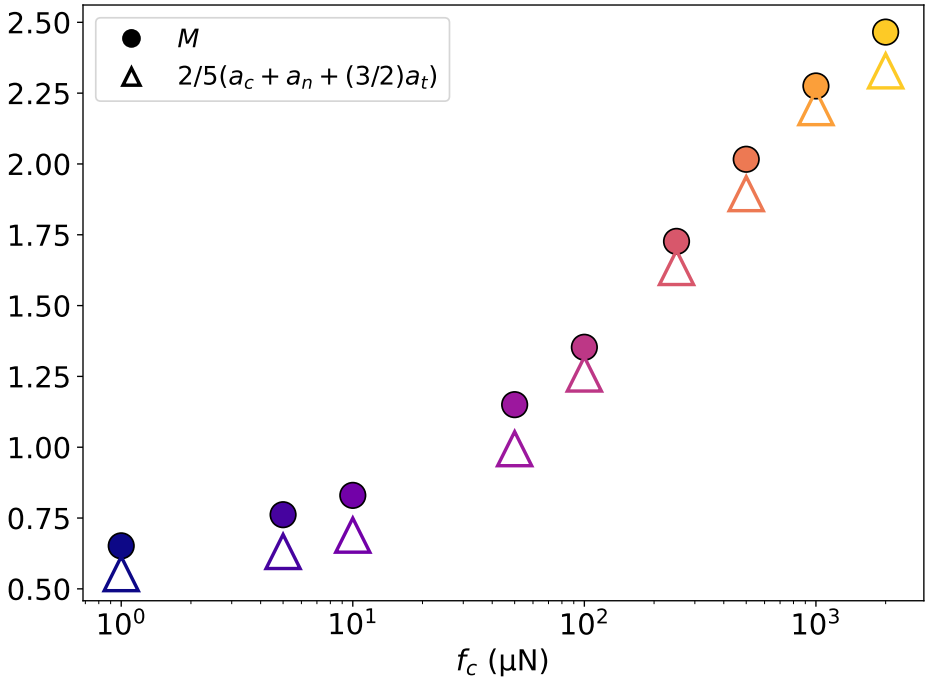

Figure 3.11: *Stress ratio M as measured from simulations and predicted by Eq. (3.15) as a function of f_c.*

dependent due to a relatively homogeneous strain field whereas in the second limit the isotropic gain of contacts occurs as a result of strong correlations across the system.

In the critical state (open circles in the figure), Z increases with the adhesion force while a_c decclines. The data points are well fit to the function

$$a_c = \frac{A_0}{Z - Z_0} \tag{3.17}$$

where $A_0 = 6 \times 10^{-2}$ and $Z_0 = 4.2$. The value of Z_0 corresponds to the lowest reachable coordination number for an infinitely high anisotropy. This relationship shows that higher cohesion between the particles leads to lower anisotropy and higher coordination number in the critical state, and that both values are linked. It defines the locus of critical fabric states, which underlies the relationship between macro-variables M and e in Eq. 3.16.

3.4 Conclusion

The microstructures obtained by isotropic compaction were used as initial conditions for triaxial compression. Interestingly, we found that the void ratio keeps a value close to its initial state. In other words, the porosity obtained by isotropic dynamic compaction is nearly the same as the critical porosity reached by triaxial shearing. During compression

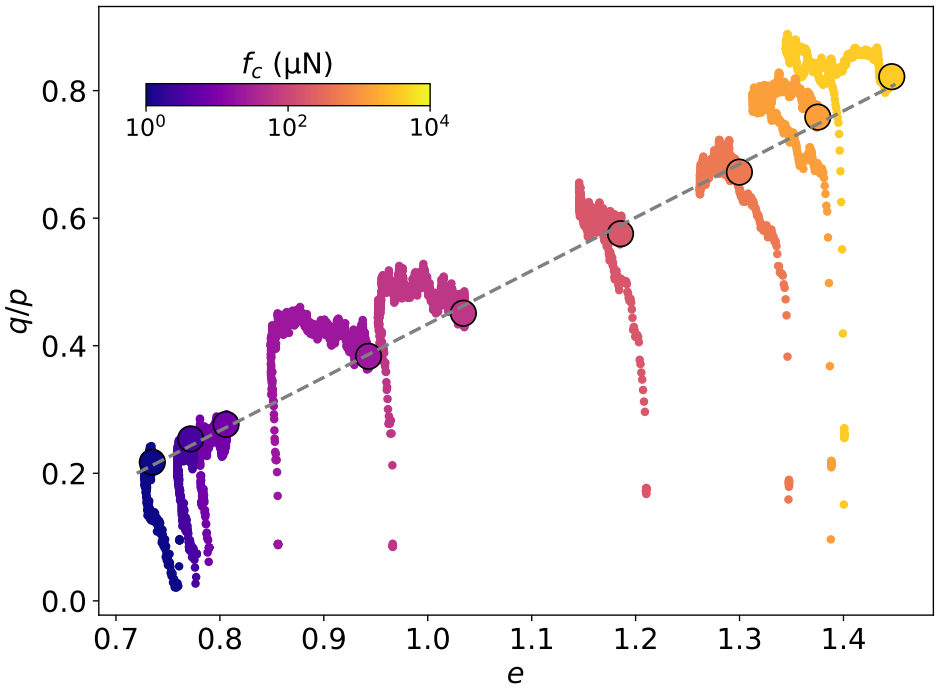

Figure 3.12: *Relationship between shear stress raio as a function of void ratio e. Open circles correspond to the values of e and $q/p = M$ in the critical state and the dotted line to a linear fit.*

the fabric and shear strength evolve towards the critical state at a rate depending on the adhesive force between the particles. Values of shear strength and proportion of cohesive contacts were shown to follow an asymmetric sigmoid evolution depending on the adhesive force, similarly to the void ratio in Chapter 2. Cohesive strength was shown to increase linearly with adhesion force and almost logarithmical with void ratio. We found a simple relationship between critical-state void ratios and shear strengths for a wide range of values of adhesion. In the same way we found that the critical values of coordination number and contact anisotropy are simply related across all values of adhesion. These relationships define correspondence between materials of different values of adhesion.

Our results clearly show that triaxial compression is not an efficient means of compaction of cohesive granular materials. The compaction requires transition from one cohesive state to a lower cohesive state, and this is possible only either when adhesion force is decreased or if confining pressure is increased. As we shall see in the next chapter, the calendering action consists in imposing a thickness reduction while the side boundaries of the sample are free as in a triaxial compression. We therefore predict from the results of this chapter that the success of compaction depends on the external stress induced by calendering.

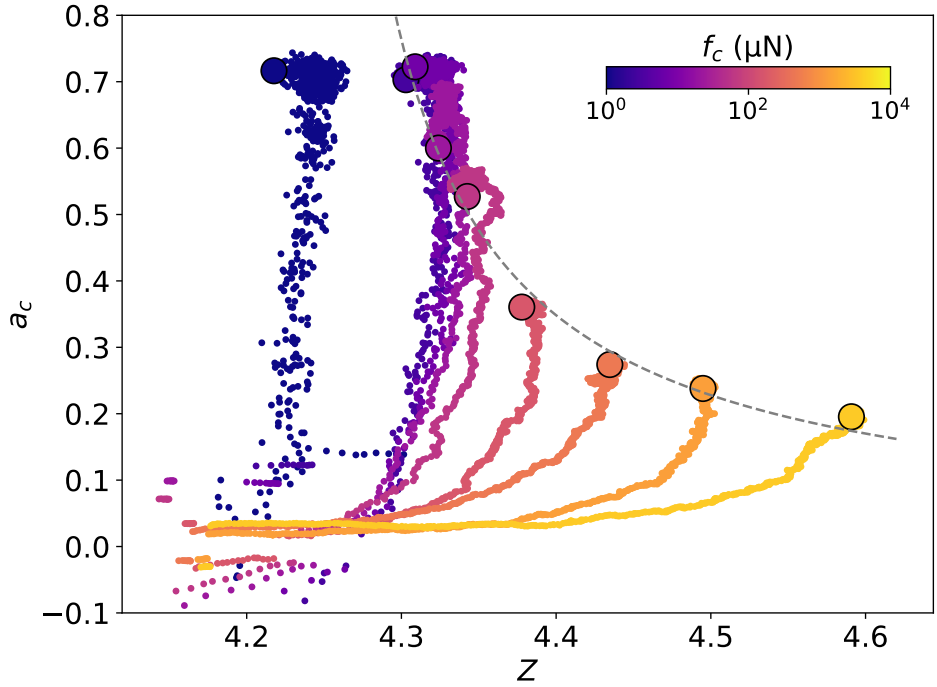

Figure 3.13: *Evolution of the samples in the fabric parametric space (Z,a_c). The open circles mark to the values of Z and a_c in the critical state and the dotted line is the function given in Eq. (3.17).*

Chapter 4

DEM simulation of the calendering process

The electronic properties of Li-ion batteries crucially depend on the microstructure of their electrodes which can widely change during the fabrication process, resulting in broad variations of energy densities and charging rates. One step of the fabrication process called 'calendering' consists in compressing the electrodes between two rotating cylinders to reduce their thickness and thereby increasing their density. We investigate the effect of calendering on microstructural and electronic properties of the electrodes by means of discrete element simulations and a realistic model of the calendering process by including the real geometry of the rotating cylinder and the compression of the electrode over its full length. The electrode is simulated using a rigid current collector and spherical particles representing theactive material particles of the electrode. We also introduce a new contact law that accounts for the behavior of the elastic active material particles and the cohesive-plastic binder layer. We perform extensive simulations for various levels of thickness reduction ratio and calendering speed. We show that our results are in good agreement with experimental data of porosity, final thickness and elongation. The calendering speed is found to affect the elongation of the electrode and the orientational anisotropy of its internal microstructure. We show that the bonding structure induced by calendering involves mostly vertical tensile contacts and horizontal compressive contacts which is in radical contrast with the expectation that vertical compression tends to induce compressive contacts along the vertical direction. This counterintuitive observation shows the importance of shear deformation induced by rolling and thickness reduction. Using the FFT method, we also measure the conductivity of the numerically calendered electrodes. We find that the electric conductivity is proportional to the connectivity and packing fraction of active particles whereas ionic conductivity is controlled by porosity. The former increases with thickness reduction ration whereas the latter declines.

Contents

3.1 Methodology 73
3.2 Evolution of state variables 74
3.2.1 Void ratio 74
3.2.2 Stresses 76
3.2.3 Cohesive strength 77
3.2.4 Coordination number 78
3.2.5 Anisotropies 79
3.3 Relationships between state variables 82
3.3.1 Void ratio and stresses 82
3.3.2 Anisotropy and coordination 82
3.4 Conclusion 83

Introduction

Li-ion batteries have proven their worth for many years in several domains and play a key role for various technologies [104]. The manufacturing process of their electrodes involves several stages designed to create a controlled material capable of storing and delivering large amounts of energy. The third generation of Li-ion batteries involves a slurry preparation, coating, drying and calendering steps for their electrodes [160]. Calendering is the compaction of the electrode between two rotating cylinders to reduce its thickness, as schematized in Fig. 4.1. The compaction of the electrode increases its energy density and enhances its storage capacity. However, this process also decreases the ionic conductivity of the electrode and thus the ability of the battery to store and deliver energy quickly [64, 86]. The reduction of porosity increases the tortuosity and leads to the clogging of the pore network. The link between calendering parameters and the final microstructure and performance of batteries is therefore a crucial feature of manufacturing Li-ion batteries that remains, however, poorly understood [39].

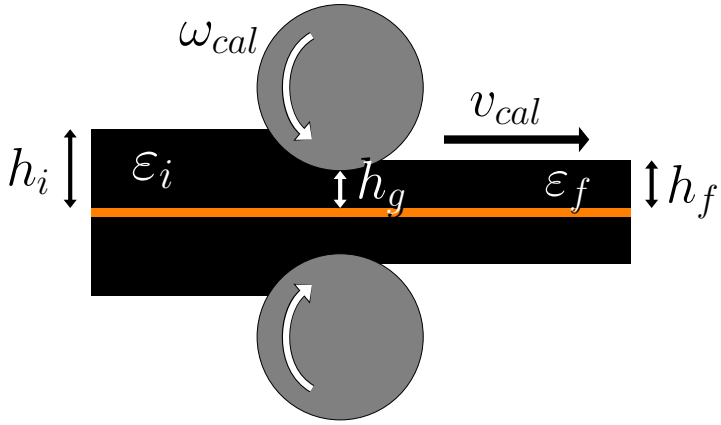

Figure 4.1: *Characteristics and geometry of the calendering process*

In this chapter, we are interested in the link between the final properties of the electrode and the calendering parameters. Since the Li-ion electrode has a granular microstructure, we employ the Discrete Element Method (DEM) to compute the mechanical behaviour of the material during the calendering process [30]. This method is based on explicit representation of the active material particles and their interactions and it has been recently employed by several authors to simulate the manufacturing process of electrodes [52, 151, 150, 117, 84]. These DEM-based models use different representations of the electrode within the algorithmic constraints imposed by the framework of DEM. A natural DEM approach proposed by some authors consists in introducing two types of particles, namely the NMC active material and CBD (Carbon Binder Domain) [165]. This approach implies, however, a high computational cost as it requires hundreds of small CBD particles for each active material particle. Computationally affordable models are based on the representation of active material as rigid particles while the CBD is accounted for through

contact interactions between particles. For example, the simplest DEM models of the electrode use a Hertzian-bond contact model to account for the elastic behavior of the active material particles and an adhesion force accounting for the action of the binding material [51]. This approach considers a solid bond formed by the binder during the drying step between the active material particles. Some models have improved this representation by adding a plastic component to the contact law, which allows one to simulate the damage of active material particles [52, 151, 89, 204]. Some other models assume that the binder induces a constant attraction force between the active material particles and the particles follow an elasto-plastic behavior [153, 48, 47]. The use of irreversible cohesive force by some authors in this context implies irreversible loss of cohesion, which contradicts the chemo-physical nature of CBD.

Another aspect of DEM-based calendering models concerns the simulation of the process itself. The loading applied on the material during the calendering process is usually represented by a triaxial compression test with a confining pressure applied on the lateral walls and vertical compression at constant speed. This simplified representation is based on the fact that the diameter of the calendering roll is much larger than the length of its contact with the electrode. The contact zone between the calendering roll and the electrode is therefore assumed to be flat, neglecting the curvature of the roll, and the shear stress is neglected. Several studies have also been reported in which the compression is modeled by considering periodic boundary conditions along horizontal directions and vertical compression between two platens [153, 150, 48]. Since the horizontal cell dimensions are fixed, such a configuration is equivalent to uniaxial compression and can not account for the free spreading of the material and its lateral extension during calendering. The shear stresses are also neglected as in triaxial compression and the contact surface is assumed to be flat. However, in the real calendering process the motion of the electrode between two counter-rotating rollers is driven by friction forces mobilized between the rollers and the surface of the electrode. Hence, shear stresses induced by friction and rolling are intrinsic to the process and should not be neglected. The effect of shear stresses is probably less crucial for understanding the process at low calendering speeds. The models using simplified boundary conditions can therefore be relevant for low calendering speeds ($< 0.1m/s$) usually employed in laboratory setups while the speeds used in industry are usually close to 1 m/s. The calendering speed affects horizontal elongation [97, 26], and beyond a certain level of elongation the collector may break during winding [201].

In this work, we present a new DEM-based model for the simulation of the calendering process of Li-ion battery electrodes. The CBD material is represented by its adhesive-plastic behavior at the interface between NMC particles and most parameters are calibrated from experiments. We also model the calendering by introducing a cylinder that drives the electrode by its rotation. We carry out a detailed parametric investigation by varying thickness reduction ratio and calendering speed and analyze their effect on porosity reduction, elongation, microstructure, and electronic properties of the calendered zone. Our results will be compared by previous DEM simulations reported in the literature when possible and, as we shall see, the full modeling of the calendering process and contact interactions turns out to be crucial for the simulated behaviors.

4.1 Materials and methods

4.1.1 Contact force laws

Numerical models for electrodes either explicitly represent both active material (NMC) and Carbon-Binder Domain (CBD) particles or only the particles of the active material and the action of the binding material is modeled through a contact force law with its plastic and cohesive components [15]. We consider the latter approach with carbon-binder phase described implicitly as a layer surrounding the particles of active material. The NMC particles define a polydisperse assembly of spheres [179] and the CBD is a layer of thickness R_p coating NMC particles, as schematized in Fig. 4.2. The thickness of the binder layer is fixed from the ratio of the total mass of the binding material to the total mass. The thickness of the surrounding CBD layer is kept constant during the calendering process.

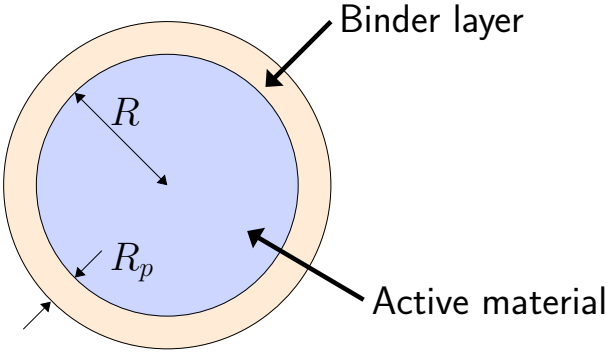

Figure 4.2: *Schematic representation of the binder-covered particle model of the electrode.*

Based on this representation of binder-covered particles, there are three types of contacts between two particles depending on the overlap δ_n: binder-binder, binder-particle, and particle-particle. We assume an elasto-plastic behavior with adhesion for binder-binder and binder-particle contacts and an elasto-plastic behavior for particle-particle contacts. Figure 4.3 shows the evolution of normal force f_n as a function of the overlap δ_n. Upon the initial contact at point A between two particles, their binding layers touch each other and the interaction is governed by a linear elastic law:

$$f_n^{AB}(\delta_n) = -k_1\delta_n, \tag{4.1}$$

where k_1 is the reduced stiffness of binder-binder and binder-particle stiffnesses. Note that overlaps are counted as negative. At point B the NMC cores of the particles touch each other ($\delta_n = -R_p$). The NMC particles being more rigid, the elastic interaction is governed by a larger stiffness k_2 when $\delta_n < -R_p$ and we have

$$f_n^{BC}(\delta_n) = k_1 R_p - k_2(\delta_n + R_p) \tag{4.2}$$

The active material particles used in Li-ion battery electrodes have relatively low yield strain and undergo cracking and fragmentation under low compression [52]. We account

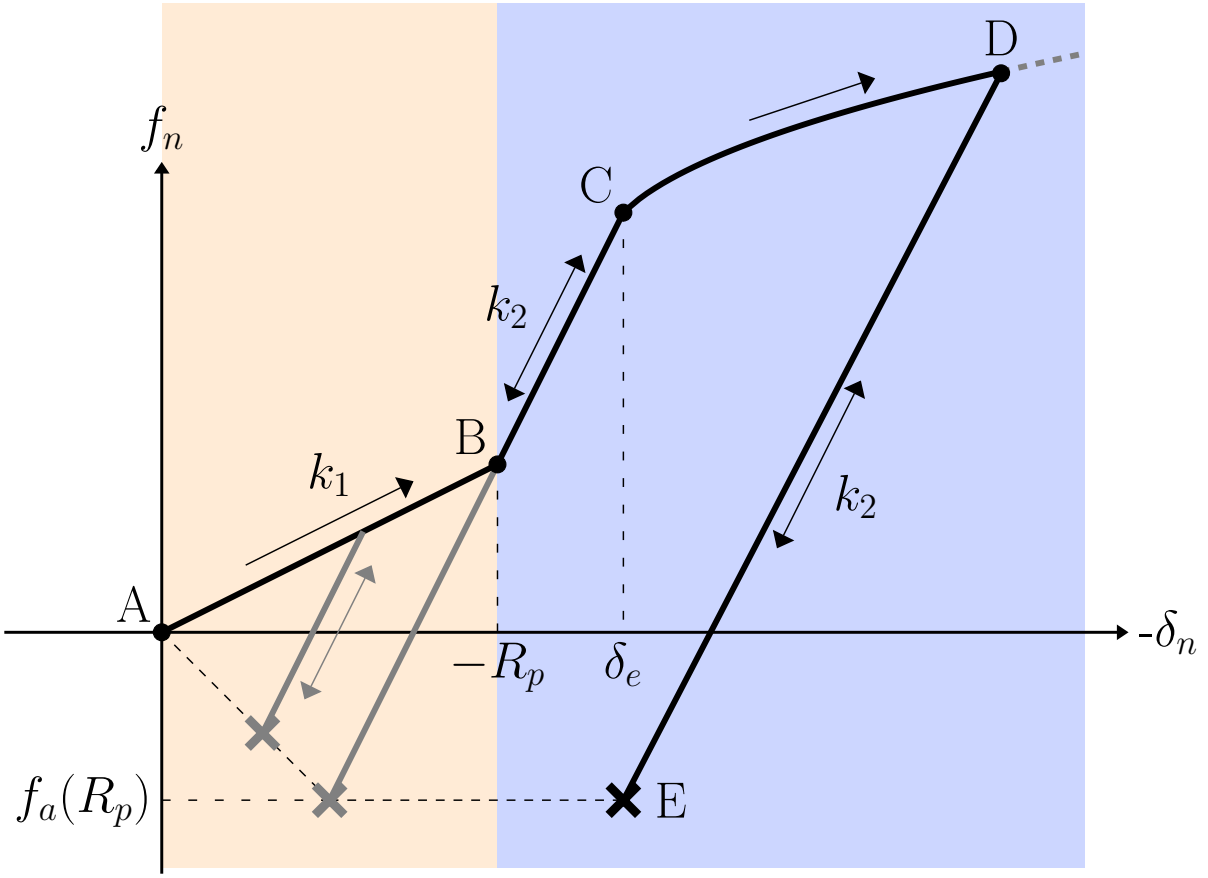

Figure 4.3: *Normal force f_n as a function of overlap δ_n. The colored zones represent the contact zones between binder layers and between particles, respectively; see Fig. 4.2.*

for the resulting plastic behavior by introducing a yield strain δ_e (point C). The normal force will then evolve following a strain-hardening power-law behavior:

$$f_n^{CD}(\delta_n) = k_1 R_p - k_2(\delta_e + R_p) + k_2\left(|\delta_n|^{\zeta}|\delta_e|^{1-\zeta} - |\delta_e|\right), \tag{4.3}$$

where the exponent ζ controls the intensity of plastic hardening.

Upon unloading from any point, the normal force will follow a linear elastic path, starting from the largest overlap δ_n^{max} reached prior to unloading. The deformation of the CBD being irreversible, the elastic stiffness of the unloading path is that of the active material (k_2). The evolution of the normal force is then given by:

$$f_n^{unload}(\delta_n) = f_n^{max} - k_2(\delta_n - \delta_n^{max}), \tag{4.4}$$

where f_n^{max} is the normal force reached at δ_n^{max} along the loading path. The adhesion of the binder is modeled by allowing the normal force to take negative values down to a pull-off force f_a depending on both binder properties and the maximum overlap reached.

Since adhesion is induced by the amount of binding material between two particles, the maximum value of $-f_a$ is reached when δ_n^{max} reaches the limit of the binder layer R_p:

$$f_a\left(\delta_n^{max}\right) = 2\pi R^* \sigma_a \min\left(\delta_n^{max}, -R_p\right) = k_p \min\left(\delta_n^{max}, -R_p\right), \tag{4.5}$$

where $R^* = \left(1/R_1 + 1/R_2\right)^{-1}$ is the reduced radius between two particles and σ_a is the yield strength of the binder. The highest bonding force $f_a\left(-R_p\right) = -2\pi R^* R_p \sigma_a$ is set equal to the adhesion force given by the DMT theory [33]:

$$f_a = -2\pi\gamma R^* \tag{4.6}$$

where $\gamma = \sigma_a R_p$ is the surface energy. This value is reached if the binder layer is totally crushed, i.e. when the contact surface area between the binder phases of the particles has its maximum value.

For the tangential force, we used a linear elastic law combined with a Coulomb dry friction criterion:

$$\boldsymbol{f}_t = \begin{cases} -k_t \boldsymbol{\delta}_t \quad \text{for } ||\boldsymbol{f}_t|| \leq \mu\left[f_n - f_a\left(\delta_n^{max}\right)\right] & , \\ -\mu\left[f_n - f_a\left(\delta_n^{max}\right)\right] \frac{\dot{\boldsymbol{\delta}}_t}{||\dot{\boldsymbol{\delta}}_t||} \quad \text{otherwise} & , \end{cases} \tag{4.7}$$

where μ is the friction coefficient and k_t is the tangential stiffness.

Throughout this work we set $\mu = 0.4$, and k_t is computed following the Hertz-Mindlin theory for frictional contacts [134]

$$\frac{k_t}{k_2} = \frac{2\left(1-\nu^*\right)}{2-\nu^*}, \tag{4.8}$$

where $\nu^* = \left(1/\nu_1 + 1/\nu_2\right)^{-1}$ is the equivalent Poisson ratio. Compared to the classical Coulomb criterion $||\boldsymbol{f}_t|| \leq \mu f_n$ for cohesionless contacts, here the Coulomb cone is shifted to account for the adhesion force present in the total normal force [135, 134]. This means that only the repulsive part $f_n^e = f_n - f_a\left(\delta_n^{max}\right)$ of the normal force comes into play for tangential force computation.

For energy dissipation, we consider a viscous normal force f_n^v equivalent to the one defined in Eq. **??**. In all simulations, we set $\alpha_n \simeq 0.25$. We set the cohesionless tangential damping to zero, thus dissipation is controlled by normal damping only.

4.1.2 Simulation of calendering

Our DEM model and its parameter values were based on the electrodes that were manufactured and characterised by means of an in-house setup performed in CEA Grenoble. The cathode structures were made of NMC-811 ($LiNi_{0.8}Mn_{0.1}Co_{0.1}O_2$) (active material), carbon black (CB) and polyvinylidene fluoride (PVDF), with mass proportions 96-2-2 of the three components. The last two components form the conductive Carbon-Binder Domain (CBD) matrix. The polydispersity of the NMC particles had a log-normal distribution, with $d_{10} = 6.1\mu m$, $d_{50} = 12.1\mu m$ and $d_{90} = 21.8\mu m$. The slurry was coated

onto an aluminium foil of thickness $h_{al} = 20$ μm, resulting in electrodes of initial thickness $h_t = 2h_i + h_{al} = 194$ μm. The initial porosity of the electrodes was $\varepsilon_0 = 44.5\%$. The electrodes were calendered with different speeds and intercylinder gaps using a rolling press with cylinders of diameter $D_c = 20$ cm. After calendering, the elongation of the electrodes was obtained by comparing their final length to the initial state. Cylindrical samples of diameter 14 mm were extracted from the calendered electrodes and the thickness h_f of each side was measured. By measuring the mass of the cylindrical samples, their porosity ε was computed from the volumes, densities, and proportions of the components. The measured values of porosity, thickness, and elongation are given in Table 4.1.

Target thickness (μm)	Calendering speed (m/s)	Measured thickness (μm)	Porosity (%)	Elongation (%)
Initial	-	87	44.5	0
65	1	66.5	27.5	1.11
	1.5	68	28.8	0.99
	2	68	29.2	0.87
62.5	1	65	26.2	1.48
	1.5	65	25.4	1.36
	2	64	25.0	1.23
60	1	62	23.4	1.72
	1.5	64	24.2	1.60
	2	63.5	24.2	1.48

Table 4.1: *Experimental data.*

For simulations, we used spherical particles with the same particle size distribution as in experiments. The thickness of the CBD layer was calculated from the experimental data and set to $R_p = 0.34$ μm. The current collector was considered to be undeformable. This assumption holds only for relatively low/medium calendering degrees since high levels of compression tend to warp the current collector [204]. The calendering rolls are represented explicitly in the simulations. Since our experimental data were obtained using a stainless steel cylinder of radius $R_c = 10$ cm, the length of our samples was set to $l = 1$ cm. The width was set to 200 μm with periodic boundary conditions. With an initial thickness $h_i = 87$ μm, we built a numerical electrode composed of 24,425 spherical particles. The values of the contact law parameters are given in Table 4.2. The values of hardening parameter ζ were calibrated through a sensitivity analysis in which the porosity and thickness of the sample were compared to their experimental values under uniaxial compression for a thickness reduction ratio of 0.25.

The simulations were performed in 3 steps. First, the particles were deposited on the current collector under their own weights. The relaxed sample is shown in Fig. 4.4. Then, the cylinder is lowered slowly until it reaches the specified level. Finally, the cylinder starts to rotate at an increasing rate until the target rotation speed is reached. The motion of the sample is thus driven by friction with the calendering roll. The translation of the

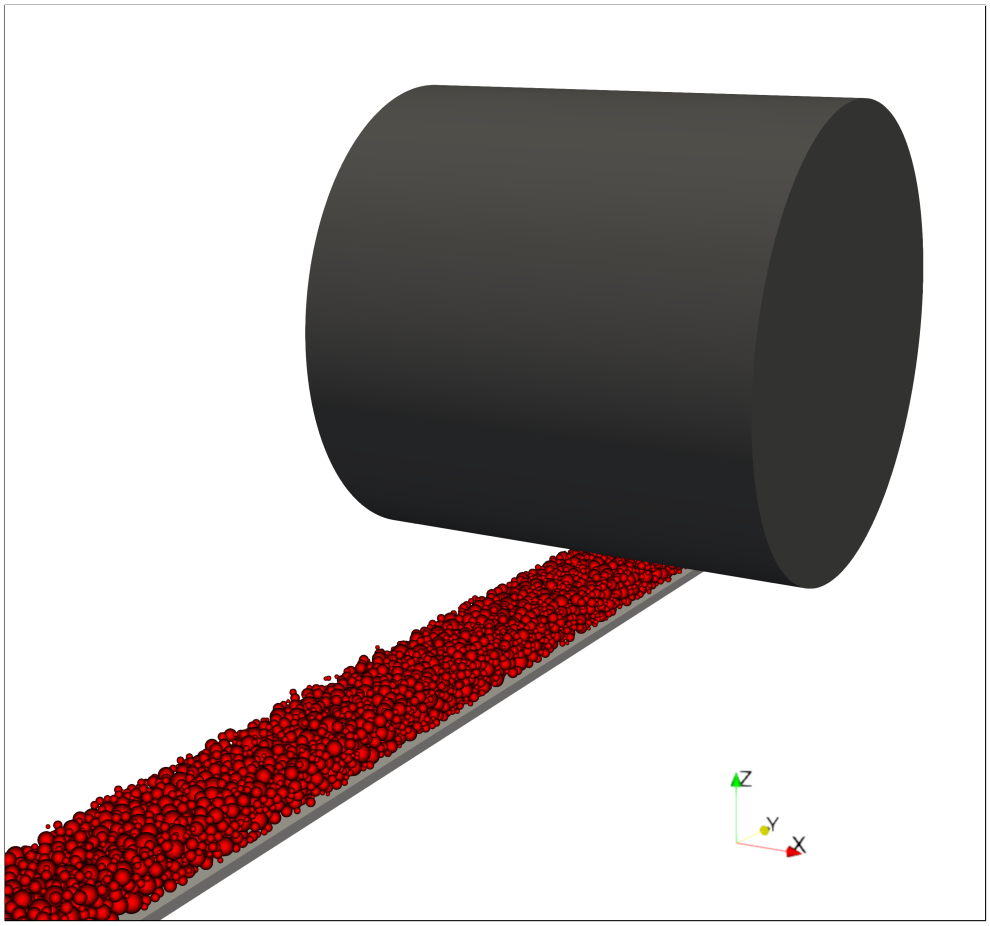

Figure 4.4: *Macro view of the calendering simulation sample before lowering the cylinder. The particles, current collector, and calendering roll are colored in red, gray, and black, respectively. Cylinder size is downscaled 40 times for better visualization.*

current collector on Z and X axes are disabled so that the gap h_g between the cylinder and current collector is constant. Figure 4.5 shows close-up snapshots of the electrode at several instants of simulation.

4.1.3 Calculation of ionic and electric conductivities

For the calculation of ionic and electric conductivites of the numerically calendered samples, we used Fast Fourier Transform [112]. FFT is a homogeneization technique which is used to compute the effective or equivalent property of a multi-phase medium. It is extensively employed in mechanics and for thermal transfer or diffusion. The multi-phase geometry of the sample is described explicitly on a cartesian meshing grid. Each voxel of the grid has a value corresponding to its local property. The diffusion gradient is considered as homogeneous inside the volume. The method assumes periodic boundary conditions and the effective properties of the matrix (mesh) is computed considering a steady state regime.

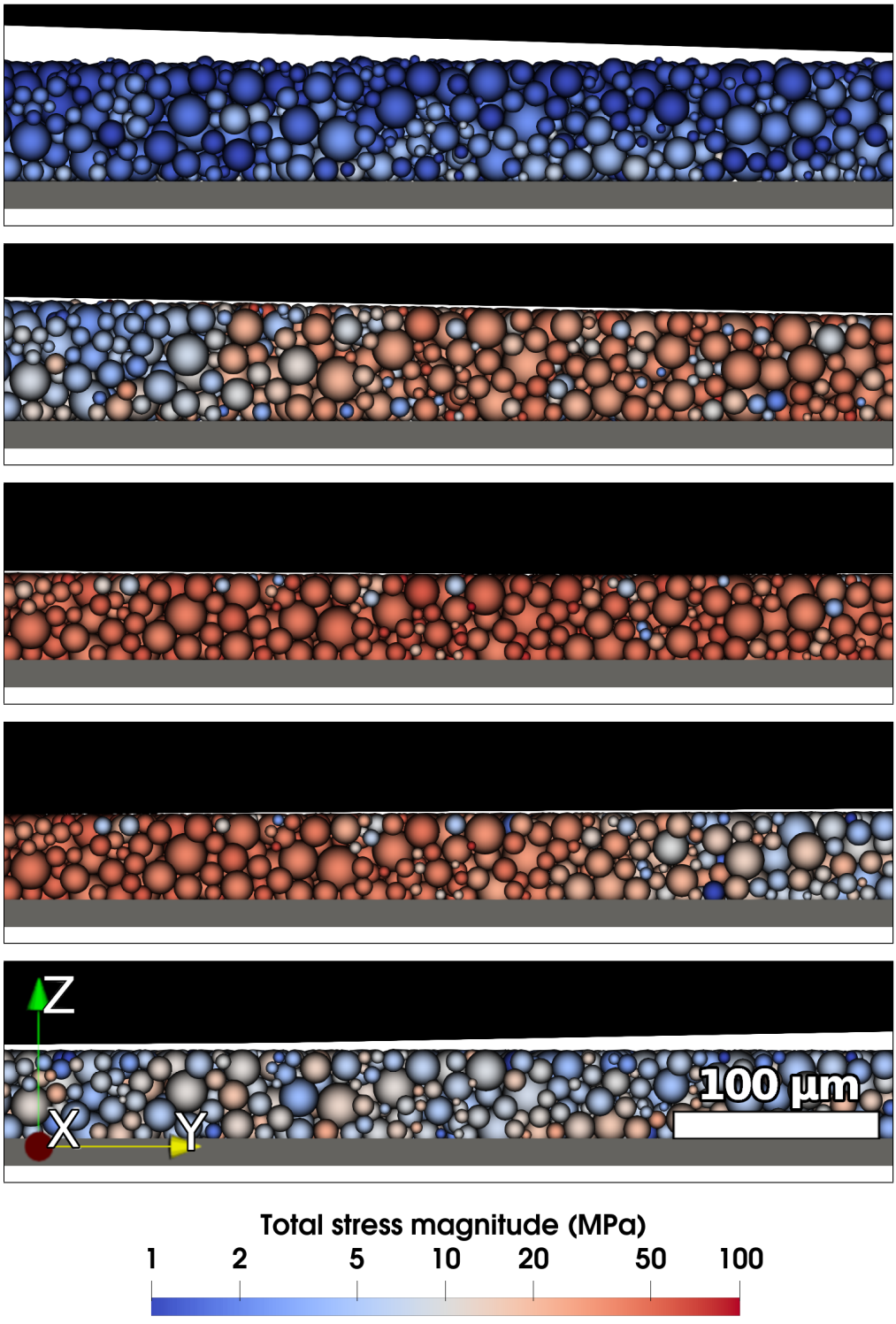

Figure 4.5: *Snapshots of a portion of the electrode during the passage of the calendering roller. Color code represents average particle stress. The snapshots correspond to the initial and final states and crossover points between the four stages of evolution of porosity and pressure identified in Fig. 4.6.*

	Sph – Sph	Sph – Col	Sph – Cyl
k_1 (kN/m)	2.5	4.5	4.7
$k_2(kN/m)$	130	93	165
k_p (kN/m)	4	27.5	0
γ (mJ/m^2)	34	240	0
ζ	0.15	0.275	1
k_t (kN/m)	117	77	138

Table 4.2: *Values of the simulation parameters for particle-particle, particle-collector, and particle-cylinder contacts.*

Compared with finite-element method, the FFT is able to handle more degrees of freedom and may be accelerated thanks to parallelization technique. Moreover, the cartesian mesh allows a very simple definition and easy to process geometry. FFT calculation needs a discretization of the bed defined on a cartesian mesh (voxelisation). It basically defines the property/value of a voxel thanks to its phase location. The details of the procedure employed applied to thermal problems can be found in [22].

4.2 Results and discussion

4.2.1 Calendering steps

We performed 28 simulations with different values of the gap h_g between the cylinder and the current collector and the calendering speed $v_{cal} = R_c\ \omega_{cal}$, where ω_{cal} is the rotation speed of the roll. The ranges of these values are given in Table 4.3. We investigate here the deformation of the electrode and evolution of its microstructure in the 'calendered zone' defined as the portion of the electrode whole length L_c is equal to that of the contact area between the cylinder and the material and which is fully compressed once it has moved a distance equal to its own length L_c due to the rotation of the cylinder. The control parameter of calendering is the *thickness reduction ratio* C_r defined by

$$C_r = \frac{h_i - h_g}{h_i}, \tag{4.9}$$

where h_i is the initial thickness of the electrode.

Calendering gap h_g $[\mu m]$	7 values $\in [75, 50]$
Calendering speed v_{cal} [m/s]	$\{0.5, 1, 2, 5\}$

Table 4.3: *Calendering parameters used in this work.*

Figure 4.6 shows the time evolution of porosity and average pressure in the calendered zone for $C_r = 0.28$ and speed $v_{cal} = 2$ m/s. The initial porosity is 0.44. We distinguish four different periods:

1. Initial state: The cylinder is away from the calendered zone and the pressure is zero. The calendered zone is stable and fully relaxed under the action of its own weight and internal cohesive forces.

2. Compression: The average pressure increases in the calendered zone and porosity declines.

3. Relaxation: The cylinder leaves the calendered zone, which relaxes with a small elastic rebound.

4. Final state: A new stable state is reached with zero internal pressure and a porosity of 0.27.

In the following, we focus on the influence of calendering parameters on this process and final relaxed state reached by the calendered zone after calendering. Note that each data point represents the average value over several calendered zones selected from the electrode during a single simulation run, and error bars are their standard deviation.

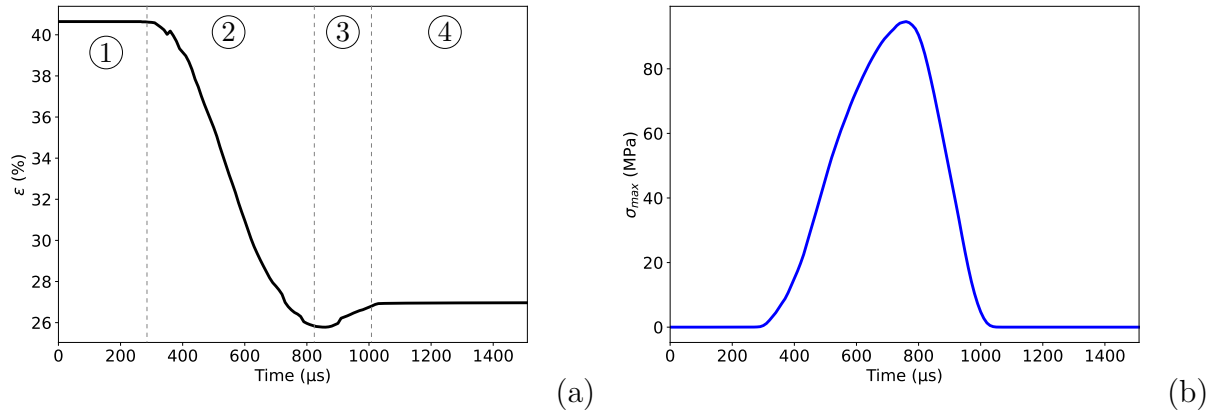

(a) (b)

Figure 4.6: *Time evolution of porosity (a) and pressure (b) for imposed thickness reduction* $C_r = 0.28$ *and calendering speed* v_{cal}*=2 m/s. The labels of four successive stages of the evolution of porosity and pressure are marked. Time is normalized by* ω^{-1}*, where* ω_{cal} *is the rotation speed of the cylinder.*

4.2.2 Thickness, porosity, and elongation

Because of elastic rebound, the final thickness reduction ratio C_f is not exactly equal to the imposed value of C_r. Figure 4.7 displays the evolution of C_f as a function of C_r for different values of calendering speed v_{cal}. The simulations are in good agreement with experimental data, and we observe that C_f is independent of v_{cal}. The relationship between C_r and C_f is linear with a shift of $\simeq 2.5\%$ between the target and measured values due to elastic rebound. This linear evolution and a constant shift from the perfectly plastic deformation $C_f = C_r$ independently of the value of C_r is obviously a consequence of linear

plastic behavior of the contacts defined in Eq. (4.4) and vanishing of the pressure exerted on the electrode during calendering. As we shall see, the compression induces a high level of self-equilibrated forces all the more that thickness reduction ratio is high. This is because the adhesion force increases with plastic surface area between particles. The elastic rebound is therefore mainly due to contacts between the cylinder and the particles. The maximum elastic displacement after the vanishing of pressure is $\simeq f_a/k_1$ at the particle-cylinder contacts, leading to a deformation of $f_a/(k_1 d_{50})$. With the values of parameters used in the simulations ($f_a = 1360$ μN, $k_1 = 4.7$ kN/m, and $d_{50} \simeq 12.1$ μm), rather find a deformation of the order of 2.4%, which is the value we measured.

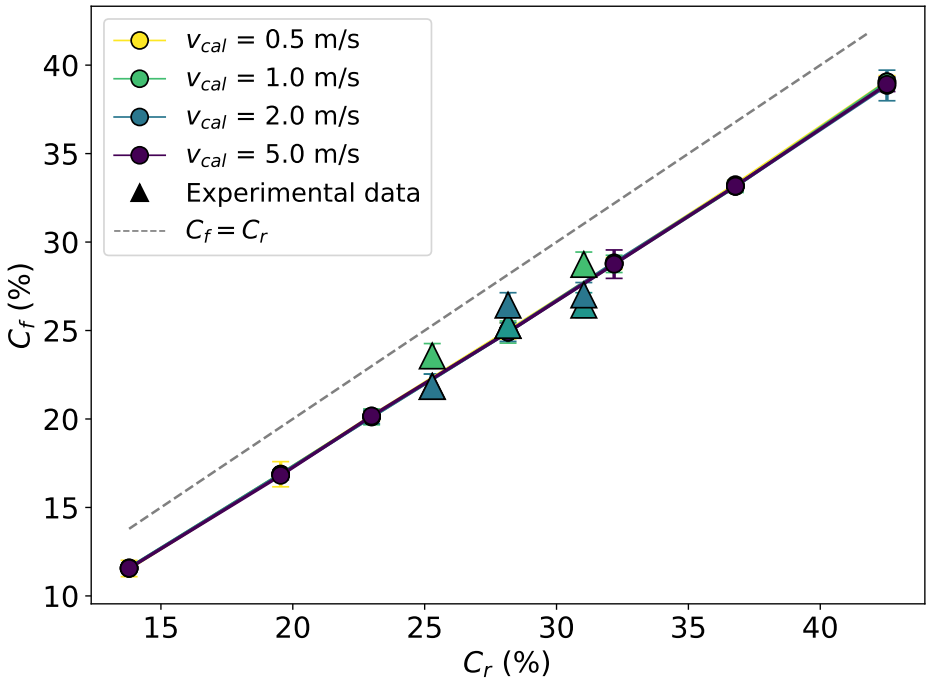

Figure 4.7: *Relation between imposed thickness reduction ratio C_r and the effective thickness reduction C_f of the electrode. The dashed line represents the ideal thickness reduction without elastic rebound ($C_f = C_r$).*

The reduction of the electrode thickness has two origins: 1) reduction of porosity and 2) elongation. Figure 4.8 shows the final porosity ε as a function of C_r for different values of calendering speed. We see that, as expected, ε declines as C_r increases but is independent of v_{cal}. The porosity seems to tend to a constant low value For this reason, it is expected that the variation of porosity will tend to a constant value at high values of C_r. The numerical data can be fitted by a power-law function:

$$\varepsilon = A\,(B + C_r)^{-\alpha} + D. \tag{4.10}$$

with $A \simeq 0.17$, $B \simeq 0.57$, $D \simeq 0.06$, and $\alpha \simeq 1.5$. We have $\varepsilon\,(C_r = 0) \simeq 0.45$, which is close to the initial porosity $\varepsilon_0 = 0.44$ of our numerical electrode. The predicted lowest value of

porosity by this function is $\simeq 0.15$ for $C_r = 1$. However, the lowest value of h_g can not be below one particle diameter, implying that the largest value of C_r is $(h_i - d_{50})/h_i \simeq 0.89$. This leads to a porosity of the order of 0.16.

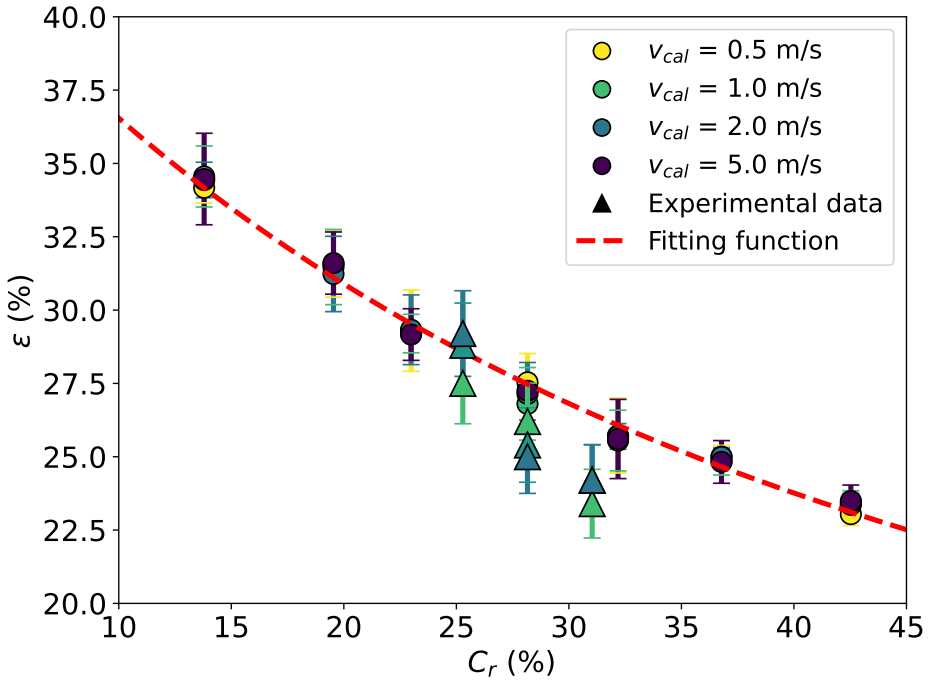

Figure 4.8: *Porosity ε as a function of thickness reduction ratio C_r for different values of the calendering speed. The red dashed line represents the fitting function given in Eq. (4.10). Triangles are experimental data points. Error bars represent standard deviation over several calendered zones from a single simulation run.*

Figure 4.8 shows also that the numerical values of porosity are close to the experimental data. However, the experimental value of porosity tends to decline faster with increasing C_r than numerical porosity. This discrepancy reflects the rather crude assumption in simulations that the binding material does not deform and remains attached to the particles as a plastic layer. In reality, the binder is unevenly distributed in the pore space and deforms with compression [179]. Furthermore, at high pressure levels, the active particles may also deform and break, allowing the material to reach even lower levels of porosity.

Since the electrode is compressed vertically and sheared horizontally, it is expected to expand, specially along its longitudinal y direction. Since in our simulations we applied periodic boundary conditions along the x direction, the electrode cannot expand along this direction. The longitudinal elongation $\Delta L/L$ of the electrode is shown in Fig. 4.9 as a function of C_r for different values of calendering speed. The elongation is nearly proportional to C_r and decreases with increasing calendering speed. This influence of the calendering speed on the elongation of the electrode, though limited, is unexpected

since both final thickness and porosity are independant of the calendering speed. As observed in Fig. 4.9, the experimental data show a similar correlation between elongation and calendering speed. It is noteworthy that none of the reported numerical calendering simulations has been able to predict this dependence on calendering speed.

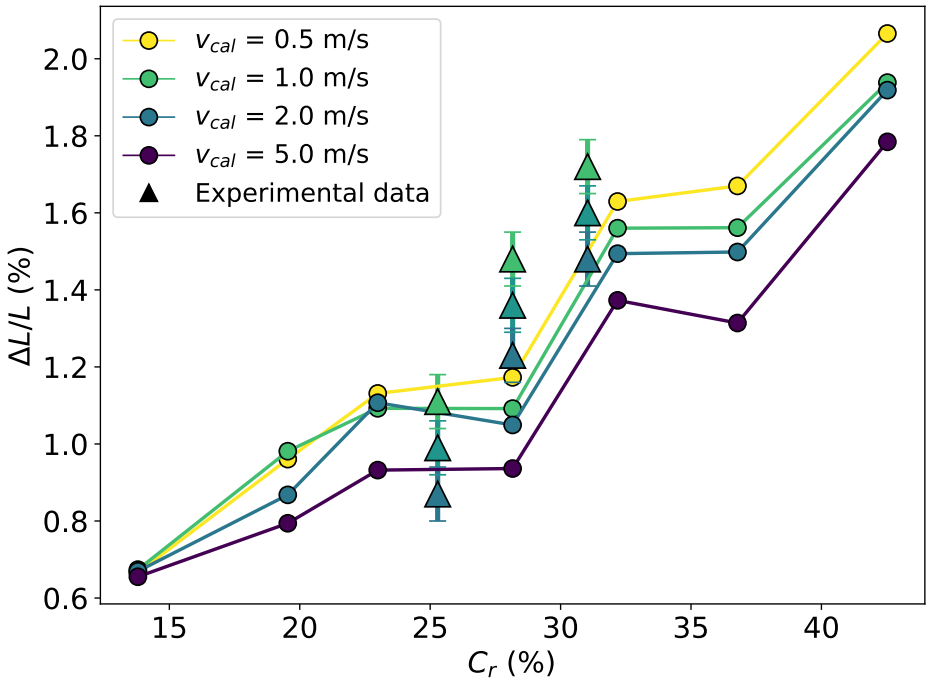

Figure 4.9: *Elongation of the electrode as a function of thickness reduction ratio C_r for different values of calendering speed in simulations and experiments.*

Since in our model we have an explicit representation of the calendering cylinder, which sets the electrode in motion via the action of friction force on top of the electrode, the observed decrease of elongation at higher speeds may well be related to the shearing of the electrode as a result of the mobilization of friction force. In particular, if at higher speeds a relative slip of the cylinder with respect to the electrode occurs to some degree, then the electrode is sheared less and the resulting elongation is smaller. It must also be remarked that high calendering speeds result in shear stresses strong enough to either rip the granular mixture from the collector or directly warp it. Cathode current collectors are usually thin aluminium foils which can not endure large deformations and tend to break during the assembly step [201]. This observation clearly shows the importance of shear stresses developed in the electrode during calendering and the importance of accounting for the real geometry of the process in numerical simulations.

The pressure acting on the calendered zone is a consequence of constriction imposed by the gap between the cylinder and collector. Figure 4.10 shows the maximum stress σ_{max} calculated on the calendering roll as a function of C_r. We see that σ_{max} increases

almost linearly with C_r, in exception to the largest values of C_r, and it is independent of calendering speed. This large increase of vertical stress means a large decrease of the cohesion number. As a result, the porosity decreases. As discussed in the last chapter, high pressures can not be be generated by triaxial compression. Therefore, the generation of high pressure requires shear strain induced by rolling. Once the external pressure returns to zero, the compacted configuration requires cohesive forces to avoir rebound and elastic release.

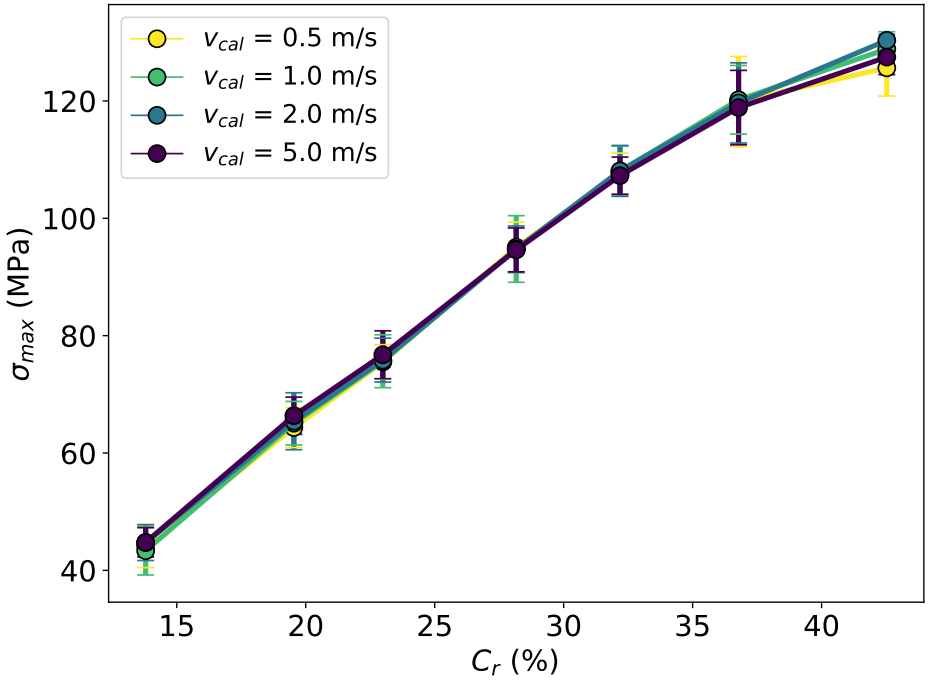

Figure 4.10: *Maximum stress induced by calendering as a function of thickness reduction ratio C_r for different values of calendering speed. The stress is directly calculated on the calendering roll.*

Figure 4.11 shows the final porosity ε as a function of σ_{max}. Considering the initial porosity at zero stress, the relationship between porosity and maximum vertical stress is not perfectly linear. It is well fit to a power-law function when forced to pass by the initial porosity at zero stress:

$$\varepsilon = G\left(\sigma_{max} + H\right)^{-\beta} + I, \tag{4.11}$$

with $G \simeq 9.5$, $H \simeq 140$ MPa, $I \simeq -0.26$, and $\beta \simeq 0.53$. We have $\varepsilon\left(\sigma_{max} = 0\right) \simeq 0.43$, which is the initial porosity of the electrode. This fitting function implies, however, that ε vanishes at a finite stress while we have seen that the fitting function (4.10) predicts a finite porosity. If we take 0.16 as the lowest porosity, as suggested by Eq. (4.10), the maximum pressure needed to reach this porosity is 212 MPa, above which the fitting form

of Eq. (4.11) is unphysical. Further simulations are necessary to check the validity of the fitting forms proposed here for higher values of C_r.

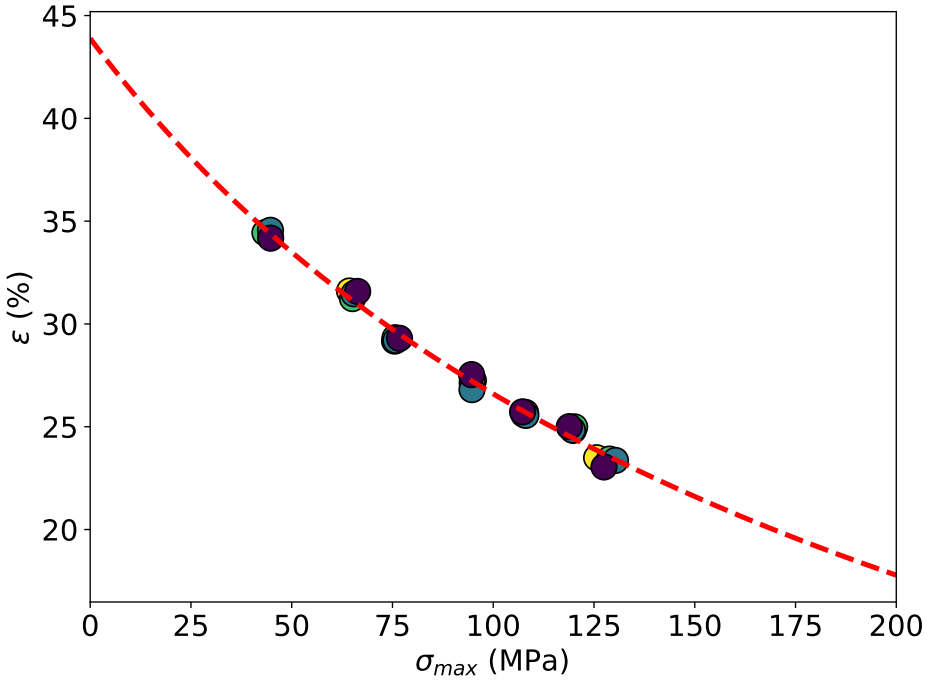

Figure 4.11: *Final porosity ε after calendering as a function of maximum stress σ_{max} for different calendering speeds. The dashed line is a power-law fitting function given by Eq. (4.11) forced to pass by the initial porosity at zero stress.*

4.2.3 Evolution of microstructure

A key advantage of DEM simulations is to provide access to microstructural variables such as the contact and force networks. Several microstructural parameters can be defined. In particular, we are interested in the parameters that control the electric conductivity across the granular microstructure. The lowest-order parameter is the coordination number Z, defined as the average number of contact neighbors per particle:

$$Z = 2\frac{N_c}{N_p - N_0}, \tag{4.12}$$

where N_c is the total number of contacts, N_p is the total number of particles, and N_0 is the total number of floating particles that have contact neighbors. In a cohesive granular medium, contacts can either be compressive or tensile. Compressive contacts are those which have a positive normal force whereas tensile contacts have a negative normal force. By restricting the contact neighbors only to compressive or tensile contacts, we also define

the coordination numbers Z^+ for compressive contacts and Z^- for tensile contacts with $Z = Z^+ + Z^-$. The proportion of tensile contacts is a descriptor of the stress state. When the external confining pressure is high (low) compared to adhesion forces acting between particles, Z^+ is larger (lower) than Z^-.

Figure 4.12 shows the time evolution of Z, Z^+, and Z^-. The coordination number increases as the cylinder approaches the calendered zone, reaches a maximum value slightly above 6, and then declines as the cylinder leaves the calendered zone. The final value of Z is much higher than its initial value. The compressive coordination number Z^+ follows a similar evolution. The tensile coordination number declines and remains nearly constant during the passage of the cylinder before relaxing to a higher value in the final state. It is noteworthy that before calendering, Z^+ and Z^- are nearly equal with a slightly lower value of Z^-, such that $Z^-/Z \simeq 0.45$. In the final state, the proportion of tensile contacts is $Z^-/Z \simeq 0.43$, which is only slightly above its initial value.

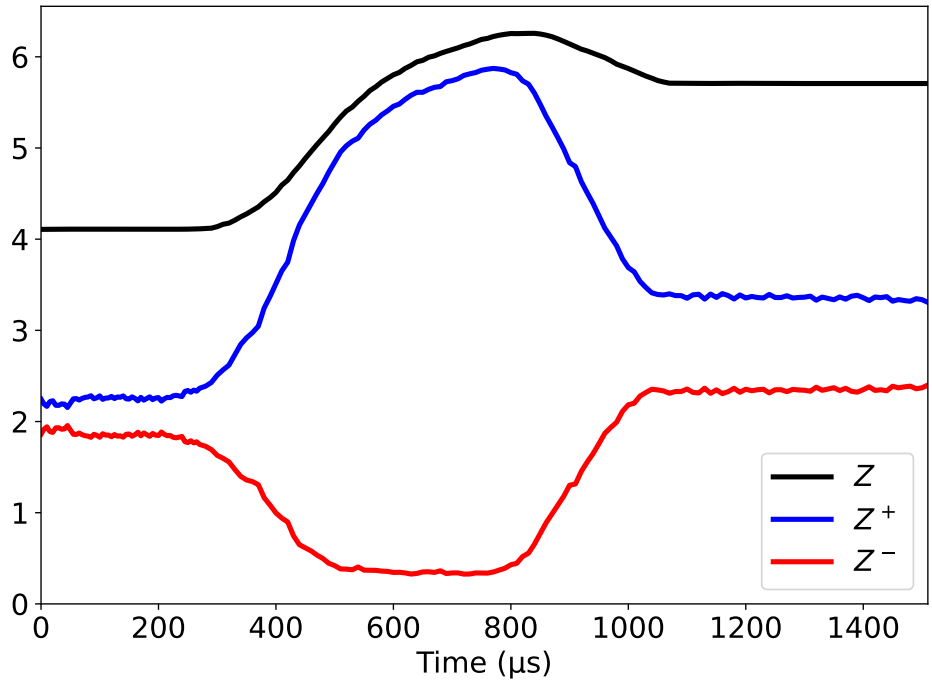

Figure 4.12: *Time evolution of coordination number Z, and the coordination numbers Z^+ and Z^- for compressive and tensile contacts, respectively, with an imposed thickness reduction $C_r = 0.28$ and calendering speed $v_{cal} = 2$ m/s.*

Figure 4.13 shows the values of Z, Z^+, and Z^- after calendering as a function of thickness reduction ratio C_r for different values of calendering speed. The latter has a small effect on average but it is not significant within the statistical precision of the data. The three coordination numbers increase linearly with C_r. Z increases from 4.1 before calendering to values as high as 6.4 for $C_r = 0.43$. Interestingly, the ratio Z^-/Z, i.e. the

proportion of tensile contacts in the system is nearly constant ($\simeq 0.43$) and independent of C_r. This shows that the stress state after relaxation and under the action of only the weights of the particles is the same and independent of C_r. In other words, the compression of the electrode due to calendering is large enough to drive the microstructure to a state which is independent of the initial state. As we shall see below, this final state reflects the anisotropic structure of the calendered material.

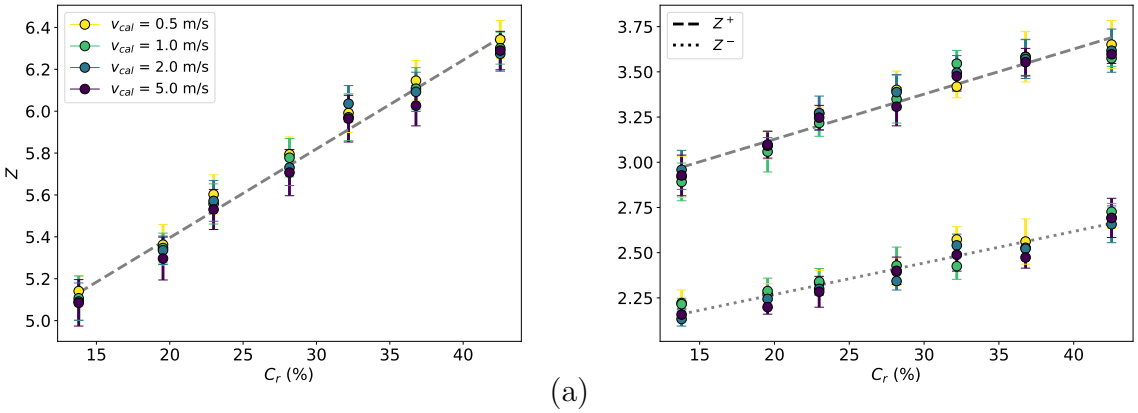

Figure 4.13: *Final values of coordination number Z (a) and compressive and tensile coordination numbers Z^+ and Z^- (b) as a function of thickness reduction ratio C_r for different values of calendering speed.*

As compared to Z, which represents the average connectivity of the particles, the anisotropy of the contact network is a higher-order descriptor of granular microstructure. It is conveniently described by the fabric tensor $\mathbf{F}$ as defined in Eq. 3.8. By definition, we have $tr(\mathbf{F}) = 1$ so that its deviatoric part is given by

$$\mathbf{F}'_{ij} = \mathbf{F}_{ij} - \frac{1}{3}\delta_{ij}, \tag{4.13}$$

where $\boldsymbol{\delta}$ is the Kronecker delta. The deviatoric fabric tensor $\mathbf{F}'$ quantifies the relative deviations of the proportions of the contacts in each direction from the perfect isotropic state, in which the contact orientations are random and uniformly distributed in all space directions. By definition, we have $tr(\mathbf{F}') = 0$. Hence, with respect to an isotropic distribution of contact orientations, a positive value of a component in a given direction reflects an excess of contacts whereas a negative value means a lack of contacts in that direction.

In the calendered zone, we consider two different tensors by either including or excluding the contacts with the cylinder. Figure 4.14 displays the time evolution of diagonal components of $\mathbf{F}'$ calculated in the calendered zone for both of these tensors. The components $\mathbf{F}'_{xx}$ and $\mathbf{F}'_{yy}$ are almost equal. The electrode is initially in an anisotropic state with higher value of $\mathbf{F}'_{zz}$ compared to $\mathbf{F}'_{xx}$ and $\mathbf{F}'_{yy}$ as a consequence of gravitational deposition used to build the electrode. As the roll advances in the calendered zone, $\mathbf{F}'_{zz}$ increases due to the new contacts created between the electrode and the roll but it declines if these

contacts are not included. At the same time, since deviatoric fabric tensor is traceless, the two planar components $\mathbf{F'}_{xx}$ and $\mathbf{F'}_{yy}$ decrease when the contacts with the roll are included and increase otherwise. As the roll quits the calendered zone, $\mathbf{F'}_{zz}$ declines and $\mathbf{F'}_{xx}$ and $\mathbf{F'}_{yy}$ increase. As a result, all components are lower in absolute value in the final state. In other words, calendering reduces the initial anisotropic structure of the electrode.

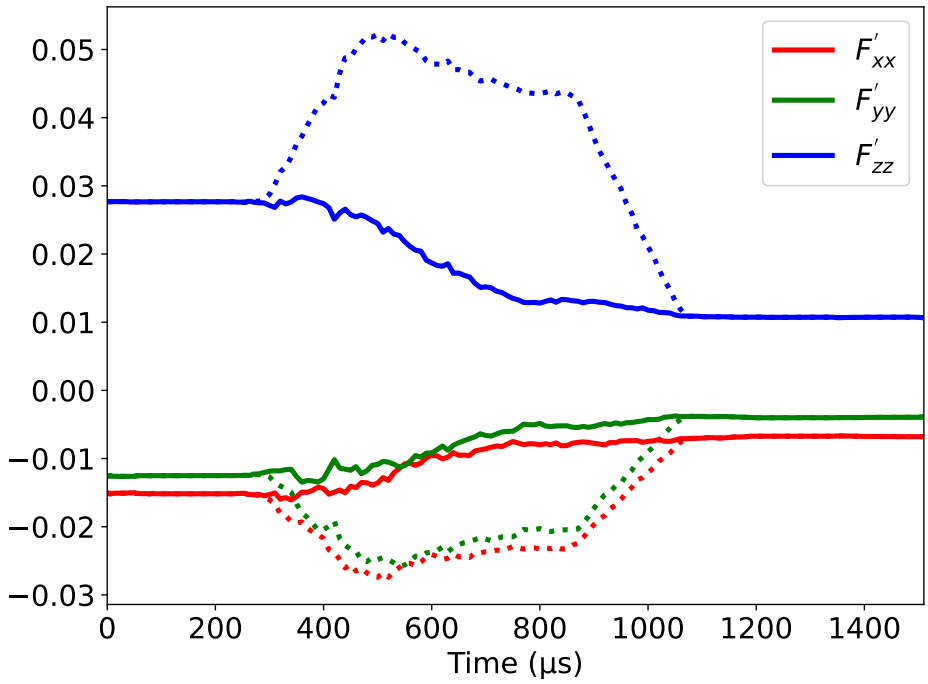

Figure 4.14: *Time evolution of deviatoric fabric tensor components for an imposed thickness reduction ratio $C_r = 0.28$ and calendering speed $v_{cal} = 2$ m/s. The components are calculated with (dotted lines) and without (plain lines) accounting for contacts with the cylinder.*

The decrease of $\mathbf{F'}_{zz}$ during calendering is counterintuitive as vertical compression is expected to induce new contacts along the vertical direction thereby increasing $\mathbf{F'}_{zz}$. This is what occurs when a granular material is subjected to triaxial compression. In contrast, in the process of calendering the variation of fabric components suggests that new contacts are gained in the horizontal direction and lost in the vertical direction! In fact, the horizontal motion of the cylinder with an imposed thickness reduction, the horizontal force exerted by the cylinder on the top calendered layer, and mobilization of friction forces at the interface between cylinder and electrode induce a complex shear deformation that controls the gain and loss of contacts. The evolution of fabric tensor reflects this deformation and its evolution during loading and unloading, showing that the calendering process can not be reduced to simple compression.

Figure 4.15(a) shows the fabric components after calendering as a function of C_r for

v_{cal}=2 m/s. We see that, independently of C_r, the two horizontal components are always nearly equal. All components decrease almost linearly in absolute value with C_r and tend to zero at $C_r = 0.43$. A similar evolution was observed in other studies [48]. Figure 4.15(b) displays $\mathbf{F'}_{zz}$ after calendering as a function of C_r for different values of the calendering speed. In all cases, the anisotropy declines with increasing C_r but we observe a slight dependence on the calendering speed. Increasing the speed leads to less reduction of $\mathbf{F'}_{zz}$. Consistently with the effect of calendering speed on the elongation of the electrode, we may attribute this effect to the overall shear deformation of the material. Less elongation implies lower shear deformation although the vertical compression is the same for a given value of C_r, and lower shear deformation leads to less evolution of the fabric.

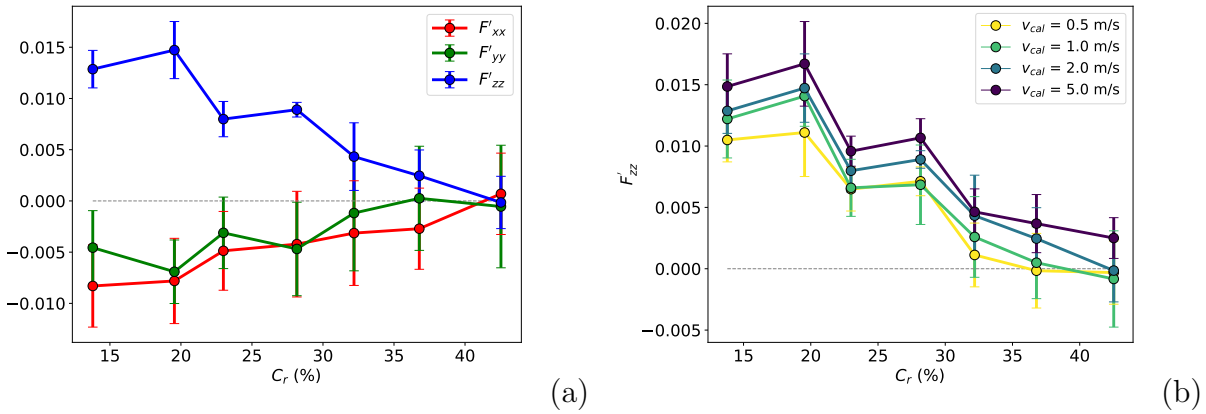

Figure 4.15: *(a) Diagonal elements of deviatoric fabric tensor after calendering as a function of thickness reduction ratio C_r for calendering speed v_{cal} = 2 m/s; (b) Vertical fabric component F'_{zz} as a function of C_r for different values of the calendering speed. The dashed line represents the isotropic state.*

The stress and fabric states of the electrode before and after calendering can be visualized through the force network as displayed in Fig. 4.16. In the initial state, the contact forces are basically induced by particle weights and the contacts are oriented around ±45° with respect to the vertical due to the initial gravitational deposition. After calendering we observe a large number of contacts oriented along the horizontal and vertical directions. Many vertical contacts are tensile whereas compressive contacts occur predominantly along the horizontal direction. This organization of the force network is consistent with the orientation of the fabric tensor. It is also important to note that both compressive and tensile forces are much larger than in the initial state. The larger values of forces is a consequence of higher mobilization of tensile forces by the action of calendering and self-balanced by compressive forces of the same order of magnitude.

4.2.4 Electronic properties

The effective electrical and ionic conductivities of our numerically calendered electrodes are computed by means of the FFT method. We extracted 5 samples of size 200×200×50 μm^3

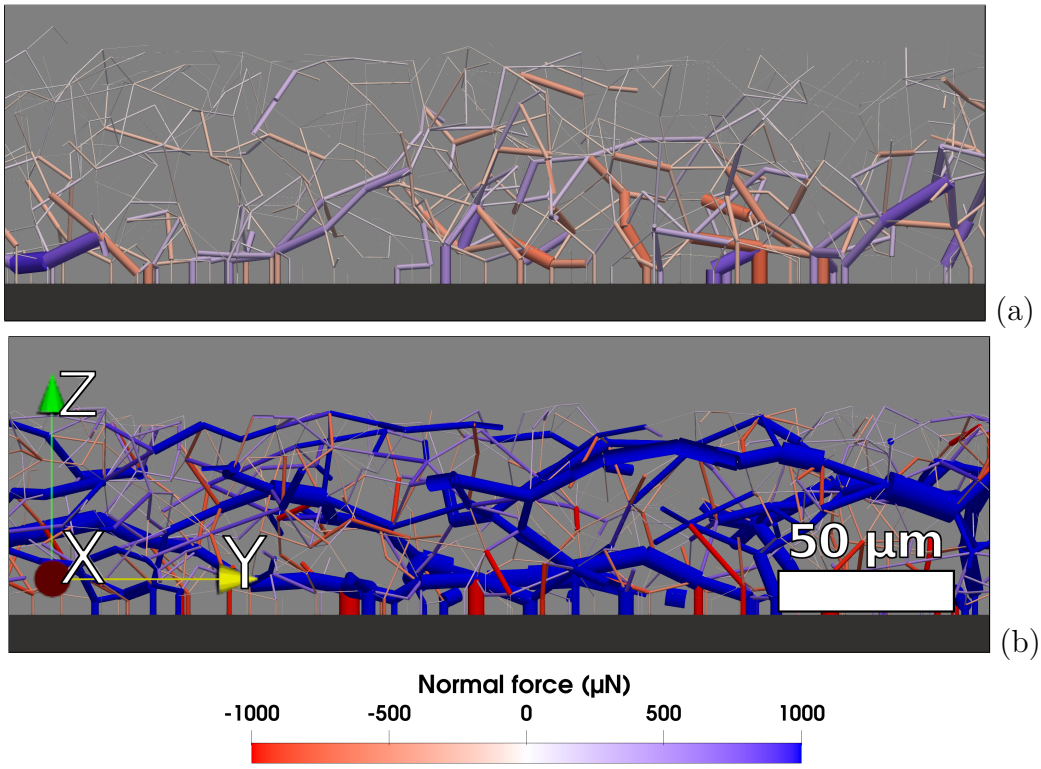

Figure 4.16: *Force chains inside the electrode before (a) and after (b) calendering. Line thickness is proportional to force magnitude (×100 in the initial state).*

from our simulations and used a homemade code to voxelize them. Figures 4.17(a) and (b) show one of the samples before and after the voxelization step. The voxel size was set to $(0.5R_p)^3$ μm^3 in order to represent efficiently the binder layer. Since FFT computations require the sample to be periodic in all directions, we did not include the current collector. The type of material attributed to each voxel is chosen from the DEM sample. If a voxel is on the edge of a particle, it is identified as CBD phase and if the voxel is inside a particle, it is considered as active material. In all other cases, the voxel is in the electrolyte phase.

Each voxel has its own bulk conductivity corresponding to its phase. The values that we employed are summarized in Table 4.4. Some conductivity values – namely the electrical conductivity of the electrolyte and the ionic conductivity of the active material – are vanishingly small. However, too high contrasts between the highest and lowest conductivities in FFT computations lead to very high computational costs and slow convergence rates. We did a parametric study on one reference case with values in the range $[10^{-7}, 10^{-3}]$ mS/cm in order to select conductivity values which reduce most the computational cost while keeping the effective conductivities of the electrode close to reference values.

Electric conductivity λ_{el} represents the flow of electric current across the active material particles to the current collector. Figure 4.18(a) shows λ_{el} as a function of thickness reduction ratio C_r for v_{cal}= 1 m/s. We observe a clear correlation between electric conductivity

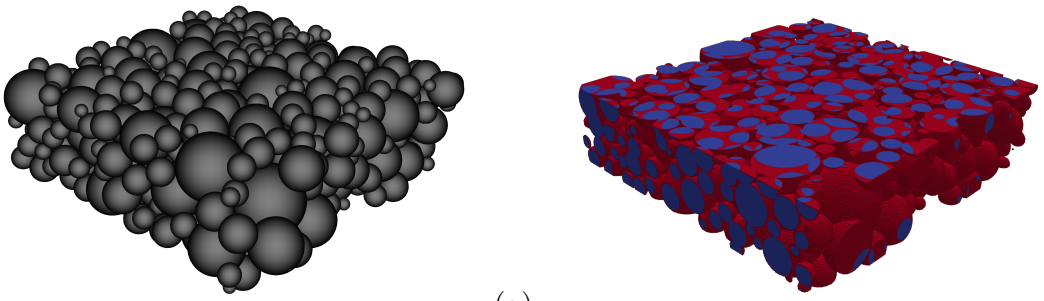

(a) (b)

Figure 4.17: *Example of voxelisation from DEM sample used for the FFT conductivities computations. (a) DEM sample; (b) Cartesian mesh after voxelisation: the blue color corresponds to active material, red color to CBD and empty voxels to electrolyte.*

	NMC	CBD	Electrolyte
Electrical conductivity (mS/cm)	10^{-2} [3]	100 [163]	10^{-5}*
Ionic conductivity (mS/cm)	10^{-4}*	10^{-2} [129]	10 [95]

Table 4.4: *Conductivity values used in the FFT computations – values marked by an asterisk (*) are adopted to ease FFT computations, as explained in text.*

and C_r. λ_{el} increases as a function of C_r along the three directions and seems to tend to a plateau value, although a clear plateau is not reached. The gain in electric conductivity is nearly the same ($\simeq 30\%$) in the three directions. Nevertheless, the electric conductivity along vertical direction is slightly above those in the other directions. Figure 4.18(b) shows λ_{el} as a function of C_r along the vertical direction for different values of calendering speed. The calendering speed does not seem to affect vertical electric conductivity while, as shown in Fig. 4.15, F'_{zz} slightly depends on the calendering speed. In fact, the variation of F'_{zz} as a function of speed is too small to affect significantly the electric conductivity.

The electric conductivity depends on both contact network and electric conductivity at each contact. The latter is a function of the contact area and varies therefore with normal force and the plastic deformation of the contact [151]. Dimensional analysis implies that λ_{el} is proportional to the conductivity λ_{el}^{NMC} of NMC particles. Furthermore, the number density of contacts $n_c = Z\phi/2V_p$, where V_p is the average volume of one particleand $\phi = 1-\varepsilon$ is the packing fraction, and their orientations through the fabric tensor control the amount of electric current and thus the conductivity of the network. Since $F_{ii} = 1/3 + F'_{ii} \simeq 1/3$, we may neglect the effect of fabric anisotropy. Hence,

$$\lambda_{el} \propto \phi Z \lambda_{el}^{NMC}, \tag{4.14}$$

Figure 4.19 shows that this relation holds for all values of C_r and the proportionality factor

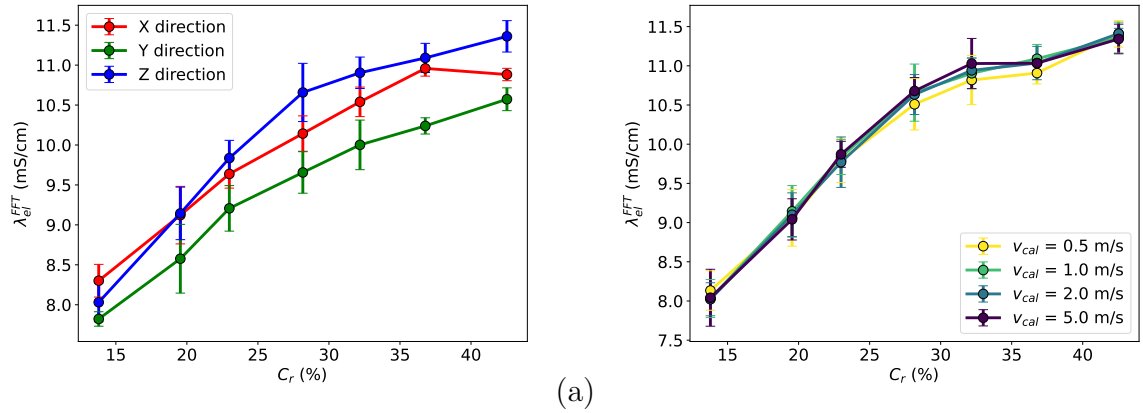

(a) (b)

Figure 4.18: *Electric conductivity λ_{el} as a function of thickness reduction ratio C_r in all directions for v_{cal}= 1 m/s (a), and along the vertical direction for different values of the calendering speed.*

is independent of C_r. This relation shows that the influence of C_r is due to the variations of ε and Z.

The voxelisation step has low precision to describe the real contact surface as it would require high computational resources. The mesh drives the computation time, it must therefore be sufficiently precise to describe correctly the domain but also not too small for the FFT to converge in a reasonable time. All the contacts have therefore almost the same surface area, which thus do not have a major effect on the effective electrical conductivity.

Ionic conductivity λ_{ion} reflects the diffusion of ions in the pore space between particles under the influence of chemical potential gradient. Figure 4.20(a) shows λ_{ion} calculated by FFT in three directions for v_{cal}= 1 m/s as a function of C_r. λ_{ion} declines with increasing C_r in all directions. Figure 4.20(b) displays λ_{ion} in the vertical direction for different values of the calendering speed. We see that λ_{ion} is independent of calendering speed. This result is expected since the ionic conductivity mainly depends on the conductivity of the electrolyte and the porosity ε [47], which was observed to be independent of the calendering speed. We have

$$\lambda_{ion}^{FFT} \propto \varepsilon \lambda_{ion}^{electrolyte}. \tag{4.15}$$

Figure 4.21 shows that this relation holds with a proportionality factor which is nearly independent of C_r.

4.3 Conclusion

We developed a DEM-based model for the simulation of the calendering process of Li-ion battery electrodes. The CBD material was taken into account as a thin layer coating NMC particles and governed by a plastic-adhesive behavior. Most parameters were calibrated from experiments. The model was applied only to one side of the electrode based on the

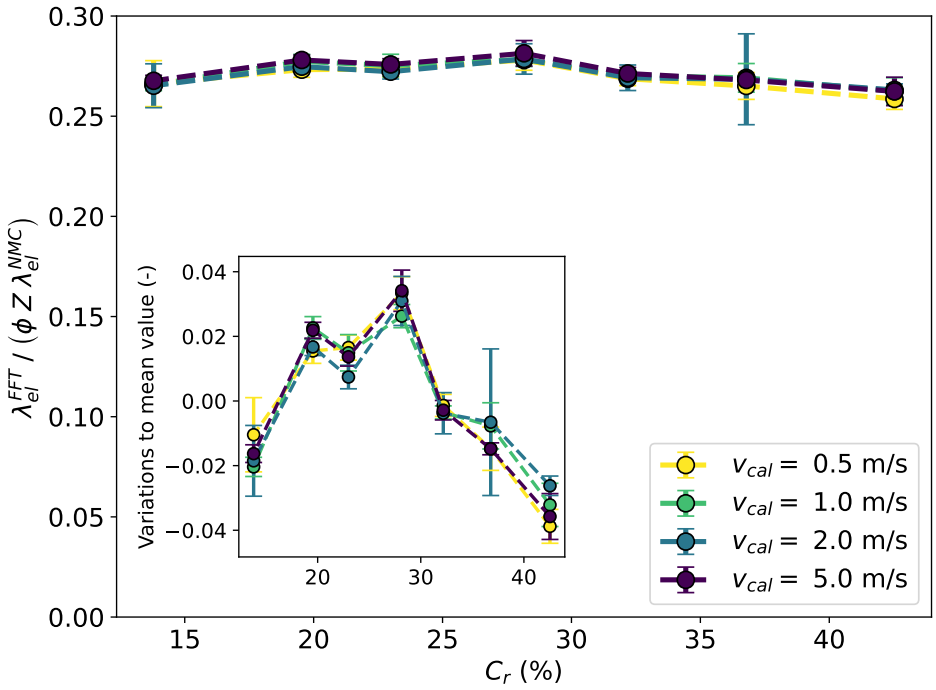

(b)

Figure 4.19: *Normalized effective electric conductivity obtained by means of the FFT method as a function of thickness reduction factor C_r for different values of calendering speed.*

assumption of rigid current collector in the middle of the electrode. The process was modeled by introducing a cylinder that drives the electrode by its rotation via friction force mobilization at its interface with electrode and a gap smaller than the initial thickness of the electrode. As a result, the calendered zone undergoes a complex deformation combining shear and compression. A parametric investigation was performed by simulations for a range of values of thickness reduction ratio and calendering speed. The effect of calendering and its parameters was analyzed in terms of porosity, elongation, microstructural parameters, and electronic properties of the electrode.

We found that most results on porosity and elongation of the electrode were in good agreement with experimental data. The elongation of the electrode and some other properties such as the vertical fabric component were shown to be slightly dependent on the calendering speed. This dependence was not observed in past simulations and in this respect shows the important role of explicit representation of the calendering roll.

We showed that, as a result of contact plastic behavior and particle rearrangements, the elastic rebound is small in full agreement with experimental data. The porosity decreases as a power law with increasing thickness reduction ratio and seems to tend to a limit value representing the lowest reachable porosity. The highest stress reached in the calendered zone was found to increase almost linearly with thickness reduction ratio. As

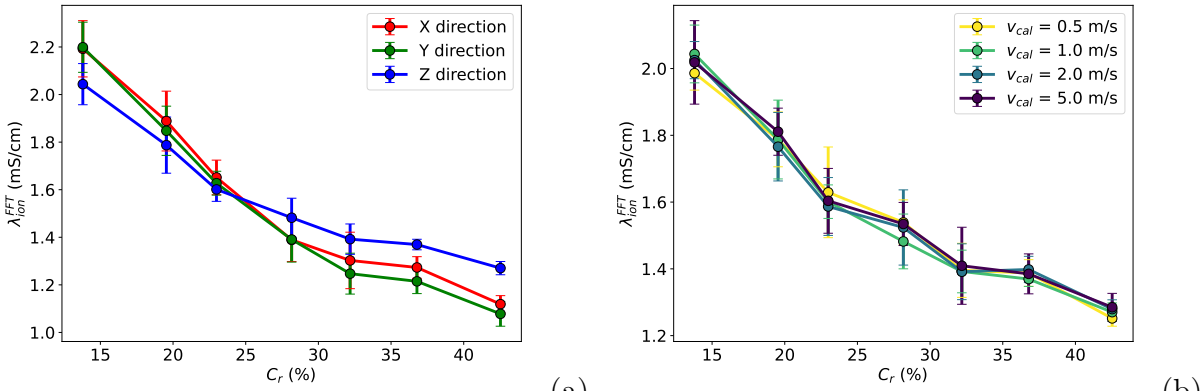

Figure 4.20: *Evolution of the ionic conductivity as a function of thickness reduction ratio C_r in all directions at calendering speed v_{cal}= 1 m/s (a) and in the vertical direction for different values of the calendering speed (b).*

a result, the coordination number and the tensile and compressive coordination numbers also increase linearly with thickness reduction ratio, resulting in much higher self-balanced tensile and compressive force chains which corresponds to the higher cohesive strength of the electrode after calendering. Interestingly, the proportion of tensile contacts is constant and independent of thickness reduction ratio, suggesting that the self-balanced structure induced by calendering is similar for all levels of thickness reduction. An important result of this study was to show that this structure involves mostly vertical tensile contacts and horizontal compressive contacts which is in radical contrast with the expectation that vertical compression tends to induce compressive contacts along the vertical direction. This counterintuitive observation was attributed to shear deformation induced by rolling and thickness reduction.

The electronic properties of our numerically calendered electrodes were computed by means of the FFT technique. The effective electric conductivity is an increasing function of thickness reduction ratio and independent of calendering speed whereas the effective ionic conductivity declines at the same time. The electrical conductivity was shown to be proportional to packing fraction, coordination number and electric conductivity of MMC particles while ionic conductivity is proportional to electrolyte conductivity filling the pore space and porosity.

This work can be extended to investigate the effects of larger calendering speeds and larger thickness reduction ratios (beyond what is used in practice). A more detailed analysis is necessary to quantify the deformation field in the calendered zone and the degrees of local slip and shear at the electrode-cylinder interface as a function of calendering speed. In this work, a constant value of adhesion force (depending on the binder layer thickness) was assumed. It is important to investigate the effect of this parameter which controls both the initial porosity and the mobility of particles during calendering. It is well known that the behavior of cohesive materials depends on the cohesion number which involves the ratio of cohesive stress and applied compressive stress. Furthermore, it was also recently found

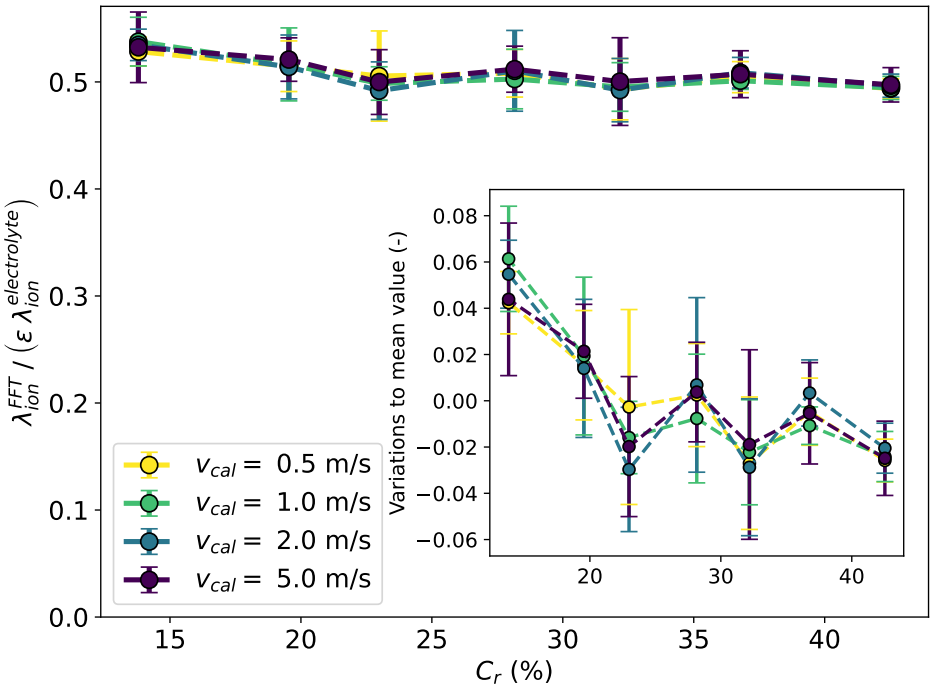

Figure 4.21: *Normalized effective ionic conductivity obtained by the FFT method as a function of thickness reduction ratio C_r for different values calendering speed.*

that contact stiffness plays a key role in the scaling of porosity [162]. The flexibility of the current collector may also play a role in the evolution of the electrode microstructure. It can be modeled by finite elements and coupled with discrete particles. The plastic-adhesive behavior of the binding material is also a model ingredient that can be adapted to the material used. Alternative representations of the binder can be tested in the framework of the developed code. For example, a spatial variability in the distribution of the binder layer thickness can be introduced to account for fabrication hazards.

General conclusions

The goal of this doctoral thesis work was to develop particle dynamics simulations to model the calendering process and understand its effects on the conductivity and energy density of Lithium-ion positive electrodes, which bear on the charging rate and autonomy of Li-ion batteries. The electrode is modeled as a cohesive granular material composed of active material grains, bound together by a matrix of binding polymers and conductive additives. We performed both Discrete Element Method (DEM) simulations based on a realistic representation of the process and dynamic compression of cohesive granular materials to obtain insights about the evolution of the porosity and microstructure during the process. For these simulations, we developed a new cohesive elasto-plastic force law to account for the binding material and a detailed model of the calendering setup, and we carried out extensive parametric study to analyze the influence of the material and process parameters on the microstructural and electronical properties of the electrode.

In Chapter 1 we reviewed the existing literature on the calendering of Li-ion battery electrodes. The first part described the history of electrical batteries and the current technology of Lithium-ion batteries. The working principle of this type of batteries was presented, as well as different versions of Li-ion batteries and their internal components: active materials, binders or electrolytes. The manufacturing process of these batteries is composed of different steps, one of them being calendering. The importance of the calendering step on the performances of the batteries was explained. We presented methods to characterize experimentally the electrodes and different measurable parameters. The second part of this review chapter was focused on the simulations used to numerically study the calendering of Li-ion battery electrodes. Since the electrodes are a granular medium, we focused our work on the DEM and used it for our simulations. Each step of the algorithm, respectively contact detection, force computation and position updating, was thoroughly described. To represent the Li-ion battery electrodes, various simulation models are used, each one accounting for the components of the electrodes in a different way. While representing explicitly all the particles composing the electrode requires high computational costs, most of the simulation models represent only the active material grains and account for the binder implicitly by considering a cohesive elasto-plastic contact law. In most past numerical work, the calendering is represented as an unaxial compaction, considering that the calendering speed is relatively low ($\simeq$ 1m/min) and the roll much larger than the electrode. The originality of the work presented in this thesis is (1) to develop a realistic model of the calendering process, (2) a new force law based on a model of the binding

material as a layer coating the active material particles, (3) a detailled parametric study of dynamic compaction to obtain a scaling law for porosity, and (4) using the simulated microstructures to compute the electrical and ionic conductivities.

Chapter 2 presents our study of microstructural properties of cohesive granular materials prepared by dynamic compaction. We study how the cohesion induced by the binder affects the porosity and microstructure of the electrodes under compaction. Using a linear elastic and cohesion contact law, we used different values of particle size, elastic stiffness, adhesion force and applied pressure. We showed that the porosity can be expressed as a unique function of a dimensionless parameter combining all our system parameters. This new parameter differs from the usual cohesion number employed in the literature by accounting for the elastic stiffness. Remarkably, we found that the bonding structure is more adequately described by the cohesion number. This suggests that similar bond networks with various porosities can be reached by modifying the elastic stiffness. We also investigated the origins of data points deviating from the proposed scaling, and showed that they arise from wall effects.

The microstructures obtained by isotropic compaction are used as initial conditions in Chapter 3 for triaxial compaction. Interestingly, we found that the void ratio keeps a value close to its initial state. In other words, the porosity obtained by isotropic compaction is nearly the same as the critical porosity reached by triaxial compaction. During compression the fabric and stress ratio evolve towards the critical state at a rate depending on the adhesive force between the particles. Values of stress ratio and proportion of cohesive contacts are shown to follow an asymmetric sigmoid evolution depending on the adhesive force, similarly to the void ratio in Chapter 2. Interestingly we found the counter-intuitive behavior that the Coulomb cohesion is an increasing function of void ratio. We also found that the microstructure evolves in all cases to a well defined state characterized by a simple relation between coordination number and anisotropy which corresponds to the critical state. Our results of this chapter suggest that cohesive granular materials have a critical state that is all the more porous that adhesion force is high. For this reason, triaxial compaction can not be used as a means to reduce significantly the porosity. This is only possible if a process such as the calendering process increases the average pressure, thereby reducing the cohesion number.

The effects of the calendering parameters on the microstructure of the electrodes is studied in Chapter 4. We represented only one side of the electrode assuming that the current collector is rigid. The active material is simulated explicitly and the binding matrix is taken into account implicitly. A new cohesive elasto-plastic contact law in 2 phases is developed specially for this model, accounting for the properties of both the active material and the binder. The calendering process is simulated by explicitly representing the calendering roll in the model. In simulations we used different heights and rotation speeds in a broad ranges of values. Final thickness, porosity and elongation show a good agreement with experimental results. We find that the porosity decreases following a power law of the thickness reduction. The elongation of the electrode depends on the calendering speed, as well as the orientation of anisotropy inside the electrode microstructure. The electrical and ionic conductivities of our numerically calendered electrodes are computed

using the FFT method. The electrical conductivity was shown to depend on solid fraction and coordination number while the ionic conductivity only on the porosity.

Perspectives of future work

Due to the complexity of the internal composition of the electrodes, the entirety of its behavior was not possible to study. One aspect that was overlooked in this study is the behavior of the electrodes under shear loading. The calendering simulation model we developed here differs from the others of the literature by the presence of the calendering roll. Its rotation induces tangential and shearing stresses inside the electrode. Faster calendering speeds imply higher stresses, which can result in the rupture of the current collector or the delamination of the particle bed. We showed in Chapter 4 that the microstructure of the electrode was influenced by the calendering speed. It would therefore be interesting to study the theoretical behavior of an representative volume element under shearing using the same strategy as in Chapters 2 and 3. This may provide information on the importance of each microstructural parameter on the mechanical behavior of the electrode. Previous works on the same subject showed a possible scaling using the cohesion number, but they did not study the influence of the elastic stiffness [93, 94]. We could use this new study to observe if the modified cohesion number defined in Chapter 2 can characterize the shearing behavior of cohesive granular materials.

Depending on the type of battery, different types of materials may be employed. For 3rd generation batteries whose cathodes use NMC particles, the representation of the active material grains as spherical particles is valid. Considering the anodes, the active material is mostly carbon which can be found in various forms, such as nanosheets or nanotubes. Spherical elements are therefore not suited to these applications. The emergence of silicium anodes with large variations of volume might not change the simulation of the calendering process. However the computation of electronical conductivities of these electrodes would require to take this into account.

High levels of compaction of the electrodes often lead to particle deformation and fragmentation. In our work we accounted for these effects by considering mechanical damage in the contact law. However, this approach works only for small deformations, and as it can be seen in Figure 1.5 the particles can be highly deformed. In order to be more representative of the real microstructural changes of the electrode, it would therefore be necessary to use deformable or fragmentable particles. On the same picture the current collector undergoes some deformation, and therefore can not be considered to be rigid anymore and its deformation should be taken into account. However this would require either different simulation methods, such as the Material Point Method [116] which uses deformable particles, and/or implement the fragmentation of the elements.

Regarding the presence of the carbon binder matrix, some improvements can be added to our model. In our simulations we considered that the binder matrix uniformly covers the active material particles while in reality it is more often located at the contact zone between particles [179]. Our choice has already been discussed and argumented in Chap-

ter 4, but this only applies to the calendering simulation and not the electronical properties computation. Indeed, by considering that the binder matrix surrounds the active material particles, the voxelisation of the electrode adds a constant layer of highly electrically conductive material around each particle, creating easier paths for the electrical current to flow. Considering the binder matrix only around the contact points or even a gradient around the particles would be more representative of the real distribution of components inside the electrode.

Résumé étendu en français

Avant propos

Dans ce résumé étendu, nous présentons une brève synthèse en français du contenu du manuscrit en respectant la chronologie de la thèse. Les principaux résultats de chaque chapitre sont rappelés et nous nous attarderons sur quelques éléments choisis illustrant la démarche numérique mise en oeuvre, les types de tests effectués, les mesures réalisées et les analyses les plus importantes. Enfin, nous espérons que ce résumé servira de guide de lecture ou d'introduction rapide pour le lecteur pressé.

Introduction

Durant les dernières décennies le nombre d'appareils électroniques a augmenté considérablement dans notre quotidien. De plus l'émergence et l'ascension fulgurante des véhicules électriques a poussé à développer de nouveaux moyens de stocker l'énergie électrique. La technologie actuelle se base sur des batteries Lithium-ion (Li-ion) qui doivent leur nom au matériau actif à base de Lithium les composant. Pour obtenir des batteries présentant de meilleures performances, il existe 2 approches : soit utiliser de nouveaux matériaux, soit améliorer les procédés existants ; c'est sur cette seconde approche que nous nous concentrerons. La fabrication des batteries Li-ion est composée de 5 grandes étapes : préparation du mélange, enduction, calandrage, mise en forme et remplissage. L'étape de calandrage consiste à comprimer les électrodes en les faisant passer entre 2 cylindres en rotation afin de réduire leur épaisseur et ainsi augmenter leur densité d'énergie. Toutefois il a été observé que trop réduire l'épaisseur des électrodes a tendance à diminuer les performances des batteries, notamment leur vitesse de charge. Les fabricants se trouvent face à un compromis, où ils doivent choisir entre des batteries pouvant stocker une large quantité d'énergie mais qui ne peuvent pas se charger/décharger rapidement, ou au contraire des batteries rechargeables rapidement mais dont le capacité de stockage de l'énergie est limitée. C'est dans ce cadre que s'inscrit cette thèse, où nous allons utiliser les outils de simulation numérique pour étudier l'influence qu'a le calandrage sur les propriétés microstructurelles et électroniques des électrodes.

Contexte

Depuis les premiers modèles au plomb, les batteries électriques ont subi de nombreuses évolutions. Il existe différents types de batteries Li-ion, identifiés en générations, qui comportent chacun des compositions différentes. Les modèles actuellement produits à échelle industrielle sont les batteries de $3^{\text{ème}}$ génération, dont les anodes sont à base de carbone et les cathodes à base de NMC. Un collecteur de courant permet de faire circuler les électrons des grains de matériau actif vers les pôles de la batterie. Un liant polymérique est ajouté dans l'électrode pour créer des liens cohésifs entre les grains de matériau actif eux mêmes et avec le collecteur de courant. Afin d'améliorer la conductivité électrique de l'électrode, des additifs électroniques sont aussi introduits et vont se mélanger au liant afin de former une matrice appelée *Carbon Binder Domain* (CBD). Un électrolyte liquide permettant aux ions Li^+ de circuler d'une électrode à l'autre est ajouté lors de la dernière étape de fabrication et ira remplir les pores des électrodes.

La fabrication des batteries Li-ion se décompose en 5 étapes : préparation du mélange, enduction, calandrage, mise en forme et remplissage. L'étape de calandrage est l'une des plus importantes en ce qui concerne les performances finales de la batterie. En effet, en réduisant l'épaisseur des électrodes, leur densité énergétique est augmentée, de même que leur conductivité électrique. Cependant, les pores internes au travers desquels l'électrolyte va s'introduire seront bouchés, ce qui allongera le trajet effectué par les ions pour passer d'une électrode à l'autre. Les batteries ainsi produites auront du mal à délivrer rapidement l'entièreté de l'énergie électrique qu'elles contiennent. Il convient donc d'étudier quelle est l'influence du calandrage sur les propriétés microstructurelles et électroniques des électrodes.

Plusieurs méthodes existent pour caractériser expérimentalement les électrodes suivant quels paramètres sont étudiés, telles que la tomographie, les tests de nanoindentation ou de traction/compression. Toutefois, certaines caractéristiques ne peuvent pas être étudiées précisément expérimentalement. Des modèles numériques sont alors développés, afin d'étudier et de comprendre plus en détail les mécanismes entrant en jeu dans les procédés expérimentaux.

Les modèles de simulation numérique représentant le calandrage des électrodes Li-ion se basent principalement sur la Méthode des Eléments Discrets (DEM). Celle-ci considère que chaque élément présent dans la simulation possède ses propres caractéristiques en termes de forme, matériau, position et vitesse. Les éléments composant les électrodes sont introduits dans la simulation de 2 manières différentes : soit explicitement avec des éléments adaptés, comme par exemple pour les grains de matériau actif et le collecteur de courant, soit implicitement en ne considérant que leurs propriétés mécaniques, comme c'est le cas pour le liant qui n'est généralement pas représenté directement mais dont les propriétés adhésives sont prises en compte dans la loi de contact entre les autres éléments. Le comportement mécanique des différents éléments est assez variable suivant les systèmes étudiés, allant de l'élasticité simple à de l'élasto-plasticité endommageable avec cohésion. Le calandrage est lui représenté de manière simplifiée sous la forme d'une compression

uniaxiale, en se basant sur les hypothèses que le cylindre de calandrage est beaucoup plus grand que l'électrode et que sa vitesse de rotation est relativement faible. Les modèles numériques développés jusqu'alors ont permis d'étudier les changements de microstructure des électrodes ainsi que les relations entre différents paramètres microstructuraux et les conductivités électroniques des électrodes.

Compaction isotrope d'un matériau granulaire cohésif

Afin détudier le comportement mécanique des électrodes, qui sont un milieu granulaire cohésif, nous avons effectué différents essais numériques. Le premier est une compaction isotrope d'un volume élémentaire représentatif, afin d'étudier l'influence de la cohésion sur la microstructure. Pour ce faire, nous avons construit un échantillon cubique rempli de particules sphériques monodisperses dont les parois rigides appliquent une pression constante. La loi de contact utilisée est une simple loi élastique linéaire avec une force d'adhésion constante. Différentes valeurs de taille des particules, pression appliquée par les parois, rigidité élastique et force d'adhésion ont été étudiées.

Les résultats ont permis de démontrer une dépendance de l'indice de vide – qui est la rapport entre la quantité de vide et de matière dans l'échantillon – avec ces différents paramètres, et surtout à la force d'adhésion. Les systèmes les plus cohésifs présentent des indices de vide à l'équilibre plus élevés que pour les systèmes moins cohésifs ; l'évolution se fait suivant une courbe sigmoïde asymétrique. A partir des équations du mouvement il est possible de définir une force d'adhésion critique en deçà de laquelle le contact entre 2 particules sera cohésif. Nous avons ainsi pu définir un nouveau paramètre adimensionné noté η^*, basé sur le nombre de cohésion η et mettant en relation cette force d'adhésion critique avec la force d'adhésion du système. La différence principale entre ces deux nombres adimensionnés est la prise en compte dans η^* de la rigidité élastique, qui jusqu'alors avait été considérée comme n'affectant pas les systèmes cohésifs. La valeur minimale d'indice de vide atteignable est indépendante de la force d'adhésion, tandis que la valeur maximale est liée à une pression critique dépendante des autres paramètres ; il est ainsi possible de définir un indice de vide relatif e_r entre ces deux valeurs extremales. Les données tracées en fonction de e_r et η^* permettent de définir une courbe d'évolution commune à tous les systèmes étudiés présentant deux régimes d'évolution distincts. Quelques points de données échappent à cette normalisation mais ce sont des cas limites soumis à des effets de bord importants.

Les réseaux de contacts des différentes microstructures obtenues ont été étudiés en termes de connectivité, forces attractives/répulsives et distributions de ces forces. Les systèmes les plus cohésifs montrent des effets de bords plus importants tout en réduisant le nombre de contacts avec les parois externes. Plus la force d'adhésion est importante, plus le système est poreux et la proportion de contacts attractifs est élevée. Le nombre de contacts attractifs peut être relié au nombre de cohésion η et non pas à η^* ; Toutefois il a été observé que pour une même proportion de contacts attractifs dans un système, l'indice de vide relatif pouvait varier grandement, et ce principalement dû à la rigidité élastique. La

distribution des forces attractives et répulsives est elle aussi dépendante de η, démontrant ainsi l'influence de la rigidité élastique sur l'équilibre statique du système.

Compression triaxiale d'un matériau granulaire cohésif

La seconde étude portant sur le comportement des milieux granulaires cohésifs se base sur une compression triaxiale, cette représentation étant relativement proche des modèles représentant le calandrage présents dans la littérature. En partant des configurations obtenues dans le chapitre précédent, les parois latérales sont maintenues à pression constante tandis que la paroi inférieure est fixée et la paroi supérieure descendue à vitesse constante. La porosité, l'anisotropie et les contraintes sont mesurées au fil de la compression. Ici toutefois seule l'influence de la force d'adhésion est étudiée. Cette étude a permis de montrer que la résistance au cisaillement augmente linéairement avec l'indice de vide dans l'état critique (état de déformation continue). On trouve que l'indice de vide obtenu par la compaction isotrope garde une valeur approximatement constante proche de l'indice de vide critique pendant la compression triaxiale. La force de cohésion du milieu granulaire est montrée comme étant linéairement proportionnelle à la force d'adhésion entre les particules. Par ailleurs nous avons étudié l'évolution de la microstructure dans un espace de phase de deux variables qui sont le nombre de coordination et l'anisotropie du réseau de contacts, et determiné deux comportements limites: (1) une augmentation du nombre de coordination à anisotropie constante (cas les plus cohésifs) (2) une augmentation de l'anisotropie à nombre de coordination constante (cas les moins cohésifs) Dans l'état critique une relation linéaire entre la résistance au cisaillement et l'indice de vide est obtenue, de même qu'une relation inverse entre l'anisotropie de contact et le nombre de coordination.

Simulation du calandrage des électrodes Lithium-Ion

Nous avons ensuite étudié le calandrage des électrodes Li-ion au travers de simulations numériques effectuées avec la DEM. Des expérimentations ont été effectuées par les membres du LITEN du CEA Grenoble sur le calandrage d'électrodes Li-ion et les données ont servi de référence à nos simulations. Dans notre modèle nous avons représenté explicitement les grains de matériau actif et le collecteur de courant, tandis que la matrice de liant-additifs a été prise en compte implicitement en considérant une couche externe enrobant les particules de matériau actif mais aussi dans la loi de contact. Celle-ci a été développé spécialement pour cette étude et se distingue en 2 phases : lorsque le contact se fait au niveau de la couche externe de liant, le comportement mécanique est considéré comme plastique cohésif tandis qu'il devient élastique endommageable lorsque l'interpénétration entre les grains dépasse la couche de liant. Les propriétés cohésives et plastiques de cette loi de contact sont directement liées aux propriétés du liant, tandis que les composantes élastiques et en endommagement sont liées au matériau actif.

Contrairement aux modèles de la litérature, le cylindre de calandrage est introduit directemenr dans nos simulations afin de représenter de manière plus réaliste le procédé de calandrage. L'échantillon est ainsi une bande de quelques millimètres de long et 100µm d'épaisseur initialement et dont les dimensions latérales sont périodiques. Les particules sont déposées sur le collecteur par dépôt gravitaire, puis une fois stabilisées le cylindre est descendu jusqu'à atteindre la hauteur désirée ; cette hauteur contrôlera la réduction d'épaisseur de l'électrode. Le cylindre est ensuite mis en rotation, entrainant ainsi l'électrode par friction avec les particules. L'électrode sera alors comprimée au fur et à mesure qu'elle avance sous le cylindre. Plusieurs simulations utilisant différentes valeurs de réduction d'épaisseur et de vitesse de calandrage ont été réalisées.

Plusieurs paramètres microstructuraux et leur évolution temporelle ont été étudiés. La porosité de l'électrode évolue en 3 phases au cours du calandrage. Au moment où le cylindre commence à comprimer l'électrode, la porosité va diminuer jusqu'à atteindre sa valeur minimale lorsque le cylindre est directement au-dessus de la zone d'étude. Ensuite la porosité va réaugmenter légèrement dû au retour élastique pour atteindre sa valeur finale. La valeur finale de porosité est dépendante de la réduction d'épaisseur imposée et une fonction a été proposée pour prédire la porosité à partir de la réduction d'épaisseur. Cependant la porosité n'a pas montré de dépendance à la vitesse de calandrage. L'épaisseur finale de l'électrode est elle linéairement dépendante de la réduction d'épaisseur, avec un retour élastique constant, mais ne dépend pas non plus de la vitesse de calandrage. Toutefois, l'élongation des électrodes est elle dépendante de la vitesse de calandrage, avec un allongement plus important pour de vitesses plus faibles, ce qui est aussi observé expérimentalement. Comme le cylindre passe plus de temps à comprimer l'électrode, les particules peuvent mieux se réarranger afin d'atteindre une configuration plus stable. Cela s'observe aussi dans l'orientation des contacts entre les particules, qui sont plus planes lorsque la compression est plus importante et la vitesse de calandrage plus faible. Le nombre de contacts attractifs reste cependant le même quelles que soient la compression ou la vitesse de calandrage utilisées, retranscrivant ainsi le comportement observé dans l'étude de compaction isotrope.

Les conductivités électriques et ioniques équivalentes des microstructures d'électrodes ainsi obtenues numériquement ont été calculées. Les microstructures ont d'abord dû être voxélisées et chacun de leurs voxels s'est vu attribué un matériau – matériau actif, CBD ou électrolyte – possédant chacun ses propres valeurs de conductivités. Les conductivités équivalentes ont été obtenues au moyen de la méthode de Transformée de Fourier Rapide (FFT). La conductivité électrique augmente la compression tandis que la conductivité ionique diminue, et toutes deux sont indépendantes de la vitesse de calandrage. Nous avons alors mis en perspectives les valeurs de conductivités obtenues ici avec les paramètres microstructuraux des électrodes calandrées numériquement afin de déterminer lesquels sont les plus influents. Il a été obsevée que la conductivité électrique était dépendante de la densité de l'électrode et du nombre de coordination, tandis que la conductivité ionique dépendait seulement de la porosité.

Conclusions et perspectives

Au cours de cette thèse, nous avons développé un modèle permettant de simuler numériquement le calandrage des électrodes Li-ion de manière réaliste. Les études préliminaires ont permis d'identifier les paramètres influents sur la microstructure cohésive des électrodes sous différentes sollicitations. Une nouvelle loi de contact prenant en compte les différents composants des électrodes a été développé et appliquée à la simulation du calandrage des électrodes Li-ion. Le modèle de calandrage introduit directement le cylindre afin d'être plus représentatif du procédé réel. Les résultats ont permis d'identifer quels étaient les principaux paramètres influençant les propriétés microstructurelles et électroniques des électrodes. Toutefois, quelques améliorations peuvent encore être apportées, notamment en ce qui concerne la représentation et la prise en compte de la matrice de liant-additifs dans les simulations.

Bibliography

[1] A. Adolfsson and C. Nyström. Tablet strength, porosity, elasticity and solid state structure of tablets compressed at high loads. *International Journal of Pharmaceutics*, 132(1):95–106, 1996. [Cited in page 41]

[2] M. P. Allen and D. J. Tildesley. *Computer Simulation of Liquids*. Oxford University Press, Nov. 2017. [Cited in page 44]

[3] R. Amin and Y.-M. Chiang. Characterization of electronic and ionic transport in $Li_{1-x}Ni_{0.33}Mn_{0.33}Co_{0.33}O_2$ (NMC-333) and $Li_{1-x}Ni_{0.5}Mn_{0.2}Co_{0.3}O_2$ (NMC523) as a function of li content. *Journal of The Electrochemical Society*, 163(8):A1512, May 2016. [Cited in page 109]

[4] E. Andò, S. A. Hall, G. Viggiani, J. Desrues, and P. Bésuelle. Experimental micromechanics: Grain-scale observation of sand deformation. *Géotechnique Letters*, 2:107–112, 2012. [Cited in page 41]

[5] B. Andreotti, Y. Forterre, and O. Pouliquen. *Granular Media: Between Fluid and Solid*. Cambridge University Press, 2013. [Cited in page 41]

[6] M. Armand and J.-M. Tarascon. Building better batteries. *Nature*, 451(7179):652–657, 2008. [Cited in page 3]

[7] M. Armand and P. Touzain. Graphite intercalation compounds as cathode materials. *Materials Science and Engineering*, 31:319–329, 1977. [Cited in page 7]

[8] E. Azéma, F. Radjai, and G. Saussine. Quasistatic rheology, force transmission and fabric properties of a packing of irregular polyhedral particles. *Mechanics of Materials*, 41(6):729–741, 2009. [Cited in page 81]

[9] S. K. Babu, A. I. Mohamed, J. F. Whitacre, and S. Litster. Multiple imaging mode X-ray computed tomography for distinguishing active and inactive phases in lithium-ion battery cathodes. *Journal of Power Sources*, 283:314–319, 2015. [Cited in page 16]

[10] E. Barsoukov, B. E. Conway, W. G. Pell, and N. Wagner. 4.5.1.3 - Expressing Electrochemical Model Parameters in Electrical Terms, Limiting Resistances, and Capacitances of Distributed Elements: Theory, Experiment, and Applications. In *Impedance Spectrocopy*, pages 376–379. Wiley, 3eme edition, 2018. [Cited in pages 14 and 15]

[11] V. Becker, O. Birkholz, Y. Gan, and M. Kamlah. Modeling the Influence of Particle Shape on Mechanical Compression and Effective Transport Properties in Granular Lithium-Ion Battery Electrodes. *Energy Technology*, 9(6):2000886, 2021. [Cited in page 32]

[12] R. P. Behringer, K. E. Daniels, T. S. Majmudar, and M. Sperl. Fluctuations, correlations and transitions in granular materials: Statistical mechanics for a non-conventional system. *Philos Transact A Math Phys Eng Sci*, 2007. [Cited in page 60]

[13] N. Berger, E. Azéma, J.-F. Douce, and F. Radjai. Scaling behaviour of cohesive granular flows. *EPL (Europhysics Letters)*, 112(6):64004, 2015. [Cited in page 51]

[14] T. Beuse, M. Fingerle, C. Wagner, M. Winter, and M. Börner. Comprehensive Insights into the Porosity of Lithium-Ion Battery Electrodes: A Comparative Study on Positive Electrodes Based on $LiNi_{0.6}Mn_{0.2}Co_{0.2}O_2$ (NMC622). *Batteries*, 7(4), 2021. [Cited in page 15]

[15] J. C. Bonaldo, S. Mazerat, S. Romero-Baivier, and C. L. Martin. Microstructure-based discrete simulations of the compaction of refractory powder composites. *Powder Technology*, 407:117577, 2022. [Cited in page 91]

[16] N. V. Brilliantov, N. Albers, F. Spahn, and T. Pöschel. Collision dynamics of granular particles with adhesion. *Phys Rev E Stat Nonlin Soft Matter Phys*, 76(5 Pt 1):051302, 2007. [Cited in page 46]

[17] N. V. Brilliantov, F. Spahn, J.-M. Hertzsch, and T. Pöschel. Model for collisions in granular gases. *Phys. Rev. E*, 53(5):5382–5392, 1996. [Cited in page 30]

[18] L. J. Budinski-Petkovi and S. B. Vrhovac. Memory effects in vibrated granular systems: Response properties in the generalized random sequential adsorption model. *Eur Phys J E Soft Matter*, 16(1):89–96, 2005. [Cited in page 41]

[19] J. B. Burland. On the compressibility and shear strength of natural clays. *Géotechnique*, 40(3):329–378, 1990. [Cited in page 47]

[20] V. Busignies, B. Leclerc, P. Porion, P. Evesque, G. Couarraze, and P. Tchoreloff. Quantitative measurements of localized density variations in cylindrical tablets using X-ray microtomography. *European journal of pharmaceutics and biopharmaceutics : official journal of Arbeitsgemeinschaft fur Pharmazeutische Verfahrenstechnik e.V*, 64(1):38–50, Aug. 2006. [Cited in page 41]

[21] R. Cabiscol, H. Shi, I. Wünsch, V. Magnanimo, J. H. Finke, S. Luding, and A. Kwade. Effect of particle size on powder compaction and tablet strength using limestone. *Advanced Powder Technology*, 31(3):1280–1289, 2020. [Cited in page 41]

[22] T. Calvet, J.-M. Vanson, and R. Masson. A DEM/FFT approach to simulate the effective thermal conductivity of granular media. *International Journal of Thermal Sciences*, 172:107339, 2022. [Cited in pages 35, 36 and 97]

[23] D. Cantor Garcìa. *Compaction Des Milieux Granulaires Fragmentables En 3D*. PhD thesis, Université de Montpellier, 2017. [Cited in page 22]

[24] A. Castellanos. The relationship between attractive interparticle forces and bulk behaviour in dry and uncharged fine powders. *Advances in Physics*, 54(4):263–376, 2005. [Cited in pages 47 and 51]

[25] H. Chen, M. Ling, L. Hencz, H. Y. Ling, G. Li, Z. Lin, G. Liu, and S. Zhang. Exploring Chemical, Mechanical, and Electrical Functionalities of Binders for Advanced Energy-Storage Devices. *Chemical Reviews*, 118(18):8936–8982, 2018. [Cited in page 9]

[26] Y. Chen, M. B. Jaksa, B. T. Scott, and Y.-L. Kuo. Numerical investigation of the performance of the 3-sided impact roller. *Computers and Geotechnics*, 157:105331, 2023. [Cited in page 90]

[27] E. J. Cheng, K. Hong, N. J. Taylor, H. Choe, J. Wolfenstine, and J. Sakamoto. Mechanical and physical properties of $LiNi_{0.33}Mn_{0.33}Co_{0.33}O_2$ (NMC). *Journal of the European Ceramic Society*, 37(9):3213–3217, 2017. [Cited in page 7]

[28] J. W. Choi and D. Aurbach. Promise and reality of post-lithium-ion batteries with high energy densities. *Nature Reviews Materials*, 1(16013):1–16, 2016. [Cited in pages 5 and 12]

[29] J.-F. Colin, V. Godbole, and P. Novák. In situ neutron diffraction study of Li insertion in $Li_4Ti_5O_{12}$. *Electrochemistry Communications*, 12(6):804–807, 2010. [Cited in page 8]

[30] P. A. Cundall and O. D. L. Strack. A discrete numerical model for granular assemblies. *Géotechnique*, 29(1):47–65, 1979. [Cited in pages 18, 42 and 89]

[31] P. N. Davies, H. E. C. Worthington, F. Podczeck, and J. M. Newton. The determination of the mechanical strength of tablets of different shapes. *European Journal of Pharmaceutics and Biopharmaceutics*, 67(1):268–276, 2007. [Cited in page 41]

[32] L. S. de Vasconcelos, R. Xu, J. Li, and K. Zhao. Grid indentation analysis of mechanical properties of composite electrodes in Li-ion batteries. *Extreme Mechanics Letters*, 9:495–502, 2016. [Cited in pages 16 and 26]

[33] B. Derjaguin, V. Muller, and Y. Toporov. Effect of contact deformations on the adhesion of particles. *Journal of Colloid and Interface Science*, 53(2):314–326, 1975. [Cited in page 93]

[34] A. Djemai and I. C. Sinka. NMR imaging of density distributions in tablets. *International journal of pharmaceutics*, 319(1-2):55–62, Aug. 2006. [Cited in pages 41 and 43]

[35] D. Doughty and P. Roth. A General Discussion of Li-Ion Battery Safety. *Electrochemical Society Interface*, 21(37), 2012. [Cited in page 7]

[36] F. Dubois, V. Acary, and M. Jean. The Contact Dynamics method: A nonsmooth story. *Comptes Rendus Mécanique*, 346(3):247–262, 2018. [Cited in page 19]

[37] B. Dunn, H. Kamath, and J.-M. Tarascon. Electrical Energy Storage for the Grid: A Battery of Choices. *Science*, 334(6058):928–935, 2011. [Cited in pages 3 and 4]

[38] M. Duquesnoy, I. Boyano, L. Ganborena, P. Cereijo, E. Ayerbe, and A. A. Franco. Machine learning-based assessment of the impact of the manufacturing process on battery electrode heterogeneity. *Energy and AI*, 5:100090, 2021. [Cited in page 32]

[39] M. Duquesnoy, C. Liu, D. Z. Dominguez, V. Kumar, E. Ayerbe, and A. A. Franco. Machine learning-assisted multi-objective optimization of battery manufacturing from synthetic data generated by physics-based simulations. *Energy Storage Materials*, 56:50–61, 2023. [Cited in page 89]

[40] M. Duquesnoy, T. Lombardo, M. Chouchane, E. N. Primo, and A. A. Franco. Data-driven assessment of electrode calendering process by combining experimental results, in silico mesostructures generation and machine learning. *Journal of Power Sources*, 480:229103, 2020. [Cited in pages 17, 24 and 32]

[41] F. Fazelpour and K. E. Daniels. Controlling rheology via boundary conditions in dense granular flows. *Soft Matter*, 19(12):2168–2175, 2023. [Cited in page 60]

[42] F. Fichtner, A. Rasmuson, and G. Alderborn. Particle size distribution and evolution in tablet structure during and after compaction. *International journal of pharmaceutics*, 292(1-2):211–25, Mar. 2005. [Cited in page 42]

[43] M. M. Forouzan, C.-W. Chao, D. Bustamante, B. A. Mazzeo, and D. R. Wheeler. Experiment and simulation of the fabrication process of lithium-ion battery cathodes for determining microstructure and mechanical properties. *Journal of Power Sources*, 312:172–183, 2016. [Cited in page 27]

[44] G. Frenning. Analysis of pharmaceutical powder compaction using multiplicative hyperelasto-plastic theory. *Powder Technology*, 172(2):103–112, 2007. [Cited in page 41]

[45] L. Froboese, P. Titscher, B. Westphal, W. Haselrieder, and A. Kwade. Mercury intrusion for ion- and conversion-based battery electrodes – Structure and diffusion coefficient determination. *Materials Characterization*, 133:102–111, 2017. [Cited in pages 15 and 35]

[46] E. Garzón, P. J. Sánchez-Soto, and E. Romero. Physical and geotechnical properties of clay phyllites. *Applied Clay Science*, 48(3):307–318, 2010. [Cited in page 42]

[47] R. Ge, A. M. Boyce, Y. S. Zhang, P. R. Shearing, D. J. Cumming, and R. M. Smith. Discrete element method and electrochemical modelling of lithium ion cathode structures characterised by X-ray computed tomography. *Chemical Engineering Journal*, 465:142749, 2023. [Cited in pages 90 and 110]

[48] R. Ge, D. J. Cumming, and R. M. Smith. Discrete element method (DEM) analysis of lithium ion battery electrode structures from X-ray tomography-the effect of calendering conditions. *Powder Technology*, 403:117366, 2022. [Cited in pages 90 and 107]

[49] F. A. Gilabert, J.-N. Roux, and A. Castellanos. Computer simulation of model cohesive powders: Influence of assembling procedure and contact laws on low consolidation states. *Phys. Rev. E*, 75(1):011303, 2007. [Cited in pages 41, 42, 56 and 69]

[50] F. A. Gilabert, J.-N. Roux, and A. Castellanos. Computer simulation of model cohesive powders: Plastic consolidation, structural changes, and elasticity under isotropic loads. *Phys. Rev. E*, 78(3):031305, 2008. [Cited in pages 42, 50 and 51]

[51] C. S. Giménez, B. Finke, C. Nowak, C. Schilde, and A. Kwade. Structural and mechanical characterization of lithium-ion battery electrodes via DEM simulations. *Advanced Powder Technology*, 29(10):2312–2321, 2018. [Cited in pages 24, 28, 29 and 90]

[52] C. S. Giménez, B. Finke, C. Schilde, L. Froböse, and A. Kwade. Numerical simulation of the behavior of lithium-ion battery electrodes during the calendaring process via the discrete element method. *Powder Technology*, 349:1–11, 2019. [Cited in pages 13, 18, 24, 26, 27, 30, 31, 32, 73, 89, 90 and 91]

[53] J. B. Goodenough and K.-S. Park. The Li-Ion Rechargeable Battery: A Perspective. *Journal of the American Chemical Society*, 135(4):1167–1176, 2013. [Cited in page 6]

[54] P. Gudmundson and P.-L. Larsson. An analytic model for effective mechanical properties and local contact stresses in lithium-ion porous electrodes. *Extreme Mechanics Letters*, 42:101067, 2021. [Cited in page 27]

[55] B. T. Habte and F. Jiang. Microstructure reconstruction and impedance spectroscopy study of LiCoO2, LiMn2O4 and LiFePO4 Li-ion battery cathodes. *Microporous and Mesoporous Materials*, 268:69–76, 2018. [Cited in page 15]

[56] W. Haselrieder, S. Ivanov, D. K. Christen, H. Bockholt, and A. Kwade. Impact of the Calendering Process on the Interfacial Structure and the Related Electrochemical Performance of Secondary Lithium-Ion Batteries. *ECS Transactions*, 50(26):59–70, Apr. 2013. [Cited in pages 10, 11 and 16]

[57] H. C. Hesse, M. Schimpe, D. Kucevic, and A. Jossen. Lithium-Ion Battery Storage for the Grid—A Review of Stationary Battery Storage System Design Tailored for Applications in Modern Power Grids. *Energies*, 10(12), 2017. [Cited in page 14]

[58] H. M. Jaeger, S. R. Nagel, and R. P. Behringer. The physics of granular materials. *Physics Today*, 49(4):32–38, 1996. [Cited in page 41]

[59] J. C. Jaeger, N. G. W. Cook, and R. Zimmerman. *Fundamentals of Rock Mechanics*. Wiley, 2007. [Cited in page 41]

[60] M. Jean and J. J. Moreau. Dynamics in the presence of unilateral contacts and dry friction : A numerical approach. In *Second Meeting on Unilateral Problems in Structural Analysis*, Proceedings of the Second Meeting on Unilateral Problems in Structural Analysis, pages 151–196, Prescudin, Italy, 1985. Springer. [Cited in page 18]

[61] L. Jing and O. Stephansson. *Fundamentals of Discrete Element Methods for Rock Engineering*. Elsevier, 1ère edition, 2007. [Cited in page 18]

[62] K. L. Johnson, K. Kendall, and A. D. Roberts. Surface energy and the contact of elastic solids. *Proceedings of the Royal Society A*, 324(1558):301–313, 1971. [Cited in pages 28 and 45]

[63] M. S. Kadiri, A. Michrafy, and J. A. Dodds. Pharmaceutical powders compaction: Experimental and numerical analysis of the density distribution. *Powder Technology*, 157(1):176–182, 2005. [Cited in pages 41 and 42]

[64] H. Kang, C. Lim, T. Li, Y. Fu, B. Yan, N. Houston, V. D. Andrade, F. D. Carlo, and L. Zhu. Geometric and Electrochemical Characteristics of $Li(Ni_{1/3}Mn_{1/3}Co_{1/3})O_2$ Electrode with Different Calendering Conditions. *Electrochimica Acta*, 232:431–438, 2017. [Cited in pages 3, 12, 41 and 89]

[65] N. A. Kaskhedikar and J. Maier. Lithium Storage in Carbon Nanostructures. *Advanced Materials*, 21(25-26):2664–2680, 2009. [Cited in page 7]

[66] O. Keles, N. P. Barcenas, D. H. Sprys, and K. J. Bowman. Effect of Porosity on Strength Distribution of Microcrystalline Cellulose. *AAPS PharmSciTech*, 16(6):1455–1464, 2015. [Cited in page 41]

[67] M. Kespe and H. Nirschl. Numerical simulation of lithium-ion battery performance considering electrode microstructure. *International Journal of Energy Research*, 39(15):2062–2074, 2015. [Cited in page 34]

[68] J. B. Knight, C. G. Fandrich, C. N. Lau, H. M. Jaeger, and S. R. Nagel. Density relaxation in a vibrated granular material. *Phys. Rev. E*, 51(5):3957–3962, 1995. [Cited in page 41]

[69] T. Kobayashi, T. Tanaka, N. Shimada, and T. Kawaguchi. DEM–CFD analysis of fluidization behavior of Geldart Group A particles using a dynamic adhesion force model. *Powder Technology*, 248:143–152, 2013. [Cited in pages 43 and 55]

[70] Q. Ku, J. Zhao, G. Mollon, and S. Zhao. Compaction of highly deformable cohesive granular powders. *Powder Technology*, 421:118455, 2023. [Cited in page 42]

[71] A. Kwade, W. Haselrieder, R. Leithoff, A. Modlinger, F. Dietrich, and K. Droeder. Current status and challenges for automotive battery production technologies. *Nature Energy*, 3(4):290–300, 2018. [Cited in pages 13 and 33]

[72] N. H. Kwon. The effect of carbon morphology on the LiCoO2 cathode of lithium ion batteries. *Solid State Sciences*, 21:59–65, 2013. [Cited in page 9]

[73] J. Landesfeind, A. Eldiven, and H. A. Gasteiger. Influence of the Binder on Lithium Ion Battery Electrode Tortuosity and Performance. *Journal of The Electrochemical Society*, 165(5):A1122–A1128, 2018. [Cited in pages 8, 9 and 15]

[74] H. Laubie, F. Radjaï, R. Pellenq, and F.-J. Ulm. A potential-of-mean-force approach for fracture mechanics of heterogeneous materials using the lattice element method. *Journal of the Mechanics and Physics of Solids*, 105:116–130, 2017. [Cited in page 54]

[75] V. Laue, F. Röder, and U. Krewer. Joint structural and electrochemical modeling: Impact of porosity on lithium-ion battery performance. *Electrochimica Acta*, 314:20–31, 2019. [Cited in page 12]

[76] J. Lennard-Jones. On the determination of molecular fields. —II. From the equation of state of a gas. *Proceedings of the Royal Society A*, 106(738):463–477, 1924. [Cited in page 28]

[77] G. Lenze, F. Röder, H. Bockholt, W. Haselrieder, A. Kwade, and U. Krewer. Simulation-Supported Analysis of Calendering Impacts on the Performance of Lithium-Ion-Batteries.

Journal of The Electrochemical Society, 164(6):A1223–A1233, 2017. [Cited in pages 11 and 17]

[78] G. Lian, M. J. Adams, and C. Thornton. Elastohydrodynamic collisions of solid spheres. *J. Fluid Mech.*, 311:141, 1996. [Cited in page 68]

[79] G. Liu, H. Zheng, X. Song, and V. S. Battaglia. Particles and Polymer Binder Interaction: A Controlling Factor in Lithium-Ion Electrode Performance. *Journal of The Electrochemical Society*, 159(3):A214–A221, 2012. [Cited in page 9]

[80] H. Liu, Y. Feng, K. Wang, and J. Xie. Synthesis and electrochemical properties of Li4Ti5O12/C composite by the PVB rheological phase method. *Journal of Physics and Chemistry of Solids*, 69(8):2037–2040, 2008. [Cited in page 8]

[81] K. Liu, Z. Wang, L. Shi, S. Jungsuttiwong, and S. Yuan. Ionic liquids for high performance lithium metal batteries. *Journal of Energy Chemistry*, 59:320–333, 2021. [Cited in pages 3, 13, 33 and 41]

[82] Y. Liu, R. Zhang, J. Wang, and Y. Wang. Current and future lithium-ion battery manufacturing. *iScience*, 24(4):102332, 2021. [Cited in pages 41 and 42]

[83] T. Lombardo, F. Caro, A. C. Ngandjong, J.-B. Hoock, M. Duquesnoy, J. C. Delepine, A. Ponchelet, S. Doison, and A. A. Franco. The ARTISTIC Online Calculator: Exploring the Impact of Lithium-Ion Battery Electrode Manufacturing Parameters Interactively Through Your Browser. *Batteries & Supercaps*, 5(3):e202100324, 2022. [Cited in pages 32 and 33]

[84] T. Lombardo, A. C. Ngandjong, A. Belhcen, and A. A. Franco. Carbon-Binder Migration: A Three-Dimensional Drying Model for Lithium-ion Battery Electrodes. *Energy Storage Materials*, 43:337–347, 2021. [Cited in pages 32 and 89]

[85] W. Lu, C. M. López, N. Liu, J. T. Vaughey, A. Jansen, and D. D. W. Overcharge Effect on Morphology and Structure of Carbon Electrodes for Lithium-Ion Batteries. *Journal of The Electrochemical Society*, 159(5):A566–A570, 2012. [Cited in page 7]

[86] X. Lu, S. R. Daemi, A. Bertei, M. D. R. Kok, K. B. O'Regan, L. Rasha, J. Park, G. Hinds, E. Kendrick, D. J. L. Brett, and P. R. Shearing. Microstructural Evolution of Battery Electrodes During Calendering. *Joule*, 4(12):2746–2768, 2020. [Cited in pages 3, 12, 13, 14 and 89]

[87] S. Luding. Shear flow modeling of cohesive and frictional fine powder. *Powder Technology*, 158(1):45–50, 2005. [Cited in page 29]

[88] S. Luding. Cohesive, frictional powders: Contact models for tension. *Granular Matter*, 10(4):235–246, 2008. [Cited in page 29]

[89] A. Lundkvist, P.-L. Larsson, and E. Olsson. A discrete element analysis of the mechanical behaviour of a lithium-ion battery electrode active layer. *Powder Technology*, 425:118574, 2023. [Cited in page 90]

[90] H. Luo, J. Zhu, E. Sahraei, and Y. Xia. Adhesion strength of the cathode in lithium-ion batteries under combined tension/shear loadings. *RSC Advances*, 8(8):3996–4005, 2018. [Cited in page 17]

[91] A. Magasinski, B. Zdyrko, I. Kovalenko, B. Hertzberg, R. Burtovyy, C. F. Huebner, T. F. Fuller, I. Luzinov, and G. Yushin. Toward Efficient Binders for Li-Ion Battery Si-Based Anodes: Polyacrylic Acid. *ACS Applied Materials & Interfaces*, 2(11):3004–3010, 2010. [Cited in page 8]

[92] T. S. Majmudar and R. P. Behringer. Contact force measurements and stress-induced anisotropy in granular materials. *Nature*, 435(7045):1079–1082, June 2005. [Cited in page 60]

[93] S. Mandal, M. Nicolas, and O. Pouliquen. Insights into the rheology of cohesive granular media. *Proceedings of the National Academy of Sciences*, 117(15):8366–8373, 2020. [Cited in pages 43, 59 and 117]

[94] S. Mandal, M. Nicolas, and O. Pouliquen. Rheology of Cohesive Granular Media: Shear Banding, Hysteresis, and Nonlocal Effects. *Phys. Rev. X*, 11(2):021017, Apr. 2021. [Cited in pages 43, 59 and 117]

[95] M. Marcinek, J. Syzdek, M. Marczewski, M. Piszcz, L. Niedzicki, M. Kalita, A. Plewa-Marczewska, A. Bitner, P. Wieczorek, T. Trzeciak, M. Kasprzyk, P.Lezak, Z. Zukowska, A. Zalewska, and W. Wieczorek. Electrolytes for Li-ion transport – Review. *Solid State Ionics*, 276:107–126, 2015. [Cited in pages 10 and 109]

[96] L. Mauler, F. Duffner, and J. Leker. Economies of scale in battery cell manufacturing: The impact of material and process innovations. *Applied Energy*, 286:116499, 2021. [Cited in page 4]

[97] D. Mayer, A.-K. Wurba, B. Bold, J. Bernecker, A. Smith, and J. Fleischer. Investigation of the Mechanical Behavior of Electrodes after Calendering and Its Influence on Singulation and Cell Performance. *Processes*, 9(11), 2021. [Cited in pages 15, 73 and 90]

[98] J. K. Mayer, L. Almar, E. Asylbekov, W. Haselrieder, A. Kwade, A. Weber, and H. Nirschl. Influence of the Carbon Black Dispersing Process on the Microstructure and Performance of Li-Ion Battery Cathodes. *Energy Technology*, 8(2):1900161, 2020. [Cited in page 28]

[99] A. Mazor, L. Orefice, A. Michrafy, A. de Ryck, and J. G. Khinast. A combined DEM & FEM approach for modelling roll compaction process. *Powder Technology*, 337:3–16, 2018. [Cited in pages 17, 18 and 41]

[100] R. Mesnage and M. N. Antoniou. Ignoring Adjuvant Toxicity Falsifies the Safety Profile of Commercial Pesticides. *Frontiers in Public Health*, 5:361, 2018. [Cited in page 8]

[101] C. Meyer, M. Kosfeld, W. Haselrieder, and A. Kwade. Process modeling of the electrode calendering of lithium-ion batteries regarding variation of cathode active materials and mass loadings. *Journal of Energy Storage*, 18:371–379, 2018. [Cited in page 12]

[102] R. D. Mindlin and H. Deresiewicz. Elastic Spheres in Contact Under Varying Oblique Forces. *Journal of Applied Mechanics*, 20(3):327–344, 1953. [Cited in page 25]

[103] J. Mitchell and K. Soga. *Fundamentals of Soil Behavior*. Wiley, 3 edition, 2005. [Cited in pages 41 and 47]

[104] K. Mizushima, P. C. Jones, P. J. Wiseman, and J. B. Goodenough. LixCoO2 (0. *Materials Research Bulletin*, 15(6):783–789, 1980. [Cited in pages 6 and 89]

[105] H. Mohammed, B. J. Briscoe, and K. G. Pitt. The intrinsic nature and the coherence of compacted pure pharmaceutical tablets. *Powder Technology*, 165(1):11–21, 2006. [Cited in page 42]

[106] J. J. Moreau. New computation methods in granular dynamics. In C. Thornton, editor, *Powders & Grains 93*, Proceedings of the Second International Conference on Micromechanics of Granular Media, pages 227–232, Birmingham, United Kingdom, 1993. A.A.Balkema. [Cited in page 18]

[107] J. J. Moreau. Some numerical methods in multibody dynamics: Application to granular materials. *European Journal of Mechanics - A/Solids*, 13(4 - suppl):93–114, 1994. [Cited in page 18]

[108] S. L. Morelly, J. Gelb, F. Iacoviello, P. R. Shearing, S. J. Harris, N. J. Alvarez, and M. H. Tang. Three-Dimensional Visualization of Conductive Domains in Battery Electrodes with Contrast-Enhancing Nanoparticles. *ACS Applied Energy Materials*, 1(9):4479–4484, 2018. [Cited in page 16]

[109] R. Moreno-Atanasio, S. J. Antony, and M. Ghadiri. Analysis of flowability of cohesive powders using Distinct Element Method. *Powder Technology*, 158(1):51–57, 2005. [Cited in page 45]

[110] R. Moreno-Atanasio, B. H. Xu, and M. Ghadiri. Computer simulation of the effect of contact stiffness and adhesion on the fluidization behaviour of powders. *Chemical Engineering Science*, 62(1):184–194, 2007. [Cited in pages 43 and 45]

[111] J. P. Morrissey. *Discrete Element Modelling of Iron Ore Pellets to Include the Effects of Moisture and Fines*. PhD thesis, University of Edinburgh, 2013. [Cited in page 30]

[112] H. Moulinec and P. Suquet. A numerical method for computing the overall response of nonlinear composites with complex microstructure. *Computer methods in applied mechanics and engineering*, 157(1-2):69–94, 1998. [Cited in pages 35, 36 and 95]

[113] A. Mukhopadhyay and B. W. Sheldon. Deformation and stress in electrode materials for Li-ion batteries. *Progress in Materials Science*, 63:58–116, 2014. [Cited in page 8]

[114] G. W. Nam, N.-Y. Park, K.-J. Park, J. Yang, J. Liu, C. S. Yoon, and Y.-K. Sun. Capacity Fading of Ni-Rich NCA Cathodes: Effect of Microcracking Extent. *ACS Energy Letters*, 4(12):2995–3001, 2019. [Cited in page 7]

[115] K. S. Nanjundaswamy, A. K. Padhi, J. B. Goodenough, S. Okada, H. Ohtsuka, H. Arai, and J. Yamaki. Synthesis, redox potential evaluation and electrochemical characteristics of NASICON-related-3D framework compounds. *Solid State Ionics*, 92(1):1–10, 1996. [Cited in page 7]

[116] S. Nezamabadi, F. Radjai, J. Averseng, and J.-Y. Delenne. Implicit frictional-contact model for soft particle systems. *Journal of the Mechanics and Physics of Solids*, 83:72–87, 2015. [Cited in pages 42 and 117]

[117] A. C. Ngandjong, T. Lombardo, E. N. Primo, M. Chouchane, A. Shodiev, O. Arcelus, and A. A. Franco. Investigating electrode calendering and its impact on electrochemical performance by means of a new discrete element method model: Towards a digital twin of Li-Ion battery manufacturing. *Journal of Power Sources*, 485:229320, 2021. [Cited in pages 13, 24, 28, 30, 31, 32, 33, 73 and 89]

[118] M. Nikpour, N. Barrett, Z. Hillman, A. Thompson, B. A. Mazzeo, and D. Wheeler. A Model for Investigating Sources of Li-Ion Battery Electrode Heterogeneity: Part I. Electrode Drying and Calendering Processes. *Journal of The Electrochemical Society*, June 2021. [Cited in pages 24 and 27]

[119] N. Nitta, F. Wu, J. T. Lee, and G. Yushin. Li-ion battery materials: Present and future. *Materials Today*, 18(5):252–264, 2015. [Cited in pages 5, 14 and 41]

[120] I.-H. Oh, N. Nomura, N. Masahashi, and S. Hanada. Mechanical properties of porous titanium compacts prepared by powder sintering. *Scripta Materialia*, 49(12):1197–1202, 2003. [Cited in page 41]

[121] W. Oliver and G. Pharr. An improved technique for determining hardness and elastic modulus using load and displacement sensing indentation experiments. *Journal of Materials Research*, 7(6):1564–1583, 1992. [Cited in page 16]

[122] L. F. Orozco, D.-H. Nguyen, J.-Y. Delenne, P. Sornay, and F. Radjai. Discrete-element simulations of comminution in rotating drums: Effects of grinding media. *Powder Technology*, 362:157–167, 2020. [Cited in page 18]

[123] H. Ouadfel and L. Rothenburg. 'Stress–force–fabric' relationship for assemblies of ellipsoids. *Mechanics of Materials*, 33(4):201–221, 2001. [Cited in page 81]

[124] M. Pasha, S. Dogbe, C. Hare, A. Hassanpour, and M. Ghadiri. A linear model of elasto-plastic and adhesive contact deformation. *Granular Matter*, 16(1):152–162, 2014. [Cited in page 30]

[125] T. Pöschel and T. Schwager. *Computational Granular Dynamics: Models and Algorithms*. Springer, 2005. [Cited in page 42]

[126] D. O. Potyondy and P. A. Cundall. A bonded-particle model for rock. *International Journal of Rock Mechanics and Mining Sciences*, 41(8):1329–1364, 2004. [Cited in page 28]

[127] E. N. Primo, M. Chouchane, M. Touzin, P. Vazquez, and A. A. Franco. Understanding the calendering processability of $Li(Ni_{0.33}Mn_{0.33}Co_{0.33})O_2$-Based Cathodes. *Journal of Power Sources*, 488:229361, 2021. [Cited in pages 13, 32 and 33]

[128] E. N. Primo, M. Touzin, and A. A. Franco. Calendering of $Li(Ni_{0.33}Mn_{0.33}Co_{0.33})O_2$-Based Cathodes: Analyzing the Link Between Process Parameters and Electrode Properties by Advanced Statistics. *Batteries & Supercaps*, 4(5):834–844, 2021. [Cited in pages 13, 32, 33, 41 and 42]

[129] J. Puértolas, J. García-García, F. Pascual, J. González-Domínguez, M. Martínez, and A. Ansón-Casaos. Dielectric behavior and electrical conductivity of PVDF filled with functionalized single-walled carbon nanotubes. *Composites Science and Technology*, 152:263–274, 2017. [Cited in page 109]

[130] J. C. Quezada, P. Breul, G. Saussine, and F. Radjai. Stability, deformation, and variability of granular fills composed of polyhedral particles. *PRE*, 86(3):031308, Sept. 2012. [Cited in page 41]

[131] M. A. Quintanilla, A. Castellanos, and J. M. Valverde. Correlation between bulk stresses and interparticle contact forces in fine powders. *Phys Rev E Stat Nonlin Soft Matter Phys*, 64(3 Pt 1):031301, Sept. 2001. [Cited in page 42]

[132] F. Radjai and E. Azéma. Shear strength of granular materials. *European Journal of Environmental and Civil Engineering*, 13(2):203–218, 2009. [Cited in pages 76 and 82]

[133] F. Radjai and F. Dubois. *Modélisation Numérique Discrète Des Matériaux Granulaires*. ISTE, 2010. [Cited in pages 18, 19, 21, 25, 26, 28 and 73]

[134] F. Radjai and F. Dubois. *Discrete-Element Modeling of Granular Materials*. ISTE, 2011. [Cited in pages 42, 45 and 93]

[135] F. Radjaï, I. Preechawuttipong, and R. Peyroux. Cohesive granular texture. In P. A. Vermeer, H. J. Herrmann, S. Luding, W. Ehlers, S. Diebels, and E. Ramm, editors, *Continuous and Discontinuous Modelling of Cohesive-Frictional Materials*, pages 149–162. Springer Berlin Heidelberg, Berlin, Heidelberg, 2001. [Cited in pages 45, 60 and 93]

[136] L. Reig, C. Tojal, D. J. Busquets, and V. Amigó. Microstructure and Mechanical Behavior of Porous Ti–6Al–4V Processed by Spherical Powder Sintering. *Materials*, 6(10):4868–4878, 2013. [Cited in page 41]

[137] V. Richefeu, M. S. El Youssoufi, E. Azéma, and F. Radjaï. Force transmission in dry and wet granular media. *Powder Technology*, 190(1):258–263, 2009. [Cited in pages 63 and 66]

[138] V. Richefeu, M. S. El Youssoufi, R. Peyroux, and F. Radjaï. A model of capillary cohesion for numerical simulations of 3D polydisperse granular media. *International Journal for Numerical and Analytical Methods in Geomechanics*, 32(11):1365–1383, 2008. [Cited in page 68]

[139] V. Richefeu, F. Radjaï, and M. S. El Youssoufi. Stress transmission in wet granular materials. *The European Physical Journal E*, 21(4):359–369, 2006. [Cited in page 60]

[140] V. Richefeu and P. Villard. *Modeling Gravity Hazards from Rockfalls to Landslides*. Elsevier, 2016. [Cited in page 44]

[141] C. J. Ridgway, K. Ridgway, and G. P. Matthews. Modelling of the Void Space of Tablets Compacted Over a Range of Pressures. *J Pharm Pharmacol*, 49(4):377–383, Apr. 1997. [Cited in page 42]

[142] P. G. Rognon, J.-N. Roux, M. Naaïm, and F. Chevoir. Dense flows of cohesive granular materials. *Journal of Fluid Mechanics*, 596:21–47, 2008. [Cited in page 42]

[143] P. G. Rognon, J.-N. Roux, D. Wolf, M. Naaïm, and F. Chevoir. Rheophysics of cohesive granular materials. *Europhysics Letters (EPL)*, 74(4):644–650, 2006. [Cited in pages 41 and 51]

[144] L. Rothenburg and R. J. Bathurst. Analytical study of induced anisotropy in idealized granular materials. *Géotechnique*, 39(4):601–614, 1989. [Cited in page 81]

[145] N. Roy, J. D. Frost, and G. Viggiani. Pore space evolution of granular assemblies under shear: An experimental study using X-ray tomography. *Granular Matter*, 24(2):63, 2022. [Cited in page 41]

[146] P. Roy and S. K. Srivastava. Nanostructured anode materials for lithium ion batteries. *J. Mater. Chem. A*, 3(6):2454–2484, 2015. [Cited in page 7]

[147] B. Saint-Cyr, J.-Y. Delenne, C. Voivret, F. Radjai, and P. Sornay. Rheology of granular materials composed of nonconvex particles. *Phys. Rev. E*, 84(4):041302, 2011. [Cited in pages 41 and 76]

[148] B. Saint-Cyr, F. Radjai, J.-Y. Delenne, and P. Sornay. Cohesive granular materials composed of nonconvex particles. *Phys. Rev. E*, 87(5):052207, 2013. [Cited in page 41]

[149] C. Sangrós, C. Schilde, and A. Kwade. Effect of Microstructure on Thermal Conduction within Lithium-Ion Battery Electrodes using Discrete Element Method Simulations. *Energy Technology*, 4(12):1611–1619, 2016. [Cited in pages 18 and 34]

[150] C. Sangrós Giménez, L. Helmers, C. Schilde, A. Diener, and A. Kwade. Modeling the Electrical Conductive Paths within All-Solid-State Battery Electrodes. *Chemical Engineering & Technology*, 43(5):819–829, 2020. [Cited in pages 89 and 90]

[151] C. Sangrós Giménez, C. Schilde, L. Froböse, S. Ivanov, and A. Kwade. Mechanical, Electrical, and Ionic Behavior of Lithium-Ion Battery Electrodes via Discrete Element Method Simulations. *Energy Technology*, 8(2):1900180, 2020. [Cited in pages 12, 16, 25, 30, 32, 34, 35, 73, 89, 90 and 109]

[152] A. Schofield and P. Wroth. *Critical State Soil Mechanics*. McGraw-Hill Inc.,US, 1968. [Cited in pages 41 and 47]

[153] D. Schreiner, A. Klinger, and G. Reinhart. Modeling of the Calendering Process for Lithium-Ion Batteries with DEM Simulation. *Procedia CIRP*, 93:149–155, 2020. [Cited in pages 18, 24, 29, 30, 33 and 90]

[154] D. Schreiner, J. Lindenblatt, F. J. Günter, and G. Reinhart. DEM Simulations of the Calendering Process: Parameterization of the Electrode Material of Lithium-Ion Batteries. *Procedia CIRP*, 104:91–97, 2021. [Cited in pages 29, 30 and 33]

[155] D. Schreiner, M. Oguntke, T. Günther, and G. Reinhart. Modelling of the Calendering Process of NMC-622 Cathodes in Battery Production Analyzing Machine/Material–Process–Structure Correlations. *Energy Technology*, 7(11):1900840, 2019. [Cited in pages 12, 13 and 25]

[156] B. Scrosati and J. Garche. Lithium batteries: Status, prospects and future. *Journal of Power Sources*, 195(9):2419–2430, 2010. [Cited in page 3]

[157] K. M. Shaju and P. G. Bruce. Macroporous Li(Ni1/3Co1/3Mn1/3)O2: A High-Power and High-Energy Cathode for Rechargeable Lithium Batteries. *Advanced Materials*, 18(17):2330–2334, 2006. [Cited in page 7]

[158] H. Shen, H. Li, and L. C. Brinson. Effect of microstructural configurations on the mechanical responses of porous titanium: A numerical design of experiment analysis for orthopedic applications. *Mechanics of Materials*, 40(9):708–720, 2008. [Cited in page 41]

[159] A. Shodiev, E. Primo, O. Arcelus, M. Chouchane, M. Osenberg, A. Hilger, I. Manke, J. Li, and A. A. Franco. Insight on electrolyte infiltration of lithium ion battery electrodes by means of a new three-dimensional-resolved lattice Boltzmann model. *Energy Storage Materials*, 38:80–92, 2021. [Cited in pages 25 and 34]

[160] J. Smekens, R. Gopalakrishnan, N. V. den Steen, N. Omar, O. Hegazy, A. Hubin, and J. Van Mierlo. Influence of Electrode Density on the Performance of Li-Ion Batteries: Experimental and Simulation Results. *Energies*, 9(2), 2016. [Cited in pages i and 89]

[161] C. Song, P. Wang, and H. Makse. A phase diagram for jammed matter. *Nature*, 453(7195):629–632, 2008. [Cited in pages 32 and 48]

[162] M. Sonzogni, J.-M. Vanson, K. Ioannidou, Y. Reynier, S. Martinet, and F. Radjai. Dynamic compaction of cohesive granular materials: Scaling behavior and bonding structures. *Soft Matter*, Submitted. [Cited in page 113]

[163] M. E. Spahr, R. Gilardi, and D. Bonacchi. Carbon black for electrically conductive polymer applications. In R. Rothon, editor, *Fillers for Polymer Applications*, pages 375–400. Springer International Publishing, Cham, 2017. [Cited in page 109]

[164] M. E. Spahr, D. Goers, A. Leone, S. Stallone, and E. Grivei. Development of carbon conductive additives for advanced lithium ion batteries. *Journal of Power Sources*, 196(7):3404–3413, 2011. [Cited in page 8]

[165] I. Srivastava, D. S. Bolintineanu, J. B. Lechman, and S. A. Roberts. Controlling Binder Adhesion to Impact Electrode Mesostructures and Transport. *ACS Applied Materials & Interfaces*, 12(31):34919–34930, 2020. [Cited in pages 24, 28, 30, 31, 73 and 89]

[166] M. Steen, N. Lebedeva, F. Di Persio, and L. Boon-Brett. EU Competitiveness in Advanced Li-ion Batteries for E-Mobility and Stationary Storage Applications – Opportunities and Actions. *Publications Office of the European Union*, 2017. [Cited in pages 4 and 5]

[167] A. J. Stershic, S. Simunovic, and J. Nanda. Modeling the evolution of lithium-ion particle contact distributions using a fabric tensor approach. *Journal of Power Sources*, 297:540–550, 2015. [Cited in pages 24 and 32]

[168] W. C. Swope, H. C. Andersen, P. H. Berens, and K. R. Wilson. A computer simulation method for the calculation of equilibrium constants for the formation of physical clusters of molecules: Application to small water clusters. *The Journal of Chemical Physics*, 76(1):637–649, 1982. [Cited in page 23]

[169] D. Tabor. Surface forces and surface interactions. *Journal of Colloid and Interface Science*, 58(1):2–13, 1977. [Cited in page 29]

[170] K. Tasaki, A. Goldberg, and M. Winter. On the difference in cycling behaviors of lithium-ion battery cell between the ethylene carbonate- and propylene carbonate-based electrolytes. *Electrochimica Acta*, 56(28):10424–10435, 2011. [Cited in page 10]

[171] S. C. Thakur. *Mesoscopic Discrete Element Modelling of Cohesive Powders for Bulk Handling Applications*. PhD thesis, University of Edinburgh, 2014. [Cited in page 25]

[172] S. C. Thakur, J. P. Morrissey, J. Sun, J. F. Chen, and J. Y. Ooi. Micromechanical analysis of cohesive granular materials using the discrete element method with an adhesive elasto-plastic contact model. *Granular Matter*, 16(3):383–400, 2014. [Cited in page 27]

[173] V. D. Than, S. Khamseh, A. M. Tang, J.-M. Pereira, F. Chevoir, and J.-N. Roux. Basic Mechanical Properties of Wet Granular Materials: A DEM Study. *Journal of Engineering Mechanics*, 143(1):C4016001, 2017. [Cited in pages 42, 50, 56, 60 and 63]

[174] V.-D. Than, J.-N. Roux, A.-M. Tang, and J.-M. Pereira. Investigation into the isotropic compression of wet granular soils using discrete element method. *E3S Web Conf.*, 9:08008, 2016. [Cited in pages 42 and 56]

[175] C. Thornton. *Granular Dynamics, Contact Mechanics and Particle System Simulations*. Springer International Publishing, 2015. [Cited in page 42]

[176] C. Thornton, S. J. Cummins, and P. W. Cleary. On elastic-plastic normal contact force models, with and without adhesion. *Powder Technology*, 315:339–346, 2017. [Cited in pages 25 and 29]

[177] C. Thornton and Z. Ning. A theoretical model for the stick/bounce behaviour of adhesive, elastic-plastic spheres. *Powder Technology*, 99(2):154–162, 1998. [Cited in pages 27 and 28]

[178] B. L. Trembacki, A. N. Mistry, D. R. Noble, M. E. Ferraro, P. P. Mukherjee, and S. A. Roberts. Mesoscale Analysis of Conductive Binder Domain Morphology in Lithium-Ion Battery Electrodes. *Journal of The Electrochemical Society*, 165(13):E725–E736, 2018. [Cited in pages 17 and 34]

[179] B. L. Trembacki, D. R. Noble, V. E. Brunini, M. E. Ferraro, and S. A. Roberts. Mesoscale Effective Property Simulations Incorporating Conductive Binder. *Journal of The Electrochemical Society*, 164(11):E3613–E3626, 2017. [Cited in pages 17, 91, 100 and 117]

[180] J. M. Valverde and A. Castellanos. Compaction of fine powders: From fluidized agglomerates to primary particles. *Granular Matter*, 9(1-2):19–24, 2007. [Cited in page 41]

[181] J. M. Valverde, A. Castellanos, and M. A. Sanchez Quintanilla. Self-Diffusion in a Gas-Fluidized Bed of Fine Powder. *PRL*, 86(14):3020–3023, Apr. 2001. [Cited in page 41]

[182] J. M. Valverde, A. Castellanos, and P. K. Watson. The effect of particle size on interparticle adhesive forces for small loads. *Powder Technology*, 118(3):236–241, 2001. [Cited in page 41]

[183] G. Van den Bergen. Efficient Collision Detection of Complex Deformable Models using AABB Trees. *Journal of Graphics Tools*, 2(4):1–13, 1997. [Cited in page 20]

[184] L. Verlet. Computer "Experiments" on Classical Fluids. I. Thermodynamical Properties of Lennard-Jones Molecules. *Phys. Rev.*, 159(1):98–103, 1967. [Cited in pages 21 and 23]

[185] B. Vijayaraghavan, D. R. Ely, Y.-M. Chiang, R. Garcìa-Garcìa, and R. E. Garcìa. An Analytical Method to Determine Tortuosity in Rechargeable Battery Electrodes. *Journal of The Electrochemical Society*, 159(5):A548–A552, 2012. [Cited in page 35]

[186] M. Wang, J. Hu, Y. Wang, and Y.-T. Cheng. The Influence of Polyvinylidene Fluoride (PVDF) Binder Properties on $LiNi_{0.33}Mn_{0.33}Co_{0.33}O_2$ (NMC) Electrodes Made by a Dry-Powder-Coating Process. *Journal of The Electrochemical Society*, 166(10):A2151–A2157, 2019. [Cited in page 17]

[187] N. Wang, Y. NuLi, S. Su, J. Yang, and J. Wang. Effects of binders on the electrochemical performance of rechargeable magnesium batteries. *Journal of Power Sources*, 341:219–229, 2017. [Cited in page 8]

[188] Z. Wang, L. Yang, S. Zhu, W.-L. Song, and H.-S. Chen. Exploring mechanical failure of porous electrode meso structure using the discrete element method. *Extreme Mechanics Letters*, 46:101252, 2021. [Cited in pages 24, 28, 29, 33 and 34]

[189] U. Westerhoff, K. Kurbach, F. Lienesch, and M. Kurrat. Analysis of Lithium-Ion Battery Models Based on Electrochemical Impedance Spectroscopy. *Energy Technology*, 4(12):1620–1630, 2016. [Cited in pages 14 and 15]

[190] M. S. Whittingham. Electrical Energy Storage and Intercalation Chemistry. *Science*, 192(4244):1126–1127, 1976. [Cited in page 4]

[191] N. Williard, W. He, C. Hendricks, and M. Pecht. Lessons Learned from the 787 Dreamliner Issue on Lithium-Ion Battery Reliability. *Energies*, 6(9):4682–4695, 2013. [Cited in pages 9 and 11]

[192] D. E. Wolf, T. Unger, D. Kadau, and L. Brendel. Compaction of cohesive powders. In *Powders and Grains 2005*, pages 525–533. Leiden, Balkema, 2005. [Cited in pages 41, 42, 56 and 57]

[193] D. L. Wood, J. Li, and C. Daniel. Prospects for reducing the processing cost of lithium ion batteries. *Journal of Power Sources*, 275:234–242, 2015. [Cited in page 3]

[194] D. M. Wood. *Soil Behaviour and Critical State Soil Mechanics*. Cambridge University Press, 1991. [Cited in page 47]

[195] C.-Y. Wu, B. C. Hancock, A. Mills, A. C. Bentham, S. M. Best, and J. A. Elliott. Numerical and experimental investigation of capping mechanisms during pharmaceutical tablet compaction. *Powder Technology*, 181(2):121–129, 2008. [Cited in page 41]

[196] K. Xu. Nonaqueous Liquid Electrolytes for Lithium-Based Rechargeable Batteries. *Chemical Reviews*, 104(10):4303–4418, 2004. [Cited in page 10]

[197] J. S. Xue, K. Myrtle, and J. R. Dahn. An Epoxy-Silane Approach to Prepare Anode Materials for Rechargeable Lithium Ion Batteries. *Journal of The Electrochemical Society*, 142(9):2927–2935, Sept. 1995. [Cited in page 8]

[198] N. Yabuuchi and T. Ohzuku. Novel lithium insertion material of $LiNi_{1/3}Mn_{1/3}Co_{1/3}O_2$ for advanced lithium-ion batteries. *Journal of Power Sources*, 119–121:171–174, 2003. [Cited in page 7]

[199] H. Yang, C. N. Savory, B. J. Morgan, D. O. Scanlon, J. M. Skelton, and A. Walsh. Chemical Trends in the Lattice Thermal Conductivity of Li(Ni, Mn, Co)O_2 (NMC) Battery Cathodes. *Chemistry of Materials*, 32(17):7542–7550, 2020. [Cited in page 7]

[200] M. Yang, M. Taiebat, P. Mutabaruka, and F. Radjaï. Evolution of granular media under constant-volume multidirectional cyclic shearing. *Acta Geotechnica*, 17(3):779–802, Mar. 2022. [Cited in page 80]

[201] H. Yasuhiko and M. Yoshiyuki. Nonaqueous electrolyte secondary battery and nonaqueous electrolyte secondary battery fabricating method, Nov. 2011. [Cited in pages 90 and 101]

[202] A. Yoshino and K. Sanechika. Japanese Patent Application 1985-127669, 1985. [Cited in page 4]

[203] S.-H. Yu, X. Feng, N. Zhang, J. Seok, and H. D. Abruña. Understanding Conversion-Type Electrodes for Lithium Rechargeable Batteries. *Accounts of Chemical Research*, 51(2):273–281, 2018. [Cited in page 5]

[204] J. Zhang, J. Sun, H. Huang, and Z. Yuan. Influence of calendering process on the structural mechanics and heat transfer characteristics of lithium-ion battery electrodes via DEM simulations. *Particuology*, 85:252–267, 2024. [Cited in pages 90 and 94]

[205] Q. Zhang, Z. Yu, P. Du, and C. Su. Carbon Nanomaterials Used as Conductive Additives in Lithium Ion Batteries. *Recent Patents on Nanotechnology*, 4(2):100–110, 2010. [Cited in page 8]

[206] Z. Zhang, T. Zeng, Y. Lai, M. Jia, and J. Li. A comparative study of different binders and their effects on electrochemical properties of LiMn2O4 cathode in lithium ion batteries. *Journal of Power Sources*, 247:1–8, 2014. [Cited in page 8]

[207] H. Zheng, L. Tan, G. Liu, X. Song, and V. S. Battaglia. Calendering effects on the physical and electrochemical properties of $LiNi_{1/3}Mn_{1/3}Co_{1/3}O_2$ cathode. *Journal of Power Sources*, 208:52–57, 2012. [Cited in pages 8, 12 and 16]

[208] X. Zhong, J. Han, L. Chen, W. Liu, F. Jiao, H. Zhu, and W. Qin. Binding mechanisms of PVDF in lithium ion batteries. *Applied Surface Science*, 553:149564, 2021. [Cited in page 8]

[209] G.-N. Zhu, Y.-G. Wang, and Y.-Y. Xia. Ti-based compounds as anode materials for Li-ion batteries. *Energy Environ. Sci.*, 5(5):6652–6667, 2012. [Cited in page 7]

[210] J. Zhu, X. Zhang, H. Luo, and E. Sahraei. Investigation of the deformation mechanisms of lithium-ion battery components using in-situ micro tests. *Applied Energy*, 224:251–266, 2018. [Cited in pages 16 and 17]

[211] L. Zielke, T. Hutzenlaub, D. R. Wheeler, I. Manke, T. Arlt, N. Paust, R. Zengerle, and S. Thiele. A Combination of X-Ray Tomography and Carbon Binder Modeling: Reconstructing the Three Phases of LiCoO2 Li-Ion Battery Cathodes. *Advanced Energy Materials*, 4(8):1301617, 2014. [Cited in page 16]

[212] X. Zuo, J. Zhu, P. Müller-Buschbaum, and Y.-J. Cheng. Silicon based lithium-ion battery anodes: A chronicle perspective review. *Nano Energy*, 31:113–143, 2017. [Cited in page 8]

Modélisation du calandrage des électrodes Li-ion en tant que matériau granulaire cohésif : des propriétés des grains aux performances de l'électrode

Résumé :

Les batteries Li-ion trouvent leurs applications dans de multiples domaines de la vie courante. Leur performances, telles que la vitesse de charge et la capacité de stockage de l'énergie, sont fortement influencées par la microstructure des électrodes et donc par leur procédé de fabrication, en particulier une étape de compaction appelée calandrage au cours de laquelle l'épaisseur de l'électrode est réduite entre deux cylindres en rotation. Cependant, cette étape de compaction augmente également la tortuosité de l'électrode, diminuant la vitesse de charge/décharge de la batterie ; un compromis est donc recherché entre capacité de stockage de l'énergie et vitesse de charge. La microstructure de l'électrode s'apparente à un milieu granulaire composé de particules actives et d'une matrice poreuse de liant polymère. Cette thèse s'attache à modéliser l'électrode et le procédé de calandrage par une approche numérique discrète. La démarche proposée intègre une étude de l'influence de la cohésion entre les grains, de la pression de confinement et de la vitesse de compaction sur la porosité, la microstructure et les propriétés mécaniques des électrodes. Une étude paramétrique détaillée a permis d'établir une loi d'échelle pour la porosité en fonction d'un nombre sans dimension, d'étudier l'influence des paramètres sur la microstructure et de les relier aux conductivités électriques et ioniques.

Mots-clés : Milieux granulaires, simulation numérique, cohésion, batterie lithium-ion.

Simulation of the calendering process of Li-ion as cohesive granular material : from grains properties to electrode performances

Abstract :

Li-ion batteries are used in many areas of everyday life. Their performance, such as charging rate and energy storage capacity, is strongly influenced by the microstructure of the electrodes and therefore by their manufacturing process, in particular a compaction step called calendering during which the thickness of the electrode is reduced between two rotating cylinders. However, this compaction step also increases the electrode's tortuosity, reducing the battery's charge/discharge rate; a compromise is therefore sought between energy storage capacity and charging rate. The electrode microstructure is a granular medium composed of active particles and a porous matrix of polymer binder. The aim of this thesis work is to model the electrode and the calendering process using a discrete numerical approach, with the goal of better understanding the influence of inter-particle cohesion, confining pressure and compaction rate on the porosity, microstructure and mechanical properties of the electrodes. By means of a detailed parametric study, a scaling law is established for porosity as a function of a dimensionless number, and the influence of the parameters on microstructure is studied and linked with electrical and ionic conductivities.

Keywords : Granular materials, numerical simulations, cohesion, lithium-ion battery.